Charge-Transfer Chemical Reactions and Chiral Discrimination in Electromagnetic Fabry-Pérot Cavities

Lorenzo Mauro

To cite this version:

Lorenzo Mauro. Charge-Transfer Chemical Reactions and Chiral Discrimination in Electromagnetic Fabry-Pérot Cavities. Physics [physics]. Université de Bordeaux, 2022. English. NNT : 2022BORD0223 . tel-03772522

HAL Id: tel-03772522
https://theses.hal.science/tel-03772522
Submitted on 8 Sep 2022

THÈSE PRÉSENTÉE

POUR OBTENIR LE GRADE DE

DOCTEUR
DE L'UNIVERSITÉ DE BORDEAUX

ECOLE DOCTORALE SCIENCES PHYSIQUES ET DE L'INGÉNIEUR

LASERS, MATIÈRE ET NANOSCIENCES

Par **Lorenzo MAURO**

Charge-Transfer Chemical Reactions and Chiral Discrimination in Electromagnetic Fabry-Pérot Cavities

Sous la direction de : **Rémi AVRILLER**

Soutenue le 12 juillet 2022

Membres du jury :

Dario BASSANI	Director of Research	ISM-CNRS in Bordeaux	Jury President
Cyriaque GENET	Director of Research	ISIS-CNRS in Strasbourg	Referee
Enrico RONCA	Permanent Researcher	IPCF-CNR in Pisa	Referee
Johannes FEIST	Professor (R. y C. Fellow)	IFIMAC in Madrid	Examiner
Neepa Maitra	Professor	Rutgers University in New York	Examiner
Gediminas JONUSAUSKAS	Director of Research	LOMA-CNRS in Bordeaux	Examiner
Rémi AVRILLER	Permanent Researcher	LOMA-CNRS in Bordeaux	Supervisor

Contents

1

Acknowledgments

First, I would like to thank my supervisor, Dr. Rémi Avriller, for his great scientific support during the three years of my PhD. The regular discussions initiated new ideas and pushed the project in the right direction. I thank the director of LOMA, Dr. Fabio Pistolesi, for all his advices related to work and life. I acknowledge the collaboration with Dr. Gediminas Jonusauskas for the first part of the PhD and his valuable experimental work. I thank Prof. Dario Bassani, my mentor as part of the graduate program Light Sciences and Technologies, for the useful and nice discussions we had along the three years. I am very pleased for the nice community I met in LOMA. I am very grateful for the collaboration with Prof. Johannes Feist and Dr. Jacopo Fregoni. Especially, I thank Prof. Johannes Feist for accepting me at Universidad Autónoma de Madrid and for the welcoming atmosphere of his group. The collaboration enabled me to achieve important results in the second part of this manuscript. I would like to thank all the jury members for their partecipation at my defense and for the positive feedbacks I received. In particular, I thank Dr. Cyriaque Genet and Dr. Enrico Ronca who read and made the reports for this manuscript. I thank my fiancée who constantly shared my emotions. I thank also my parents who gave their kind support from abroad. I thank all the other people I have met in these years who have been part of this adventure. Finally, I acknowledge the CNRS, the ANR, the graduate program Light Sciences and Technologies, and Quantum Matter of Bordeaux that funded and supported my research.

2

Summary

2.1 English version

The first part of the thesis concerns an investigation on the chemical reactivity of molecular populations confined inside a nanofluidic Fabry-Pérot cavity. Due to strong light-matter interactions developing between a resonant electromagnetic cavity mode and the electric dipole moment of the confined molecules, a collective Polariton excitation is formed. The former gets dressed by environmental vibrational and rotational degrees of freedom of the solvent. We call the resulting Polariton dressed by its cloud of environmental excitation a "*Reacton*", since it further undergoes chemical reactions. We characterize how the *Reacton* formation modifies the kinetics of a photoisomerization chemical reaction involving an elementary charge-transfer process. We show that the reaction driving force and reorganization energy are both modulated optically by the reactant concentration, the vacuum Rabi splitting, and the detuning between the Fabry-Pérot cavity frequency and targeted electronic transition. Finally, by computing the ultrafast picosecond dynamics of the whole photochemical reaction, we predict that, despite optical cavity losses and solvent-mediated nonradiative relaxation, measurable signatures of the reacton formation can be found in state-of-the-art pump-probe experiments.

The second part focuses on the chiral discrimination in Fabry-Pérot cavities. A Fabry-Pérot interferometer filled with chiral molecules has a well defined Differential Circular Transmission (DCT) signal under normal illumination of circularly polarized light. Based on this figure of merit, we firstly provide analytical and numerical evidence that traditional Fabry-Pérot interferometers cannot enhance the chiroptical response of molecules, because the mirrors perfectly convert the circular polarization of light rays. We hence propose and model an helicity-preserving cavity, with chiral mirrors, satisfying time-reversal symmetry. The empty cavity, made by the modelled chiral mirrors, generates a spectral helicity-preserving region which is not available with a traditional interferometer. The region breaks, in a small frequency range, the perfect internal conversion of polarized light and thus it enables to discriminate the otherwise achiral cavity light modes. Polaritons which are generated at resonance with the preserving region thus inheritates a partial chiral character. By subtracting the helicity-preserving cavity contribution to the total DCT, we show that our proposed setup is up to two orders of magnitude more sensitive with respect to the chiroptical response of the isolated molecules. We reveal that the registered enhancement is consistent even for an extremely weak molecular chiroptical responses, and that our setup can enhance the chiral signal of molecules either in the weak or in the strong coupling (Polaritonic) regime.

Keywords: Optical cavities, light-matter interactions, polaritons, polaritonic chemistry, charge transfer chemical reactions, polarization, circular dichroism, chirality, chiral sensing.

2.2 Résumé (french version)

La première partie de la thèse concerne l'étude de la réactivité chimique d'une population de molécules confinées à l'intérieur d'une cavité Fabry-Pérot nanofluidique. En raison de l'interaction forte lumière-matière qui se développe entre un mode résonant de la cavité et le moment dipolaire électrique des molécules confinées, une excitation collective de type « Polariton » est formée. Nous montrons que le Polariton est habillé par un nuage d'excitation environnemental dû aux degrés de liberté vibrationnels et rotationnels du solvant. Nous appelons l'excitation résultante un "Réacton", car ce dernier est susceptible de réagir chimiquement. Nous caractérisons la modification de cinétique d'une réaction chimique de type photoisomérisation impliquant un processus élémentaire de transfert de charge dû à la formation du Reacton. Nous montrons que l'enthalpie de réaction et l'énergie de réorganisation sont modulées optiquement par la concentration du réactif, le vacuum Rabi splitting, et l'écart entre la fréquence optique de la cavité Fabry-Pérot et la transition électronique ciblée. Enfin, nous calculons la dynamique pico-seconde de cette réaction de transfert de charge, et prédisons que, malgré les pertes de la cavité optique et les pertes non-radiatives dues au solvant, une signature mesurable par expérience pompe-sonde de la formation du Réacton peut être trouvée.

La deuxième partie est consacrée à l'étude des propriétés optiques de cavités Fabry-Pérot chirales. Un interféromètre Fabry-Pérot rempli de molécules chirales présente un signal de dichroisme circulaire en transmission (DCT) bien défini sous illumination normale par une lumière polarisée circulairement. Nous caractérisons cette figure de mérite théoriquement et fournissons une preuve analytique et numérique que les interféromètres Fabry-Pérot traditionnels ne peuvent pas améliorer la réponse chiroptique des molécules, du fait de la conversion de polarisation à chaque réflexion de la lumière sur les miroirs de la cavité. Nous proposons donc de remplacer les miroirs par des métamatériaux diélectriques symétriques par renversement du temps. Cette cavité génère une fenêtre de fréquences pour laquelle l'hélicité des rayons réfléchis est conservée, réalisant de fait une discrimination chirale des modes optiques de la cavité. Les Polaritons générés héritent au voisinage de cette région d'un caractère chiral. Nous montrons que ce dispositif permet de réaliser une mesure de DCT relative jusqu'à deux ordres de grandeur plus sensible que celle obtenue avec une cavité traditionnelle, et peut être utilisé comme dispositif innovant et alternatif pour améliorer le sensing de molécules chirales en cavité.

Mots-clés: Cavités optiques, interactions lumière-matière, polaritons, chimie polaritonique, réactions de transfert de charge, polarisation, dichroism circulaire, chiralité, sensing.

Part I

Charge-Transfer Chemical Reactions in Fabry-Pérot Cavities

3

Introduction

Enzymatic catalysis is one of the most important chemical reactions for living organisms. Enzymes reduce the activation energy, the energetic barrier, to accelerate the conversion of reactants into products or viceversa [172, 42], without modifying the nature of the chemical reaction (see Figure 3.1). Many biological reactions cannot even start without the presence of enzymes. Some fundamental questions can be raised about the fascinating properties of these proteins. Is there an engineered way to mimic the action of enzymes? Is it possible to design alternative routes, by analogy to enzymatic catalysis, to speed up or slow down a chemical reaction without altering the reaction itself?

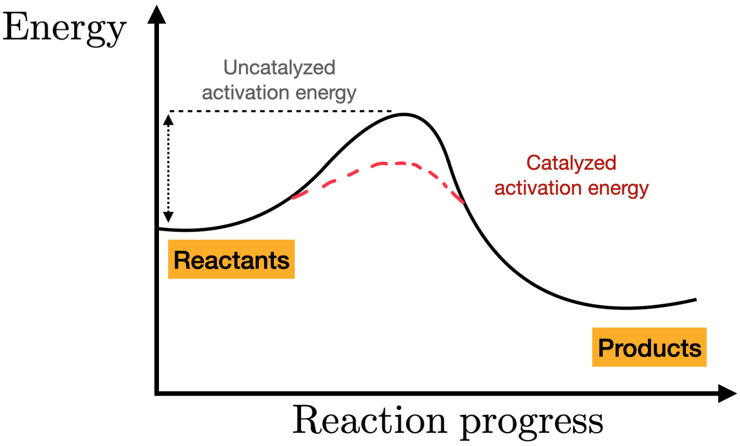

Figure 3.1: Change of the activation energy due to the action of enzymes.

An emergent and very active scientific field of research called "*Polaritonic Chemistry*" [39, 48, 72, 116, 46, 69, 133, 71] aims to study, theoretically understand and experimentally verify the modification of chemical reactions through strong coupling between light and molecules. In this context, the enzymes are in some sense replaced by a reorganization of energy levels due to the strong light-matter interaction. The result is the formation of hybrid light-matter states, called *Polaritons*. They are collective excitations which originate for the strong interaction of the quantized electromagnetic vacuum field of a cavity with the molecules interacting with it. What is surprising is that the reaction energy landscape is modified by coupling to vacuum fluctuations, without the need for an external laser field in order to alter the chemical processes.

Achieving strong coupling has a long history, and early developments are briefly presented below.
The first experimental demonstration of the strong light-matter coupling was reported, in 1975, by V. A. Yakovlev *et al.* [174]. They found the so-called Polariton splitting for the resonant surface interactions of thin metals on dielectrics. In particular, the first experiment revealed surface Polaritons originating from the lateral confinement of metal-dielectric interfaces.

Other early experiments reached the strong coupling regime with Fabry-Pérot resonators and Rydberg atoms [65, 88, 132], at low temperature. Serge Haroche and David J. Wineland were awarded the Noble

Prize for their experiments in the framework of Cavity Quantum Electrodynamics. The Fabry-Pérot cavity consists of two plane metallic mirrors, made by silver (Ag), aluminium (Al) or gold (Au) for their high reflectivity, separated by an intracavity space where the molecules or dielectric layers are inserted. The length of the intracavity space is adjusted so that the photons, which probe the inserted molecular layer many times, resonate with the molecular transition. Thus, when the light-matter interaction becomes higher than dissipative mechanisms (photon leakage or non-resonant decay of molecules), which tend to decrease the perfect confinement, the strong coupling regime is achieved. The first experiments adopted inorganic materials. The first pioneering experiment in Fabry-Pérot microcavity with organic molecules was made, in 1998, by D. G. Lidzey *et al.* [101]. They measured a Rabi splitting, the light-matter coupling, of approximately 160 meV, more than 30 times the typical splitting observed for quantum-well microcavities at room temperature. Indeed, organic molecules have large transition dipole moments that increase naturally the strength of the coupling. This work was also an experimental demonstration of a theoretical work by Agranovich *et al.* [1], and opened future investigations on strong light-matter interactions at room temperature.

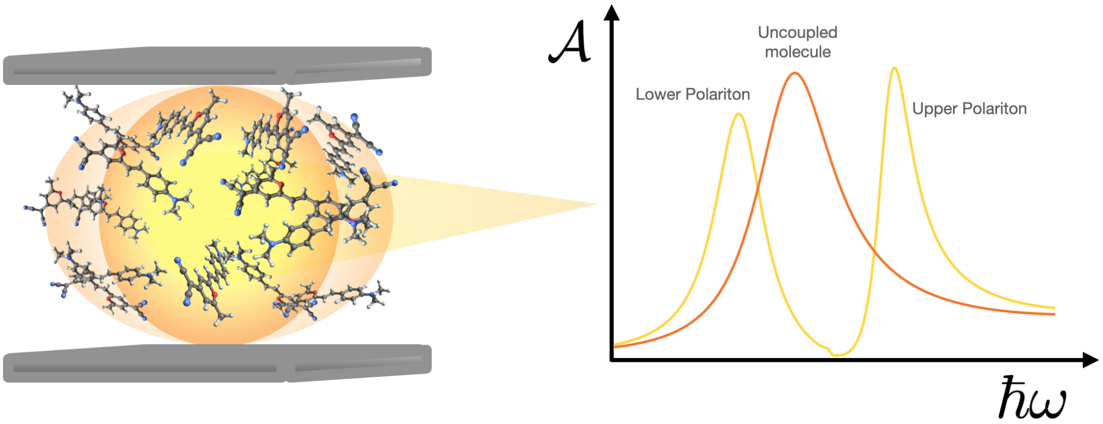

Figure 3.2: Strong coupling achieved in a Fabry-Pérot cavity between the vacuum field and a molecular ensemble (on the left-hand side). On the right-hand side typical Polaritonic states resolved in absorption ($\mathcal{A}$) spectrum, by using an home-made classical transfer matrix method (see Section 13.8), as a function of energy $\hbar\omega$.

Recent experimental works, at room temperature, have shown on the one hand that liquid Fabry-Pérot nanocavities have excellent optical qualities to observe strong coupling effects for molecular solutions [6] and on the other hand that Polaritons can be obtained even for a single molecule placed in a tiny nanogap (approximately 0.9 nm) by coupling to localized plasmons (see Figure 3.3) [24].

The idea of using the strong coupling regime to change chemical reactions in a reversible manner was primarily due to Thomas Ebbesen. Over the past decade, Ebbesen and his collaborators have experimentally designed many scenarios in which strong coupling changes different types of chemical reactions [143, 159, 60, 144, 80, 139, 39, 179, 180, 79, 167, 119, 6]. The research field called “Polaritonic Chemistry” was born with those experiments. One of those experiments inspired particularly the first part of this manuscript [111]. That work [80] consists in a slowing of a photoisomerization (spiropyran-merocyanine) in a Fabry-Pérot cavity as the system enters strong-coupling conditions (see Figure 3.4). The strong coupling is achieved at resonance with the electronic transition of merocyanine and Polaritons, the Upper Polariton (at higher energy) and the Lower Polariton (at lower energy), are spectroscopically resolved. They are clearly distinguishable in the absorption spectrum as two peaks well separated by a splitting of the order of 700 meV. An amount of about 80% molecules (merocyanine species) are strongly coupled to fluctuations of vacuum field of the cavity, and this collective ensemble of molecules alter significantly the chemical reaction. An important point is precisely that the strong coupling is a collective effect which involves a significant fraction of molecules but not all the molecules are coupled.

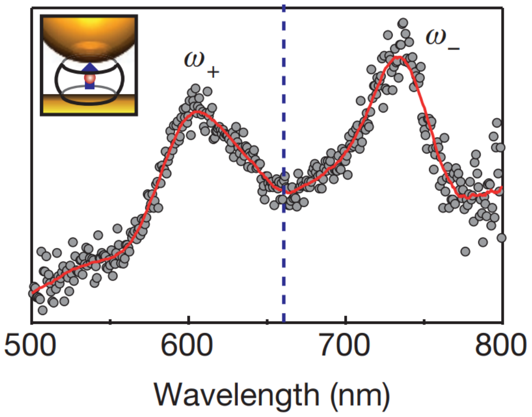

Figure 3.3: Strong coupling seen in scattering spectra of individual NPoMs. Adapted from [24].

To get more information about the coupled and uncoupled molecules, the authors use a technique called *pump-probe spectroscopy*. A pump, an ultrafast laser field (pulses with durations of hundreds of femtoseconds), is used to photoexcite the system with minimal perturbation of it, and a second pulse, the probe, detect the changes of the system. In cavity-coupled materials, pump-probe experiments measure reflectance, transmittance or absorbance as a function of the delay time between the pump and the probe. Changes in these observables can be seen in the *transient spectra*, which are the difference between the spectra after and before the pumpe has "gently" perturbed the system. Using this technique, J. A. Hutchison *et al.* discovered that the coupled and uncoupled molecules, in a disordered molecular system, contribute to the transient spectrum. In the strong coupling regime, the transient absorption spectrum is dominated by the coupled system. Furthermore, by exciting in the ground state to the Lower Polariton absorption band, the transient spectrum is only slightly modified. The conclusion was that the Upper Polariton relaxes faster to the Lower Polariton, which is the longest-lived excited state (fractions of picoseconds). In 2015 this fact was theoretically studied with a "dressing" of vibrational relaxation rates for the onset of the Polariton formation [19].

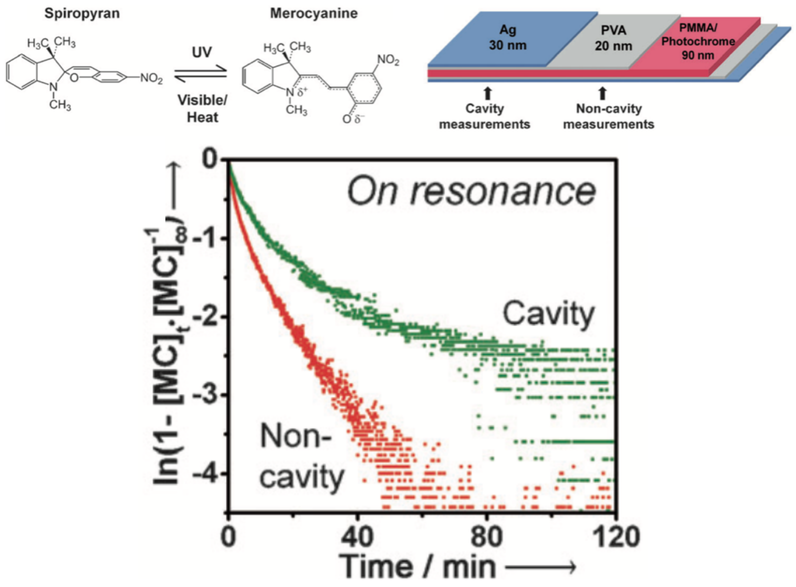

Figure 3.4: Kinetics of the growth of the MC concentration measured for the bare molecules (red) and the coupled system (green) in the cavity configuration shown above the plot. Adapted from [80].

The presented experiment achieved the strong coupling at resonance with the molecular electronic transition. An alternative approach is to achieve the so-called vibrational strong coupling (VSC). VSC is the strong interaction between the cavity mode and a vibrational mode of the molecules. The strong interaction results in the formation of vibropolaritonic states that can be observed via infrared spectroscopy. The first experimental prediction of VSC was reported in 2014 [69]. Subsequent works have shown that reactivity can be slow down or catalyzed by VSC [160, 96, 158, 73, 178, 121, 171]. In particular, a recent experiment [121] emphasizes the important role of symmetry of the coupled vibrational modes to provide an explanation for the induced chemical modifications.

Experimental results were accompanied by intense and deep theoretical studies. One of the simplest phenomenological theoretical model which describes the Polariton formation due to a collective strong coupling is the Jaynes-Cummings model [157]. It gives the exact solution of N identical, non-interacting two-level systems coupled to a single quantized mode of the cavity. The exact solution is given by the Upper and Lower Polaritons plus N−1 degenerate uncoupled states (see Figure 3.5), in the single photon sector. These uncoupled states, *i.e.* states which are not coupled to cavity light mode, were called *Dark states*. The number of Dark states increases rapidly in comparison with Polaritons. For this reason, they were also denoted as exciton bath or reservoir. These degenerate states remain in the middle of the two Polaritons, at the energy of the bare excited state, but may play a role in energy transfer and dissipative processes. An important investigation of a disordered system of N atoms described by the Jaynes-Cummings model was done by R. Houdré *et al.* [77]. They show that the peak separation of the splitting between the Lower and the Upper Polariton is independent of an inhomogeneous broadening induced at the level of the excited states. A more realistic situation of a disordered molecular system. In contrast, the degeneracy of Dark states is lifted with a resulting creation of mini-band of states. The scenario is valid for a weak disorder, smaller than the Rabi coupling. An higher disorder would mix the Polaritonic states with the Dark state manifold.

The Jaynes-Cummings model offers a collective description in the so-called homogeneous limit [69]. It is based on a simple two-level system that cannot describe the vibrational and rotational degrees of freedom of molecules. Moreover, it gives an homogeneous description because it neglects the local spatial variations that are also difficult to monitor in experiments, which usually show an average contribution of a macroscopic ensemble of molecules. In 2015, Javier Galego *et al.* developed a first-principles model that fully takes

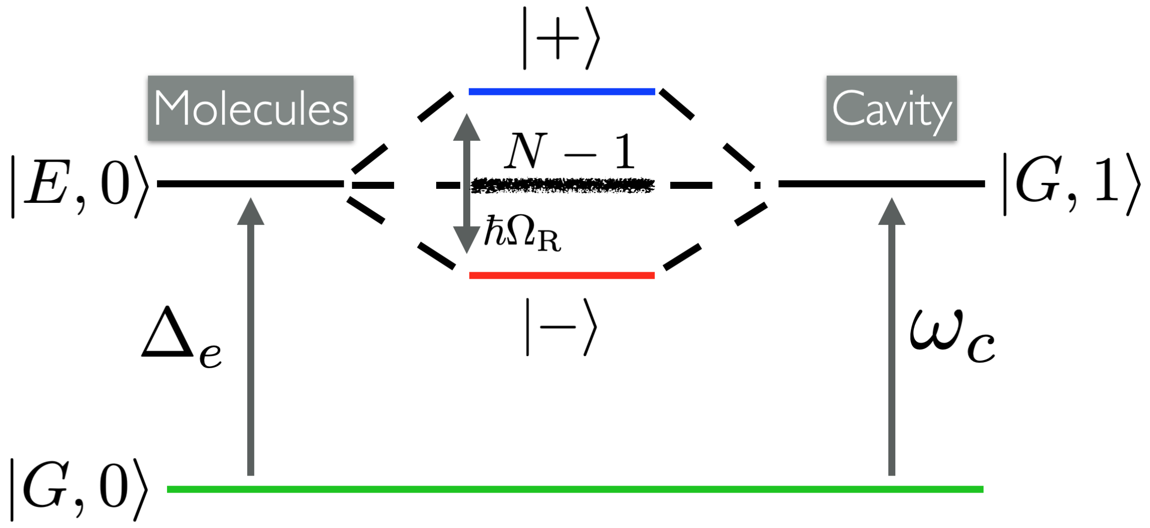

Figure 3.5: Polaritonic splitting (Upper Polariton denoted as $|+\rangle$ and Lower Polariton denoted as $|-\rangle$) due to the collective strong Rabi energy ($\hbar\Omega_\mathrm{R}$). The electronic transition (Δ_e) is at resonance with the cavity mode (ω_c). In the middle of the Polaritonic splitting there is a manifold of N−1 Dark states (predicted by the Jaynes-Cummings model [36]). The ground state of the molecular ensemble is denoted as $|G,0\rangle$. The excitation, the matter part, shared by the N molecules is denoted as $|E,0\rangle$. The ground state with one photon, the light part, is denoted by $|G,1\rangle$.

into account both electronic and nuclear degrees of freedom [55]. The Polaritons are described using the Born-Oppenheimer approximation, which separates the fast electron dynamics and the slow nuclear motion. In this way, they were able to describe the Polariton dynamics with the corresponding Potential Energy Surface (PES), when the Rabi splitting is large, a concept widely used in chemistry to investigate chemical reactions along different reaction coordinates [113]. Eventually, they show an almost complete suppression of a general kind of photochemical reactions using the previously developed model with PESs [56].

Another generalization of the Jaynes-Cummings model, with the aim of including nuclear degrees of freedom, has been suggested, in 2016, by Felipe Herrera and Franck C. Spano [70]. The model has been called Holstein-Tavis-Cummings model (HTC). It describes N identical "vibrating" molecules strongly coupled to a single cavity mode. The model considers the intramolecular modes of the molecules coupled and uncoupled to the cavity. Furthermore, it adds the modification of *reorganization energy* for the electronic transition from the ground state to the excited one. In case of negligible Rabi coupling (out of the cavity), the proposed model recovers a standard Holstein model with optical photons [75]. The Holstein-Tavis Cummings model inspired other theoretical works, in the same year, as a way to better quantify the conformational change of coupled molecules [176, 173]. Importantly, a recent experiment with rubrene microcavities [155] shows a very good agreement with the HTC model to describe the optical response and chemical reactivity of Polaritons in the optical regime.

The work of Herrera and Spano [70], using the so-called HTC model, showed that the resonant collective strong coupling decouple electronic and nuclear degrees of freedom with a resulting significant modification of intramolecular electron-transfer (ET) reactions. ET reactions in solution are one of the most common and fundamental chemical reactions that play a crucial role in various chemical processes [127]. In the simplest case, an electron of charge $-e$ (e is the elementary charge) is transferred from an anion (A^-) to a cation (C^+), following the ET reaction $A^- + C^+ \longrightarrow A + C$. The theoretical description of ET reactions has a long history [127], which was fully developed after the works of Marcus and co-workers [107, 109, 145, 108], and Kestner *et al.* [89], with later successful applications for biological molecules [76]. At the heart of Marcus theory is the necessity to take into account explicitly the solvent in the modelling of ET reaction rates. Out-of-equilibrium fluctuations in the solvent nuclear coordinates are indeed necessary to reach the crossing point of the reactant (R) and product (P) potential energy surfaces, at which the electron transfer occurs. Recent theoretical works on ET reactions in confined electromagnetic environment reported a cavity-induced significant enhancement of the ET reaction rate for a single molecule [141, 106]. Another work included N channels with an incoherent pumping of photons [170], using a quantum optics Lindblad master equation.

The change of chemical reactions, as the class of ET transfer reactions, in cavity are phenomenologically described by the presented Jaynes-Cummings and the HTC model. In experiments, the Polariton formation is usually detected by measuring transmission, reflection or absorption spectra of the coupled molecules. These spectra can be theoretically computed using a completely classical model. The collective Rabi coupling is replaced by the classical oscillator strength of a linear and dispersive modelling of dielectric media [181]. The total response of structured systems such as a cavity with a material inside or complex multilayer systems is obtained with the *transfer matrix* method (the second part of this manuscript deals with this technique) [105, 86]. This method is based on classical light propagation through different layers in terms of length and refractive index (the right-hand side of Figure 3.2 is obtained with the transfer matrix method). ***All these phenomenological, quantum and classical approaches only partially describe the experiments. One of the unclear and debated aspects is the interplay between collective and local effects and their reciprocal interaction in order to generate a strong light-matter coupling.*** Moreover, how the energy is transferred between Polaritons, Dark states and other uncoupled states, in a disordered molecular system, is poorly understood.

A promising trend in Polaritonic Chemistry is the development of semi-*ab initio* and full *ab initio* methods. The semi-*ab initio* methods treat the material degrees of freedom using quantum chemical methods, but the cavity field and the light-matter coupling parameters are obtained from experiments [135, 52, 50, 104, 49]. The full *ab initio* methods, despite the higher computational complexity, would in principle describe the quantum electrodynamical problem without the need for experimental input [146, 147, 134, 67, 66, 164, 135, 74]. Most of the full *ab initio* methods have been developed over the last few years. One is the so-called quantum electrodynamical density-functional theory (QEDFT) [136, 147], an extension of density functional theory

(DFT) [124] to quantum electrodynamics (QED), which describes interacting electrons and photons on an equal footing. It provides an optimal balance between accuracy and computational efficiency to reproduce the main polaritonic features for large systems. Unfortunately, it is based on an unknown form of the exchange correlation functional for the electron-photon interaction. In 2020, QEDFT has been combined with another method: the quantum electrodynamics coupled cluster theory (QED-CC) [66]. This nonperturbative theory accurately treats electron correlation in both ground and excited states of molecular systems and it has been used to reveil, for instance, that the ground-state potential energy surface of pyrrole molecule is modified in cavity [66]. Eventually, both discussed methods have been compared to investigate cavity-induced effects on different types of intermolecular interactions suggesting the possibility to modify the ground state properties of molecular systems [67]. Recently, a novel *ab initio* method which considers a chain of few dimers in cavity, without the presence of a solvent, has been developed by Dominik Sidler *et al.* [148]. They confirm different collective effects predicted by phenomenological models. The novelty of this *ab initio* method consists in adding a small perturbation, an impurity, of the bond length in one of the dimers. Doing this, they demonstrated that collective coupling can induce strong local modifications of molecular systems in the proximity of the perturbation. In addition, the simulation contains the first *ab initio* description of collective dark states in Polaritonic Chemistry.

Many questions are open at the actual stage of this exciting field of Polaritonic Chemistry. Experiments, that have been followed by many theoretical investigations [17, 50, 54, 68, 100, 122], and *ab initio* methods are struggling to reconcile results on VSC. The mechanisms of VSC and how it influences the chemical reactions are unknown and under debate. A complete picture of the energetic pathways between Polaritons and Dark States is missing. Experiments using pump-probe spectroscopy are reaching the *ultrastrong coupling* regime (a Rabi splitting of order of 1-1.6 eV, 10-50% of the molecular transition) to have well-separated Polariton peaks, free of spectral congestion. In this way, Polaritons can be selectively photoexcite by trying to decouple the different energy pathways [34, 33]. Studies are starting to investigate thermodynamic properties of the coupled and uncoupled states [138]. The role of the solvent could be important to better understand dissipative mechanisms and reorganization of nuclear coordinates during charge transfer reactions [111]. Furthermore, technological applications of molecular polaritonic systems could be found in novel photonic and chemical systems: solar cells, OLEDs, OLET [5], or screen displays.

Experiments and theory have already contributed to a rapid increase in knowledge of phenomena that were totally unknown ten years ago. *Ab initio* theory seems a promising direction for future theoretical works, but a good understanding of the dominant mechanisms could help the development of simple analytical descriptions for experimental results.

The state of the art of Polaritonic Chemistry shows the multitude of classical and quantum approches available, and different setups to achieve electronic or vibrational strong coupling in order to modify photochemical or ET transfer reactions. Our theoretical work focuses on Fabry-Pérot cavities as the platform for achieving electronic strong coupling in order to study, using an HTC-based model, the modification of intramolecular charge-transfer reactions (reactions where the charge is only partially transferred during the chemical process but they are described by the same theoretical framework of ET reactions). In the contents below, the detailed structure of the work is presented.

3.1 Contents

The first part of this manuscript starts with the description of a simple model, the Jaynes-Cummings model (see Section 4.1 and Section 4.2). The Hamiltonian of the model is diagonalized analytically under the Rotating-Wave approximation and it is compared with the full numerical diagonalization. In particular, the light-matter strong coupling regime, achieved for the confinement in a cavity, is investigated. Eventually, the Jaynes-Cummings Hamiltonian is extended for N molecules and "weak" vibrational degrees of freedom are taken into account (see Section 4.3). The extended model is called Holstein-Tavis-Cummings model. From this generalization, the quadratic Potential Energy Surface is derived analytically, performing an adiabatic approximation (see Sections 4.3.2 and 4.3.3). A numerical check is added. Furthermore, the Potential Energy Surfaces for the light-matter states, Polaritonic states, are perturbed by inhomogeneous broadening (Section 4.4).

The Chapter 5 presents the electron-transfer theory and contains the derivation of the nonadiabatic electron-transfer rate. The same Chapter also shows a comparison between the classical Marcus rate and the derived quantum nonadiabatic rate (see Section 5.4).

The tools and theory of Chapter 4 and Chapter 5 enable the construction of the last two important chapters. Chapter 6 unifies the construction of the Potential Energy Surfaces for light-matter states with the theoretical framework of electron-transfer reactions to investigate an intramolecular charge-transfer reaction in a nanofluidic Fabry-Pérot cavity (see Section 6.1 and Section 6.2). The new concept of *Reacton*, as a collective molecular excitation dressed by interaction with vibrational and solvent modes, is introduced (see Section 6.1.5). The end of Chapter 6 shows how the *Reacton* formation influences the intramolecular charge-transfer reaction in cavity at thermal equilibrium. The last Chapter contains a minimal microscopic model to induce dissipative mechanisms, radiative and nonradiative, to the *Reacton* states (see Section 7.1). The formulation of the rates takes similarities from the previously derived nonadiabatic charge-transfer rates. Finally, a first-order rate equation, collecting chemical and dissipative rates, is numerically solved to study the out-of-equilibrium fast time evolution of *Reacton* (Section 7.2).

4

Coherent Description of Molecules Strongly coupled to Radiation and Weakly coupled to Vibration

4.1 Jaynes-Cummings model

The Jaynes-Cummings Model (J-C), first developed in 1963 by Edwin Jaynes and Fred Cummings (also known as Jaynes-Cummings-Paul Model[1]), is the most simple theoretical model that describes the interaction of a two-level atom system with a single mode of the quantized electromagnetic field, in a lossless cavity.
This first section shows the J-C Model with an exact and numerical diagonalization of the corresponding Hamiltonian.

4.1.1 Two-level atom and radiation

The physics of exact two-level systems constitutes the basis for Quantum Optics (QO) and Cavity Quantum Electrodynamics (CQED). Such systems are mathematically simple models and they bring out some general and important physical ideas as the interaction between atom, molecules and the collection of Degrees of Freedom (DOF) surrounding them. The two-level atom is represented by two states called $|g\rangle$ and $|e\rangle$, where g is the ground state and e is the first excited state. These two states are connected by an electric dipole transition at angular frequency ω_0. This system is equivalent to a spin 1/2 evolving in a given space [27], with a magnetic field oriented along the vertical axis z; accounting for energy difference between the two states. Indeed the Hamiltonian for this two-level atom is:

$$\hat{\mathrm{H}}_{\mathrm{atom}} = \frac{\Delta}{2}\hat{\sigma}_z, \tag{4.1}$$

where $\hbar\omega_0 \equiv \Delta$ and $\hat{\sigma}_z$ is a Pauli matrix.
The lowering and raising operators $\hat{\sigma}_\pm$ are defined as:

$$\hat{\sigma}_\pm = \frac{1}{2}\left(\hat{\sigma}_x \pm i\hat{\sigma}_y\right), \tag{4.2}$$

where $\hat{\sigma}_x$ and $\hat{\sigma}_x$ are two Pauli matrices.
In terms of the ground and the excited states:

$$\hat{\sigma}_+ = |e\rangle\langle g|\,, \quad \hat{\sigma}_- = |g\rangle\langle e|\,. \tag{4.3}$$

In this way it is possible to rewrite the atomic Hamiltonian:

$$\hat{\mathrm{H}}_{\mathrm{atom}} = \frac{\Delta}{2}\left(|e\rangle\langle e| - |g\rangle\langle g|\right), \tag{4.4}$$

where the relation $\hat{\sigma}_z = \hat{\sigma}_+\hat{\sigma}_- - \hat{\sigma}_-\hat{\sigma}_+$ is used.
The usual Hamiltonian that takes into account electromagnetic radiation in cavity (only one mode) is:

$$\hat{\mathrm{H}}_{\mathrm{field}} = \hbar\omega_c\hat{a}^\dagger\hat{a}, \tag{4.5}$$

---

[1] The model was independently created in the same year by Harry Paul [126].

where it is rescaled the zero-point energy value and ω_c is the angular frequency of the cavity. So the bare Hamiltonian, atom plus the cavity mode without interaction, is:

$$\boxed{\hat{\mathrm{H}}_0 = \left(\varepsilon_g \left|g\right\rangle \left\langle g\right| + \varepsilon_e \left|e\right\rangle \left\langle e\right|\right) + \hbar\omega_c \hat{a}^\dagger \hat{a},} \tag{4.6}$$

where $\varepsilon_g \equiv -\Delta/2$, and $\varepsilon_e \equiv \Delta/2$.

4.1.2 Interaction

The two-level atom system interacts with the radiation through a dipole interaction:

$$\hat{\mathrm{H}}_{\text{int}} = \hat{\vec{d}} \cdot \hat{\vec{E}} = \hat{\vec{d}} \cdot \sqrt{\frac{\hbar\omega_c}{2\epsilon_0 V}} \cdot \vec{\epsilon}_p \left(\hat{a} + \hat{a}^\dagger\right), \tag{4.7}$$

where $\sqrt{\hbar\omega_c/2\epsilon_0 V}$ is the amplitude of the quantized electric field, $\vec{\epsilon}_p$ is the vector polarization and $\hat{\vec{d}}$ is the dipole operator. The resulting interaction is an approximation called "*dipole approximation*" where the spatial change over the atom is discarded and the electron interacts with a constant electric field. The dipole operator can be written in terms of the lowering and raising operators (see eq. (4.2)) and thanks to the parity symmetry ($x \to -x$) of orbital its matrix representation has only off-diagonal contributions. Then

$$\hat{\vec{d}} = \vec{d}\left(\hat{\sigma}_+ + \hat{\sigma}_-\right) = \vec{d}\left(\left|e\right\rangle \left\langle g\right| + \left|g\right\rangle \left\langle e\right|\right), \tag{4.8}$$

where d is a real value.
The interacting Hamiltonian becomes:

$$\hat{\mathrm{H}}_{\text{int}} = \frac{\hbar\Omega_R}{2} \left(\left|e\right\rangle \left\langle g\right| + \left|g\right\rangle \left\langle e\right|\right) \cdot \left(\hat{a} + \hat{a}^\dagger\right), \tag{4.9}$$

where $\hbar\Omega_R = 2\hat{\vec{d}} \cdot \sqrt{\hbar\omega_c/2\epsilon_0 V} \cdot \vec{\epsilon}_p$ is the vacuum Rabi coupling.
Finally the Hamiltonian of the J-C model is:

$$\boxed{\hat{\mathrm{H}}_{\text{J}-\text{C}} = \left(\varepsilon_g \left|g\right\rangle \left\langle g\right| + \varepsilon_e \left|e\right\rangle \left\langle e\right|\right) + \hbar\omega_c \hat{a}^\dagger \hat{a} + \frac{\hbar\Omega_R}{2} \left(\left|e\right\rangle \left\langle g\right| + \left|g\right\rangle \left\langle e\right|\right) \cdot \left(\hat{a} + \hat{a}^\dagger\right).} \tag{4.10}$$

4.1.3 Diagonalization of the Hamiltonian under RWA

The state space of our total system is composed by the tensor product of the two states of the atom ($\left|g\right\rangle$, $\left|e\right\rangle$) and the state of a single mode of the field $\left|n\right\rangle$. An exact diagonalization of the Hamiltonian given by the eq. (4.10) is not easily expressible in terms of standard operators, because the result is an infinite matrix. The total Hamiltonian can be exactly diagonalized using an approximation, the so-called *Rotating-Wave Approximation* (RWA) [63]. Under RWA it is possible to neglect terms that oscillate too fast with respect to the atomic response. This truncation can be seen by expressing the operators in the "Interaction Picture":

$$\begin{aligned} \hat{a}(t) &= \hat{a} e^{-i\omega_c t}, \quad \hat{a}^\dagger(t) = \hat{a}^\dagger e^{+i\omega_c t} \\ \hat{\sigma}_-(t) &= \hat{\sigma}_- e^{-i\omega_0 t}, \quad \hat{\sigma}_+(t) = \hat{\sigma}_+ e^{+i\omega_0 t}. \end{aligned} \tag{4.11}$$

Now by substituting these operators into the interacting Hamiltonian (4.9) and working near resonance $\omega_c - \omega_0 \approx 0$, terms with 2Δ in the argument of the exponential appear. Neglecting these very fast oscillating terms, the J-C Hamiltonian becomes:

$$\boxed{\hat{\mathrm{H}}_{\text{J}-\text{C,RW}} = \left(\varepsilon_g \left|g\right\rangle \left\langle g\right| + \varepsilon_e \left|e\right\rangle \left\langle e\right|\right) + \hbar\omega_c \hat{a}^\dagger \hat{a} + \frac{\hbar\Omega_{\mathrm{R}}}{2} \left(\left|e\right\rangle \left\langle g\right| \hat{a} + \left|g\right\rangle \left\langle e\right| \hat{a}^\dagger\right).} \tag{4.12}$$

This Hamiltonian is exactly solvable. By taking the basis for the first excitation sector ($n = 1$), that is $|g, 1\rangle$ and $|e, 0\rangle$, the eigenvalues and the eigenstates of the Hamiltonian under RWA are:

$$\begin{aligned}
\mathcal{E}_{\pm} &= \frac{1}{2}\left(\varepsilon_g + \varepsilon_e + \hbar\omega_c \pm \hbar\sqrt{\delta^2 + \Omega_R^2}\right), \\
\mathcal{E}_g &= \varepsilon_g, \\
|+\rangle &= \cos\theta\,|g, 1\rangle + \sin\theta\,|e, 0\rangle\,, \\
|-\rangle &= -\sin\theta\,|g, 1\rangle + \cos\theta\,|e, 0\rangle\,, \\
|\mathcal{G}\rangle &= |g\rangle\,,
\end{aligned} \tag{4.13}$$

where $\delta \equiv \omega_c + \varepsilon_g/\hbar - \varepsilon_e/\hbar$ is the detuning, $\sin\theta = \frac{1}{\sqrt{2}}\sqrt{1 - \delta/\Omega_R}$ and $\cos\theta = \frac{1}{\sqrt{2}}\sqrt{1 + \delta/\Omega_R}$. Using this approximation the ground state $|\mathcal{G}\rangle$ is not affected by the interacting Hamiltonian. Figure 4.1 and Figure 4.2 show how the energy levels $\mathcal{E}_{\pm}$ change by increasing the cavity mode energy $\hbar\omega_c$. Figure 4.1 displays the case of $\hbar\Omega_R = 0\,\mathrm{eV}$ and the detuning δ is 0 for $\hbar\omega_c = 2\,\mathrm{eV}$. At that value the two energy levels have a crossing point. The cross disappears for a non-zero value of $\hbar\Omega_R$, as the Figure 4.2 shows. The interacting Hamiltonian (4.9) does indeed have the effect of splitting the two energy levels.

The two eigenstates $|\pm\rangle$, at resonance ($\delta = 0$) between the cavity mode and the atomic transition, are hybrid light-matter states since they are combinations of a Fermionic electronic part and a bosonic photonic part. These states are usually called *Polaritons* [39]. At strong detuning ($\delta \to \pm\infty$), the Upper and Lower Polariton coincide back with the states $|g, 1\rangle$ and $|e, 0\rangle$, respectively.

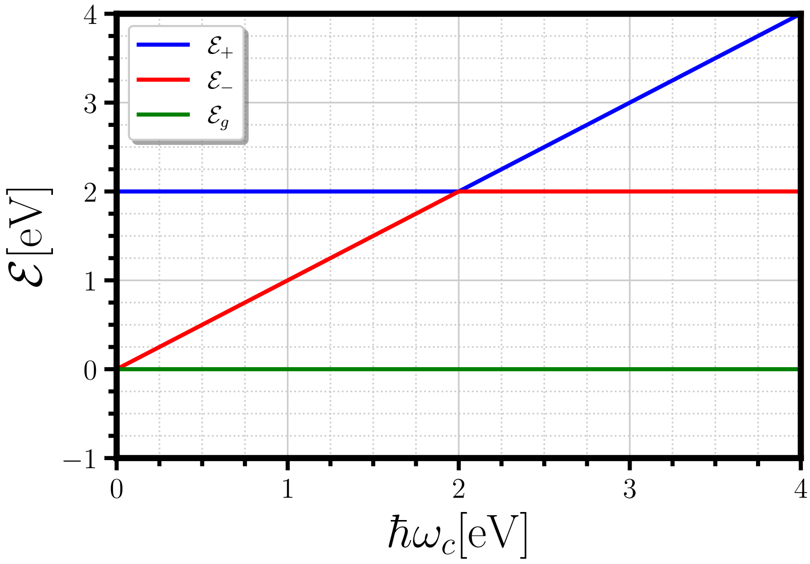

Figure 4.1: Energies $\mathcal{E}_+$ (blue line), $\mathcal{E}_-$ (red line) and $\mathcal{E}_g$ (green line) as a function of $\hbar\omega_c$. Parameters are as follows: $\varepsilon_g = 0\,\mathrm{eV}$, $\varepsilon_e = 2\,\mathrm{eV}$, and $\hbar\Omega_R = 0\,\mathrm{eV}$.

4.1.4 Diagonalization of the total Hamiltonian

In the previous section the diagonalization of the J-C Hamiltonian is carried out using the Rotating Wave Approximation. The J-C Hamiltonian can be diagonalized numerically and at the end it is useful to compare the analytical model (under RWA) with the numerical one. Figure 4.3 and Figure 4.4 show the numerically and analytically computed energy levels as a function of $\hbar\omega_c$.

The Figure 4.3, for the case $\hbar\Omega_R = 0.7\,\mathrm{eV}$, shows that there is a very good match between the model under RWA and the numerical one, near resonance ($\hbar\omega_c \approx 2.75\,\mathrm{eV}$) and for higher values of $\hbar\omega_c$. The upper sequence of black dots concerns higher energy levels, in particular they represent the second excitation sector. If $\hbar\Omega_R$ increases and it becomes of the same order of the atomic transition, a deviation between the two

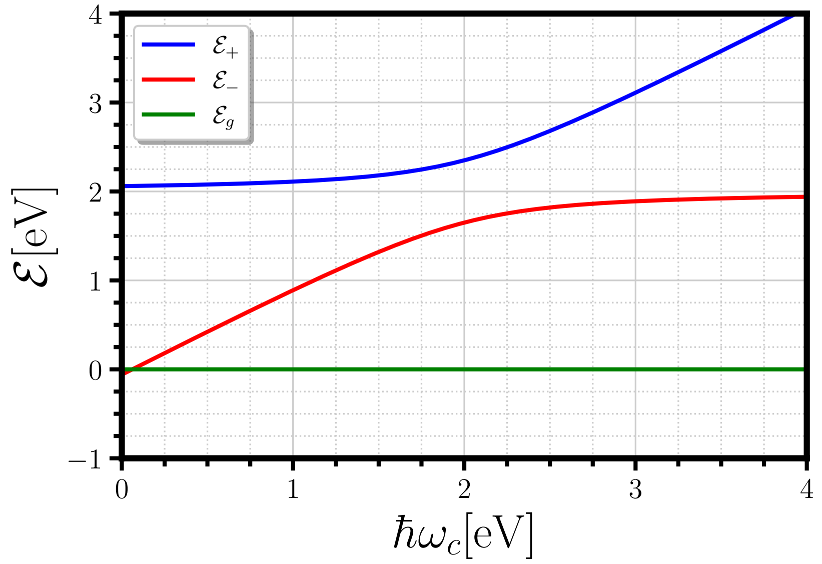

Figure 4.2: Energies $\mathcal{E}_+$ (blue line), $\mathcal{E}_-$ (red line) and $\mathcal{E}_g$ (green line) as a function of $\hbar\omega_c$. Parameters are as follows: $\varepsilon_g = 0\,\text{eV}$, $\varepsilon_e = 2\,\text{eV}$, and $\hbar\Omega_R = 0.7\,\text{eV}$.

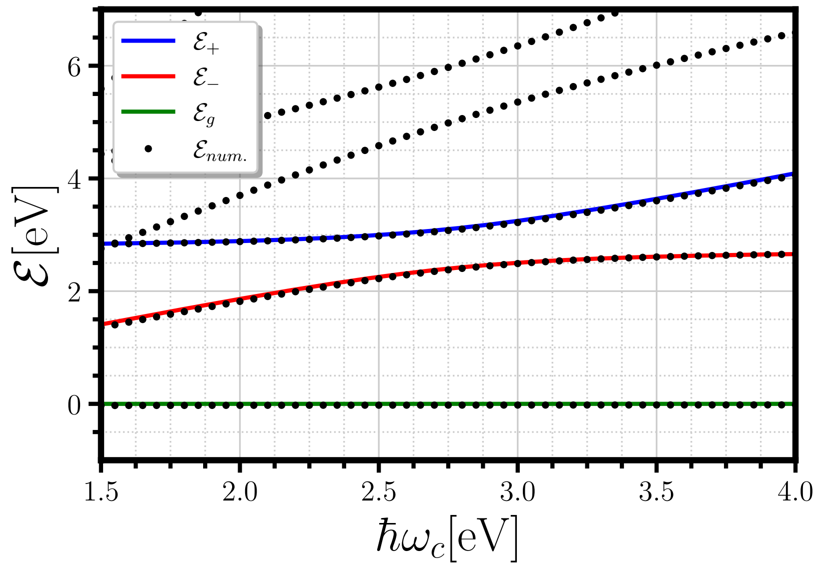

Figure 4.3: Energies $\mathcal{E}_+$ (blue line), $\mathcal{E}_-$ (red line), $\mathcal{E}_g$ (green line) for the exact diagonalization (see the eq. (4.25)) and $\mathcal{E}_{num.}$ for the numerical diagonalization as a function of $\hbar\omega_c$. Parameters are as follows: $\varepsilon_g = 0\,\text{eV}$, $\varepsilon_e = 2.75\,\text{eV}$, and $\hbar\Omega_R = 0.7\,\text{eV}$.

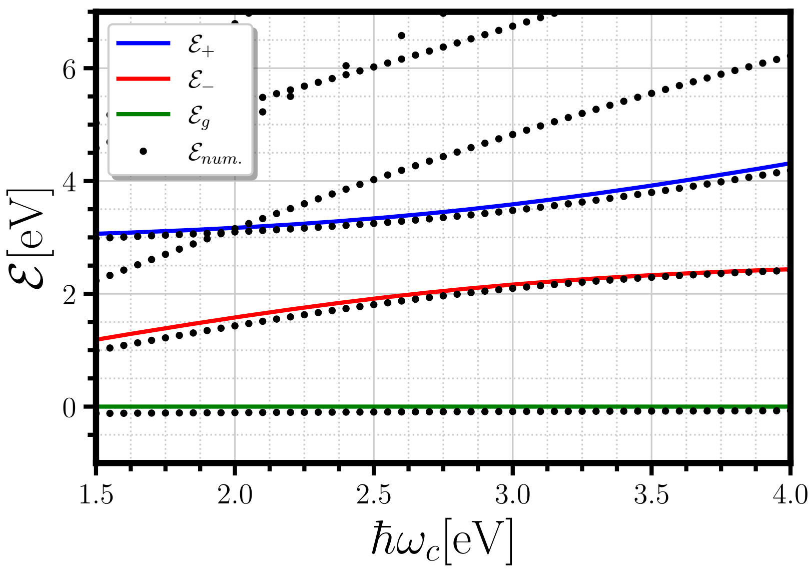

Figure 4.4: Energies $\mathcal{E}_+$ (blue line), $\mathcal{E}_-$ (red line), $\mathcal{E}_g$ (green line) for the exact diagonalization (see the eq. (4.25)) and $\mathcal{E}_{num.}$ for the numerical diagonalization as a function of $\hbar\omega_c$. Parameters are as follows: $\varepsilon_g = 0\,\text{eV}$, $\varepsilon_e = 2.75\,\text{eV}$, and $\hbar\Omega_R = 1.4\,\text{eV}$.

models start to appear. This behaviour is shown in Figure 4.4. The "discrepancy" between the numerical computation and the analytical result is due by the strength of $\hbar\Omega_R$ that causes a breaking of perturbation theory.

4.1.5 Strong coupling

The coupling, that in this model is Ω_R, could increase by reaching a regime in which the interacting part of the Hamiltonian enables the onset of Polaritons. This regime is called *strong coupling regime.* In experiments the strong coupling regime is achieved when the Rabi coupling is larger than the dissipative mechanism in cavity. If the Rabi coupling gets of the some order or even higher than the molecular transition, the strong coupling regime is replaced by the *ultrastrong coupling regime* [34, 33]. Figure 4.3 shows the strong coupling regime [80]. The energy of the ground state does not change its value for a "weak-coupling", but in the strong coupling regime it does. By comparing Figure 4.3 and Figure 4.4 it is visible a lowering of the ground state passing from $\hbar\Omega_R = 0.7\,\text{eV}$ to $\hbar\Omega_R = 1.4\,\text{eV}$. This behaviour can be investigated by performing a computation at second order of perturbation theory. The result is a "shift" of the ground state. The computation can be carried out taking the mean value of the J-C Hamiltonian on the ground state. The correction gives:

$$
\begin{aligned}
\langle g,0|\,\hat{\mathrm{H}}_{\mathrm{int}}\,|g,0\rangle &= \sum_k \frac{\langle g,0|\,\hat{\mathrm{H}}_{\mathrm{int}}\,|\varphi_k\rangle\,\langle\varphi_k|\,\hat{\mathrm{H}}_{\mathrm{int}}\,|g,0\rangle}{\mathcal{E}_g - \mathcal{E}_k} = \\
&= \frac{\langle g,0|\,\hat{\mathrm{H}}_{\mathrm{int}}\,|e,1\rangle\,\langle e,1|\,\hat{\mathrm{H}}_{\mathrm{int}}\,|g,0\rangle}{\mathcal{E}_g - \mathcal{E}_{e,1}} = \frac{-\hbar^2\Omega_R^2}{4}\cdot\frac{1}{(\varepsilon_e - \varepsilon_g + \hbar\omega_c)},
\end{aligned}
\tag{4.14}
$$

where $\hat{\mathrm{H}}_{\mathrm{int}}$ is the Hamiltonian in eq. (4.9), $\mathcal{E}_g = \varepsilon_g$ and $\mathcal{E}_{e,1} = \varepsilon_e + \hbar\omega_c$.

Figure 4.5 shows this correction (yellow line) to the energy value of the ground state. The numerical model again converges very-well to the correction given by eq. (4.14) near resonance and for higher values of ω_c. However the physical interest and experimental setups focus on the resonance's "window" (in this case the resonance is at $\hbar\omega_c = 2.75\,\text{eV}$). The Hamiltonian $\hat{\mathrm{H}}_{\mathrm{J-C,RW}}$ (see the eq. (4.12)) represents the analytical starting point for the development of the arguments in the next sections. The Hamiltonian does not contain the counter-rotating and self-dipole terms. These corrections are here neglected because of their relative small amplitudes. The Appendix A shows the effect of the inclusion of those terms.

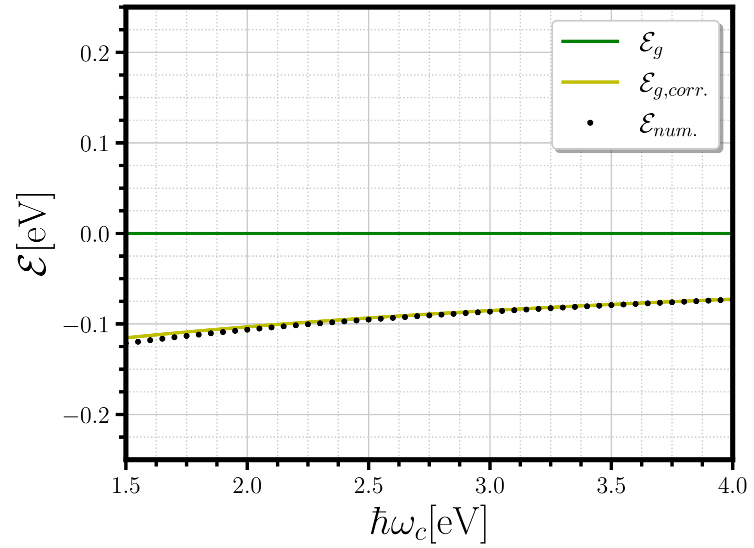

Figure 4.5: Energies $\mathcal{E}_g$ (green line), $\mathcal{E}_{g,corr.}$ (see the eq. (4.14)) and $\mathcal{E}_{num.}$ for the numerical diagonalization as a function of $\hbar\omega_c$. Parameters are as follows: $\varepsilon_g = 0\,\mathrm{eV}$, $\varepsilon_e = 2.75\,\mathrm{eV}$, and $\hbar\Omega_R = 1.4\,\mathrm{eV}$.

4.2 Jaynes-Cummings Model for Several Atoms

In this section a generalization of Jaynes-Cummings Model considering 2, 3 . . . N atoms is given.

4.2.1 Hamiltonian of N two-level atoms coupled to radiation

Now N identical (with the same ε_g and ε_e) level-atoms are coupled to the same photon mode with frequency ω_c.
The bare Hamiltonian is simply the sum of N atomic terms and the field term:

$$\hat{\mathrm{H}}_{\mathrm{N,\,0}} = \sum_{i=1}^{N} \left(\varepsilon_g \left|g_i\right\rangle \left\langle g_i\right| + \varepsilon_e \left|e_i\right\rangle \left\langle e_i\right|\right) + \hbar\omega_c \hat{a}^\dagger \hat{a}, \tag{4.15}$$

where the subscript $_i$ means the i-th atom.
The interacting Hamiltonian is given by

$$\hat{\mathrm{H}}_{\mathrm{N,\,int}} = \frac{\hbar\Omega_R}{2}\left(\hat{a} + \hat{a}^\dagger\right) \cdot \sum_{i=1}^{N} \left(\left|e_i\right\rangle \left\langle g_i\right| + \left|g_i\right\rangle \left\langle e_i\right|\right). \tag{4.16}$$

Under Rotating-Wave-Approximation (RWA), in which the counter-rotating terms are neglected because do not conserve energy at leading order of perturbation theory, the total Hamiltonian is

$$\boxed{\hat{\mathrm{H}}_{\mathrm{N\,atoms}} = \sum_{i=1}^{N} \left(\varepsilon_g \left|g_i\right\rangle \left\langle g_i\right| + \varepsilon_e \left|e_i\right\rangle \left\langle e_i\right|\right) + \hbar\omega_c \hat{a}^\dagger \hat{a} + \frac{\hbar\Omega_{\mathrm{R}}}{2} \sum_{i=1}^{N} \left(\left|e_i\right\rangle \left\langle g_i\right| \hat{a} + \left|g_i\right\rangle \left\langle e_i\right| \hat{a}^\dagger\right).} \tag{4.17}$$

4.2.2 Diagonalization of N=2 two-level atoms under RWA

The Hilbert space of the two atoms plus the radiation is generated by the vectors $\{\left|g_1 g_2\right\rangle, \left|g_1 e_2\right\rangle, \left|e_1 g_2\right\rangle, \left|e_1 e_2\right\rangle\} \otimes \left|n\right\rangle$, where $\left|n\right\rangle$ is the photon state.
An exact diagonalization of the Hamiltonian is possible by working on the resonance ($\hbar\omega_c \approx \varepsilon_e - \varepsilon_g \equiv \Delta_{ge}$) and focusing on the first atom-excitation, namely $\mathcal{E}_{e,1} - \mathcal{E}_g = \Delta_{ge}$. $\mathcal{E}_{e,1}$ is the energy of the first excitation

and $\mathcal{E}_g = 2\varepsilon_g$, the energy of the ground state $|g_1 g_2\rangle \otimes |0\rangle$ of $\hat{\mathrm{H}}_{\mathrm{N\,atoms}}$ (4.17).
By following this argument, the basis related to the subspace of a single-photon excitation is composed by $|g_1 e_2\rangle \otimes |0\rangle$, $|e_1 g_2\rangle \otimes |0\rangle$ and $|g_1 g_2\rangle \otimes |1\rangle$ (see Figure 4.6). In this basis the eigenvalues and the eigenvectors of (4.17) are respectively:

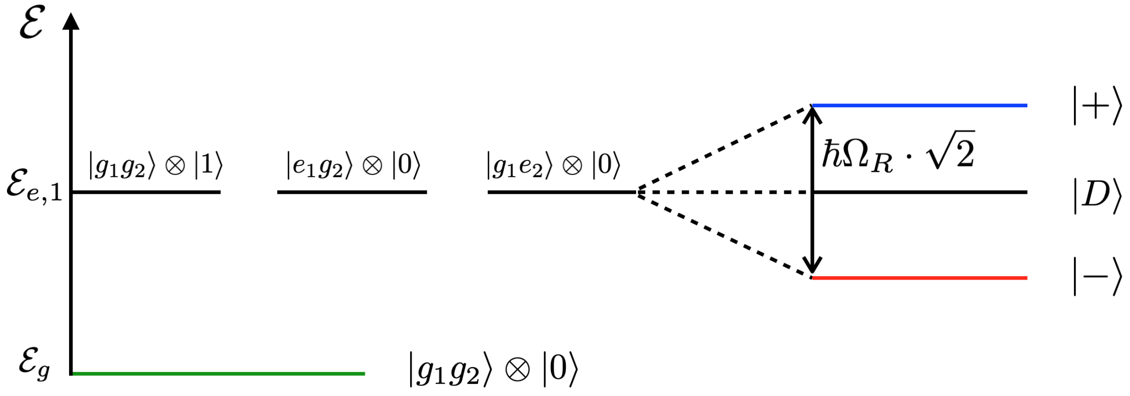

Figure 4.6: Energy levels of $\hat{\mathrm{H}}_{\mathrm{N},0}$ (see the eq. (4.15)) working on the resonance and splitting of these levels due to the interacting Hamiltonian $\hat{\mathrm{H}}_{\mathrm{N,\,int}}$ (see the eq. (4.16)) for $\mathrm{N} = 2$ two-level systems.

$$\begin{aligned} \mathcal{E}_+ &= \mathcal{E}_{e,1} + \frac{\hbar\Omega_R}{2} \cdot \sqrt{2}, \quad |+\rangle = \frac{|G,1\rangle + |E,0\rangle}{\sqrt{2}}, \\ \mathcal{E}_- &= \mathcal{E}_{e,1} - \frac{\hbar\Omega_R}{2} \cdot \sqrt{2}, \quad |-\rangle = \frac{-|G,1\rangle + |E,0\rangle}{\sqrt{2}}, \\ \mathcal{E}_D &= \mathcal{E}_{e,1}, \quad |D\rangle = \frac{|g_1 e_2\rangle - |e_1 g_2\rangle}{\sqrt{2}} \otimes |0\rangle, \end{aligned} \tag{4.18}$$

where $|E,0\rangle \equiv (|g_1 e_2\rangle + |e_1 g_2\rangle)/\sqrt{2} \otimes |0\rangle$ and $|G,1\rangle \equiv |g_1 g_2\rangle \otimes |1\rangle$. The states $|+\rangle$ and $|-\rangle$ are the *Polaritonic states* for two atoms (molecules). They are separated by $\mathcal{E}_+ - \mathcal{E}_- = \hbar\Omega_R\sqrt{2}$.
The state $|D\rangle$ is generally called *Dark state* because it is not coupled to the light mode and the transitions from the ground state and from the other two states to the Dark state are not allowed. Thus, this state is an optical inactive state for this “Coherent Description” that does not involve any kind of dissipative mechanism [71].
In fact, if a classical laser source with a Hamiltonian given by

$$\hat{\mathrm{H}}_{\mathrm{las}} = \hat{\vec{d}} \cdot \vec{E} \cos(\omega_{\mathrm{L}} t) \tag{4.19}$$

where $\hat{\vec{d}} = \vec{d} \sum_{i=1}^{2} (|e_i\rangle \langle g_i| + |g_i\rangle \langle e_i|)$, $\vec{E}$ is the classical electric field oscillating at the laser frequency ω_{L}, and $\vec{d}$ is the dipole, is considered the computation of the associated matrix elements gives:

$$\begin{aligned} &\langle G,0| \hat{\mathrm{H}}_{\mathrm{las}} |-\rangle \neq 0, \quad \langle G,0| \hat{\mathrm{H}}_{\mathrm{las}} |+\rangle \neq 0, \\ &\langle D| \hat{\mathrm{H}}_{\mathrm{las}} |-\rangle = 0, \quad \langle +| \hat{\mathrm{H}}_{\mathrm{las}} |D\rangle = 0, \end{aligned} \tag{4.20}$$

where $|G,0\rangle \equiv |g_1 g_2\rangle \otimes |0\rangle$.

This means that the only allowed transitions are between the ground state $|G,0\rangle$ and the lower Polaritonic state $|-\rangle$ or between $|G,0\rangle$ and the Upper Polaritonic state $|+\rangle$.
It is a justification to the fact that Polaritonic states are “bright” states the others are “dark”. Figure 4.7 shows the allowed transitions.

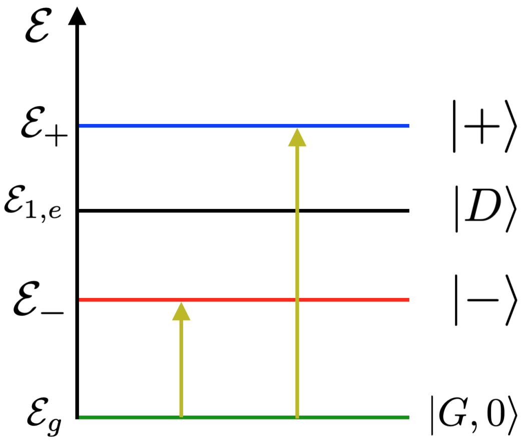

Figure 4.7: Allowed transitions (in gold) between the Polaritonic states $|-\rangle, |+\rangle$ and the ground state $|G,0\rangle$.

4.2.3 More than N=2 two-level atoms coupled to radiation

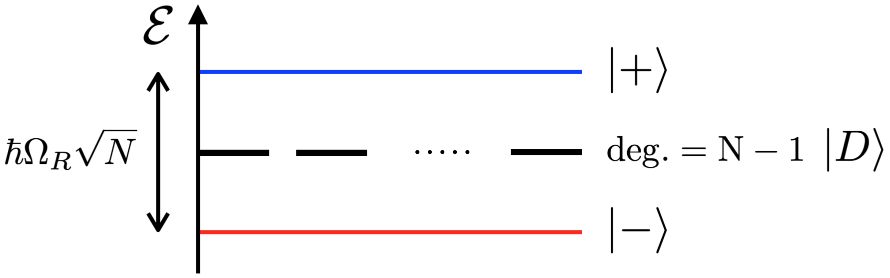

Figure 4.8: Polaritonic states and Dark states for N two-level systems.

Up to now, the Jaynes-Cummings Model for 2 two-level atoms has been described. The generalization for N atoms [157] can be easily done for what it concerns the "distance" between $|+\rangle$ and $|-\rangle$ which is $\mathcal{E}_+ - \mathcal{E}_- = \hbar\Omega_\mathrm{R}\sqrt{N}$.
Another direct prediction is related to the number of the Dark states. There are N−1 degenerate Dark states if the two-level atoms are N. These Dark states constitute a gap between the Polaritonic states and they are often referred to as an *exciton reservoir* or *exciton bath* [71].
The eigenvalues and the eigenstates for N atoms are:

$$\boxed{\begin{aligned} &\mathcal{E}_g = N\varepsilon_g, \quad |G,0\rangle \equiv |g_1\cdots g_N\rangle \otimes |0\rangle\,, \\ &\mathcal{E}_\pm = N\varepsilon_g + \hbar\omega_c \pm \frac{\hbar\Omega_R}{2}\cdot\sqrt{N}, \quad |\pm\rangle = \frac{\pm|G,1\rangle + |E,0\rangle}{\sqrt{2}}, \\ &\mathcal{E}_{D_p} = N\varepsilon_g + \Delta_{ge}, \quad |D_p\rangle = \frac{\sum_{k=1}^{p}|(e_k)\rangle - \sqrt{p}\,|(e_{p+1})\rangle}{\sqrt{p(p+1)}} \otimes |0\rangle \text{ with } p = 1,\dots N-1, \end{aligned}} \tag{4.21}$$

where $|E,0\rangle \equiv \sum_{i=1}^{N}|(e_i)\rangle/\sqrt{N}\otimes|0\rangle$, $|G,1\rangle \equiv |g_1\cdots g_N\rangle\otimes|1\rangle$ and $\Delta_{ge} \equiv \varepsilon_e - \varepsilon_g$. The states $|(e_i)\rangle$ are states of the form $|g_1\cdots g_{i-1}(e_i)g_{i+1}\cdots g_N\rangle$.
The totally symmetric molecular state $|E,0\rangle$ is obtained as the sum of all states containing $N-1$ molecules in the ground-state and one molecule i in the excited state $|(e_i)\rangle \equiv |g_1\cdots g_{i-1}(e_i)g_{i+1}\cdots g_N\rangle$. The electronic excitation in this $|E,0\rangle$ Dicke-state is thus delocalized on the whole molecular ensemble, the former playing

the role of a *giant collective dipole* oscillating in phase with the electromagnetic cavity-mode [36]. The Polaritons in eq. (4.21) are linear combinations of two states: one involving the manybody electronic ground-state $|G\rangle$ with one photon populating the cavity and the other the collective Dicke-state $|E, 0\rangle$ with the cavity in its quantum mechanical ground-state. Figure 4.8 shows the Polaritonic states and Dark states for N atoms.

4.3 Holstein-Tavis-Cummings model

The Holstein-Tavis-Cummings Model provides a description of the interaction, in a lossless cavity, between N two-levels molecules and a single mode of radiation. This model takes into account the Vibrational Degrees of Freedom (VDOF) of the molecules [70, 176]. After an explanation of the Hamiltonian describing the system it follows a derivation of the Potential Energy Surface (PES) for the Polaritonic states, their equilibrium positions and the corresponding eigenstates. In conclusion a numerical diagonalization of the Hamiltonian is performed.

4.3.1 Hamiltonian of N “vibrating” molecules coupled to radiation

The Hamiltonian that describes the interaction between N two-levels molecules, with their VDOF, and one mode of the quantized electromagnetic field is

$$\boxed{\begin{aligned} \hat{\mathrm{H}}_{\mathrm{Nmol}} = \sum_{i=1}^{N} \left\{ \left[\varepsilon_g + \frac{1}{2}\omega_{\mathrm{v}}^2 \left(Q_{\mathrm{v},i} - \overline{Q}_{\mathrm{v},g}\right)^2\right] |g_i\rangle \langle g_i| + \left[\varepsilon_e + \frac{1}{2}\omega_{\mathrm{v}}^2 \left(Q_{\mathrm{v},i} - \overline{Q}_{\mathrm{v},e}\right)^2\right] |e_i\rangle \langle e_i| \right\} + \\ + \hbar\omega_c \hat{a}^\dagger \hat{a} + \frac{\hbar\Omega_R}{2} \sum_{i=1}^{N} \left(|e_i\rangle \langle g_i| \hat{a} + |g_i\rangle \langle e_i| \hat{a}^\dagger \right), \end{aligned}} \tag{4.22}$$

where $\varepsilon_{g,e}$ are the electronic energies, ω_c is the frequency of the cavity, ω_{v} the vibration frequency of the molecules (all the molecules have the same vibration frequency), $Q_{\mathrm{v},i}$ are the mass-weighted nuclear coordinates corresponding to the vibration mode of molecule i, $\overline{Q}_{\mathrm{v},g/e}$ are the displaced nuclear equilibrium positions for the electronic states, and Ω_R is the coupling due to the dipole interaction between the molecule and radiation in cavity (see Section 4.1.2). The interaction term (in the second line of equation (4.22)) is written using the RWA (see the Section 4.1.3). The Hamiltonian $\hat{\mathrm{H}}_{\mathrm{Nmol}}$ is also written using the *Born-Oppenheimer approximation* where the kinetic energies (the mass of the nuclei is much higher than the electronic mass) are neglected for the slow nuclei motion ($\hbar\omega_{\mathrm{v}} \approx 50\,\mathrm{meV}$) in comparison to the fast dynamics of strongly coupled electrons and cavity mode ($\Delta_{ge} \equiv \varepsilon_e - \varepsilon_g \approx \hbar\omega_c \approx 2.8\,\mathrm{eV}$).

The new term $\frac{1}{2}\sum_i \omega_{\mathrm{v}}^2 \left(Q_{\mathrm{v},i} - \overline{Q}_{\mathrm{v}}\right)^2$ (for the electronic states g or e), that appears in eq. (4.22) with respect to the eq. (4.17), may be seen as the potential energy of the mass-weighted nuclear coordinates. In particular, the quantity $\lambda_{\mathrm{v}} \equiv \frac{1}{2}\omega_{\mathrm{v}}^2 \left(\overline{Q}_{\mathrm{v},e} - \overline{Q}_{\mathrm{v},g}\right)^2$ is usually called *reorganization energy* because it is the required energy to restore and reorganize the nuclear coordinates for the shifted equilibrium position $\overline{Q}_{\mathrm{v},e}$.

The reorganization energy is a sort of electron-phonon coupling and it is directly related to dimensionless factors, called *Huang-Rhys factors* [78]. These factors are defined as $g_{\mathrm{v}} = \left(\overline{Q}_{\mathrm{v},e} - \overline{Q}_{\mathrm{v},g}\right)/2x_{0\mathrm{v}}$, which are nothing but the shifts of the modes' equilibrium positions in units of the zero-point motion $x_{0\mathrm{v}} = \sqrt{\hbar/2\omega_{\mathrm{v}}}$. Huang-Rhys factors are related to reorganization energies by the relations $g_{\mathrm{v}}^2 = \lambda_{\mathrm{v}}/\hbar\omega_{\mathrm{v}}$.

4.3.2 Eigenvalues at order λ_{v}

In order to derive analytical expressions for the eigenvalues of $\hat{\mathrm{H}}_{\mathrm{Nmol}}$, an adiabatic approximation is performed [111]. The regime of validity of this approximation is for $\lambda_{\mathrm{v}} < \hbar\Omega_R$. Thus, the analytical expressions of the eigenvalues can be found by using perturbation theory [27] at leading order in λ_{v}. To perform a perturbative expansion at order λ_v, it is easier to collect all the λ_v-terms that appear in $\hat{\mathrm{H}}_\mathrm{Nmol}$. So the Hamiltonian becomes:

$$
\begin{aligned}
\hat{\mathrm{H}}_\mathrm{Nmol} = \hat{\mathrm{H}}_0 + \hat{\mathrm{V}}_{\lambda_\mathrm{v}} = \sum_{i=1}^{N} \left(\varepsilon_g \left|g_i\right\rangle \left\langle g_i\right| + \varepsilon_e \left|e_i\right\rangle \left\langle e_i\right|\right) + \hbar\omega_c \hat{a}^\dagger \hat{a} + \frac{\hbar\Omega_R}{2} \sum_{i=1}^{N} \Big(\left|e_i\right\rangle \left\langle g_i\right| \hat{a} + \left|g_i\right\rangle \left\langle e_i\right| \hat{a}^\dagger\Big) + \\
+ \lambda_\mathrm{v} \sum_{i=1}^{N} \left[\frac{Q_{\mathrm{v},i}^2}{\overline{Q}_{\mathrm{v},e}^2} \left|g_i\right\rangle \left\langle g_i\right| + \Big(1 + \frac{Q_{\mathrm{v},i}^2}{\overline{Q}_{\mathrm{v},e}^2} - 2\frac{Q_{\mathrm{v},i}}{\overline{Q}_{\mathrm{v},e}}\Big) \left|e_i\right\rangle \left\langle e_i\right| \right],
\end{aligned}
\tag{4.23}
$$

where $\overline{Q}_{\mathrm{v},g}$ is set to 0 as the reference nuclear equilibrium position and consequently $\lambda_\mathrm{v} \equiv \frac{1}{2}\omega_\mathrm{v}^2 \overline{Q}_{\mathrm{v},e}^2$. Restricting the Hilbert space to the first excitation sector for N molecules, that is $\{\left|G,1\right\rangle, \left|E,0\right\rangle\}$ (the same procedure for one atom is reported in Section 4.1.3) where

$$
\begin{aligned}
&\left|G,1\right\rangle \equiv \left|g_1 \cdots g_N\right\rangle \otimes \left|1\right\rangle, \\
&\left|E,0\right\rangle \equiv \frac{1}{\sqrt{N}} \sum_{i=1}^{N} \left|(e_i)\right\rangle \otimes \left|0\right\rangle \;\text{ with } \left|(e_i)\right\rangle \equiv \left|g_1 \cdots g_{i-1}(e_i) g_{i+1} \cdots g_N\right\rangle,
\end{aligned}
\tag{4.24}
$$

the eigenvalues of the Lower and Upper Polariton at leading order in λ_v are respectively:

$$
\begin{aligned}
\mathcal{E}_- &= N\varepsilon_g + \hbar\omega_c - \frac{\hbar\delta}{2} - \frac{\hbar\tilde{\Omega}_R}{2} + \lambda_\mathrm{v} \left\langle -\right| \hat{\mathrm{V}}_{\lambda_\mathrm{v}} \left|-\right\rangle, \\
\mathcal{E}_+ &= N\varepsilon_g + \hbar\omega_c - \frac{\hbar\delta}{2} + \frac{\hbar\tilde{\Omega}_R}{2} + \lambda_\mathrm{v} \left\langle +\right| \hat{\mathrm{V}}_{\lambda_\mathrm{v}} \left|+\right\rangle,
\end{aligned}
\tag{4.25}
$$

with

$$
\begin{aligned}
\tilde{\Omega}_R &= \sqrt{\delta^2 + \left(N\Omega_R^2\right)}, \quad \delta \equiv \omega_c - \Delta_{ge}/\hbar, \\
\left|-\right\rangle &= -\sin\theta \left|G,1\right\rangle + \cos\theta \left|E,0\right\rangle, \\
\left|+\right\rangle &= +\cos\theta \left|G,1\right\rangle + \sin\theta \left|E,0\right\rangle, \\
\sin\theta &= \frac{1}{\sqrt{2}}\sqrt{1 - \frac{\delta}{\tilde{\Omega}_R}}, \quad \cos\theta = \frac{1}{\sqrt{2}}\sqrt{1 + \frac{\delta}{\tilde{\Omega}_R}},
\end{aligned}
\tag{4.26}
$$

where $\Delta_{ge} \equiv \varepsilon_e - \varepsilon_g$.
The evaluation of the matrix elements in eq. (4.25) gives

$$
\begin{aligned}
\left\langle -\right| \hat{\mathrm{V}}_{\lambda_\mathrm{v}} \left|-\right\rangle &= \sum_{i=1}^{N} \left[\sin^2\theta \left(1 - \frac{2Q_{\mathrm{v},i}}{N\overline{Q}_{\mathrm{v},e}}\right) + \frac{Q_{\mathrm{v},i}^2}{\overline{Q}_{\mathrm{v},e}^2} \right] \\
\left\langle +\right| \hat{\mathrm{V}}_{\lambda_\mathrm{v}} \left|+\right\rangle &= \sum_{i=1}^{N} \left[\cos^2\theta \left(1 - \frac{2Q_{\mathrm{v},i}}{N\overline{Q}_{\mathrm{v},e}}\right) + \frac{Q_{\mathrm{v},i}^2}{\overline{Q}_{\mathrm{v},e}^2} \right].
\end{aligned}
\tag{4.27}
$$

The final form of $\mathcal{E}_\pm$, by using the expressions of $\sin\theta$ and $\cos\theta$ (see eq. (4.26)), is

$$
\mathcal{E}_\pm = N\varepsilon_g + \hbar\omega_c - \frac{\hbar\delta}{2} \pm \frac{\hbar\tilde{\Omega}_R}{2} + \lambda_\mathrm{v} \sum_{i=1}^{N} \left[\frac{1}{2}\left(1 \pm \frac{\delta}{\tilde{\Omega}_R}\right) \cdot \left(1 - \frac{2}{N}\frac{Q_{\mathrm{v},i}}{\overline{Q}_{\mathrm{v},e}}\right) + \frac{Q_{\mathrm{v},i}^2}{\overline{Q}_{\mathrm{v},e}^2} \right].
\tag{4.28}
$$

4.3.3 Equilibrium positions and Potential Energy Surfaces

The Potential Energy Surface (PES) is essential for a microscopic understanding of molecular transfer phenomena and it is a key quantity to investigate chemical reaction dynamics or nuclear motions. The topology

of the PES can be explored by calculating the first and second derivatives with respect to the nuclear coordinates $Q_{\mathrm{v},i}$ [113]. Of particular interest are the stationary points on a PES that may correspond to stable conformations of the molecule. Near these equilibrium positions it is often possible to analyze nuclear motions in terms of weak normal-mode vibrations.
Solving

$$\frac{\partial \mathcal{E}_\pm}{\partial Q_{\mathrm{v},1}} = 0, \ldots, \frac{\partial \mathcal{E}_\pm}{\partial Q_{\mathrm{v},N}} = 0, \tag{4.29}$$

where $\mathcal{E}_\pm$ are given by eq. (4.28), the equilibrium positions are:

$$\overline{Q}_{\mathrm{v},\pm} = \frac{\overline{Q}_{\mathrm{v},e}}{2N}\left(1 \mp \frac{\delta}{\tilde{\Omega}_R}\right), \tag{4.30}$$

where the ground state equilibrium nuclear configuration $\overline{Q}_{\mathrm{v},g}$ is set to 0.
These equilibrium positions depends on detuning δ, the collective Rabi frequency $\tilde{\Omega}_R$, and number of molecules denoted by N. The shifts in equilibrium positions in eq. (4.30) are the same for each molecule, thus corresponding to the excitation of a long-range vibrational mode, in which each molecular vibration couples in phase with the same Polariton. In the large-N limit, the results of the collective decoupling mechanism between nuclear motion and the Polariton are recovered, as derived in ref. [70], for which the configuration of the nuclear equilibrium positions gets back to the ground state configuration, that is $\overline{Q}_{\mathrm{v},\pm} \to \overline{Q}_{\mathrm{v},g}$.

Now with the knowledge of the stationary points it follows the calculation of the PES of the system described by the Hamiltonian (4.23). In particular the *adiabatic Born-Oppenheimer PES*, in which the non-adiabatic operators are neglected, is considered [113]. The definition is

$$\mathcal{E}(Q_{\mathrm{v},i}) = \mathcal{E}(\overline{Q}_{\mathrm{v}}) + \sum_{i,j=1}^{\mathrm{N}} \frac{1}{2} h_{ij}(\overline{Q}_{\mathrm{v}}) \Delta Q_{\mathrm{v},i} \Delta Q_{\mathrm{v},j} + O(Q^3_{\mathrm{v},i,j}), \tag{4.31}$$

where $\overline{Q}_{\mathrm{v}}$ are the equilibrium positions, $h_{ij}(\overline{Q}_i) = \partial^2 E(\overline{Q}_{\mathrm{v},i})/\partial Q_{\mathrm{v},i} \partial Q_{\mathrm{v},j}$ and $\Delta Q_{\mathrm{v},i} \equiv Q_{\mathrm{v},i} - \overline{Q}_{\mathrm{v},i}$.
Using the eq. (4.28), (4.30) and (4.31) the quadratic Polariton Potential Energy Surfaces (PPESs) of the described system are [111]:

$$\begin{aligned} \mathcal{E}_\pm(Q_{\mathrm{v},i}) &= \varepsilon_\pm + \sum_{i=1}^{N} \frac{\omega_{\mathrm{v}}^2}{2} \left(Q_{\mathrm{v},i} - \overline{Q}_{\mathrm{v},\pm}\right)^2, \\ \varepsilon_\pm &= N\varepsilon_g + \hbar\omega_c - \frac{\hbar}{2}\left(\underline{\delta} \mp \underline{\tilde{\Omega}}_R\right), \\ \underline{\delta} &= \delta - \frac{\lambda_{\mathrm{v}}}{\hbar}\left(1 - \frac{\alpha_+^2 + \alpha_-^2}{N}\right), \\ \underline{\tilde{\Omega}}_R &= \tilde{\Omega}_R - \frac{\lambda_{\mathrm{v}}}{\hbar}\frac{\delta}{\tilde{\Omega}_R}\left(1 - \frac{1}{N}\right), \end{aligned} \tag{4.32}$$

where $\lambda_{\mathrm{v}} \equiv \frac{1}{2}\omega_{\mathrm{v}}^2 \overline{Q}_{\mathrm{v},e}^2$ and $\alpha_\pm \equiv \frac{1}{2}\left(1 \mp \frac{\delta}{\tilde{\Omega}_R}\right)$.
It is interesting to note that the Polariton energy $\varepsilon_\pm$ depends on both the molecule-cavity detuning $\underline{\delta}$ and collective vacuum Rabi frequency $\underline{\tilde{\Omega}}_R$. Both quantities are renormalized and become explicitly dependent on the reorganization energy λ_{v}, as well as on the number N of molecules. The PPESs $\mathcal{E}_\pm(Q_{\mathrm{v},i})$ are a direct physical consequence of the generalized Born-Oppenheimer approximation and perturbation expansion at the lowest-order of the electron-phonon coupling strength. They interpolate smoothly between the limits of single-molecule $N = 1$ and large number of molecules $N \gg 1$ inside the cavity (terms of leading order $\approx 1/N$).

4.3.4 Eigenstates

The expression (4.32) is nothing else the sum of two Polaritonic energies plus N independent harmonic oscillators with the same frequency ω_{v} centered at the positions $\overline{Q}_{\mathrm{v},\pm}$. Then the total eigenstate of the system is

$$|\pm, m_{1\cdots N}\rangle = |\pm\rangle \bigotimes_{i=1}^{\mathrm{N}} \hat{D}^{\dagger}(\bar{Q}_{\mathrm{v},\pm})\,|m_i\rangle\,, \tag{4.33}$$

where m_i are the labels for the vibrational levels ($m_i \in \mathbb{Z}^{+}$) and $\hat{D}^{\dagger}(\bar{Q}_{\mathrm{v},\pm})$ are the displacement operators defined as $\hat{D}(\bar{Q}_{\mathrm{v},\pm}) \equiv \exp[\bar{Q}_{\mathrm{v},\pm}(\hat{a}^{\dagger} - \hat{a})]$ [165].

4.3.5 Eigenstates for N$\rightarrow \infty$

In the limit N $\rightarrow \infty$ there is an analogy with an infinite number of atoms in a crystal. Bearing in mind this idea, it comes natural to Fourier transform the PPESs:

$$\mathcal{E}_{\pm}(Q_{\mathrm{v},k}) = \varepsilon_{\pm} + \frac{1}{2}\omega_{\mathrm{v}}^2\left(Q_{\mathrm{v},0} - \overline{Q}_{\mathrm{v},\pm}\right)^2 + \sum_{k\neq 0}{}^{'} \frac{\omega_{\mathrm{v}}^2}{2} Q_{\mathrm{v},k}Q^{*}_{\mathrm{v},k} + O(Q^3_{\mathrm{v},k}), \tag{4.34}$$

where $\varepsilon_{\pm}$ contain the "Q-independent" terms of eq. (4.32) and $\sum_{k\neq 0}^{'}$ is the sum over $k \neq 0$ in the First Brillouin Zone [27]. The definitions of Fourier transform and Kronecker's δ are respectively $q_{\mathrm{v},j} = \frac{1}{\sqrt{N}}\sum_k^{'} q_{\mathrm{v},k}e^{-ikja}$ and $\frac{1}{N}\sum_j e^{i(k+k^{'})ja} = \delta_{k,-k'}$ where $q_{\mathrm{v},j} \equiv Q_{\mathrm{v},j} - \overline{Q}_{\mathrm{v},\pm}$ and a is the unit distance of the atomic oscillator chain. Thus, in k-space the total eigenstate is given by the two Polaritonic states times a displaced harmonic oscillator for $k = 0$ times all the other independent harmonic oscillators for $k \neq 0$ [70]:

$$|\pm, m_k\rangle = |\pm\rangle_k \otimes \hat{D}^{\dagger}(\overline{Q}_{\mathrm{v},\pm})\,|m_{k=0}\rangle \otimes |m_{k\neq 0}\rangle\,. \tag{4.35}$$

This total state is in agreement with the eq. (4) of ref. [70] when the detuning δ (see eq. (4.26)) is 0 and terms of order 1/N are neglected.

4.3.6 Numerical diagonalization of $\hat{\mathrm{H}}_{\mathrm{Nmol}}$

It is interesting to compare the analytical PPES (see eq. (4.32)) with a numerical diagonalization of $\hat{\mathrm{H}}_{\mathrm{Nmol}}$ (4.23) [56, 111]. In the moderate to strong coupling regime, $\hbar\omega_c > \hbar\tilde{\Omega}_R > \lambda_{\mathrm{v}}$, there is a very good matching of the exact numerical curves with the analytical results of eq. (4.32) based on the adiabatic approximation. Figure 4.9 also shows the PES of the many-body ground state and the Dark states. Their analytical expressions are [111]:

$$\begin{aligned} \mathcal{E}_{D_p}(Q_{\mathrm{v},i}) &= N\varepsilon_g + \Delta_{ge} + \sum_{i=1}^{N}\frac{\omega_{\mathrm{v}}^2}{2}Q^2_{\mathrm{v},i}, \\ \mathcal{E}_{g}(Q_{\mathrm{v},i}) &= N\varepsilon_g + \sum_{i=1}^{N}\frac{\omega_{\mathrm{v}}^2}{2}Q^2_{\mathrm{v},i}, \end{aligned} \tag{4.36}$$

where $p = 1, \cdots, N-1$ is an index labelling the Dark state (see eq. (4.21)), $\Delta_{ge} \equiv \varepsilon_e - \varepsilon_g$ and $\overline{Q}_{\mathrm{v},g}$ is set to 0.

Within RWA, the Dark states do not couple directly to the optical cavity-mode. Their PES is thus independent of the collective vacuum Rabi splitting. In the case of finite arbitrary electron-phonon interactions, the Dark PES can only be computed numerically, similarly to the Holstein polaron problem [75].

Some details about the adiabatic approximation for one molecule are given in Appendix B.

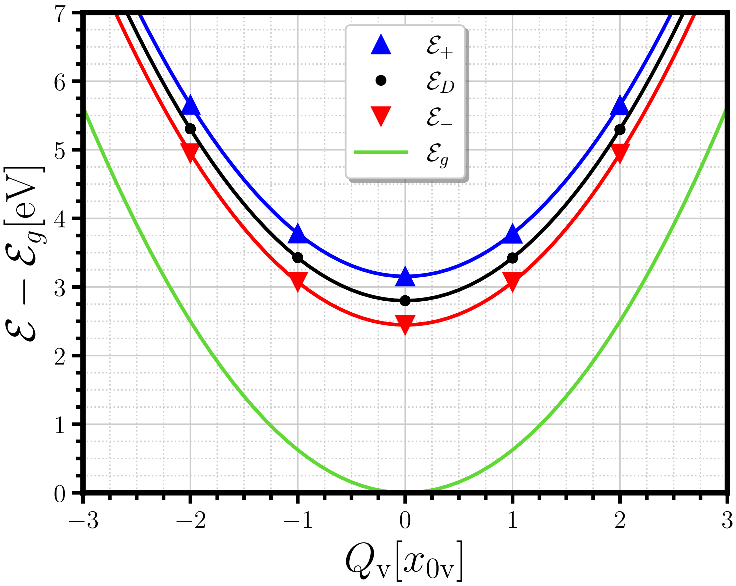

Figure 4.9: PPESs for the Lower Polariton $\mathcal{E}_-$ (red, downward pointing triangles), Upper Polariton $\mathcal{E}_+$ (blue, upward pointing triangles), and Dark states $\mathcal{E}_D$ (solid black circles) computed from numerical diagonalization of $\hat{\mathrm{H}}_{\mathrm{Nmol}}$ (see eq. (4.23)). The corresponding solid curves are obtained from analytical formulas in eq. (4.32) and (4.36). Parameters are as follows: $N = 50$, $Q_{\mathrm{v},i}$ fixed for all $i = 1, \cdots, N$ to the same value Q_v which is varied, $\varepsilon_g = 0\,\mathrm{eV}$, $\varepsilon_e = 2.8\,\mathrm{eV}$, $\hbar\omega_c = 2.8\,\mathrm{eV}$, $\hbar\omega_\mathrm{v} = 50\,\mathrm{meV}$, $\hbar\tilde{\Omega}_R = 0.7\,\mathrm{eV}$, $\hbar\delta = 0\,\mathrm{eV}$, and $\lambda_\mathrm{v} = 0.1\,\mathrm{meV}$.

4.4 Randomness on PPESs

In 1958, Philip Warren Anderson derived a “simple” model for spin diffusion in the impurity bands of crystals [2]. He showed that at low density no diffusion takes place by introducing randomness, or equivalently disorder or *inhomogeneous broadening*, on the energies of spin sites in a lattice. The “no-transport” theorem (no diffusion) has been shown to be valid when the randomness of the probability distribution of energies, characterized by a width W, is weak with respect to the interaction involved in spin transfer between adjacent sites.

In 1995, the effect of inhomogeneous broadening of the electronic state on vacuum Rabi splitting was investigated by R. Houdré *et al.* [77]. The conclusion of the study was that the Rabi splitting is independent of the nature of the broadening of the electronic state. Recent investigations on strongly coupled molecular ensembles [14, 22] show that Anderson disorder on Dark states can very efficiently contribute to coherent energy transport and open new perspectives towards the change and the control of disorder to manipulate the Polaritons lifetime by changing the environmental fluctuations.

This Section presents the result of the introduction of disorder on the calculated PPESs (see Figure 4.9). In particular the disorder is induced at the level of the numerical diagonalization of the Hamiltonian given by eq. (4.22). Two types of disorder are studied: i) By generating an “Anderson disorder” for which each molecular excited-state energy ε_e is perturbated by a random energy equally distributed in the range $[-W, W]$, with W the disorder strength (see Figure 4.10). ii) By generating a disorder at the level of reaction coordinates, that is an effective “electron-phonon disorder”, in which the excited-state nuclear position $Q_{\mathrm{v,i}}$ of each molecule $i = 1, \cdots, N$ are shifted by a random value in the range $[-Q_{\mathrm{v},W}, Q_{\mathrm{v},W}]$ (see Figure 4.11). In both cases, adding inhomogeneous disorder induces a lifting of degeneracy of the Dark states, which are distributed in an enlarged miniband of states, while the Polaritons remain weakly perturbed (if $\tilde{\Omega}_R > W$). This picture is consistent with the results of Houdré et al. [77].

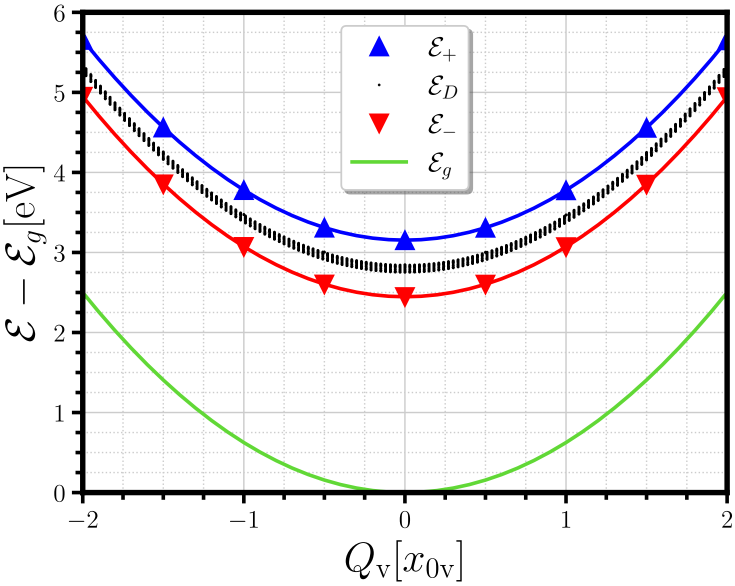

Figure 4.10: PPESs for the Ground state (green line), Lower Polariton $\mathcal{E}_-$ (red line), and Upper Polariton $\mathcal{E}_+$ (blue line) computed from numerical diagonalization of $\hat{\mathrm{H}}_{\mathrm{Nmol}}$ (see eq. (4.23)) and analytical formulas in eq. (4.32) and (4.36). The Dark states $\mathcal{E}_D$ (black dots) are only computed from numerical diagonalization of $\hat{\mathrm{H}}_{\mathrm{Nmol}}$ (see eq. (4.23)). Anderson disorder with disorder strength $W = 0.05\,\mathrm{eV}$ is included. Parameters are as follows: $N = 50$, $Q_{\mathrm{v},i}$ fixed for all $i = 1, \cdots, N$ to the same value Q_v which is varied, $\varepsilon_g = 0\,\mathrm{eV}$, $\varepsilon_e = 2.8\,\mathrm{eV}$, $\hbar\omega_c = 2.8\,\mathrm{eV}$, $\hbar\omega_\mathrm{v} = 50\,\mathrm{meV}$, $\hbar\tilde{\Omega}_R = 0.7\,\mathrm{eV}$, $\hbar\delta = 0\,\mathrm{eV}$, and $\lambda_\mathrm{v} = 0.1\,\mathrm{meV}$.

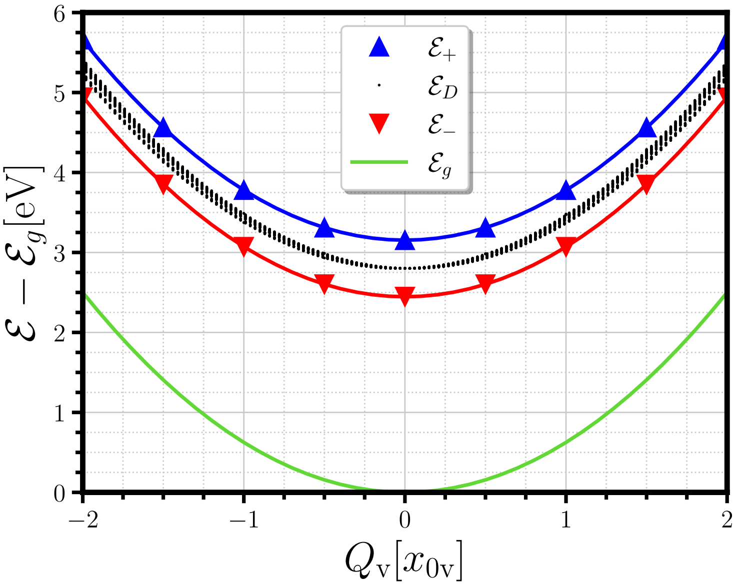

Figure 4.11: PPESs for the Ground state (green line), Lower Polariton $\mathcal{E}_-$ (red line), and Upper Polariton $\mathcal{E}_+$ (blue line) computed from numerical diagonalization of $\hat{\mathrm{H}}_{\mathrm{Nmol}}$ (see eq. (4.23)) and analytical formulas in eq. (4.32) and (4.36). The Dark states $\mathcal{E}_D$ (black dots) are only computed from numerical diagonalization of $\hat{\mathrm{H}}_{\mathrm{Nmol}}$ (see eq. (4.23)). Disorder on the nuclei position with disorder strength $Q_{\mathrm{v},W} = 0.05\,x_{0\mathrm{v}}$ is included. Parameters are as follows: $N = 50$, $Q_{\mathrm{v},i}$ fixed for all $i = 1, \cdots, N$ to the same value Q_v which is varied, $\varepsilon_g = 0\,\mathrm{eV}$, $\varepsilon_e = 2.8\,\mathrm{eV}$, $\hbar\omega_c = 2.8\,\mathrm{eV}$, $\hbar\omega_\mathrm{v} = 50\,\mathrm{meV}$, $\hbar\tilde{\Omega}_R = 0.7\,\mathrm{eV}$, $\hbar\delta = 0\,\mathrm{eV}$, and $\lambda_\mathrm{v} = 0.1\,\mathrm{meV}$.

5

Thermal Electron-Transfer Rate

Electron-transfer (ET) reactions are common and important elementary chemical reactions. They have a fundamental role in enzymatic activity, photosynthesis and electrochemistry [113, 117]. ET reactions involve spontaneous transfer or redistribution of charges between initial *reactants* (R) and well-defined *products* (P), in a typically polar or weakly polar solution. Generically, these reactions take place at room temperature.

A famous example of self-exchange electron transfer reactions in aqueous solution is given by

$$\mathrm{Fe}^{+3} + \mathrm{Fe}^{+2} \rightarrow \mathrm{Fe}^{+2} + \mathrm{Fe}^{+3}. \tag{5.1}$$

The reaction is a simple reaction because the R and the P are identical and no chemical bonds is broken during the ET process [109]. Chemical reactions are usually described and represented with the corresponding Potential Energy Surface (PES) (see Section 4.3.3). The concept of PES is well adapted to describe the mechanism of an ET reaction. Figure 5.1 displays, on the right-hand side, the PES of reactants and products as a function of a nuclear reaction coordinate. The ET transfer process occurs at the crossing point of the two PESs (indicated with a red star). At that point, energy is conserved and the *Franck-Condon principle* is satisfied, *i.e.*, the electronic transition occurs at fixed nuclear reaction coordinates. The charge redistribution is fast compared to the nuclei movement. The fast process involves the reorganization and rearrangement of the multi-dimensional configuration of nuclei in the vicinity of R and in the solvent. The dashed and solid gold line on the left-hand side of Figure 5.1 represent the region, where the ET occurs, and the nearest region where the time-scale is governed by the solvent, respectively.

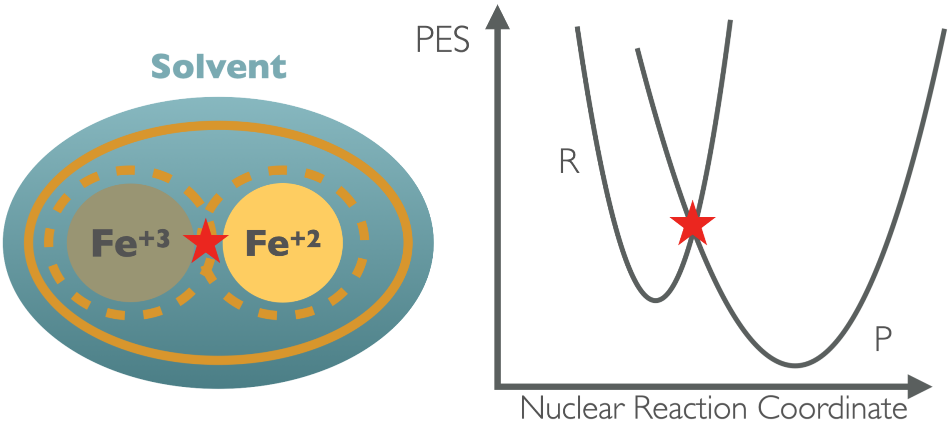

Figure 5.1: Sketch of self-exchange ET reaction (see eq. (5.1)).

The ET reaction can be *non-adiabatic* or *adiabatic*. The non-adiabatic ET is represented on the right-hand side of Figure 5.1. The nonadiabaticity of the process consists in a weak electron exchange perturbation (coupling) V_{ET} between the R and the P states. In contrast, the adiabatic ET is usually described with the double-well potential, where metastable initial R and the stable final P are separated by a potential barrier along the nuclear reaction coordinate. The barrier is overcome by thermal activation or nuclear tunneling. Another specification of ET is made whether or not the R and the P belong to the same molecule. If the R and P belong to the same molecule the ET is an *intramolecular* process, otherwise it is called *intermolecular* ET.

An important contribution to the developing of theoretical descriptions of ET reactions was provided by the extensive studies of Rudolph Arthur Marcus [107, 109, 145, 108]. The Marcus theory is a classical theory to describe the classical reorganization and fluctuations of solvent nuclear coordinates when the ET occurs. The reactants are treated as dielectric spheres embedded in a continuos dielectric medium, the solvent. One of the most important results of Marcus is the famous Marcus rate. The expression of the rate is the following one:

$$k_{\mathrm{ET}} = k_e \exp\left(-\Delta G^*/k_B T\right) \text{ with } \Delta G^* = \left(\Delta G^0 + \lambda\right)^2/4\lambda, \tag{5.2}$$

where k_e a reaction-dependent global rate, T the temperature, k_B the Boltzmann constant and $\Delta G^* = \left(\Delta G^0 + \lambda\right)^2/4\lambda$ an effective activation energy depending on the vibrational and solvent reorganization energy $\lambda = \lambda_{\mathrm{v}} + \lambda_{\mathrm{S}}$ and variation of the reaction thermodynamic Gibbs potential ΔG^0 (reaction driving strength or force). The Marcus rate k_{ET} has a simple expression with only three "fitting parameters": the driving strength ΔG^0, the reorganization energy λ and the temperature T (see Figure 5.2). The rate formulation was experimentally confirmed and the best experimental evidence was provided in 1984 by J. R. Miller, L. T. Calcaterra and G. L. Closs [115]. Figure 5.3 shows the experimental confirmation of the theoretically predicted *inverted region*. The experimental evidence came 25 years after the theoretical prediction. Marcus defined the rate evaluation as a function of $-\Delta G^0$ in two regions: the "normal region" and the "inverted region". The normal region is the region where the rate increases as the $-\Delta G^0$ increases untill it becomes equal to the reorganization energy λ. This region was called normal because it represents an expected trend of acid- (base-) catalyzed reactions and electrochemical reactions. The second region where the ET rate decreases for a further increase in $-\Delta G^0$, called the inverted region, was an unexpected behavior before the theory was introduced.

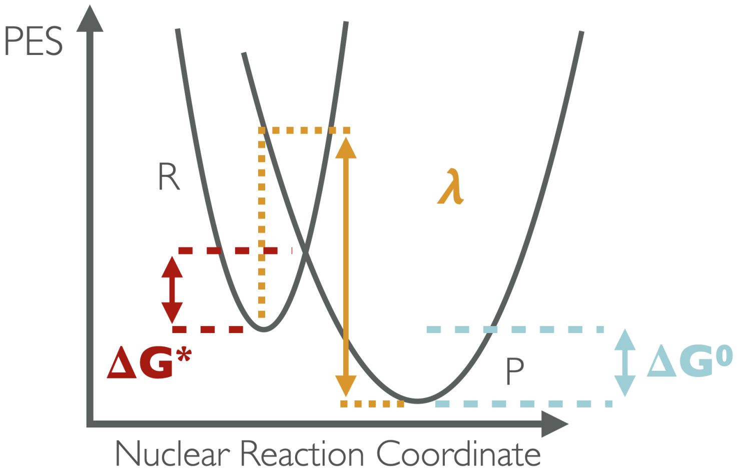

Figure 5.2: PESs of reactants and products with the correlated quantities of the Marcus rate (see eq. (5.2)).

Subsequent developments in ET theory have been directed to include quantum effects. In particular, V. G. Levich and R. R. Dogonadze, in 1966-1972, wrote a reaction rate in terms of the thermally averaged quantum mechanical transition probability between vibronic levels of the system and they maintained the classical description of the solvent [99, 37]. Eventually, a generalization of the quantum mechanical description was made, in 1974-1975, by Nell R. Kestner, Jean Logan and Joshua Jortner [89]. They derived a non-adiabatic ET rate including quantum fast modes ($\hbar\omega_{\mathrm{v}} > k_B T$) for reactants shells (see gold dashed lines in Figure 5.1), called first coordination layers, and low frequency modes for the solvent (see solid gold line in Figure 5.1).

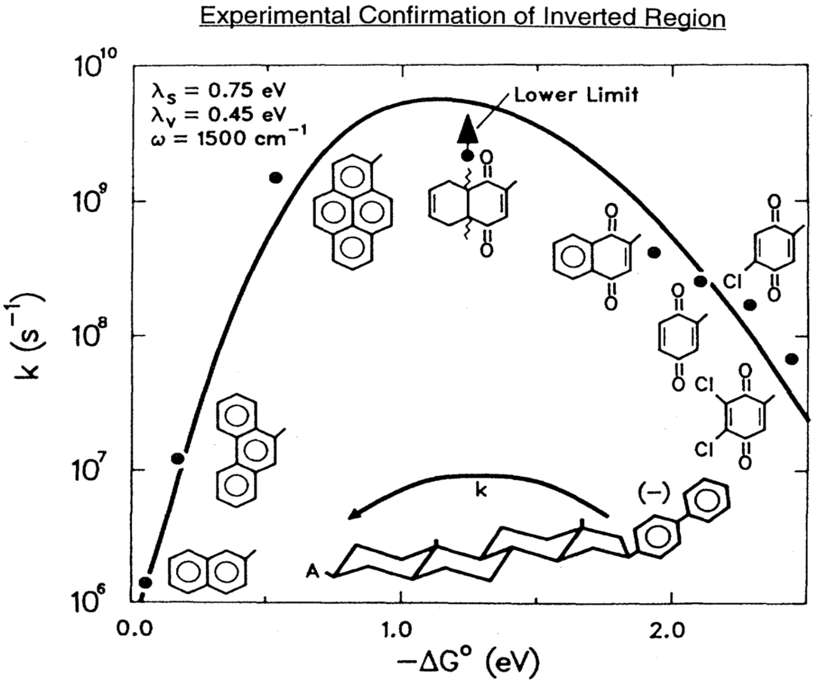

Figure 5.3: Experimental confirmation of the inverted region, in the chemical electron transfer from a biphenyl group to an acceptor, (solid black dots) and Marcus rate (black line) as a function of the Gibbs pontential $-\Delta G^0$ in unit of eV [115].

The rest of the Chapter contains the derivation of the non-adiabatic rate and for the high-temperature limit the Marcus rate is retrieved. Finally, the two rates are compared.

5.1 Non-adiabatic ET rate

This Section contains all the steps to get the quantum non-adiabatic ET rate at temperature T and for one vibrational mode ω_V. Eventually, the classical Marcus rate is derived in the high-temperature limit. Afterwards the expression of the ET rate is modified embedding the electron transfer reaction in a solvent and the final expressions are compared with respect the Marcus' result. The starting point is an ET reaction between a reactant (R) and a final product (P). The PES of P is shifted relative to R along the reaction coordinates. If $k_BT < \hbar\omega_\text{V}$ a quantum description is needed. Furthermore if the electron exchange is a weak perturbation, a non-adiabatic treatment is necessary. Hence the Fermi's Golden Rule is the appropriate framework:

$$\boxed{k_\text{ET} = \frac{2\pi}{\hbar}|\text{V}_\text{ET}|^2 \sum_{n,\,\tilde{m}=0}^{\infty} \frac{e^{-n\hbar\omega_\text{V}\beta}}{Z}|\langle n|\tilde{m}\rangle|^2 \delta\left(\Delta E + \hbar\omega_\text{V}(n-\tilde{m})\right),} \tag{5.3}$$

where V_ET is the crossing-coupling between the PES of R and P, $\beta \equiv 1/k_BT$, n is the vibrational index related to R, $\tilde{m}$ is connected to the displaced P ($|\tilde{m}\rangle = \exp[g_\text{V}(\hat{b} - \hat{b}^\dagger)]\,|m\rangle$), $\hat{b}$ ($\hat{b}^\dagger$) is a boson operator, g_V is the Huang-Rhys factor (see Section 4.3.1), Z is the partition function, $|\langle n|\tilde{m}\rangle|$ is the *Franck-Condon factor*, and ΔE is the *driving force* of the electron transfer reaction (see Figure 5.4).

5.1.1 Step 1: Fourier representation of δ

The first step is to replace δ with its Fourier representation:

$$\delta\left(\Delta E + \hbar\omega_\text{V}(n-\tilde{m})\right) = \frac{1}{2\pi\hbar}\int dt\, e^{\frac{it}{\hbar}[\Delta E + \hbar\omega_\text{V}(n-\tilde{m})]}. \tag{5.4}$$

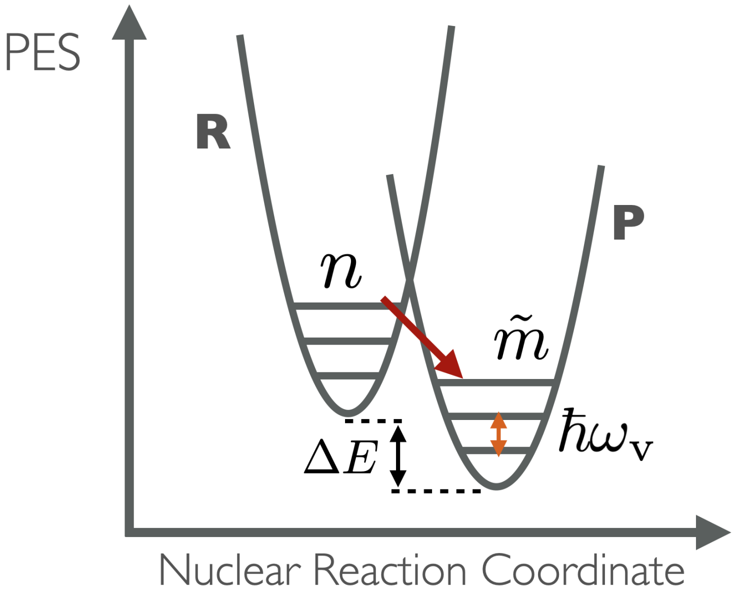

Figure 5.4: Non-adiabatic ET reaction (see red arrow) between R and the displaced P. The PESs have their vibrational levels with "distance" $\hbar\omega_{\mathrm{v}}$ (see orange arrow).

Now, the eq. (5.3) is given by

$$k_{\mathrm{ET}} = \frac{|\mathrm{V}_{\mathrm{ET}}|^2}{\hbar^2}\sum_{n,\,\tilde{m}=0}^{\infty}\int dt\frac{e^{-n\hbar\omega_{\mathrm{v}}\beta}}{Z}|\langle n|\tilde{m}\rangle|^2 e^{\frac{it}{\hbar}[\Delta E+\hbar\omega_{\mathrm{v}}(n-\tilde{m})]}. \tag{5.5}$$

5.1.2 Step 2: Autocorrelation function of combined displacement operators

This second step starts by considering the following term:

$$|\langle n|\tilde{m}\rangle|^2 e^{\frac{it}{\hbar}[\Delta E+\hbar\omega_{\mathrm{v}}(n-\tilde{m})]}.$$

The exponential can be inserted between $\langle n|$ and $|\tilde{m}\rangle$ in the following way:

$$|\langle n|\tilde{m}\rangle|^2 e^{\frac{it}{\hbar}[\Delta E+\hbar\omega_{\mathrm{v}}(n-\tilde{m})]} = e^{\frac{it}{\hbar}\Delta E}\langle n|\, e^{\frac{i\hat{\mathrm{H}}_{\mathrm{v}}t}{\hbar}} e^{\frac{-i\tilde{\hat{\mathrm{H}}}_{\mathrm{v}}t}{\hbar}}\,|\tilde{m}\rangle\langle\tilde{m}|n\rangle, \tag{5.6}$$

where $\hat{\mathrm{H}}_{\mathrm{v}} = \hbar\omega_{\mathrm{v}}\hat{a}^{\dagger}\hat{a}$, $\tilde{\hat{\mathrm{H}}}_{\mathrm{v}} = \hat{D}(g_{\mathrm{v}})\hat{\mathrm{H}}_{\mathrm{v}}\hat{D}^{\dagger}(g_{\mathrm{v}})$ and $\hat{D}^{\dagger}(g_{\mathrm{v}}) \equiv \exp[g_{\mathrm{v}}(\hat{b}-\hat{b}^{\dagger})]$.
Afterwards, using the completeness relation $\sum_{\tilde{m}}|\tilde{m}\rangle\langle\tilde{m}| = I$ and subtituting the eq. (5.6) in eq. (5.5) the result is

$$k_{\mathrm{ET}} = \frac{|\mathrm{V}_{\mathrm{ET}}|^2}{\hbar^2}\sum_{n=0}^{\infty}\int dt\frac{e^{-n\hbar\omega_{\mathrm{v}}\beta}}{Z}e^{\frac{it}{\hbar}\Delta E}\langle n|\, e^{\frac{i\hat{\mathrm{H}}_{\mathrm{v}}t}{\hbar}} e^{\frac{-i\tilde{\hat{\mathrm{H}}}_{\mathrm{v}}t}{\hbar}}\,|n\rangle\,. \tag{5.7}$$

Furthermore, the expression $\langle n|\, e^{\frac{i\hat{\mathrm{H}}_{\mathrm{v}}t}{\hbar}} e^{\frac{-i\tilde{\hat{\mathrm{H}}}_{\mathrm{v}}t}{\hbar}}\,|n\rangle$ can be rewritten in terms of the displacement operators $\hat{D}(g_{\mathrm{v}})$ and $\hat{D}^{\dagger}(g_{\mathrm{v}})$:

$$\langle n|\, e^{\frac{i\hat{\mathrm{H}}_{\mathrm{v}}t}{\hbar}} e^{\frac{-i\tilde{\hat{\mathrm{H}}}_{\mathrm{v}}t}{\hbar}}\,|n\rangle = \langle n|\, e^{\frac{i\hat{\mathrm{H}}_{\mathrm{v}}t}{\hbar}}\hat{D}(g_{\mathrm{v}})e^{\frac{-i\hat{\mathrm{H}}_{\mathrm{v}}t}{\hbar}}\hat{D}^{\dagger}(g_{\mathrm{v}})\,|n\rangle\,. \tag{5.8}$$

By recalling the evolution of an operator in the Heisemberg's representation, the last expression becomes

$$\langle n|\, e^{\frac{i\hat{\mathrm{H}}_{\mathrm{v}}t}{\hbar}}\hat{D}(g_{\mathrm{v}})e^{\frac{-i\hat{\mathrm{H}}_{\mathrm{v}}t}{\hbar}}\hat{D}^{\dagger}(g_{\mathrm{v}})\,|n\rangle = \langle n|\,\hat{D}(t)\hat{D}^{\dagger}(0)\,|n\rangle\,, \tag{5.9}$$

where $\hat{D}(t) = e^{\frac{i\hat{\mathrm{H}}_{\mathrm{v}}t}{\hbar}} \hat{D}(g_{\mathrm{v}}) e^{\frac{-i\hat{\mathrm{H}}_{\mathrm{v}}t}{\hbar}}$ and $\hat{D}^{\dagger}(0) \equiv \hat{D}^{\dagger}(g_{\mathrm{v}})$.
The rate k_{ET} (see eq. (5.7)) in the terms of the autocorrelation function of combined displacement operators given by eq. (5.9) reads

$$\boxed{k_{\mathrm{ET}} = \frac{|\mathrm{V}_{\mathrm{ET}}|^2}{\hbar^2} \sum_{n=0}^{\infty} \int dt \frac{e^{-n\hbar\omega_{\mathrm{v}}\beta}}{Z} e^{\frac{it}{\hbar}\Delta E} \langle n| \hat{D}(t)\hat{D}^{\dagger}(0) |n\rangle \,. \qquad (5.10)}$$

5.1.3 Step 3: Calculation of the autocorrelation function

First of all, the operator $\hat{D}(t)$ can be Taylor expanded to get a simpler formula:

$$\begin{aligned} \hat{D}(t) &= e^{\frac{i\hat{\mathrm{H}}_{\mathrm{v}}t}{\hbar}} \hat{D}(g_{\mathrm{v}}) e^{\frac{-i\hat{\mathrm{H}}_{\mathrm{v}}t}{\hbar}} = e^{\frac{i\hat{\mathrm{H}}_{\mathrm{v}}t}{\hbar}} e^{g_{\mathrm{v}}(\hat{b}^{\dagger}-\hat{b})} e^{\frac{-i\hat{\mathrm{H}}_{\mathrm{v}}t}{\hbar}} = e^{\frac{i\hat{\mathrm{H}}_{\mathrm{v}}t}{\hbar}} \left\{ \sum_{m=0}^{\infty} \frac{[g_{\mathrm{v}}(\hat{b}^{\dagger} - \hat{b})]^m}{m!} \right\} e^{\frac{-i\hat{\mathrm{H}}_{\mathrm{v}}t}{\hbar}} = \\ &= \frac{1}{m!} \underbrace{e^{\frac{i\hat{\mathrm{H}}_{\mathrm{v}}t}{\hbar}} g_{\mathrm{v}}(\hat{b}^{\dagger} - \hat{b}) e^{\frac{-i\hat{\mathrm{H}}_{\mathrm{v}}t}{\hbar}}}_{m \text{ times}} = \exp\left\{ g_{\mathrm{v}} \left[e^{\frac{i\hat{\mathrm{H}}_{\mathrm{v}}t}{\hbar}} (\hat{b}^{\dagger} - \hat{b}) e^{\frac{-i\hat{\mathrm{H}}_{\mathrm{v}}t}{\hbar}} \right] \right\} = \exp\left\{ -g_{\mathrm{v}} \left[\hat{b} e^{-i\omega_{\mathrm{v}}t} - \hat{b}^{\dagger} e^{i\omega_{\mathrm{v}}t} \right] \right\}. \end{aligned} \tag{5.11}$$

If $t \to 0$, $\hat{D}(t) \to \hat{D}(0)$.
The autocorrelation function by using (5.11) has the form

$$\langle n| \hat{D}(t)\hat{D}^{\dagger}(0) |n\rangle = \langle n| \exp\left\{ -g_{\mathrm{v}} \left[\hat{b} e^{-i\omega_{\mathrm{v}}t} - \hat{b}^{\dagger} e^{i\omega_{\mathrm{v}}t} \right] \right\} e^{g_{\mathrm{v}}(\hat{b}-\hat{b}^{\dagger})} |n\rangle \tag{5.12}$$

To further simplify the autocorrelation function, the *Glauber's Formula* (GF) is useful. Its definition is

$$e^{A+B} = e^{A} e^{B} e^{-\frac{1}{2}[A,B]} \quad \text{with} \quad [A,[A,B]] = [B,[A,B]] = 0, \tag{5.13}$$

where A, B are two different operators.
By applying twice GF, the eq. (5.12) gets

$$\begin{aligned} &\langle n| \exp\left\{ -g_{\mathrm{v}} \left[\hat{b} e^{-i\omega_{\mathrm{v}}t} - \hat{b}^{\dagger} e^{i\omega_{\mathrm{v}}t} \right] \right\} e^{g_{\mathrm{v}}(\hat{b}-\hat{b}^{\dagger})} |n\rangle \\ &\overset{\mathrm{GF}}{=} e^{\frac{g_{\mathrm{v}}^2}{2}(e^{-i\omega_{\mathrm{v}}t} - e^{i\omega_{\mathrm{v}}t})} \langle n| \exp\left\{ g_{\mathrm{v}} \left[\hat{b}(1 - e^{-i\omega_{\mathrm{v}}t}) - \hat{b}^{\dagger}(1 - e^{i\omega_{\mathrm{v}}t}) \right] \right\} |n\rangle \overset{\mathrm{GF}}{=} \\ &\overset{\mathrm{GF}}{=} e^{\frac{g_{\mathrm{v}}^2}{2}(e^{-i\omega_{\mathrm{v}}t} - e^{i\omega_{\mathrm{v}}t} - |1 - e^{i\omega_{\mathrm{v}}t}|^2)} \langle n| e^{z\hat{b}^{\dagger}} e^{-z^{*}\hat{b}} |n\rangle \,, \end{aligned} \tag{5.14}$$

where $z \equiv g_{\mathrm{v}}(e^{i\omega_{\mathrm{v}}t} - 1)$.
It remains to calculate

$$S(z) \equiv \langle n| e^{z\hat{b}^{\dagger}} e^{-z^{*}\hat{b}} |n\rangle \,.$$

It is quite straightforward to calculate the action of the exponential operator on the $|n\rangle$ states using a Taylor expansion.

$$S(z) = \lim_{n\to\infty} \sum_{l=0}^{n} (-1)^l \frac{l!}{(l!)^2 (l-n)!} |z|^{2l}, \tag{5.15}$$

where it is applied

$$b^l |n\rangle = \sqrt{\frac{n!}{(n-l)!}} |n-l\rangle \,.$$

The "new" expression of $S(z)$ given by eq. (5.15) is the limit of special polynomials, Laguerre's polynomials $L_n^k(x)$:

$$L_n^k(x) = \sum_{m=0}^{n} (-1)^m \frac{(n+k)!}{(n-m)!(k+m)!m!} x^m \quad \text{with } x \in \mathcal{C},\ k > -1. \tag{5.16}$$

In the present case

$$S(z) = \lim_{n\to\infty} L_n^0(|z|^2). \tag{5.17}$$

Finally, the autocorrelation function (see eq. (5.12)) becomes

$$\langle n|\, \hat{D}(t)\hat{D}^{\dagger}(0)\, |n\rangle = e^{\frac{g_{\mathrm{v}}^2}{2}\left(e^{-i\omega_{\mathrm{v}}t}-e^{i\omega_{\mathrm{v}}t}-|1-e^{i\omega_{\mathrm{v}}t}|^2\right)} \lim_{n\to\infty} L_n^0(|z|^2). \tag{5.18}$$

5.1.4 Step 4: Final step

It remains to rewrite the rate k_{ET} (see eq. (5.10)), using the eq. (5.18), and compute the sum inside:

$$k_{\mathrm{ET}} = \frac{|\mathrm{V_{ET}}|^2}{\hbar^2}\left(1-e^{-\hbar\omega_{\mathrm{v}}\beta}\right)\int dt e^{\frac{it}{\hbar}\Delta E} A_{\mathrm{v}}(t)\sum_{n=0}^{\infty} e^{-n\hbar\omega_{\mathrm{v}}\beta} L_n^0(|z|^2), \tag{5.19}$$

where

$$\left(1-e^{-\hbar\omega_{\mathrm{v}}\beta}\right) = 1/Z$$

and

$$A_{\mathrm{v}}(t) \equiv e^{\frac{g_{\mathrm{v}}^2}{2}\left(e^{-i\omega_{\mathrm{v}}t}-e^{i\omega_{\mathrm{v}}t}-|1-e^{i\omega_{\mathrm{v}}t}|^2\right)}.$$

The calculation of the sum inside the eq. (5.19) is easy by using

$$\sum_{n=0}^{\infty} L_n^k(x) y^n = \frac{e^{-xy/(1-y)}}{(1-y)^{k+1}} \quad \text{with } |y|<1. \tag{5.20}$$

Thus

$$\sum_{n=0}^{\infty} e^{-n\hbar\omega_{\mathrm{v}}\beta} L_n^0(|z|^2) = \frac{e^{-|z|^2\frac{e^{-\hbar\omega_{\mathrm{v}}\beta}}{1-e^{-\hbar\omega_{\mathrm{v}}\beta}}}}{1-e^{-\hbar\omega_{\mathrm{v}}\beta}}. \tag{5.21}$$

Then the rate reads

$$k_{\mathrm{ET}} = \frac{|\mathrm{V_{ET}}|^2}{\hbar^2}\int dt e^{\frac{it}{\hbar}\Delta E} A_{\mathrm{v}}(t) e^{-|z|^2 n_{\mathrm{B}}}, \tag{5.22}$$

where $n_{\mathrm{B}} = e^{-\hbar\omega_{\mathrm{v}}\beta}/\left(1-e^{-\hbar\omega_{\mathrm{v}}\beta}\right) = 1/(e^{\hbar\omega_{\mathrm{v}}\beta}-1)$ is the Bose-Einstein distribution.
Finally it is possible to simplify $A_{\mathrm{v}}(t)e^{-|z|^2 n_{\mathrm{B}}}$ by doing few multiplications, obtaining

$$k_{\mathrm{ET}} = \frac{|\mathrm{V_{ET}}|^2}{\hbar^2}\int dt e^{\frac{it}{\hbar}\Delta E} e^{-g_{\mathrm{v}}^2(1+2n_{\mathrm{B}})} \exp\left\{g_{\mathrm{v}}^2\left[(1+n_{\mathrm{B}})e^{-i\omega_{\mathrm{v}}t}+n_{\mathrm{B}}e^{i\omega_{\mathrm{v}}t}\right]\right\}. \tag{5.23}$$

The last thing is to note that

$$\lim_{t\to 0}\left(\exp\left\{g_{\mathrm{v}}^2\left[(1+n_{\mathrm{B}})e^{-i\omega_{\mathrm{v}}t}+n_{\mathrm{B}}e^{i\omega_{\mathrm{v}}t}\right]\right\}\right) = e^{g_{\mathrm{v}}^2(1+2n_{\mathrm{B}})}. \tag{5.24}$$

In this way by defining $G(t) \equiv g_{\mathrm{v}}^2\left[(1+n_{\mathrm{B}})e^{-i\omega_{\mathrm{v}}t}+n_{\mathrm{B}}e^{i\omega_{\mathrm{v}}t}\right]$, the eq. (5.18) becomes

$$\boxed{k_{\mathrm{ET}} = \frac{|\mathrm{V_{ET}}|^2}{\hbar^2}\int dt\, e^{\frac{it}{\hbar}\Delta E} e^{-G(0)+G(t)}.} \tag{5.25}$$

The derived rate k_{ET} is consistent with the ref. [89].

5.1.5 High-temperature limit

The final expression of k_{ET} (see eq. (5.25)) is calculated bearing in mind $k_B T < \hbar\omega_{\mathrm{v}}$ to perform a Quantum calculation. However, if $k_B T \gg \hbar\omega_{\mathrm{v}}$ the famous Marcus rate (see eq. (5.2)) is recovered.
The expression $e^{-g_{\mathrm{v}}^2(1+2n_{\mathrm{B}})}\exp\left\{g_{\mathrm{v}}^2\left[(1+n_{\mathrm{B}})e^{-i\omega_{\mathrm{v}}t}+n_{\mathrm{B}}e^{i\omega_{\mathrm{v}}t}\right]\right\}$ at high-T is

$$\begin{aligned}
&e^{-g_{\mathrm{v}}^2(1+2n_{\mathrm{B}})}\exp\left\{g_{\mathrm{v}}^2\left[(1+n_{\mathrm{B}})e^{-i\omega_{\mathrm{v}}t}+n_{\mathrm{B}}e^{i\omega_{\mathrm{v}}t}\right]\right\}\xrightarrow{k_BT\gg\hbar\omega_{\mathrm{v}}}\\
&\xrightarrow{k_BT\gg\hbar\omega_{\mathrm{v}}} e^{-g_{\mathrm{v}}^2(1+2n_{\mathrm{B}})}\exp\left\{g_{\mathrm{v}}^2[(1+n_{\mathrm{B}})(1-i\omega_{\mathrm{v}}t-\frac{\omega_{\mathrm{v}}^2}{2}t^2)+n_{\mathrm{B}}(1+i\omega_{\mathrm{v}}t-\frac{\omega_{\mathrm{v}}^2}{2}t^2)]\right\}=\\
&=\exp\left[\frac{-it}{\hbar}\lambda_{\mathrm{v}}\right]\cdot\exp\left[-t^2\frac{\lambda_{\mathrm{v}}k_BT}{\hbar^2}\right],
\end{aligned}\tag{5.26}$$

where it is introduced $g_{\mathrm{v}}^2=\lambda_{\mathrm{v}}/(\hbar\omega_{\mathrm{v}})$, λ_{v} is the reorganization energy, and $1+2n_{\mathrm{B}}\approx 2k_BT/\hbar\omega_{\mathrm{v}}$.
By replacing the result in eq. (5.26) inside the rate k_{ET} (5.25), the classical Marcus rate $k_{\mathrm{ET}}^{(\mathrm{cl})}$ is

$$k_{\mathrm{ET}}^{(\mathrm{cl})}=\frac{2\pi}{\hbar}\frac{|\mathrm{V}_{\mathrm{ET}}|^2}{\sqrt{4\pi\lambda_{\mathrm{v}}k_BT}}e^{-\beta\frac{(\Delta E-\lambda_{\mathrm{v}})^2}{4\lambda_{\mathrm{v}}}}.\tag{5.27}$$

The expression $k_{\mathrm{ET}}^{(\mathrm{cl})}$ differs with respect to the eq. (5.2) for a minus sign in the exponent. The sign in eq. (5.2) comes from the thermodynamic convention on ΔG^0. This aspect is only a matter of convention for the initial starting point and it does not affect the result.

5.2 Other way for the Classical Rate

In the limit $k_BT \gg \hbar\omega_\nu$, the description of the vibrational motion is pursued in the framework of classical physics [113]. The most simple explanation can be done considering a two-level system for R and P given by the RP Hamiltonian

$$\hat{\mathrm{H}}_{\mathrm{RP}}=E_{\mathrm{R}}\left|R\right\rangle\left\langle R\right|+E_{\mathrm{P}}\left|P\right\rangle\left\langle P\right|+\mathrm{V}_{\mathrm{RP}}\left|R\right\rangle\left\langle P\right|+\mathrm{V}_{\mathrm{PR}}\left|P\right\rangle\left\langle R\right|,\tag{5.28}$$

and the following PES

$$\mathrm{E}_{\mathrm{R/P}}(Q)=E^0_{\mathrm{R/P}}(0)+\frac{1}{2}\omega_{\mathrm{v}}^2(Q-Q_{\mathrm{R/P}})^2,\tag{5.29}$$

for R and P respectively.
According to the fact that during the ET process at high-T there is no change in the vibrational kinetic energy, the classical Marcus rate can be written as

$$k_{\mathrm{ET}}^{(\mathrm{cl})}=\frac{2\pi}{\hbar}|\mathrm{V}_{\mathrm{RP}}|^2\int dQ\,\frac{e^{-\beta\mathrm{E}_{\mathrm{R}}(Q)}}{Z}\delta\left(\mathrm{E}_{\mathrm{R}}(Q)-\mathrm{E}_{\mathrm{P}}(Q)\right).\tag{5.30}$$

One way to carry out this integration is to find the zero of δ, the crossing point between the two PES, and to use $\delta(g(x))=\frac{\delta(x-x_0)}{|g'(x_0)|}$. By performing this, the eq. (5.30) reads

$$k_{\mathrm{ET}}^{(\mathrm{cl})}=\frac{2\pi}{\hbar}|\mathrm{V}_{\mathrm{RP}}|^2\int dQ\,\frac{e^{-\beta\mathrm{E}_{\mathrm{R}}(Q)}}{Z}\frac{\delta\left(Q-Q_\times\right)}{\omega_{\mathrm{v}}^2(Q_{\mathrm{R}}-Q_{\mathrm{P}})},\tag{5.31}$$

where the crossing point is

$$Q_\times=\frac{\Delta E+\left[\omega_{\mathrm{v}}^2(Q_{\mathrm{R}}^2-Q_{\mathrm{P}}^2)\right]/2}{\omega_{\mathrm{v}}^2(Q_{\mathrm{R}}-Q_{\mathrm{P}})},\quad\text{with}\quad\Delta E=E^0_{\mathrm{R}}(0)-E^0_{\mathrm{P}}(0).\tag{5.32}$$

Now it remains to carry out a Gaussian integration and the result is

$$k_{\mathrm{ET}}^{(\mathrm{cl})}=\frac{2\pi}{\hbar}\frac{|\mathrm{V}_{\mathrm{RP}}|^2}{\sqrt{4\pi\lambda_{\mathrm{v}}k_BT}}e^{-\beta E_{\mathrm{a}}}\quad\text{with}\quad E_{\mathrm{a}}=\frac{1}{2}\omega_{\mathrm{v}}^2(Q_\times-Q_{\mathrm{R}})^2.\tag{5.33}$$

The last step concerns the rearrangement of the *activation energy* E_a for the ET, namely

$$E_\mathrm{a} = \frac{(\Delta E - \lambda_\mathrm{v})^2}{4\lambda_\mathrm{v}} \quad \text{with} \quad \lambda_\mathrm{v} = \frac{\omega_\mathrm{v}^2}{2}\left(Q_\mathrm{P} - Q_\mathrm{R}\right)^2 . \tag{5.34}$$

Thus the rate $k_{\mathrm{ET,\,cl}}$ (see eq. (5.33)) becomes exactly the same of eq. (5.27)

$$k_\mathrm{ET}^{(\mathrm{cl})} = \frac{2\pi}{\hbar}\frac{|\mathrm{V_{RP}}|^2}{\sqrt{4\pi\lambda_\mathrm{v} k_B T}} e^{-\beta\frac{(\Delta E - \lambda_\mathrm{v})^2}{4\lambda_\mathrm{v}}} . \tag{5.35}$$

5.3 Rate in presence of a Solvent

The solvent S is represented by a collection of k harmonic oscillators with modes ω_k in addition to the vibrational mode ω_v. Now the corresponding PESs are

$$\mathrm{E}_{\mathrm{R/P}}(Q) = E^0_{\mathrm{R/P}}(0) + \frac{1}{2}\omega_\mathrm{v}^2 (Q - Q_{\mathrm{R/P}})^2 + \frac{1}{2}\sum_k \omega_k^2 (Q_k - Q_{k,\mathrm{R/P}})^2 . \tag{5.36}$$

Adding the solvent, the eq. (5.5) has to be modified to get

$$k_\mathrm{ET} = \frac{|\mathrm{V_{ET}}|^2}{\hbar^2}\sum_{n,\,\tilde m = 0}^{\infty}\int dt \left[\frac{e^{-n\hbar\omega_\mathrm{v}\beta}}{Z} |\langle n|\tilde m\rangle|^2 e^{\frac{it}{\hbar}[\Delta E + \hbar\omega_\mathrm{v}(n-\tilde m)]} \prod_k \frac{e^{-n_k\hbar\omega_k\beta}}{Z_k} |\langle n_k|\tilde m_k\rangle|^2 e^{it\omega_k(n_k - \tilde m_k)} \right] . \tag{5.37}$$

This rate can be reduced by following all the steps already introduced in Section 5.1. The final rate is

$$k_\mathrm{ET} = \frac{|\mathrm{V_{ET}}|^2}{\hbar^2}\int dt\, e^{\frac{it}{\hbar}\Delta E} f_\mathrm{v}(t) f_\mathrm{S}(t), \tag{5.38}$$

where

$$f_\mathrm{v}(t) \equiv e^{-G(0)+G(t)}, \quad f_\mathrm{S}(t) \equiv e^{\sum_k(-G_k(0)+G_k(t))} \tag{5.39}$$

with

$$G_k(t) \equiv g_k^2 \left[(1 + n_{\mathrm{B},k}) e^{-i\omega_k t} + n_{\mathrm{B},k} e^{i\omega_k t} \right] . \tag{5.40}$$

5.3.1 High-temperature limit

If $k_B T \gg \hbar\omega_\mathrm{v}$ and $k_B T \gg \hbar\omega_k$ the rate in eq. (5.38), by redoing the same Taylor expansion applied to eq. (5.25), reads

$$k_\mathrm{ET}^{(\mathrm{cl})} = \frac{2\pi}{\hbar}\frac{|\mathrm{V_{ET}}|^2}{\sqrt{4\pi\Lambda k_B T}} e^{-\beta\frac{(\Delta E - \Lambda)^2}{4\Lambda}} , \quad \text{with } \Lambda \equiv \lambda_\mathrm{v} + \underbrace{\sum_k \hbar\omega_k g_k^2}_{\lambda_\mathrm{S}} . \tag{5.41}$$

5.3.2 Classical solvent

A classical solvent is characterized by low-frequency modes with respect to the high-frequency vibrational mode ω_v. Thus, it is possible to substitute in eq. (5.38)

$$f_\mathrm{v}(t) = \sum_{n,\,\tilde m = 0}^{\infty} \frac{e^{-n\hbar\omega_\mathrm{v}\beta}}{Z} |\langle n|\tilde m\rangle|^2 e^{\frac{it}{\hbar}\hbar\omega_\mathrm{v}(n-\tilde m)} \tag{5.42}$$

and to apply the high-temperature limit to $f_\mathrm{S}(t)$ obtaining

$$\boxed{k_{\mathrm{ET}} = \frac{2\pi}{\hbar}\frac{|\mathrm{V}_{\mathrm{ET}}|^2}{\sqrt{4\pi\lambda_{\mathrm{S}} k_B T}}\sum_{n,\tilde{m}=0}^{\infty}\frac{e^{-n\hbar\omega_{\mathrm{v}}\beta}}{Z}|\langle n|\tilde{m}\rangle|^2 e^{-\beta\frac{[\Delta E-\lambda_{\mathrm{S}}+\hbar\omega_{\mathrm{v}}(n-\tilde{m})]^2}{4\lambda_{\mathrm{S}}}},} \tag{5.43}$$

where $\lambda_{\mathrm{S}} \equiv \sum_k \hbar\omega_k g_k^2$ and the *Franck-Condon overlap* is

$$\langle\tilde{m}|n\rangle = e^{-g_{\mathrm{v}}^2/2}\sum_{i=0}^{n}\sum_{j=0}^{m}\frac{(-1)^i (g_{\mathrm{v}})^{i+j}}{i!\;j!}\sqrt{\frac{n!\;m!}{(n-i)!(m-j)!}}\delta_{n-i,\,m-j}. \tag{5.44}$$

The Franck-Condon overlap can also be computed using (see the ref. [90])

$$\langle\tilde{m}|n\rangle = e^{-g_{\mathrm{v}}^2/2}[\mathrm{sgn}(n-m)]^{m-n} g^{Q-q}\sqrt{\frac{q!}{Q!}}L_q^{Q-q}(g^2), \tag{5.45}$$

where L_q^{Q-q} are Generalized Laguerre's polynomials.
The form of this rate is one of the several variations of Marcus Rate that was greatly contributed by Nell R. Kestner, Jean Logan and Joshua Jortner [89].

The rate in eq. (5.43) can also be written as a convolution of two lineshapes [111]:

$$\boxed{k_{\mathrm{ET}} = \frac{2\pi}{\hbar}|\mathrm{V}_{\mathrm{ET}}|^2\mathcal{L}_{\mathrm{v}} \star \mathcal{L}_{\mathrm{cl}}(\Delta E, \lambda_{\mathrm{S}}),} \tag{5.46}$$

with

$$\begin{aligned}\mathcal{L}_{\mathrm{v}}(\Delta E) &= \sum_{n,\tilde{m}=0}^{\infty} F_{n\tilde{m}}\delta\left[\Delta E + \hbar\omega_{\mathrm{v}}(\tilde{m}-n)\right],\\ \mathcal{L}_{\mathrm{cl}}(\Delta E, \lambda_{\mathrm{S}}) &= \frac{1}{\sqrt{4\pi\lambda_{\mathrm{S}} k_B T}}\exp\left[-\beta\frac{(\Delta E+\lambda_{\mathrm{S}})^2}{4\lambda_{\mathrm{S}}}\right],\end{aligned} \tag{5.47}$$

where $F_{n\tilde{m}} \equiv \frac{e^{-n\hbar\omega_{\mathrm{v}}\beta}}{Z}|\langle n|\tilde{m}\rangle|^2$, $\beta \equiv 1/k_B T$ and ΔE is sent to $-\Delta E$ to then vary $-\Delta E$ as the Figure 5.3 (the choice of the author does not affect the result).

The formulation of the rate written in terms of the vibrational lineshape and the classical lineshape of the solvent clarifies the effect of the solvent on the quantum vibrational modes. The solvent broadens the quantum discrete vibrational lineshapes. The Figure 5.5 is a pictorial representation of the broadening made by the solvent.

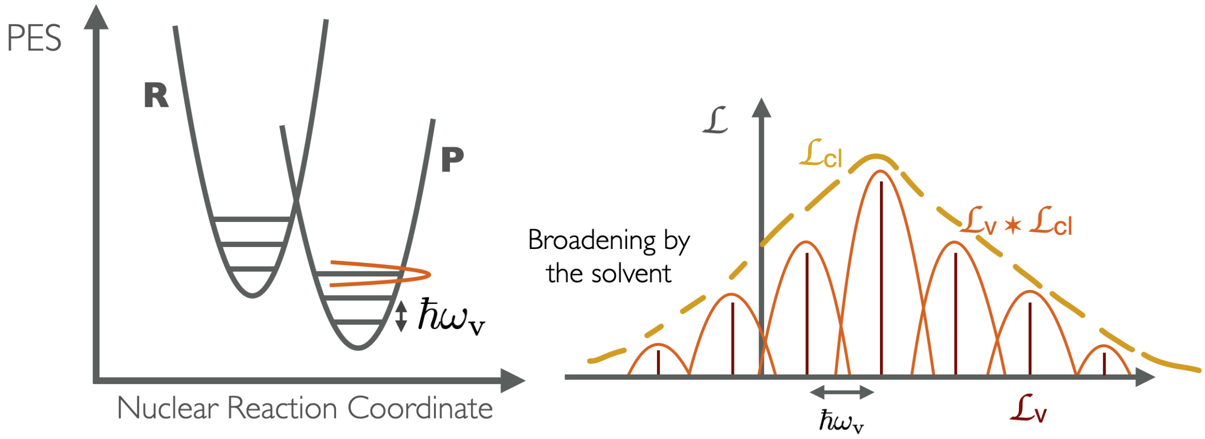

Figure 5.5: Broadening of the vibrational lineshapes $\mathcal{L}_{\mathrm{v}}$ by the classical one $\mathcal{L}_{\mathrm{cl}}$.

5.4 Rates in comparison

This section shows how the derived non-adiabatic rate (see eq. (5.46)) and the Marcus rate (see eq. (5.41) with $\Delta E \rightarrow -\Delta E$) behave varying the driving force $-\Delta E$. The following Figures display three different regimes: $k_B T = 5 \cdot \hbar\omega_\mathrm{v}$, $k_B T = \hbar\omega_\mathrm{v}/5$ and $k_B T \approx \hbar\omega_\mathrm{v}$. All the rate are normalized in the unit of k_e:

$$k_e \equiv \frac{2\pi}{\hbar} \frac{|\mathrm{V_{ET}}|^2}{\sqrt{4\pi\Lambda k_B T}}, \quad \text{with } \Lambda \equiv \lambda_\mathrm{v} + \lambda_\mathrm{S}. \tag{5.48}$$

Figure 5.6 represents the high-temperature limit where the two rates are equal and the maximum is reached for $\Delta E = \lambda_\mathrm{v} + \lambda_\mathrm{S}$. The deviation between the Marcus rate and the other rate is represented in Figure 5.7. In this case the derived non-adiabatic rate has the maximum for $\Delta E \approx \lambda_\mathrm{S}$ and it does not reach the maximum of 1.0 for the separation of fast vibrational modes and slow solvent modes, which modifies the behaviour of the classical lineshape. Finally, Figure 5.8 shows the intermediate regime $k_B T \approx \hbar\omega_\nu$. In this intermediate regime, for two comparable λs, a good match is reached and a tiny displacement along the ΔE-axis is visible.

In conclusion the difference between the classical regime and the quantum regime, although a deviation is visible when $\hbar\omega_\mathrm{v} \gg k_B T$, is not substancially remarkable and for some range of parameters the classical rate $k_\mathrm{ET}^{(\mathrm{cl})}$ can be considered a convenient and simple tool to describe the ET reaction in a solvent.

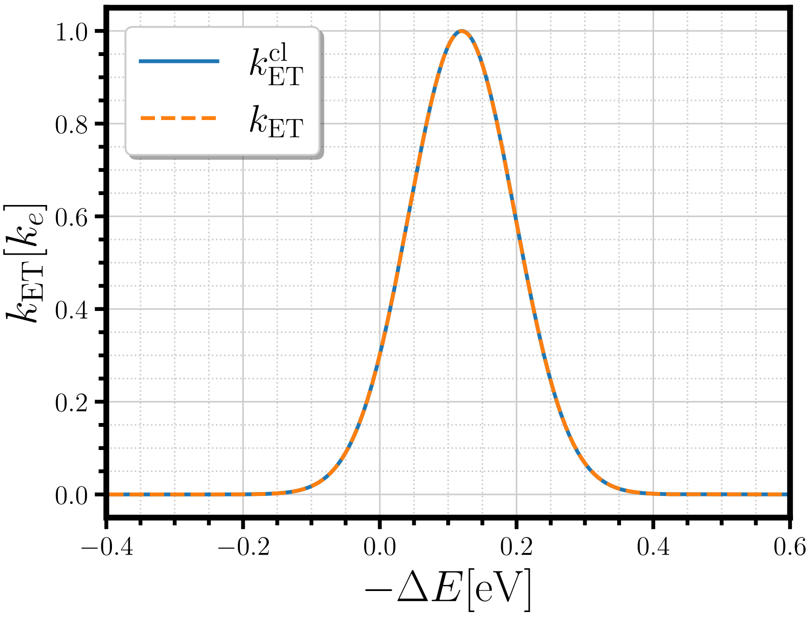

Figure 5.6: Marcus ET rate $k_\mathrm{ET}^{(\mathrm{cl})}$ (light-blue line) and non-adiabatic ET rate k_ET (see (5.46)) (orange dashed line) as a function of the driving force $-\Delta E$ in unit of eV. Parameters are as follows: $k_B T = 26\,\mathrm{meV}$, $\hbar\omega_\mathrm{v} = 0.52\,\mathrm{meV}$, $\lambda_\mathrm{v} = 40\,\mathrm{meV}$, and $\lambda_\mathrm{S} = 80\,\mathrm{meV}$.

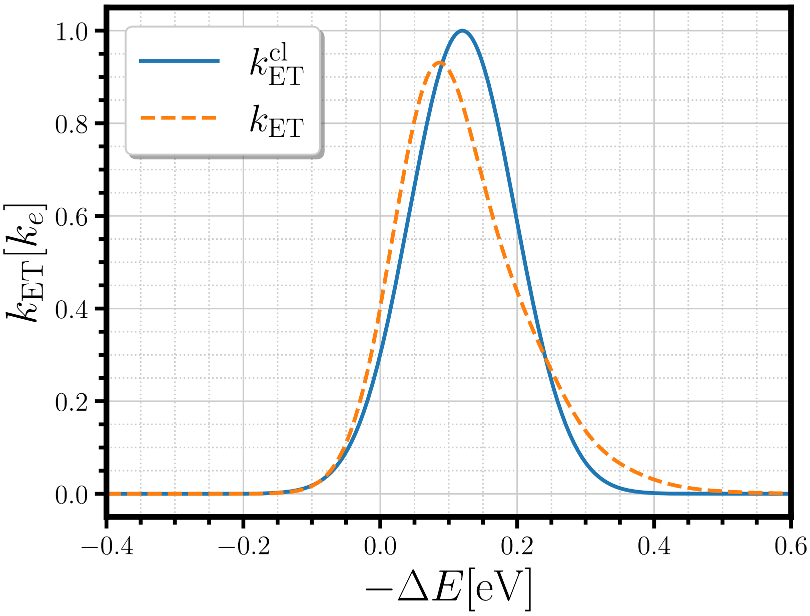

Figure 5.7: Marcus ET rate $k_{\mathrm{ET}}^{(\mathrm{cl})}$ (light-blue line) and non-adiabatic ET rate k_{ET} (see (5.46)) (orange dashed line) as a function of the driving force $-\Delta E$ in unit of eV. Parameters are as follows: $k_B T = 26\,\mathrm{meV}$, $\hbar\omega_{\mathrm{v}} = 130\,\mathrm{meV}$, $\lambda_{\mathrm{v}} = 40\,\mathrm{meV}$, and $\lambda_{\mathrm{S}} = 80\,\mathrm{meV}$.

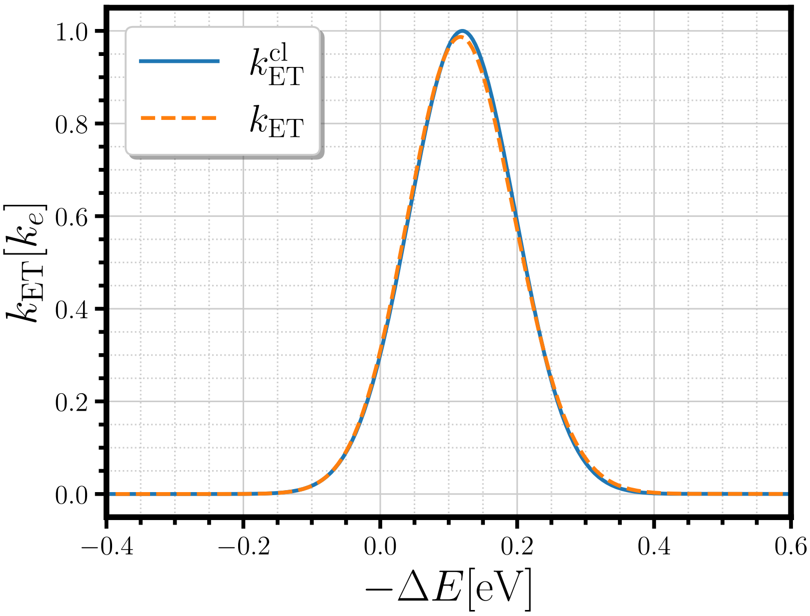

Figure 5.8: Marcus ET rate $k_{\mathrm{ET}}^{(\mathrm{cl})}$ (light-blue line) and non-adiabatic ET rate k_{ET} (see (5.46)) (orange dashed line) as a function of the driving force $-\Delta E$ in unit of eV. Parameters are as follows: $k_B T = 26\,\mathrm{meV}$, $\hbar\omega_{\mathrm{v}} = 30\,\mathrm{meV}$, $\lambda_{\mathrm{v}} = 40\,\mathrm{meV}$, and $\lambda_{\mathrm{S}} = 80\,\mathrm{meV}$.

6

Charge-Transfer Reactions in Cavity

Electron-transfer (ET) chemical reactions in solution constitute a paradigmatic class of chemical reactions [127] (see Chapter 5). In the more general class of charge-transfer (CT) chemical reactions, a modification of the local-charge density of states occurs between different chemical groups of the reacting molecules, thus resulting in a partially transferred (shifted) charge δ_{e} during the CT process. Such is the case for intramolecular CT reactions in $D - A$ molecules where an electron donor (D) group is connected to an electron acceptor (A) group through a molecular bridge ($-$), thus resulting in the following intramolecular CT mechanism

$$D - A \longrightarrow D^{+\delta_{\mathrm{e}}} - A^{-\delta_{\mathrm{e}}}. \tag{6.1}$$

In this Chapter, the chemical reactivity of a solution of molecules inside a Fabry-Pérot nanofluidic cavity is studied [111]. For this purpose, bi-phenyl molecules have been studied extensively [112, 70], since they have interesting photochemical properties due to a rotational degree of freedom around a C-C bond connecting the phenyl groups, as well as a possibility of being functionalized by various chemical groups with electron donating or accepting character. Other donor-acceptor molecules with an internal high-frequency vibrational mode are also good candidates for investigating CT reaction rates in solution.

Herein, typical organic molecules with interesting photoactive properties are considered. These molecules are embedded inside the cavity. Such is the case for the molecule represented in Figure 6.1 (a), and written (E)-4-[2-(1-methylpyridin-1-ium-4-yl)vinyl]phenolate; this nomenclature describes the structure of the molecule in its aromatic form. Figure 6.1 (b) shows a sketch of the PES (solid curves) for such a molecule described within BOA (see Section 4.3.1) [161], as a function of the reaction coordinate (RC). In this case the RC corresponds to an *intramolecular vibration* or a rotation mode of the molecule. The electronic structure of this molecule is described by an electronic ground state with two relative minima labelled g and g', and an electronic excited-state with two minima e and f. Upon photoexcitation from g to e, the molecule can reach the more stable excited-state f by changing its conformation and undergoing an elementary CT process. For simplicity, the complex electronic structure of the molecule is approximated by displaced parabolic PES [70], in the spirit of the parabolic approximation (see Section 4.3.3) in Marcus theory [109] (see dashed curves in Figure 6.1 (b)). Thus, the system made of N molecules in solution coupled to a single electromagnetic cavity mode (see Fig.6.1 (a)) is described by the microscopic Hamiltonian $\hat{\mathcal{H}}$:

$$\hat{\mathcal{H}} = \hat{\mathcal{H}}_0 + \hat{\mathrm{V}}_{\mathrm{CT}} = \hat{\mathrm{H}}_{\mathrm{CaM}} + \hat{\mathrm{V}}_{\mathrm{M-Ca}} + \hat{\mathrm{V}}_{\mathrm{CT}}\,, \tag{6.2}$$

as the sum of the Hamiltonian $\hat{\mathrm{H}}_{\mathrm{CaM}}$ describing the free electromagnetic cavity mode (Ca) and quadratic PES of the solvated molecules (M), plus the Hamiltonian $\hat{\mathrm{V}}_{\mathrm{M-Ca}}$ standing for electromagnetic interactions between the molecules and the cavity mode. The Hamiltonian describing weak coupling between electronic excited states e and f of the molecule, at the origin of intramolecular charge transfer is denoted by $\hat{\mathrm{V}}_{\mathrm{CT}}$. The explicit expressions are:

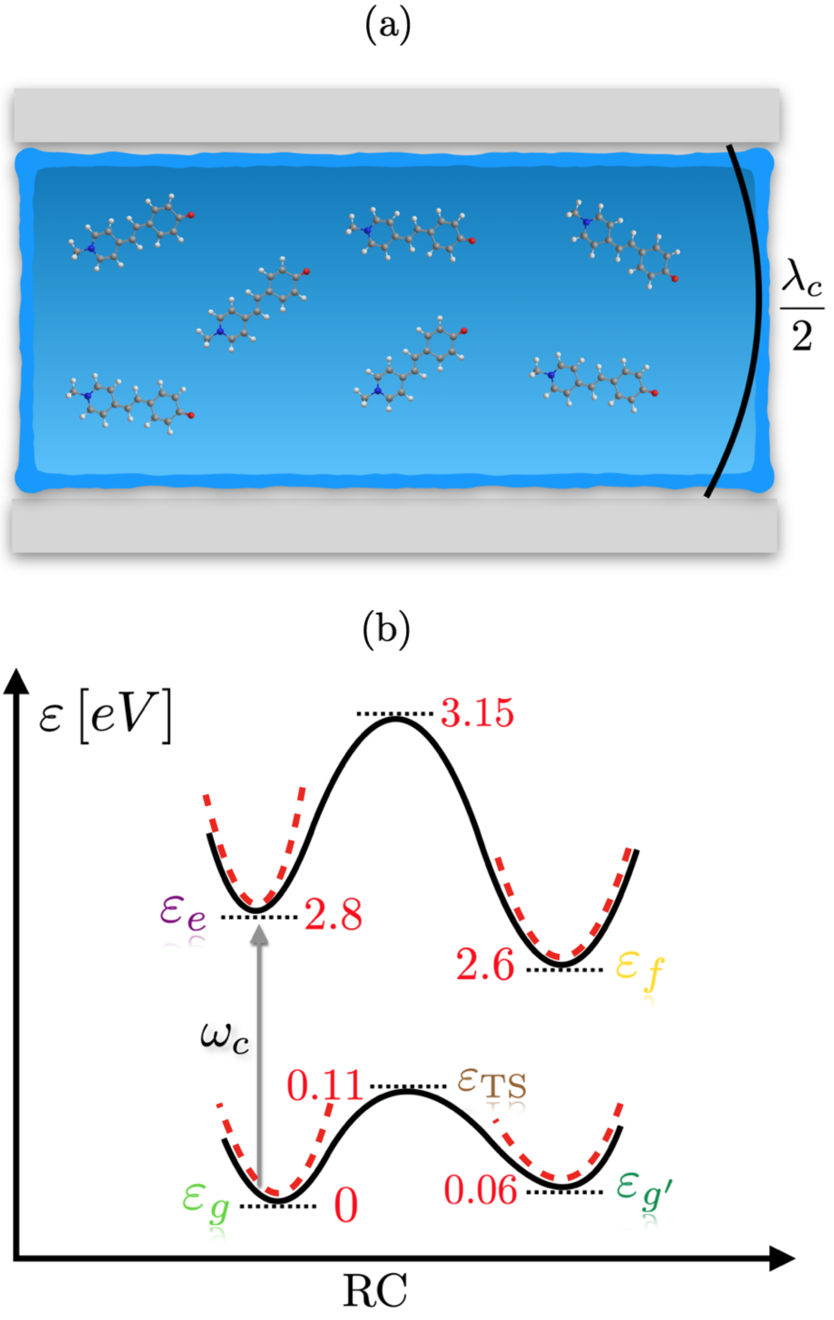

Figure 6.1: (a) Pictorial representation of molecules of (E)-4-[2-(1-methylpyridin-1-ium-4yl)vinyl]phenolate, in solution inside a nanofluidic Fabry-Pérot cavity. The nomenclature describes this photoactive molecule in its aromatic form. $\lambda_c/2 = \pi c/n\omega_c$ is the wavelength of the cavity fundamental electromagnetic mode, with c the speed of light and n the refractive index of the medium. (b) Sketch of the PES (solid curves) for such molecules as a function of the RC. Parabolic approximations of the PES are shown as dashed curves. The electronic ground-state minima g and g' and excited-state minima e and f for the molecule are presented as well as their typical energies ε_g, $\varepsilon_{g'}$, ε_e and ε_f in eV. The grey arrow stands for the cavity mode of frequency ω_c that is resonant with the $g-e$ electric dipole transition [111].

$$\hat{\mathrm{H}}_{\mathrm{CaM}} = \sum_{i=1}^{N} \sum_{r=g,g',e,f} \varepsilon_{ri} \left| r_i \right\rangle \left\langle r_i \right| + \hbar\omega_c \hat{a}^\dagger \hat{a} \,, \tag{6.3}$$

$$\varepsilon_{ri} = \varepsilon_r + \frac{\omega_{\mathrm{v}}^2}{2} \left(Q_{\mathrm{v},i} - \overline{Q}_{\mathrm{v},r} \right)^2 + \sum_k \frac{\omega_k^2}{2} \left(Q_{\mathrm{S},ik} - \overline{Q}_{\mathrm{S},rk} \right)^2 \,, \tag{6.4}$$

$$\hat{\mathrm{V}}_{\mathrm{M-Ca}} = \frac{\hbar\Omega_R}{2} \sum_{i=1}^{N} \Big(\left| e_i \right\rangle \left\langle g_i \right| \hat{a} + \hat{a}^\dagger \left| g_i \right\rangle \left\langle e_i \right| \Big) \,, \tag{6.5}$$

$$\hat{\mathrm{V}}_{\mathrm{CT}} = \sum_{i=1}^{N} \left(\mathrm{V}_{ef} \left| e_i \right\rangle \left\langle f_i \right| + \mathrm{V}_{ef}^* \left| f_i \right\rangle \left\langle e_i \right| \right) \,, \tag{6.6}$$

where ε_{ri} is the PES corresponding to $|r_i\rangle$ the electronic state $r = g, g', e, f$ belonging to the molecule number $i = 1, \cdots, N$. The PES in eq. (6.4) is the sum of an electronic part ε_r (bottom of the dashed parabola in Figure 6.1 (b)) plus a quadratic dependence along the mass-weighted nuclear coordinate $Q_{\mathrm{v},i}$ corresponding to the intra-molecular vibration mode of molecule i, plus molecular vibrations $Q_{\mathrm{S},ik}$ of the bath of solvent molecules labelled with a quasicontinuum index k. It is assumed that each molecule has the same intra-molecular vibration frequency ω_{v} and bath mode frequency ω_k along the RC, independent of its electronic state r (same curvature around each minimum of the bare PES in Figure 6.1 (b)). The quantities $\overline{Q}_{\mathrm{v},r}$ and $\overline{Q}_{\mathrm{S},rk}$ are the displaced nuclear equilibrium positions in the electronic state r, associated with the intramolecular and solvent modes, respectively.

The free electromagnetic mode of the cavity is described in eq. (6.3) by $\hat{a}$ ($\hat{a}^\dagger$) the annihilation (creation) operator of a photon excitation inside the cavity of frequency ω_c. The light-matter interaction Hamiltonian in eq. (6.5) is an electric dipole coupling term, written within rotating-wave approximation (RWA) [28, 36, 157]. It couples the electronic ground state g to the excited state e of each molecule i through the same cavity mode, with a coupling strength given by half the bare vacuum Rabi frequency $\Omega_R/2$. For simplicity, no direct dipole coupling between the g' and f states is taken into account, either because the corresponding dipole matrix elements are weak, or the cavity frequency is detuned from the corresponding electronic transition.

The microscopic model is similar to the model described in Section 4.3.1. Here, the model contains the solvent modes, additional states and the interaction $\hat{\mathrm{V}}_{\mathrm{CT}}$ as the main differences. The counter-rotating terms and self-dipole energy terms are neglected as it explained at the end of Section 4.1.5.

Finally, the matrix element $\hat{\mathrm{V}}_{ef}$ in eq. (6.6) is at the origin of the intramolecular CT process between any e and f state of one molecule. The Hamiltonian $\hat{\mathrm{V}}_{\mathrm{CT}}$ is supposed to be a weak perturbation to the Hamiltonian $\hat{\mathcal{H}}_0$ (see eq. (6.2)) containing the molecular population coupled to the cavity mode, but uncoupled to the excited states f and g'. This approach holds in the incoherent (nonadiabatic) regime of electron transfer for which $|\hat{\mathrm{V}}_{ef}| \ll k_B T$.

6.1 PESs and “*Reacton*” Formation

The Potential Energy Surfaces of the Ground state $|G, 0\rangle$, Polaritons and Dark states, by assuming a vanishing $\hat{\mathrm{V}}_{\mathrm{CT}}$, are equal to the PESs in eqs. (4.32) and (4.36) plus the solvent contribution which is equivalent to adding a sum over the solvent modes ω_ks for the quadratic (parabolic) approximation and the reorganization energy λ_{v} is sent to $\lambda_{\mathrm{v}} + \lambda_{\mathrm{S}}$.
The expressions of the PESs and the corresponding states are reported in the next subsections.

6.1.1 Ground state

The exact many-body ground state $|\mathcal{G}\rangle$ and PES $\mathcal{E}_g(Q_{\mathrm{v},i}, Q_{\mathrm{S},ik})$ are given by

$$\begin{aligned} &\left|G,0\right\rangle \equiv \left|g_1\cdots g_N\right\rangle \otimes \left|0\right\rangle , \\ &\mathcal{E}_g(Q_{\mathrm{v},i},Q_{\mathrm{S},ik}) = N\varepsilon_g + \sum_{i=1}^{N}\frac{\omega_{\mathrm{v}}^2}{2}Q_{\mathrm{v},i}^2 + \sum_{i=1}^{N}\sum_{k}\frac{\omega_k^2}{2}Q_{\mathrm{S},ik}^2, \end{aligned} \tag{6.7}$$

where the ground state equilibrium nuclear configurations $\overline{Q}_{\mathrm{v},g}$ and $\overline{Q}_{\mathrm{S},gk}$ are set to 0.

6.1.2 Upper and lower Polaritons

The Polariton Potential Energy Surface (PPES) obtained with an adiabatic approximation at order λ (see Section 4.3.2) and the corresponding eigenstates are:

$$\begin{aligned} \left|-\right\rangle &= -\sin\theta\left|G,1\right\rangle + \cos\theta\left|E,0\right\rangle , \\ \left|+\right\rangle &= +\cos\theta\left|G,1\right\rangle + \sin\theta\left|E,0\right\rangle , \\ \mathcal{E}_\pm(Q_{\mathrm{v},i},Q_{\mathrm{S},ik}) &= \varepsilon_\pm + \sum_{i=1}^{N}\frac{\omega_{\mathrm{v}}^2}{2}\left(Q_{\mathrm{v},i}-\overline{Q}_{\mathrm{v},\pm}\right)^2 + \sum_{i=1}^{N}\sum_{k}\frac{\omega_k^2}{2}\left(Q_{\mathrm{S},ik}-\overline{Q}_{\mathrm{S},\pm k}\right)^2 , \\ \varepsilon_\pm &= N\varepsilon_g + \hbar\omega_c - \frac{\hbar}{2}\left(\underline{\delta} \mp \underline{\tilde{\Omega}}_R\right) , \\ \underline{\delta} &= \delta - \frac{\lambda_{\mathrm{v},e}+\lambda_{\mathrm{S},e}}{\hbar}\left(1-\frac{\alpha_+^2+\alpha_-^2}{N}\right) , \\ \underline{\tilde{\Omega}}_R &= \tilde{\Omega}_R - \frac{\lambda_{\mathrm{v},e}+\lambda_{\mathrm{S},e}}{\hbar}\frac{\delta}{\tilde{\Omega}_R}\left(1-\frac{1}{N}\right) , \end{aligned} \tag{6.8}$$

where $\left|E,0\right\rangle$ is a collective Dicke state defined in Section 4.2.3, $\sin\theta = \frac{1}{\sqrt{2}}\sqrt{1-\delta/\tilde{\Omega}_R}$, $\cos\theta = \frac{1}{\sqrt{2}}\sqrt{1+\delta/\tilde{\Omega}_R}$ (the detuning δ and the collective Rabi frequency $\tilde{\Omega}_R$ are defined in eq. (4.26)), $\lambda_{\mathrm{v},e} \equiv \frac{1}{2}\omega_{\mathrm{v}}^2\overline{Q}_{\mathrm{v},e}^2$ (where the subscript e denotes the electronic state with energy ε_e) and $\lambda_{\mathrm{S},e} \equiv \sum_k \frac{1}{2}\omega_k^2\overline{Q}_{\mathrm{S},ek}^2$. The intramolecular and solvent modes' equilibrium positions are defined by

$$\overline{Q}_{\mathrm{v},\pm} = \frac{\overline{Q}_{\mathrm{v},e}}{2N}\left(1\mp\frac{\delta}{\tilde{\Omega}_R}\right), \; \overline{Q}_{\mathrm{S},\pm k} = \frac{\overline{Q}_{\mathrm{S},ek}}{2N}\left(1\mp\frac{\delta}{\tilde{\Omega}_R}\right), \tag{6.9}$$

where the ground state equilibrium nuclear configurations $\overline{Q}_{\mathrm{v},g}$ and $\overline{Q}_{\mathrm{S},gk}$ are set to 0.

The PPES in eq. (6.8) generalizes previous results of ref. [70, 141, 106] by taking into account on the same footing the finite number N of molecules, finite molecule-cavity detuning, and dressing of the polariton by molecular vibrations of the solvent environment.

6.1.3 Dark states

The spectrum of $\hat{\mathcal{H}}_0$ in the single-photon excitation sector, also contains a manifold of N$-$1 degenerate states uncoupled to the cavity mode. The expression of those Dark states $\left|\mathcal{D}_p\right\rangle$ is more complex than the one of the bright Polaritons [38, 120]. They are obtained in the limit of vanishing electron-phonon coupling ($\lambda_{\mathrm{v},e} = \lambda_{\mathrm{S},e} = 0$) (see Section 4.2):

$$
\begin{aligned}
|D_p\rangle &= \frac{\sum_{k=1}^{p} |(e_k)\rangle - \sqrt{p}\,|(e_{p+1})\rangle}{\sqrt{p(p+1)}} \otimes |0\rangle\,,\\
\mathcal{E}_{D_p}(Q_{\mathrm{v},i}, Q_{\mathrm{S},ik}) &= N\varepsilon_g + \Delta_{ge} + \sum_{i=1}^{N} \frac{\omega_{\mathrm{v}}^2}{2} Q_{\mathrm{v},i}^2 + \sum_{i=1}^{N} \sum_{k} \frac{\omega_k^2}{2} Q_{\mathrm{S},ik}^2,
\end{aligned}
\tag{6.10}
$$

where $p = 1, \cdots, N-1$ is an index labelling the Dark state (see eq. (4.21)), $\Delta_{ge} \equiv \varepsilon_e - \varepsilon_g$ and the ground state equilibrium nuclear configurations $\overline{Q}_{\mathrm{v},g}$ and $\overline{Q}_{\mathrm{S},gk}$ are set to 0.

6.1.4 Uncoupled states f and g'

Finally, there are additional eigenstates of $\hat{\mathcal{H}}_0$ that do not couple to the optical cavity mode and are thus "dark"; however, they play an important role regarding the chemical reactivity of the confined molecules. Such is the case for the excited states $|(r_i)\rangle \equiv |g_1 \cdots g_{i-1}(r_i)g_{i+1} \cdots g_N\rangle$ containing the molecule number i in the excited electronic state $r = f$ or second ground state $r = g'$, while the remaining N-1 molecules are in the ground state g. The corresponding many-body state $|(R_i)\rangle$ and the corresponding PES $\mathcal{E}_{\mathrm{R_i}}$ for $r = f$, g' are given by

$$
\begin{aligned}
&|R_i, 0\rangle \equiv |(r_i)\rangle \otimes |0\rangle\,,\\
\mathcal{E}_{R_i}(Q_{\mathrm{v},i}, Q_{\mathrm{S},ik}) &= \varepsilon_R + \frac{\omega_{\mathrm{v}}^2}{2}\left(Q_{\mathrm{v},i} - \overline{Q}_{\mathrm{v},r}\right)^2 + \sum_{j=1, j\neq i}^{N} \frac{\omega_{\mathrm{v}}^2}{2} Q_{\mathrm{v},j}^2 +\\
&+ \sum_{k} \frac{\omega_k^2}{2}\left(Q_{\mathrm{S},ik} - \overline{Q}_{\mathrm{S},rk}\right)^2 + \sum_{j=1, j\neq i}^{N} \sum_{k} \frac{\omega_k^2}{2} Q_{\mathrm{S},jk}^2,
\end{aligned}
\tag{6.11}
$$

where $\varepsilon_R \equiv N\varepsilon_g + \Delta_{gr}$ ($r = f$, g') and the ground state equilibrium nuclear configurations $\overline{Q}_{\mathrm{v},g}$ and $\overline{Q}_{\mathrm{S},gk}$ are set to 0. The PESs $\mathcal{E}_{R_i}$ are N-fold degenerate.

6.1.5 The concept of *Reacton*

The PPES in eq. (6.8) have a simple interpretation. They arise from the collective dipole coupling between the electronic g and e states of the molecules and a single electromagnetic cavity mode, resulting in the formation of a Polariton. This Polariton gets further dressed by interactions with a bath of intramolecular and solvent vibrational modes, thus sharing some similarities with the concept of polaron [75] in solid-state physics. The dressed Polariton is, however, more complex than a single polaron excitation, since it involves many different energy scales [80] ranging from molecular vibrational frequencies $\hbar\omega_{\mathrm{v}} \approx 10$ meV to electronic transitions and cavity optical frequency $\Delta_{ge} \approx \hbar\omega_c \approx 2$ eV, as well as to the collective vacuum Rabi frequency $\hbar\tilde{\Omega}_R \approx 0.7$ eV that is intermediate between the vibronic and optical frequency scales. We call this dressed and collective polariton excitation a *Reacton* [111], since the formation of this entity modifies significantly the chemical properties of confined and resonant molecules inside the cavity. The concept of *Reacton* is a key concept that generalizes and unifies several previous investigations in the field of polaritonic chemistry [57, 70, 31], and shares conceptual similarities to the *dressed-atom* approach in quantum optics [19, 28]. While here the *Reacton* properties are computed within the range of validity of the BOA [55], in general, those have to be computed numerically self-consistently [31].

6.2 Charge-Transfer Reaction Rate

In this Section, the modification of chemical reactivity for cavity-confined molecules, induced by the *Reacton* formation is investigated. Due to the weak but non-vanishing matrix elements ($\mathrm{V}_{ef} \neq 0$) in the Hamiltonian

$\hat{\mathrm{V}}_{\mathrm{CT}}$ (see eq. (6.6)), molecules that are in the excited electronic state e may undergo an intramolecular CT process towards the other excited electronic state f, assisted by a reorganization of the molecular nuclei configuration. The theoretical framework for describing the kinetics of such CT chemical reactions in solution was developed mainly by the works of Marcus and co-workers [107, 109, 145], Kestner *et al.* [89], Freed and Jortner [51], and Hopfield [76] (see Chapter 5). Herein, that framework is generalized to the case of PPES for the chemical reaction written in the *Reacton* basis (see Section 6.1), rather than in the bare (uncoupled) molecular basis.

6.2.1 Non-adiabatic CT rate for Polaritons

The non-adiabatic rate for the CT reaction between the vibrational manifold of the PPES (see eq. (6.8)) and the vibrational manifold of uncoupled excited states (see eq. (6.11)) is calculated using the eq. (5.46). The resulting rates for the transitions $\rho \equiv \pm \rightarrow F$ are [111]:

$$k_{\mathrm{CT},F\rho} = \sum_{i=1}^{N} k_{\mathrm{CT},F_i\rho} = \alpha_\rho \frac{2\pi}{\hbar} |\mathrm{V}_{ef}|^2 \mathcal{L}_{\mathrm{v},\rho F} \star \mathcal{L}_{\mathrm{cl}}(\Delta_{\rho F}, \tilde{\lambda}_{\mathrm{S},\rho F}), \tag{6.12}$$

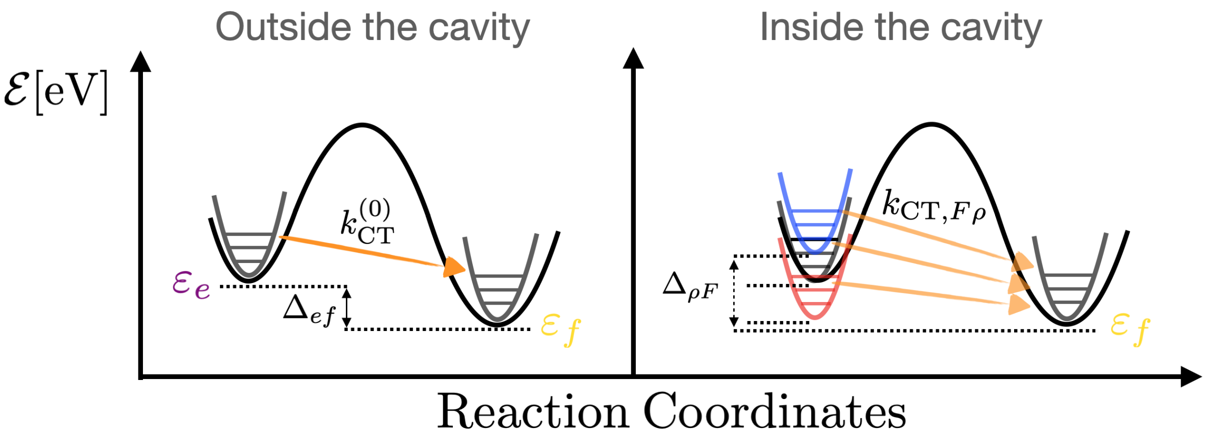

Figure 6.2: PESs involved in the non-adiabatic CT reaction.

with

$$\begin{aligned} \mathcal{L}_{\mathrm{v},\rho F}(\Delta_{\rho F}) &= \sum_{n,\tilde{m}=0}^{\infty} F_{n\tilde{m}} \delta\left[\Delta_{\rho F} + \hbar\omega_{\mathrm{v}}(\tilde{m} - n)\right], \\ \mathcal{L}_{\mathrm{cl}}(\Delta_{\rho F}, \tilde{\lambda}_{\mathrm{S},\rho F}) &= \frac{1}{\sqrt{4\pi\tilde{\lambda}_{\mathrm{S},\rho F} k_B T}} \exp\left[-\beta \frac{(\Delta_{\rho F} + \tilde{\lambda}_{\mathrm{S},\rho F})^2}{4\tilde{\lambda}_{\mathrm{S},\rho F}}\right], \end{aligned} \tag{6.13}$$

where a factor 1/N, which comes from the modulo squared of the Dicke states (see eq. (4.21)), is compensated by a factor N for the transition between a Polaritonic state and N uncoupled many-body states, the coefficients $\alpha_\rho \equiv \left(1 - \rho\delta/\tilde{\Omega}_R\right)/2$ come from the modulo squared of the projection of Polaritonic states onto the uncoupled many-body state $|F_i, 0\rangle$ (see eq. (6.11)). The driving force $\Delta_{\rho F} \equiv \varepsilon_F - \varepsilon_\rho$, the solvent reorganization energy $\tilde{\lambda}_{\mathrm{S},\rho F}$ and the factor $F_{n\tilde{m}}$ are renormalized quantities due to the *Reacton* formation. Figure 6.2 shows a pictorial representation of the CT reaction outside and inside the cavity.

The reorganization energy of intramolecular vibrations for the bare transition $e \rightarrow F$ (outside the cavity) is defined as

$$\lambda_{\mathrm{v},eF} = \frac{\omega_{\mathrm{v}}^2}{2} \left(\overline{Q}_{\mathrm{v},f} - \overline{Q}_{\mathrm{v},e}\right)^2, \tag{6.14}$$

where $\overline{Q}_{\mathrm{v},f}$ and $\overline{Q}_{\mathrm{v},e}$ are the equilibrium reaction coordinates of the state F and e, respectively. The reorganization energy of intramolecular vibrations for the "dressed" transition (inside the cavity) is

$$\tilde{\lambda}_{\mathrm{v},\rho F} = \frac{\omega_{\mathrm{v}}^2}{2}\left(\overline{Q}_{\mathrm{v},f} - \overline{Q}_{\mathrm{v},\rho}\right)^2 + \frac{N-1}{2}\omega_{\mathrm{v}}^2\overline{Q}^2_{\mathrm{v},\rho}, \tag{6.15}$$

where the ground state equilibrium nuclear configuration $\overline{Q}_{\mathrm{v},g}$ is set to 0.
The second term in eq. (6.15) is a result of the N-fold degeneracy of the PESs $\mathcal{E}_{F_i}$ (see eq. (6.11)). The solvent reorganization energy $\tilde{\lambda}_{\mathrm{S},\rho F}$ is obtained by adding the bath of solvent modes to the eq. (6.15), to get

$$\boxed{\tilde{\lambda}_{\mathrm{S},\rho F} = \sum_k \frac{\omega_k^2}{2}\left(\overline{Q}_{\mathrm{S},fk} - \overline{Q}_{\mathrm{S},\rho k}\right)^2 + \frac{N-1}{2}\sum_k \omega_k^2\overline{Q}^2_{S,\rho k}. \qquad (6.16)}$$

The factor $F_{n\tilde{m}}$ (it is defined for the "bare" case in Section 5.3) can be written as

$$F_{n\tilde{m}} = e^{-g^2_{\mathrm{v},\rho F}(1+2\overline{n}_{\mathrm{v}})}\frac{g^{2(n+\tilde{m})}_{\mathrm{v},\rho F}}{n!\tilde{m}!}\left(1+\overline{n}_{\mathrm{v}}\right)^{\tilde{m}}\overline{n}_{\mathrm{v}}^{n}\,, \tag{6.17}$$

where $\overline{n}_{\mathrm{v}} \equiv n_{\mathrm{B}}\left(\hbar\omega_{\mathrm{v}}\right)$ the thermal equilibrium Bose distribution $n_{\mathrm{B}}\left(E\right) = \left(e^{E/k_BT} - 1\right)^{-1}$ for the intramolecular vibrational modes. It involves the Franck-Condon overlap [145] $|\langle n|\tilde{m}\rangle|^2$ between the reactant intramolecular vibrational state $|n\rangle$ and the product intramolecular vibrational state $|\tilde{m}\rangle$ (see Section 5.1), the former being displaced by the renormalized Huang-Rhys factors

$$g^2_{\mathrm{v},\rho F} = \left(g_{\mathrm{v},f} - \alpha_\rho\frac{g_{\mathrm{v},e}}{N}\right)^2 + \alpha_\rho\frac{g^2_{\mathrm{v},e}}{2N}\left(1 - \frac{1}{N}\right)\,, \tag{6.18}$$

where $\alpha_\rho \equiv \left(1 - \rho\delta/\tilde{\Omega}_R\right)/2$, $g^2_{\mathrm{v},\rho F}$ is directly obtained from the eq. (6.15) using eq. (6.9) and $g^2_{\mathrm{v},\rho F} = \tilde{\lambda}_{\mathrm{v},\rho F}/\hbar\omega_{\mathrm{v}}$.

6.2.2 Non-adiabatic CT rate for Dark states

The CT rate for the transition between the degenerate N−1 Dark states and the states $|F_i, 0\rangle$ can be obtained, for instance, choosing the Dark state N−1. The resulting rate contains a factor 1/N(N−1) in the denominator; that factor comes from the modulo squared of the projection of the Dark states onto the uncoupled many-body state $|F_i, 0\rangle$ (see eqs. (6.10) and (6.11)). It follows that this single rate has to be multiplied by N(N−1) because

$$k_{\mathrm{CT},FD} = \sum_{i=1}^{N} k_{\mathrm{CT},FD_{N-1}}, \tag{6.19}$$

and there are N−1 degenerate dark states as "Reactants". Consequently, the rate $k_{\mathrm{CT},FD}$ is the following:

$$\boxed{k_{\mathrm{CT},FD} = \frac{2\pi}{\hbar}|\mathrm{V}_{ef}|^2\mathcal{L}_{\mathrm{v},DF} \star \mathcal{L}_{\mathrm{cl}}(\Delta_{ef}, \lambda_{\mathrm{S},f}), \qquad (6.20)}$$

with

$$\begin{aligned} \mathcal{L}_{\mathrm{v},DF}(\Delta_{ef}) &= \sum_{n,\tilde{m}=0}^{\infty} F_{n\tilde{m}}\delta\left[\Delta_{ef} + \hbar\omega_{\mathrm{v}}(\tilde{m} - n)\right], \\ \mathcal{L}_{\mathrm{cl}}(\Delta_{ef}, \lambda_{\mathrm{S},f}) &= \frac{1}{\sqrt{4\pi\lambda_{\mathrm{S},f}k_BT}}\exp\left[-\beta\frac{(\Delta_{ef} + \lambda_{\mathrm{S},f})^2}{4\lambda_{\mathrm{S},f}}\right], \end{aligned} \tag{6.21}$$

where $\Delta_{ef} \equiv \varepsilon_f - \varepsilon_e$, $\lambda_{\mathrm{S},f} \equiv \sum_k \frac{1}{2}\omega_k^2\overline{Q}^2_{\mathrm{S},fk}$, and the factor $F_{n\tilde{m}}$ is now a function of the bare $g^2_{\mathrm{v},f}$.

6.2.3 High-temperature limit

In the limit of "slow" intramolecular vibrational mode $\omega_\text{v} < k_B T/\hbar$, eqs. (6.12) and (6.20) formally recover the "semiclassical" approximation derived by Marcus [145]. In this limit, the classical CT rate $k^{(\text{cl})}_{\text{CT}}$ is given by:

$$k^{(\text{cl})}_{\text{CT,F}\rho} = \alpha_\rho \frac{2\pi}{\hbar} |V_{ef}|^2 \mathcal{L}_\text{cl}\left(\Delta_{\rho\mathcal{F}}, \tilde{\Lambda}_{\rho\mathcal{F}}\right), \tag{6.22}$$

with total reorganization energy $\tilde{\Lambda}_{\rho\mathcal{F}} = \tilde{\lambda}_{\text{v},\rho\mathcal{F}} + \tilde{\lambda}_{\text{S},\rho\mathcal{F}}$.

6.3 CT Thermal Reaction in Cavity

In this Section, the case of room temperature $k_B T = 26$ meV and a cavity frequency ω_c that is resonant ($\delta = 0$) with the molecular transition $\Delta_{ge}/\hbar = 2.8$ eV$/\hbar$ is studied (see Figure 6.1 (b)). For a typical Fabry-Pérot cavity of surface 10^4 μm^2 with distant mirrors of the fundamental optical cavity-mode wavelength $\lambda_c/2 \approx \pi c/\omega_c \approx 0.221$ μm (for $n \approx 1$), and for molecules of electric dipole moment $\mu \approx 5$ D, the corresponding very weak bare vacuum Rabi-splitting is $\hbar\Omega_R \approx 0.70$ μeV. In best cases for which the molecules are in average packed 25 Å away one from each other and equally coupled to the cavity mode, the maximum number of embedded molecules are supposed to be $N \approx 10^{11}$ thus leading to an upper-bound for the collective vacuum Rabi splitting of about $\hbar\tilde{\Omega}_R = 0.22$ eV. Experimental values of $\hbar\tilde{\Omega}_R \approx 0.11$ eV were reported in nanofluidic Fabry-Pérot cavities [6]. In the following, a bare vacuum Rabi splitting of $\hbar\Omega_R = 10$ meV $> \lambda_{\text{v},e}, \lambda_{\text{S},e}$ is adopted, that is sufficiently high to ensure the validity of the PPES calculation in Section 4.3.2, and it is still consistent with the highest single-molecule-cavity couplings (≈ 100 meV) reported in plasmonic cavities [24]. A population of $N = 5000$ molecules coherently coupled to the same optical cavity mode is considered, for which the collective vacuum Rabi splitting $\hbar\tilde{\Omega}_R = 0.7$ eV is close to reported experimental values in optical microcavities [80]. The frequency of intramolecular vibrational modes is chosen to be $\hbar\omega_\text{v} \approx 50$ meV and solvent ones $\hbar\omega_k \approx 0.1$ meV. The dressed reorganization energies are fixed to $\tilde{\lambda}_{\text{v},\rho\mathcal{F}} = 80$ meV and $\tilde{\lambda}_{\text{S},\rho\mathcal{F}} = 10$ meV leading to a total reorganization energy $\tilde{\Lambda}_{\rho\mathcal{F}} = 90$ meV. This chosen value corresponds to a solvent that is sufficiently apolar [98] not to screen too much electric interactions in solution but is still sufficiently polar to increase the impact of solvent fluctuations on the kinetics of the CT reaction.

Figure 6.3 shows the evolution of the CT thermal reaction rate (solid yellow circles), defined as

$$k_\text{CT} = \sum_{\rho=\pm,D} \frac{e^{-\varepsilon_\rho/k_B T}}{Z_e} k_{\text{CT},F\rho}, \tag{6.23}$$

where $\varepsilon_{\rho=\pm}$ is defined in eq. (6.8) and Z_e is the partition function.
The thermal rate k_CT is the sum ponderated by Boltzmann weights of the reaction rates $k_{\text{CT},F\rho}$ (see eq. (6.12)) and the rate $k_{\text{CT},FD}$ (see eq. (6.12)) for $\rho = D$.
The rate is plotted in units of $2k_e/3$ with

$$k_e \equiv \frac{2\pi}{\hbar}|V_{ef}|^2 / \sqrt{4\pi\tilde{\Lambda}_{-F} k_B T} \quad (\tilde{\Lambda}_{-\mathcal{F}} = \tilde{\lambda}_{\text{v},-\mathcal{F}} + \tilde{\lambda}_{\text{S},-\mathcal{F}}), \tag{6.24}$$

as a function of the bare reaction driving force $\Delta_{ef} \equiv \varepsilon_f - \varepsilon_e$, at fixed $\hbar\tilde{\Omega}_R = 0.7$ eV. The classical CT rates $k^{(\text{cl})}_{\text{CT},F\rho}$ given by eq. (6.22) are also plotted as dashed curves. The contribution of Dark states $k^{(\text{cl})}_{\text{CT},FD}$ (in black) dominates over the two polariton satellite peaks of half amplitudes $k^{(\text{cl})}_{\text{CT},F-}$ (in red) and $k^{(\text{cl})}_{\text{CT,F}+}$ (in blue). The former are strongly dependent on both the detuning δ and collective vacuum Rabi frequency $\tilde{\Omega}_R$. They are given by two Gaussian satellite peaks centered on $\Delta_{ef} \approx -\tilde{\Lambda}_{\pm F} + \left(\lambda_{\text{v},e} + \lambda_{\text{S},e} \pm \hbar\tilde{\Omega}_R\right)/2$, thus approximately equal to ± 350 meV away from the main Dark state peak. The standard deviation of those curves is $\approx \sqrt{2\tilde{\Lambda}_{\pm F} k_B T}$, corresponding to a full width at half maximum (FWHM) of ≈ 161 meV. It is important to note that the actual CT thermal rate k_CT is very well approximated by the classical contribution of the lower polariton $k^{(\text{cl})}_{\text{CT},F-}$. On one side, this is due to the fact that $\hbar\tilde{\Omega}_R \gg k_B T$, so that only the lowest-energy PPES channel is significantly populated at thermal equilibrium and is thus open for the ET reaction: The other channels $k_{\mathrm{CT},FD}^{(\mathrm{cl})}$ and $k_{\mathrm{CT},F+}^{(\mathrm{cl})}$ are far away in energy and thus do not contribute significantly to k_{CT}. On the other side, *a priori* the fact that the classical approximation in eq. (6.22) holds is not expected, since for the chosen range of parameters, the intramolecular vibrational modes are quantum mechanically frozen ($k_B T < \hbar\omega_{\mathrm{v}}$). Departures from the Gaussian limit are indeed seen on the numerical plots, that manifest as the appearance of weak vibrational sidebands and asymmetries in the tails of the $k_{\mathrm{CT}}(\Delta_{ef})$ curve. The former features are partially smeared out by convolution of the intramolecular lineshape by the solvent lineshape (see Section 5.3.2), thus explaining the unexpected good qualitative match of the CT rate with the classical limit (see also ref. [145]). For comparison with the cavity-induced rate k_{CT}, the corresponding CT rate $k_{\mathrm{CT}}^{(0)}$ outside cavity (see Figure 6.2) (computed for $\hbar\tilde{\Omega}_R = 0.0$ meV) is shown in green diamonds.

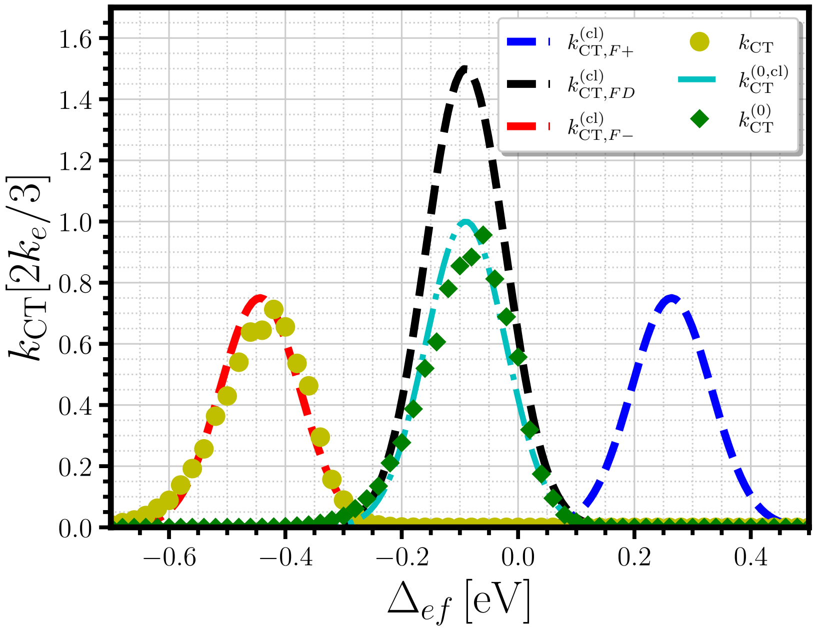

Figure 6.3: CT thermal reaction rate inside cavity, k_{CT} (solid yellow circles), as a function of the bare reaction driving force Δ_{ef}. Classical contributions of the PPES to k_{CT} are shown as dashed curves for the rates $k_{\mathrm{CT},F-}^{(\mathrm{cl})}$ (in red), $k_{\mathrm{CT},F+}^{(\mathrm{cl})}$ (in blue), and $k_{\mathrm{CT},FD}^{(\mathrm{cl})}$ (in black). The thermal rate $k_{\mathrm{CT}}^{(0)}$ and classical rate $k_{\mathrm{CT}}^{(0,\mathrm{cl})}$ outside the cavity (for $\hbar\tilde{\Omega}_R \approx 0.0$ eV) are shown as green diamonds and dashed-dotted cyan curve, respectively. Chosen parameters are as follows: $N = 5000$, $k_B T = 26$ meV, $\varepsilon_g = 0$ eV, $\varepsilon_e = 2.8$ eV, $\varepsilon_f = 2.6$ eV, $\hbar\omega_c = 2.8$ eV, $\hbar\omega_{\mathrm{v}} = 50$ meV, $\hbar\omega_k = 0.1$ meV, $\hbar\tilde{\Omega}_R = 0.7$ eV, $\hbar\delta = 0$ eV, $\tilde{\lambda}_{\mathrm{v},\rho F} = 80$ meV, $\tilde{\lambda}_{\mathrm{S},\rho F} = 10$ meV [111].

6.3.1 Tuning the CT reaction

Rate	$k_{GG'}$	$k_{\mathrm{CT},-F}$	$k_{\mathrm{CT},FD}$	$k_{\mathrm{CT},F+}$
meV	3.7	41.4	42.2	0.001
THz	0.9	10	10.2	0.0003

Table 6.1: Computed and dominant thermal reaction rates. The parameters are those of Figure 6.3, for $\Delta_{ef} = -0.2$ eV [111].

To complete the picture of the reaction kinetics, Figure 6.4 (solid yellow curve) shows the CT thermal rate k_{CT} inside cavity (with $\Omega_R = 10$ meV) and the same rate $k_{\mathrm{CT}}^{(0)}$ outside cavity (for which $\Omega_R = 0.0$ meV), as a function of the number N of molecules coupled to the cavity mode. The parameters are those of Figure 6.3, with the reaction driving force fixed at $\Delta_{ef} \approx -0.2$ eV. This choice of Δ_{ef} corresponds to the PES for the chosen molecule in Figure 6.1 (b). For the case of $N = 5000$ and $\Delta_{ef} = -0.2$ eV, both Figure 6.3 and Figure 6.4 show that $k_{\mathrm{CT}} \ll k_{\mathrm{CT}}^{(0)}$, thus the reaction kinetics gets much slower inside than outside cavity. Interestingly, in Figure 6.4, the CT rate does not evolves in a monotonous fashion with N. It first increases with N, reaching a maximum at $N \approx 500$ for which $k_{\mathrm{CT}} > k_{\mathrm{CT}}^{(0)}$ and finally slows down to 0 with $k_{\mathrm{CT}} \ll k_{\mathrm{CT}}^{(0)}$ at large N. There is thus an optimal value of N (and thus of molecular concentration N/V for the coupled molecules) for which the effect of vacuum quantum fluctuations of the cavity mode is maximum. This behavior can be interpreted by the modification of the reaction driving force Δ_{-F} upon increasing the cVRS frequency $\tilde{\Omega}_R \approx \Omega_R \sqrt{N}$, thus resulting in an effective change of CT rate along the Marcus parabola (see eq. 6.22). The maximum of $k_{\mathrm{CT},F-}^{(\mathrm{cl})}$ is obtained at the transition point to the inverted Marcus region (see Figure 5.3), as is shown on Figure 6.4 (dashed red curve). This optimal sensitivity of the CT reaction rate close to the inverted region of Marcus parabola, is in contrast to ref. [70] that reported a monotonous increase of the reaction rate with N in the resonant nuclear tunneling regime.

Table 6.1 provides typical values for the cavity-induced CT reaction rates $k_{\mathrm{CT},\mathcal{F}\rho}$ associated with the case of $N = 5000$ and $\Delta_{ef} = -0.2$ eV. Furthermore, the reaction rate $k_{G'G}$ from the manybody ground-state G to the other manybody state G', is estimated using transition-state theory [40, 172, 92, 42]

$$k_{G'G} = k_0 e^{-\frac{\Delta_{G\mathrm{TS}}}{k_B T}}, \tag{6.25}$$

with the energy barrier $\Delta_{G\mathrm{TS}} = \varepsilon_{\mathrm{TS}} - \varepsilon_r$ (see Figure 6.1 (b)) between the ground state $r = g, g'$ and the transition state, and the typical reaction rate $k_0 \approx k_B T / 2\pi\hbar$.

Finally, for completeness, Figure 6.5 shows the evolution of the CT thermal rate k_{CT} inside cavity as a function of number N of coupled molecules, but for a different value of reaction driving force fixed at $\Delta_{ef} \approx -0.4$ eV. For the case of $N = 5000$ and $\Delta_{ef} = -0.4$ eV, the kinetics of the CT reaction is much faster inside than outside cavity ($k_{\mathrm{CT}} \gg k_{\mathrm{CT}}^{(0)}$) in both Figure 6.3 and Figure 6.5. A similar trend as in Figure 6.4 is recovered in Figure 6.5, with a nonmonotonous evolution of the CT rate with N. It is thus interesting to notice that depending on the range of parameters (reaction driving force, concentration of molecules, detuning), the reaction kinetics can be either slowed down or accelerated significantly by interaction with the cavity mode.

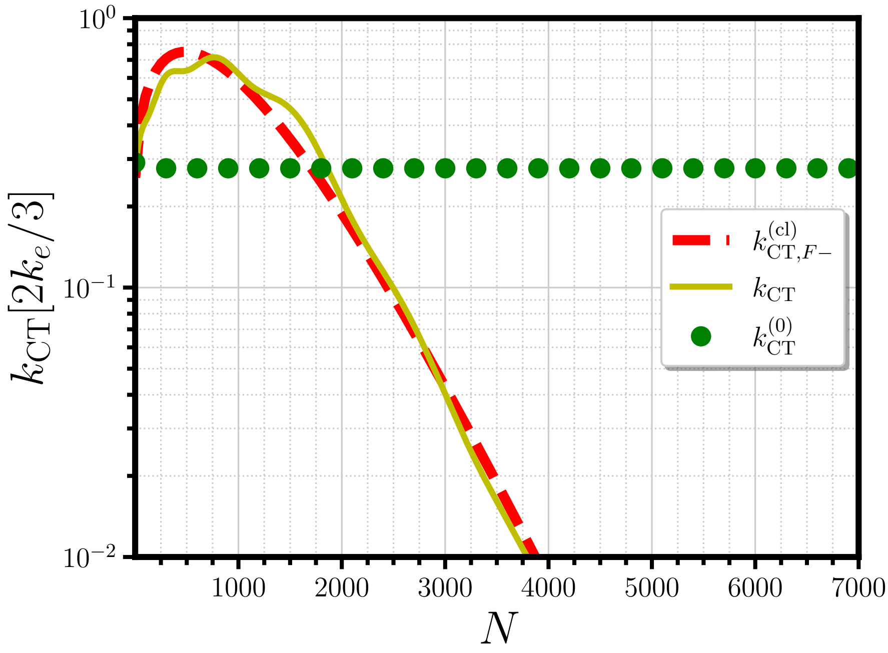

Figure 6.4: Thermal reaction rate k_{CT} (solid yellow curve) and partial classical reaction rate $k^{(\mathrm{cl})}_{\mathrm{CT},F-}$ (dashed red curve) as a function of the number of coupled molecules N. The thermal rate out of cavity $k^{(0)}_{\mathrm{CT}}$ is shown as a solid green circles. Parameters are those of Figure 6.3, except for N, with the reaction driving force fixed to the value $\Delta_{ef} = -0.2$ eV [111].

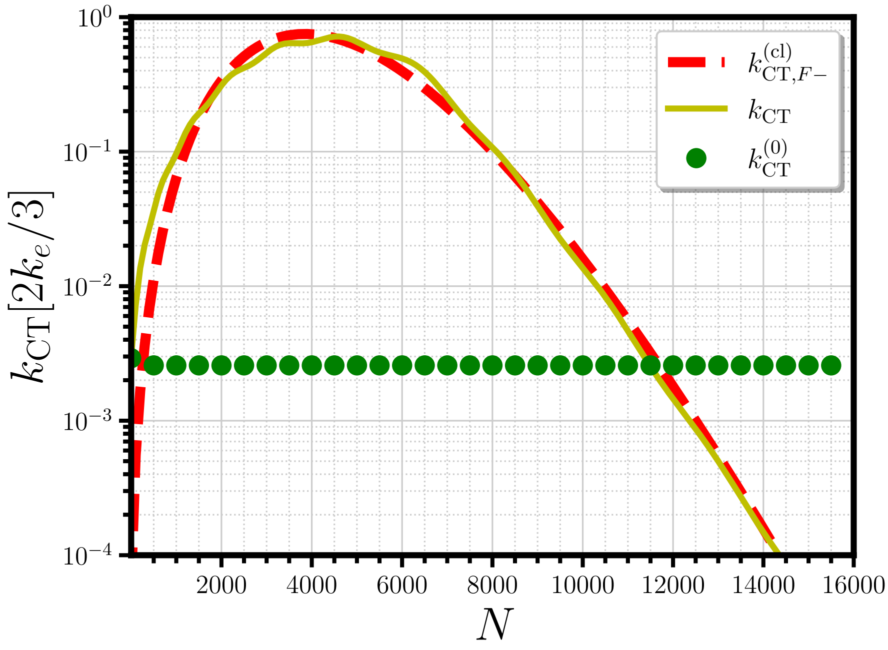

Figure 6.5: Thermal reaction rate k_{CT} (solid yellow curve) and partial classical reaction rate $k^{(\mathrm{cl})}_{\mathrm{CT},F-}$ (dashed red curve) as a function of the number of coupled molecules N. The thermal rate out of cavity $k^{(0)}_{\mathrm{CT}}$ is shown as a solid green circles. Parameters are those of Figure 6.3, except for N, with the reaction driving force fixed to the value $\Delta_{ef} = -0.4$ eV [111].

7

Incoherent Description applied to Reacton *states*

The Fabry-Pérot cavity consists in two mirrors of a given thickness and length. The molecules inside the cavity interact with the solvent, and external photons can induce relaxation mechanisms to the coherent and unperturbed assembly. The total system is a finite object which dissipates and exchanges energy internally via dephasing mechanisms between molecules and solvent modes and externally via interaction with the photon bath.

In this Chapter, the rates involved in radiative and nonradiative relaxations are calculated and applied to the *Reacton*'s formation (see Section 6.1.5). Moreover, the evolution of *Reacton* states as a function of time is described by a global first order rate equation. All the CT, radiative and nonradiative rates are included in the *Reacton*'s evolution to study the competition between them along the photochemical reaction.

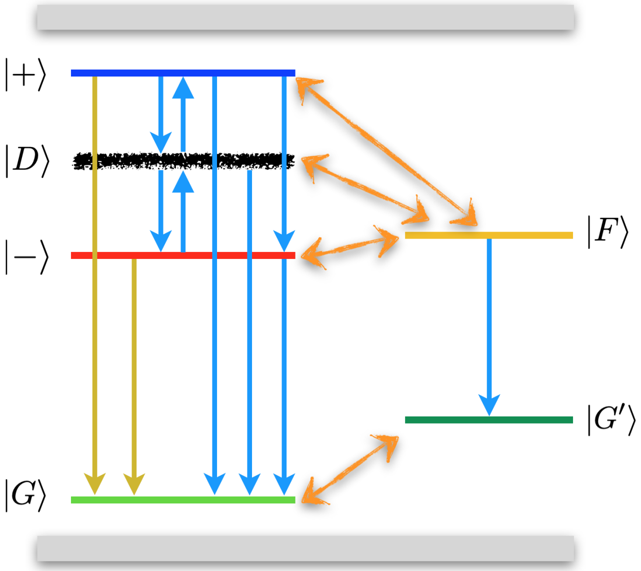

Figure 7.1: Schematics of dissipation and dephasing rates originating from interaction between the *Reacton* states and the external environment. Radiative relaxation rates are presented as gold arrows, while non-radiative relaxation and dephasing rates are both respectively shown with light-blue arrows. The reaction rates involved in the photochemical reaction are pictured with orange double arrows [111].

7.1 Microscopic model for Dissipation

In this section, a minimal microscopic model of dissipation and dephasing, induced by coupling of the *Reacton* states to the external environment is introduced (see Figure 7.1). Two main external environments are considered: the electromagnetic environment (EM) of the cavity mode, and the solvent vibrational environment (ph). The total Hamiltonian $\hat{\mathcal{H}}_{\mathcal{R}-\text{env}}$ describing the external bath environments (env) and their coupling to the *Reacton* ($\mathcal{R}$) is given by

$$\hat{\mathcal{H}}_{\mathcal{R}-\text{env}} = \hat{\text{H}}_{\text{EM}} + \hat{\text{H}}_{\text{ph}} + \hat{\text{V}}_{\text{Ca}-\text{EM}} + \hat{\text{V}}_{\text{M}-\text{ph}}, \tag{7.1}$$

with

$$\begin{aligned}
\hat{\text{H}}_{\text{EM}} &= \sum_q \hbar\omega_q \hat{a}_q^\dagger \hat{a}_q, \\
\hat{\text{H}}_{\text{ph}} &= \sum_{i=1}^{N}\sum_k \hbar\omega_k \hat{b}_{ik}^\dagger \hat{b}_{ik}, \\
\hat{\text{V}}_{\text{Ca}-\text{EM}} &= i\hbar \sum_q \left(f_q \hat{a}_q^\dagger \hat{a} - f_q^* \hat{a}^\dagger \hat{a}_q \right), \\
\hat{\text{V}}_{\text{M}-\text{ph}} &= \sum_{i=1}^{N}\sum_k \left(\hat{b}_{ik} + \hat{b}_{ik}^\dagger \right) \{ \lambda_{e,ik} \left| e_i \right\rangle \left\langle e_i \right| + \lambda_{ge,ik} \left(\left| g_i \right\rangle \left\langle e_i \right| + \left| e_i \right\rangle \left\langle g_i \right| \right) \},
\end{aligned} \tag{7.2}$$

where ω_q and ω_k are the respective frequencies of the electromagnetic and vibrational modes of the baths, $a_q^\dagger$ is the creation operator for a photon in the external EM mode with momentum q, $b_{ik}^\dagger$ the creation operator for a vibron in the solvent bath associated to molecule i with quasi-momentum k (see eq. (6.4) for the associated mass-weighted nuclear coordinates of the solvent modes). The interaction $\hat{\text{V}}_{\text{Ca}-\text{EM}}$ is at the origin of photon losses out of the cavity[1], and $\hat{\text{V}}_{\text{M}-\text{ph}}$ is the general Hamiltonian describing coupling between the solvated molecules and the vibrational modes of the solvent. The term f_q is the probability amplitude for a cavity photon to tunnel out of the cavity to the EM bath [58, 26]. The electron-phonon interactions, described by $\hat{\text{V}}_{\text{M}-\text{ph}}$, couple the quantized phonon displacement operators $\hat{b}_{ik} + \hat{b}_{ik}^\dagger$ both to the electronic density of the excited state e of molecule i with amplitude $\lambda_{e,ik}$ (Holstein-like term [75]) and to the off-diagonal hopping terms between states e and g with amplitude $\lambda_{ge,ik}$ (Su-Schrieffer-Heeger-like terms [153]).

7.1.1 Radiative relaxation

The starting point to calculate all the dissipative rates (radiative and nonradiative) is the Fermi's Golden Rule:

$$\Gamma_{fi} = \frac{2\pi}{\hbar} \left| \left\langle f \right| \hat{\text{V}} \left| i \right\rangle \right|^2 \delta(E_f - E_i), \tag{7.3}$$

where $|i\rangle$ and $|f\rangle$ are respectively the initial and the final states, and $\hat{\text{V}}$ is the interaction that couples the states.
The states involved in the dissipative mechanism are the many-body Ground state $|G, 0\rangle$, the Lower Polariton $|-\rangle$, the Dark states $|D_p\rangle$ ($p \in [1, \text{N} - 1]$), and the Upper Polariton $|+\rangle$. Their expressions are defined in eqs. (6.7), (6.8) and (6.10). The interaction which gives rise to the radiative relaxation is the Hamiltonian $\hat{\text{V}}_{\text{Ca}-\text{EM}}$ given by:

$$\hat{\text{V}}_{\text{Ca}-\text{EM}} = i\hbar \sum_q \left(f_q \hat{a}_q^\dagger \hat{a} - f_q^* \hat{a}^\dagger \hat{a}_q \right). \tag{7.4}$$

Thus, the radiative rates for the transitions $|-\rangle \to |G, 0\rangle$, $|D\rangle \to |G, 0\rangle$, $|+\rangle \to |G, 0\rangle$ are:

$$\begin{aligned}
\Gamma_{G\rho} &= \hbar\pi \left(1 + \rho \frac{\delta}{\tilde{\Omega}_R} \right) \sum_q |f_q|^2 J_q^{(em)} \delta(\Delta_{G\rho} - \hbar\omega_q), \\
\Gamma_{GD} &= 0,
\end{aligned} \tag{7.5}$$

where $J_q^{(em)} \equiv 1 + n_{\text{B},q}$ (n_B is the Bose-Einstein distribution) is associated with the emission (em) process of a photon into the electromagnetic environment that assists the downward transition, $\Delta_{G\rho} \equiv \varepsilon_\rho - N\varepsilon_g$

---

[1] The terms at the origin of spontaneous emission are not taken into account in eq. (7.1), since the former occurs on a nanosecond time scale, while the picosecond relaxation dynamics of the *reacton* is investigated.

($\varepsilon_{\rho=\pm}$ is defined in eq. (6.8)). The Dark states do not contribute to the radiative relaxation since they are not coupled to the cavity mode.
By introducing the density of states $\nu_{\mathrm{EM}}(\omega) \equiv \sum_q \delta(\omega - \omega_q)$, the rates $\Gamma_{G\rho}$ read

$$\boxed{\Gamma_{G\rho} = \alpha_{-\rho} \int dE\, \kappa\left(E/\hbar\right) J^{(em)}\left(E\right) \mathcal{L}_{\mathrm{ph},G\rho}\left(E - \Delta_{G\rho}\right),} \tag{7.6}$$

where $\alpha_{-\rho} \equiv \left(1 + \rho\delta/\tilde{\Omega}_R\right)/2$, $\kappa(\omega = E/\hbar) \equiv 2\pi |f(\omega)|^2 \nu_{\mathrm{EM}}(\omega)$ is the energy-dependent radiative dissipation rate of the cavity, given by the product of the matrix-element square $|f_q|^2$ evaluated at energy $\hbar\omega_q \equiv \hbar\omega$, and the density of states of the external electromagnetic bath $\nu_{\mathrm{EM}}(\omega)$. The decay rate $\Gamma_{G\rho}$ [111] is written as the convolution between the cavity spectral distribution $\kappa(E/\hbar) J^{(em)}\left(E\right)$ and the generalized vibrational lineshape $\mathcal{L}_{\mathrm{ph},G\rho}\left(E\right) \equiv \mathcal{L}_{\mathrm{v},\rho F} \star \mathcal{L}_{\mathrm{cl}}\left(E, \tilde{\lambda}_{\mathrm{S},\rho F}\right)$ by comparison with eq. (6.12).

The eq. (7.6) is a generalization of refs. [19, 129, 110] to the case of the many-body *Reacton* states. The radiative rates $\Gamma_{G\rho}$ are calculated using the simplified assumptions:

(i) the energy-dependent vibrational lineshape $\mathcal{L}_{\mathrm{ph},G\rho}\left(E\right)$ is thinner than the cavity lineshape $\kappa\left(E/\hbar\right)$, such that $\Gamma_{G\rho} \approx \alpha_{-\rho} J^{(em)}\left(\Delta_{G\rho}\right) \kappa\left(\Delta_{G\rho}\right)$;

(ii) the energy dependence of $\kappa(\omega) \approx \kappa(\omega_c) \equiv \kappa$ can be neglected on the scale of the energy difference $\Delta_{G\rho}$ for the considered radiative transition (Markovian assumption),

such that

$$\boxed{\Gamma_{G\rho} \approx \alpha_{-\rho} J^{(em)}\left(\Delta_{G\rho}\right) \kappa.} \tag{7.7}$$

Within assumptions (i) and (ii), the corresponding upward transition rates $\Gamma_{\rho G}$ from the ground state G to the Polariton state $\rho = \pm$ is obtained as

$$\boxed{\Gamma_{\rho G} \approx \quad \alpha_{-\rho} J^{(abs)}\left(\Delta_{G\rho}\right) \kappa,} \tag{7.8}$$

where $J^{(abs)}\left(E\right) = n_{\mathrm{B}}(E)$ is associated to the absorption (abs) process of a photon of the electromagnetic environment during the upward transition.

Rate	Γ_{G-}	Γ_{G+}
meV	28	28
THz	6.8	6.8

Table 7.1: Computed radiative relaxation rates due to cavity losses. Parameters are the same as in Figure 6.3, for $\Delta_{ef} = -0.2$ eV. The cavity quality factor is $Q = 50$, which corresponds to a bare cavity damping rate $\kappa \approx 56$ meV [111].

When the cavity mode $\hbar\omega_c \gg k_B T$, at room temperature, it follows that $n_{\mathrm{B}}\left(\Delta_{G\rho}\right) \ll 1$ and $\Gamma_{G\rho} \approx \alpha_{-\rho}\kappa \gg \Gamma_{\rho G} \approx 0$. By relaxing assumption (ii) keeping assumption i) valid, one recovers the non-Markovian calculation for the radiative relaxation made in ref. [19], which is postulated to be at the origin of the observed much shorter lifetime for the UP compared to the LP. In the following, both approximations (i) and (ii) are assumed, since those are the ones that minimize the knowledge about the microscopic damping mechanism. Generalization to eq. (7.6) is possible if additional information about the energy-dependence of both optical cavity and vibrational lineshapes become available from experiments. Table 7.1 shows the values of typical radiative relaxation rates $\Gamma_{\mathcal{G}\rho}$ written in the *Reacton* basis (downward gold arrows in Figure 7.1), from the knowledge of the bare cavity damping rate κ and optical-cavity quality factor $Q(\equiv \omega_c/\kappa)$ in experiments [140, 166, 19, 6].

7.1.2 Nonradiative relaxation

The nonradiative rates are responsible for the vibrational relaxation in a generic bath and the dephasing rates are related to transitions between the Upper Polariton, Dark states and Lower Polariton induced by the same bath. Figure 7.1 represents the allowed transitions for a solvent bath. Here, the bath is a vibrational solvent bath according to the Hamiltonian $\hat{\mathrm{H}}_{\mathrm{ph}} = \sum_{i=1}^{N}\sum_k \hbar\omega_k \hat{b}^{\dagger}_{ik}\hat{b}_{ik}$. The interaction that generates these rates is:

$$\hat{\mathrm{V}}_{\mathrm{M-ph}} = \sum_{i=1}^{N}\sum_{k}\left(\hat{b}_{ik}+\hat{b}^{\dagger}_{ik}\right)\{\lambda_{e,ik}\left|e_i\right\rangle\left\langle e_i\right| + \lambda_{ge,ik}\left(\left|g_i\right\rangle\left\langle e_i\right| + \left|e_i\right\rangle\left\langle g_i\right|\right)\}. \tag{7.9}$$

The following rates are computed as the radiative rates of the previous Section. The expressions of the nonradiative rates are:

$$\boxed{\begin{aligned}\gamma_{G\rho} &= \frac{2\pi}{\hbar^2}\frac{\alpha_\rho}{N}\int dE\sum_{i=1}^{N}|\lambda_{ge,i}(\omega)|^2\nu_{\mathrm{v}}(\omega)J^{(em)}(E)\mathcal{L}_{\mathrm{ph},G\rho}\left(E-\Delta_{G\rho}\right),\\ \gamma_{GD} &= \frac{2\pi}{\hbar^2}\int dE\sum_{i=1}^{N}|c_{ip}\lambda_{ge,i}(\omega)|^2\nu_{\mathrm{v}}(\omega)J^{(em)}(E)\mathcal{L}_{\mathrm{ph},GD}\left(E-\Delta_{GD}\right),\end{aligned}} \tag{7.10}$$

where $\alpha_\rho \equiv \left(1-\rho\delta/\tilde{\Omega}_R\right)/2$, $\nu_{\mathrm{v}}(\omega) \equiv \sum_q \delta(\omega-\omega_q)$, $J^{(em)}(E) \equiv 1+n_{\mathrm{B}}$, $\Delta_{GD} \equiv \Delta_{ge}$ (see eq. (6.10)). The rate γ_{GD} is calculated using $|D_p\rangle = \sum_{i=1}^{N} c_{ip}\left|(e_i)\right\rangle \otimes |0\rangle$ with $\sum_{i=1}^{N} c_{ip} = 0$ (see eq. (6.10)) as the Dark states representation. In contrast with the radiative rates, the interaction $\hat{\mathrm{V}}_{\mathrm{M-ph}}$ opens a relaxation channel between the Dark-state manifold and the many-body ground state.

The dephasing rates are also obtained from the interaction given by eq. (7.9), but are due to the diagonal matrix elements $\lambda_{e,ik}$:

$$\boxed{\begin{aligned}\gamma_{-+} &= \frac{2\pi}{\hbar^2}\frac{\alpha_+\alpha_-}{N^2}\int dE\sum_{i=1}^{N}|\lambda_{e,i}(\omega)|^2\nu_{\mathrm{v}}(\omega)J^{(em)}(E)\mathcal{L}_{\mathrm{ph},-+}\left(E-\Delta_{-+}\right),\\ \gamma_{D+} &= \frac{2\pi}{\hbar^2}\alpha_+\left(1-\frac{1}{N}\right)\int dE\sum_{i=1}^{\mathrm{N}}|c_{ip}\lambda_{e,i}(\omega)|^2\nu_{\mathrm{v}}(\omega)J^{(em)}(E)\mathcal{L}_{\mathrm{ph},D+}\left(E-\Delta_{D+}\right),\\ \gamma_{-D} &= \frac{2\pi}{\hbar^2}\frac{\alpha_-}{N}\int dE\sum_{i=1}^{\mathrm{N}}|c_{ip}\lambda_{e,i}(\omega)|^2\nu_{\mathrm{v}}(\omega)J^{(em)}(E)\mathcal{L}_{\mathrm{ph},-D}\left(E-\Delta_{-D}\right),\end{aligned}} \tag{7.11}$$

where $\alpha_{\rho=\pm} \equiv \left(1-\rho\delta/\tilde{\Omega}_R\right)/2$, $\nu_{\mathrm{v}}(\omega) \equiv \sum_q \delta(\omega-\omega_q)$, $J^{(em)}(E) \equiv 1+n_{\mathrm{B}}$, $\Delta_{-+} \equiv \varepsilon_+ - \varepsilon_-$ (see eq. (6.8)), $\Delta_{D+} \equiv \varepsilon_+ - \varepsilon_D$ ($\varepsilon_D \equiv N\varepsilon_g + \Delta_{ge}$) (see eq. (6.10)), and $\Delta_{-D} \equiv \varepsilon_D - \varepsilon_-$. The N-prefactors in front of the derived rates come from the definition of the states involved in the transitions (Dicke states contain $1/\sqrt{N}$ that gets 1/N under the application of the modulo squared) and take into consideration the fact that some transitions go from a many-body states to a single state that require a division over the number of the involved states, and other transitions go from a single state to many-body states that require a multiplication for the number of the final states.

The nonradiative rates in eq. (7.10) and the dephasing rates in eq. (7.11) can be simplified assuming that the diagonal and the off-diagonal matrix elements are independent of the molecular index. This implies that $\lambda_{ge,i}(\omega) \to \lambda_{ge}(\omega)$ and $\lambda_{e,i}(\omega) \to \lambda_e(\omega)$. Furthermore, the assumptions (i) and (ii), of Section 7.1.1, are again cosidered. It follows that the dominant nonradiative rates given by eq. (7.10) read [111]

$$\boxed{\begin{aligned}\gamma_{G\rho} &\approx \alpha_\rho\gamma_{\mathrm{v}},\\ \gamma_{GD} &\approx \gamma_{\mathrm{v}},\end{aligned}} \tag{7.12}$$

where $\gamma_{\mathrm{v}}(\omega) \equiv 2\pi|\lambda_{ge}(\omega)|^2\nu_{\mathrm{v}}(\omega)/\hbar^2$ is the vibronic relaxation rate given by the product of the matrix-element square $|\lambda_{ge}(\omega_k)|^2$ evaluated at energy $\hbar\omega_k \equiv \hbar\omega$.
The same assumptions are applied to the dephasing rates (see eq. (7.11)). Their new expressions are [111]

$$\boxed{\begin{aligned}
\gamma_{-+} &\approx \frac{\alpha_+\alpha_-}{N} J^{(em)}\left(\Delta_{-+}\right)\gamma_\phi,\\
\gamma_{+-} &\approx \frac{\alpha_+\alpha_-}{N} J^{(abs)}\left(\Delta_{-+}\right)\gamma_\phi,\\
\gamma_{D+} &\approx \alpha_+\left(1-\frac{1}{N}\right) J^{(em)}\left(\Delta_{D+}\right)\gamma_\phi,\\
\gamma_{+D} &\approx \frac{\alpha_+}{N} J^{(abs)}\left(\Delta_{D+}\right)\gamma_\phi,\\
\gamma_{D-} &\approx \alpha_-\left(1-\frac{1}{N}\right) J^{(abs)}\left(\Delta_{-D}\right)\gamma_\phi,\\
\gamma_{-D} &\approx \frac{\alpha_-}{N} J^{(em)}\left(\Delta_{-D}\right)\gamma_\phi,
\end{aligned}} \tag{7.13}$$

where $J^{(abs)}(E) = n_{\mathrm{B}}(E)$ and the dephasing rate $\gamma_\phi(\omega) \equiv 2\pi|\lambda_e(\omega)|^2\nu_{\mathrm{v}}(\omega)/\hbar^2$. The bare dephasing rate is defined as γ_ϕ and the dressed rates derived above are called “dephasing” rates. The theoretical approach to compute the vibrational relaxation rates is consistent

Rate	$\gamma_{G'F}$	$\gamma_{G\pm}$	γ_{GD}	γ_{D+}
meV	6.6	3	6	41.3
THz	1.6	0.7	1.4	10

Table 7.2: Computed and dominant nonradiative relaxation rates due to electron-phonon interactions. The parameters are those of Fig.6.3, for $\Delta_{ef} = -0.2$ eV. The bare vibronic relaxation rate is $\gamma_{\mathrm{v}} \approx 6$ meV and the dephasing rate is chosen to be $\gamma_\phi \approx 82.7$ meV [111].

with refs. [129, 110] which focused on the vibrational strong-coupling regime in microcavities. Table 7.2 provides typical values [140, 166, 19, 6] for the bare vibronic relaxation rate γ_{v}, bare vibronic dephasing rate γ_ϕ, as well as for the computed and dominant dressed relaxation rates obtained from eqs. (7.12) and (7.13) (see blue arrows in Figure 7.1).

7.2 Ultrafast Reaction Kinetics

The evolution of the population of the states in cavity can be estimated using *first-order reactions.* A first-order reaction depends on the concentration of only one reactant. As such, a first-order reaction is sometimes referred to as a unimolecular reaction:

$$A \underset{k^{\leftarrow}}{\overset{k^{\rightarrow}}{\rightleftharpoons}} B, \tag{7.14}$$

where A is the reactant and B is the product.
Thus, the rate law for an elementary reaction that is first order with respect to a reactant A is given by:

$$\frac{d\,[\mathrm{A}]}{dt} \equiv [\dot{\mathrm{A}}] = \pm k\,[\mathrm{A}]\,, \tag{7.15}$$

where $-$ indicates if A$\rightharpoonup$ B, $+$ if A$\leftharpoondown$ B and $k^{\rightarrow}$, $k^{\leftarrow}$ are the associated reaction rates.

In this section, the (out of equilibrium) occupation probabilities $P_i(t)$ are computed as a function of time t of the *Reacton* states i involved in the whole photochemical process. CT chemical reactions (see Section 6.3), radiative relaxation (see Section 7.1.1) and nonradiative relaxation mechanisms (see Section 7.1.2) by the environment induce incoherent transitions amongst the *Reacton* states (see arrows in Figure 7.1).

7.2.1 Rate equation in the *Reacton* basis

The resulting time-evolution of the populations by a rate equation, written in the *Reacton* basis [111], is described by

$$\boxed{\begin{aligned}\dot{\vec{P}}(t) =& \mathbb{\Gamma}\vec{P}(t),\\ \vec{P}(0) =& \frac{1}{2}\left[0,0,1,0,1,0\right]\end{aligned}} \tag{7.16}$$

where $\vec{P}(t) = [P_G(t), P_{G'}(t), P_-(t), P_D(t), P_+(t), P_F(t)]$ is the vector of populations $P_i(t)$, and $\mathbb{\Gamma}$ is the rate matrix with matrix elements $\mathbb{\Gamma}_{ij}$ corresponding to the total transition rate (including chemical reaction rates, radiative and non-radiative relaxation rates) from the many-body state j to the many-body state i. The initial condition $\vec{P}(0)$ corresponds physically to an initial photon that has been absorbed at $t = 0^-$ in order to initiate the photoreaction at $t = 0^+$. For a resonant situation (the detuning $\delta = 0$), this leads to the choice $P_-(0) = P_+(0) = 1/2$. The solution of eq. (7.16) with the associated initial condition is found by computing numerically $\vec{P}(t) = e^{\mathbb{\Gamma}t}\vec{P}(0)$.

The vector of populations can be expressed more conveniently as a linear combination of exponentially damped eigenmodes characterizing the whole photochemical process

$$\boxed{\begin{aligned}\vec{P}(t) =& \vec{P}^{(st)} + \sum_{\lambda\neq 0} c_\lambda \vec{v}_\lambda e^{\lambda t},\\ c_\lambda =& {}^{\mathrm{T}}\vec{w}_\lambda\, \vec{P}(0) \equiv \frac{w_{\lambda,-} + w_{\lambda,+}}{2},\end{aligned}} \tag{7.17}$$

with $\vec{v}_\lambda$ the right eigenvector and ${}^{\mathrm{T}}\vec{w}_\lambda$ the left eigenvector of the $\mathbb{\Gamma}$ matrix, associated to the real negative eigenvalue λ. The left and right eigenvectors of $\mathbb{\Gamma}$ form a biorthogonal basis [16], which allows by projection to find the unique coefficient c_λ in eq. (7.17) as a function of the initial condition. The constant vector $\vec{P}^{(st)} \equiv \vec{v}_0$ in eq. (7.17) is the null right eigenvector (solution of $\mathbb{\Gamma}\vec{P}^{(st)} = \vec{0}$) providing the stationary populations of the *Reacton* states. The expression for $\vec{P}^{(st)}$ and $P_F(t)$ are:

$$\begin{aligned}\vec{P}^{(st)} =& \frac{1}{k_{G'G} + k_{GG'}}\left[k_{GG'}, k_{G'G}, 0, 0, 0, 0\right],\\ P_F(t) =& \sum_{\lambda\neq 0} \frac{w_{\lambda,-} + w_{\lambda,+}}{2} v_{\lambda,F} e^{\lambda t}.\end{aligned} \tag{7.18}$$

The stationary state in eq. (7.18) corresponds to a chemical equilibrium between the electronic ground state populations $P_G^{(st)}$ and $P_{G'}^{(st)}$.

7.2.2 Time evolution of the photoreaction

Figure 7.2 shows the time evolution of $P_i(t)$, corresponding to the molecule of Figure 6.1. As shown in Table 7.1 and 7.2, the dominating relaxation rates are the radiative ones $\Gamma_{G\pm}$ (see gold downward arrows in Figure 7.1) and the dephasing rate γ_{D+} (downward blue arrow in Figure 7.1). We obtain that on time scales $t \gg 1/\Gamma_{G\pm}, 1/\gamma_{D+}$, all the populations in the excited states vanish, the stationary regime being a chemical equilibrium between the states G and G' in eq. (7.18) (see solid green lines in Figure 7.2). The population of the Upper Polariton (UP) $P_+(t)$ (blue pluses in Figure 7.2) is a monotonically decreasing function of time, well approximated by a single exponential decay $P_+(t) \approx e^{-\Gamma_+ t}/2$. The UP lifetime $1/\Gamma_+ = 1/\left(\Gamma_{G+} + \gamma_{G+} + \gamma_{D+}\right)$ results mainly from both optical cavity damping (Γ_{G+}) and fast relaxation (γ_{D+}) towards the Dark-state manifold mediated by the vibrational dephasing mechanism. The Dark states thus play the role of a sink for the UP (this feature was already noticed in ref. [129]). The population of the Dark states $P_D(t)$ is shown as solid black circles in Figure 7.2. Its time evolution is not monotonous, but well approximated by $P_D(t) \approx \gamma_{D+}\left(e^{-\Gamma_+ t} - e^{-\Gamma_D t}\right)/\left[2\left(\Gamma_D - \Gamma_+\right)\right]$, with the additional Dark-state lifetime

$1/\Gamma_D = 1/\left(\gamma_{GD} + k_{\mathrm{CT},FD}\right)$. The existence of a maximum of $P_D(t)$ results from a competition between the filling of the dark-state from the UP with a rate Γ_+, and its emptying towards the ground state G and excited state F with rate Γ_D. Compared to the UP, the occupation of the Lower Polariton (LP) $P_-(t)$ (dashed red curve in Figure 7.2) is still a monotonically decreasing function of time, but with a slower rate due to the absence of ultrafast relaxation towards the Dark-state manifold.

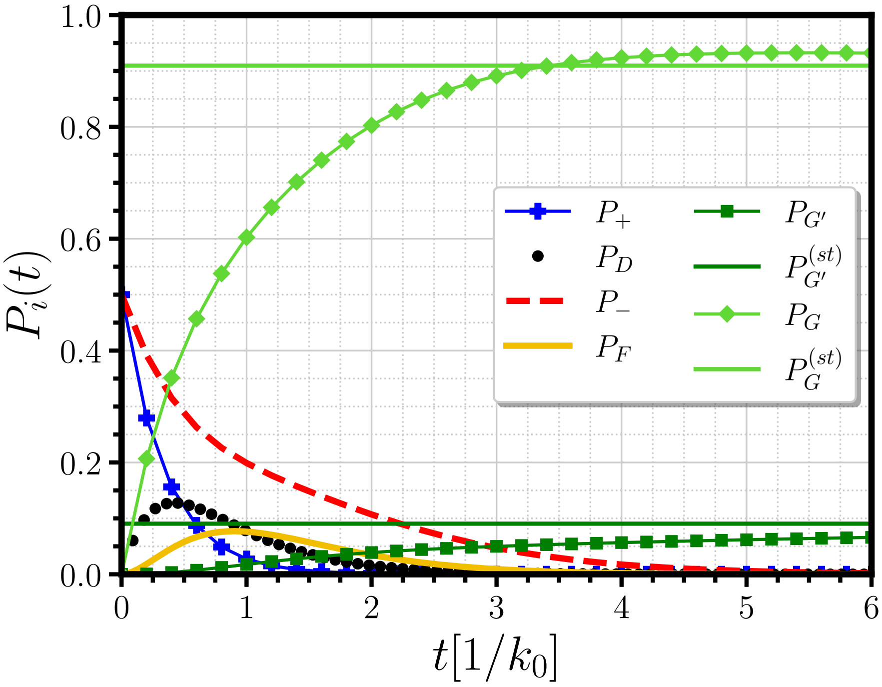

Figure 7.2: Probabilities $P_i(t)$ of occupying the *Reacton* states i, as a function of time t in units of $1/k_0$ (defined in eq. (6.25)). The parameters are those of Figure 6.3 for $\Delta_{ef} = -0.2\,\mathrm{eV}$, and of Tables 6.1-7.2 [111].

Of particular interest for photochemistry is the time evolution of the occupation probability for the reaction product $P_F(t)$ (solid yellow curve in Figure 7.2). Figure 7.3 shows a zoom on $P_F(t)$ inside the cavity ($\tilde{\Omega}_R = 0.7$ meV for the plain-solid yellow curve) and the same quantity $P_F^{(0)}(t)$ outside cavity ($\tilde{\Omega}_R \approx 0.0$ meV for the dotted thin yellow curve with solid circles). For the range of parameters corresponding to the reaction driving force $\Delta_{ef} = -0.2$ eV (the case of the molecule in Figure 6.1 and case $\Delta_{ef} = -0.2\,\mathrm{eV}$ in Figure 6.3) and choice of initial condition, $P_F(t) \leq P_F^{(0)}(t)$ at all times. The cavity-molecule coupling has thus an effect to slow down the photochemical reaction compared to what is obtained outside cavity. The same curve is plotted in Figure 7.4, for the different value of $\Delta_{ef} = -0.4$ eV. In contrast to the previous case, one observes for each times that $P_F(t) \geq P_F^{(0)}(t)$, so that the effect of coupling the reactant to vacuum quantum fluctuations of the electromagnetic cavity mode is to speed up (and thus to enhance) the formation of the reaction product significantly, compared to the case outside cavity. The cavity-induced slowing down or acceleration of the appearance rate for the photoreaction product depends thus crucially on the reaction driving force Δ_{ef} (and thus the choice of the coupled molecules), which is consistent with the analysis of the thermal CT rate performed in Sections 6.3 and 6.2.

The main feature observed in both Figure 7.3 and Figure 7.4, is the nonmonotonous dependence of $P_F(t)$ with time t.

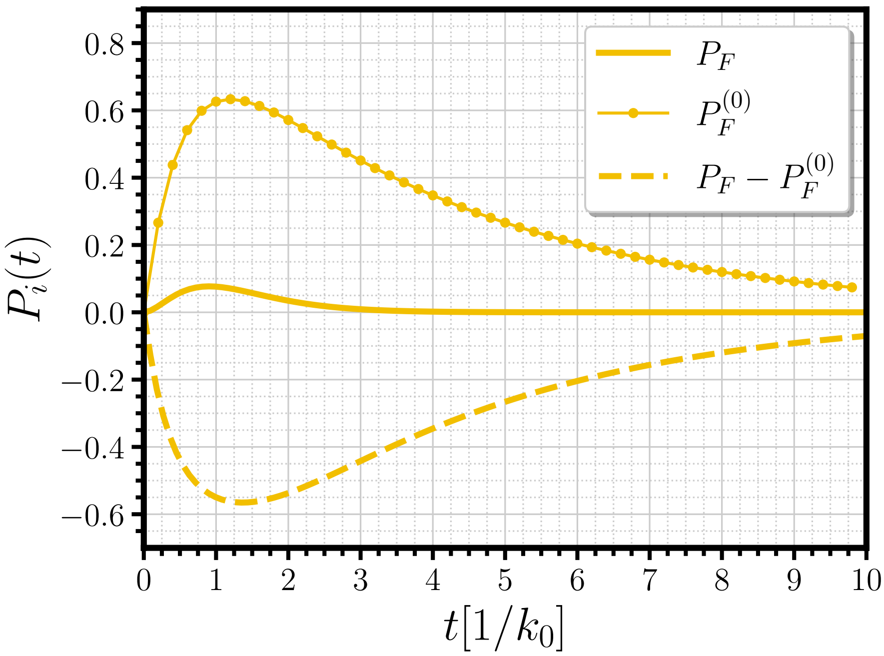

Figure 7.3: Probability $P_F(t)$ of occupying the product state F inside cavity ($\tilde{\Omega}_R = 0.7$ meV) shown as a solid yellow curve, as a function of time t in units of $1/k_0$ (defined in eq. (6.25)). The corresponding occupation probability $P_F^{(0)}(t)$ outside cavity ($\tilde{\Omega}_R \approx 0.0$ meV) is shown as a thin yellow curve with solid circles. For comparison, the difference of occupations $P_F(t) - P_F^{(0)}(t)$ is plotted as a dashed yellow curve. Parameters are those of Figure 6.3 for $\Delta_{ef} = -0.2\,\text{eV}$, and of Tables 6.1-7.2 [111].

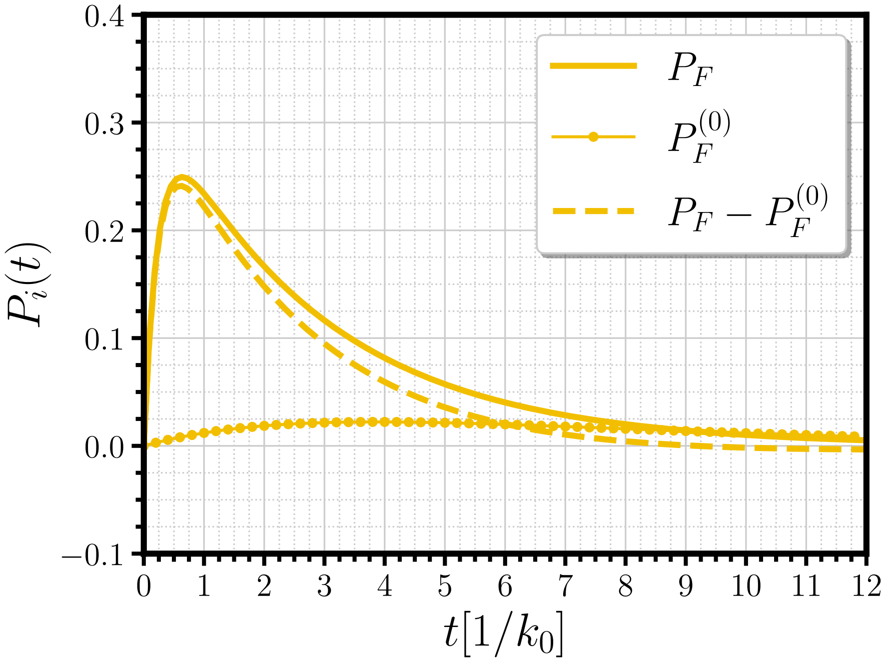

Figure 7.4: Same as figure in Figure 7.3, but with a modified reaction driving force $\Delta_{ef} = -0.4$ eV [111].

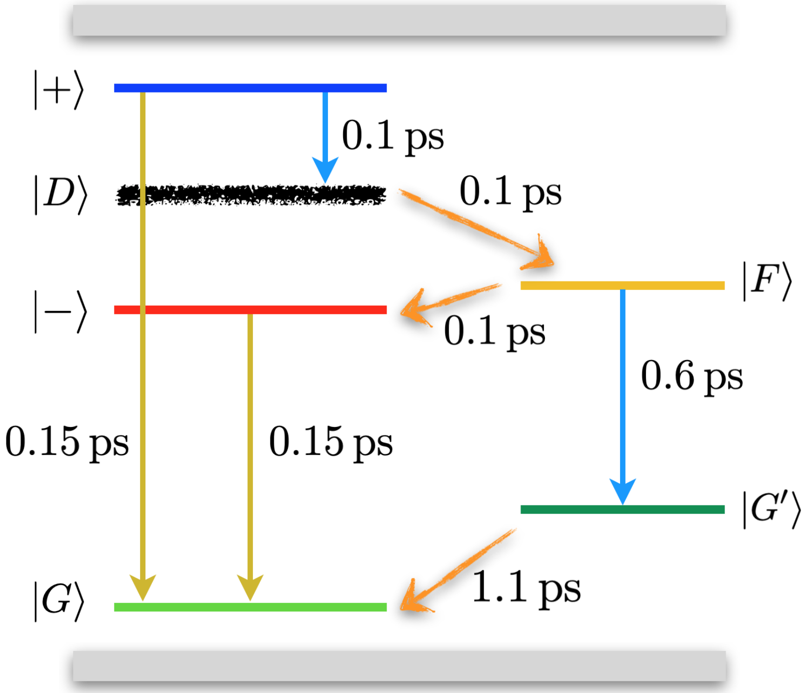

Figure 7.5: Dominant and relevant rates to describe the evolution of P_F in picosecond time scale.

Figure 7.5 shows the dominant and the relevant rates to follow the evolution of the state F (see also Figure 7.3). Initially, $P_F(0) = 0$, since the two polariton states are equally populated ($P_{\pm}(0) = 1/2$). At short times $t \leq 1/\Gamma_{G\pm}, 1/\gamma_{D+}$, the UP decays toward the Dark-states manifold. When the D states are significantly filled, the CT chemical reaction gets initiated, mainly by the dominant reaction rate $k_{\mathrm{CT},FD}$ (see Table 6.1) which is modulated by the strong light-matter coupling inside cavity. This results in a short-time increase of the F product-state occupancy. The existence of a maximum of $P_F(t)$ for $t \approx 1/k_0$ and a later decrease of the product-state occupancy is due to the onset of the relaxation back to G' due to the nonradiative relaxation rate $\gamma_{G'F}$ (see Table 7.2) and to the cavity-mediated backward reaction rate $k_{\mathrm{CT},-F}$ (see Table 7.1). At longer time all the states relax on the ground states G and G'.

It is important to note the effect of the losses induced by dissipation and non-radiative relaxation towards the environment in describing the photoreaction kinetics. The nonmonotonous behavior of $P_F(t) - P_F^{(0)}(t)$ in Figure 7.3 and Figure 7.4 is a signature of the *Reacton* formation, that should be observable using pump-probe spectroscopy. Its sign provides the information whether or not the strong coupling of reactants to the cavity mode enhances or inhibits the formation of the reaction product. There is a large room of possibilities to engineer and optimize this reaction kinetics by fine-tuning of the system parameters.

8

Conclusion

The first part of this manuscript has been devoted to study intramolecular charge-transfer reactions of solvated molecules confined in a Fabry-Pérot cavity. The modelling of the “vibrating” molecules, strongly coupled to the cavity mode, has been performed using the generalization of the Jaynes-Cummings model, the so-called Holstein-Tavis-Cummings model. In the limit of weak vibrational reorganization energies compared to the collective electron-photon coupling, analytical expressions of the Potential Energy Surfaces have been calculated. They offer a significant understanding of the collective motion along the equilibrium reaction coordinates. The strong coupling regime between light, the cavity-photon mode, and matter, the N solvated molecules, generate the Polaritonic states and N-1 Dark states. Important conditions for the onset of Polaritons are the resonance condition between the cavity mode and the bare molecular transition, and an higher electron-photon coupling compared to the total losses of the cavity.

The Polaritonic Potential Energy Surfaces are not perturbed by the introduction of inhomogeneous broadening at the level of the molecular excited-energy nor at the level of reaction coordinates. Polaritons retain their coherence nature in absence of dissipative mechanisms. In contrast, the broadening induces a lifting of degeneracy of the Dark states which are distributed in a sort of miniband of states.

Polaritons are dressed by both intramolecular and solvent vibrational degrees of freedom. This collective excitation shared coherently by all the reactant molecules is called *Reacton*, by analogy with the polaron excitation in solid-state physics. The dressed Potential Energy Surfaces, due to the *Reacton* formation, and the corresponding nuclear equilibrium positions of the vibro-solvent modes have been computed.

Reacton’s formation is responsible for a modification of the chemical reactivity of confined molecules compared with unconfined ones. In particular, a class of photoactive molecules which undergo intramolecular charge-transfer chemical reactions have been studied. The theoretical framework to deal with charge transfer is based on Marcus theory with the famous Marcus rate. It has been shown that the classical Marcus rate is a convenient and simple tool to describe electron and charge transfer for coupled and uncoupled molecules in the quantum regime. The rate has been generalized taking into account the *Reacton* Potential Energy Surface. The resulting new rate is composed by renormalized quantities for the vibro-solvent and collective nature of *Reacton*.

Indeed, the thermal charge transfer reaction in cavity can be tuned (acceleration or slowing down) by changing the bare vacuum Rabi frequency (the electron-photon coupling), the molecule-cavity detuning, the concentration of reacting molecules, the driving force of the chemical reaction, and the vibro-solvent reorganization energies. These results pave the way for new possibilities in molecular engineering, using strong coupling of the molecules to vacuum quantum fluctuations of the electromagnetic cavity modes.

The *Reacton* coherent nature is altered by cavity losses and dephasing mechanisms due to the interaction between molecules and solvent modes. Hence, a minimal microscopic model of dissipation and dephasing has been adopted. Radiative and nonradiative rates have been written in accordance with the *Reacton* Potential Energy Surface as generalized expressions involving the convolution of cavity spectral distributions and vibrational line shapes. Dissipative rates, that is radiative and nonradiative rates, and chemical rates are necessary to study the kinetics of the whole photochemical process.

For this purpose, a generalized rate-equation approach expressed in the basis of many-body *Reacton* states has been developed, the solution of which provides the ultrafast picosecond dynamics of the photochemical reaction. Inside the cavity, either an increase or a decrease of the occupation probability for the product state compared to outside cavity is predicted, depending on the bare reaction driving force. The time at which a maximum amount of reaction product is obtained, results from a delicate balance between competing environment-induced dissipation tending to decrease the net rate of product formation and the enhanced chemical reactivity due to the formation of the *Reacton*. The signature of the CT reaction should be visible in time scales ranging from hundreds of femtoseconds to few picoseconds and in some cases to several hundreds of picoseconds; these time scales are easily attainable in regular pump-probe experiments.

Several perspectives are assigned to extend the present work. One of them is to investigate how to define properly a thermodynamical potential describing the *Reacton* thermodynamic properties inside the nanofluidic cavity. Although pioneer studies [18] investigated the thermodynamics of cavity-confined molecules, a proper definition and quantitative calculation of the corresponding *Reacton* chemical potential is still missing. The former task involves taking into account into the theoretical description the spatial dependence of the cavity-mode electric field, which is responsible for spatial inhomogeneities [77] in the vacuum Rabi frequency and detuning experienced by each coupled molecule. Moreover, thermal fluctuations of each molecular dipole with respect to the local electric-field direction induces the necessity to perform an additional rotational averaging [30], on top of the previous spatial one.

Another interesting direction of research is to investigate the case of an open chemical reactor, namely, a flow of reactants in solution that enters the optical cavity, undergoes a chemical reaction inside, and finally leaves the cavity with reaction products being collected outside. In the case of a hydrodynamic Poiseuille flow [64, 95], there is a characteristic time scale $t_L \approx L/4v_0$, with L being the longitudinal dimension of the nanofluidic cavity and $v_0 = 3D_m/2\rho_m$ being the maximum velocity at the center of the flow (D_m is the mass flow, and ρ_m is the liquid volumic mass). The ratio of t_L to the typical time scale of the chemical reaction $t_\chi \approx 1/k_{\mathrm{CT}}$ provides an adimensional parameter $\xi = k_{\mathrm{CT}}L/4v_0$. While in the present study, the CT reaction is very fast compared to the flow velocity, thus resulting in $\xi \gg 1$, it would be of interest to look for other kinds of chemical reactions for which $\xi \approx 1$. The former case would result in an interesting nonlinear dependence of the reaction rate on the hydrodynamic flow and reactant concentration.

It is hoped that the first part of the manuscript will stimulate further theoretical and experimental investigations in this direction.

Part II

Chiral Discrimination in Electromagnetic Fabry-Pérot Cavities

9

Introduction

A chiral object such as glucose, a spiral, a hand or another microscopic or macroscopic entity is characterized by a lack of symmetry. The mirror image of the chiral object, designed as *enantiomer*, and itself cannot be directly superimposed (see Figure 9.1). An object which is not chiral is called achiral.

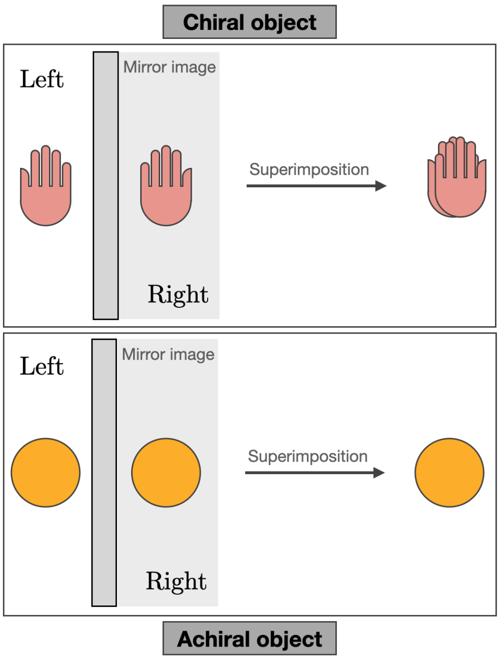

Figure 9.1: Sketch of a chiral and an achiral object.

Chirality, or equivalently *handedness*, is intrinsically linked to the origin of life and it has a very important role in molecular, biological and all vital processes. For instance, amino acids, the building blocks of proteins, are chiral as well as the DNA. Snails have typically helicospiral shells and a preferential direction of shell coiling is predominant in certain species. Interestingly, repeated modifications of both the soft mollusk body and the shell coiling, during evolution, could be correlated to generate the final chiral shape [25]. This aspect shows the importance of the mutual interaction between the shape of the body and the handedness of the shell in a resulting *symmetry-breaking* mechanism. The snails are one example of the tendency of nature to manifest *homochirality*, a chiral entity which appears only left or right.

The chirality of an object or a chemical compound can be probed by polarized light. Light propagates everywhere and during its propagation light interacts with the objects it encounters. The interaction between a light ray and a chiral entity is called *chiroptical* effect. Experimental works aiming at studying chiroptical effects date back to early 19th century and during the 20th century intense theoretical research activity was devoted to find appropriate models for describing and characterizing chiral light-matter interactions. Some important steps (at our knowledge) in the history of chiroptical effects are reported in the following lines. The first discovery of chiroptical effects on macroscopic chiral media, the family of quartz, was attributed to François Arago. In 1811 he discovered the phenomenon of *optical activity* in crystals of quartz, where the quartz rotates the plane of polarization of linearly polarized light that is transmitted through it [3]. Eventually, other experiments of Jean-Baptiste Biot (dating from 1812 to 1838) and Augustin-Jean Fresnel (in 1822) showed the dependence of optical activity on the thickness of the material [11] and that a ray of light traveling in a crystal of quartz is resolved into two circularly polarized rays, one with a left handedness and the other with the opposite handedness [53]. In 1848 Louis Pasteur studied two chiral forms of tartaric acid crystals and its discovery was confirmed by J.-B. Biot two years later [125]. Most of the experiments of that period were well annotated and contained in a book by Thomas Martin Lowry [103].

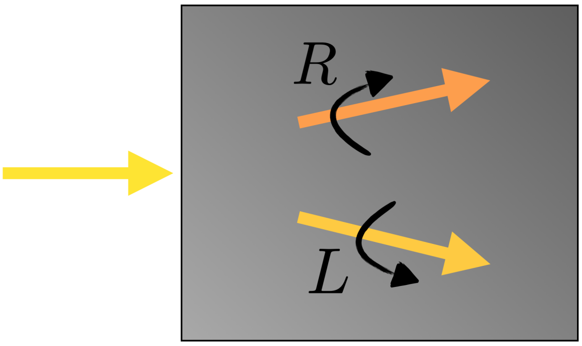

Figure 9.2: Sketch of a ray of light which is resolved into two circularly polarized rays, left-handed (L) and right-handed (R), inside a chiral medium.

A detailed and particularly clear study of the microscopic origin of chirality, by interaction of molecular electric and magnetic dipoles induced by classical light, was given by Edward Uhler Condon. In 1937 he derived the famous Condon constitutive equations, which describe the chirality of a macroscopic, homogeneous and isotropic medium in connection with his microscopic model [29]. Other equivalent constitutive relations for macroscopic chiral media were derived by E. J. Post, in 1962, making an explicit treatment of general covariance in electromagnetism [131]. The same set of equations was also obtained by Jaggard *et al.* [85], in 1978, considering the scattering of electromagnetic waves from a metallic single-turn helices. The generalized relations for reciprocal bianisotropic media were suggested by B.V. Bokut and F. I. Federov [12]. The chiral constitutive relations were adopted to study the transmission and reflection of light at the interface of macroscopic chiral and achiral materials [8, 150, 151]. In particular, Dwight L. Jaggard and Xiaoguang Sun developed a Transfer matrix approach for multi-chiral homogeneous layers and an initial-value approach suitable for inhomogeneous slabs [86]. This work provided the fundamental building blocks for the chiral multilayer problem and it brought to light the physical processes involved in the wave interactions with planar chiral layers.

The phenomenon of optical activity, resulting from the classical interaction of light with chiral molecules, was difficult to detect due to its inherent weakness (of the relative order of $10^{-3}-10^{-5}$). This weak interaction was a limitation in understanding molecular properties and a barrier to discover interesting aspects of the chirality itself. Clearly, there was a need to find methods to enhance the chiral asymmetries, and the concept of enhancement or amplification of *light-matter* interaction led to usage of the Fabry-Pérot interferometer [13]. Pioneering theoretical studies of optically active Fabry-Pérot interferometers were carried out by I. J. Lalov *et al.* [152, 94], using the Condon constitutive relations. They analyzed the propagation of light into a chiral layer and the multiple reflection mechanism, inside the layer, to calculate some quantities as the intensities of the transmitted and reflected beams, or other observables as the *differential circular reflection* and the *ellipticity* of the optical rotation of linearly polarized light. The last two describe the degree of chiral asymmetries. Sliverman and Badoz showed theoretically that the chiral asymmetries, of a macroscopic chiral layer, are a consequence of a relative phase difference between the propagating circularly polarized waves of opposite handedness, inside the medium. The asymmetries, of the order of the chirality of the medium (encoded by the so-called Pasteur coefficient), can be enhanced increasing the thickness of the medium for a given finite incident angle of the incoming light ray.

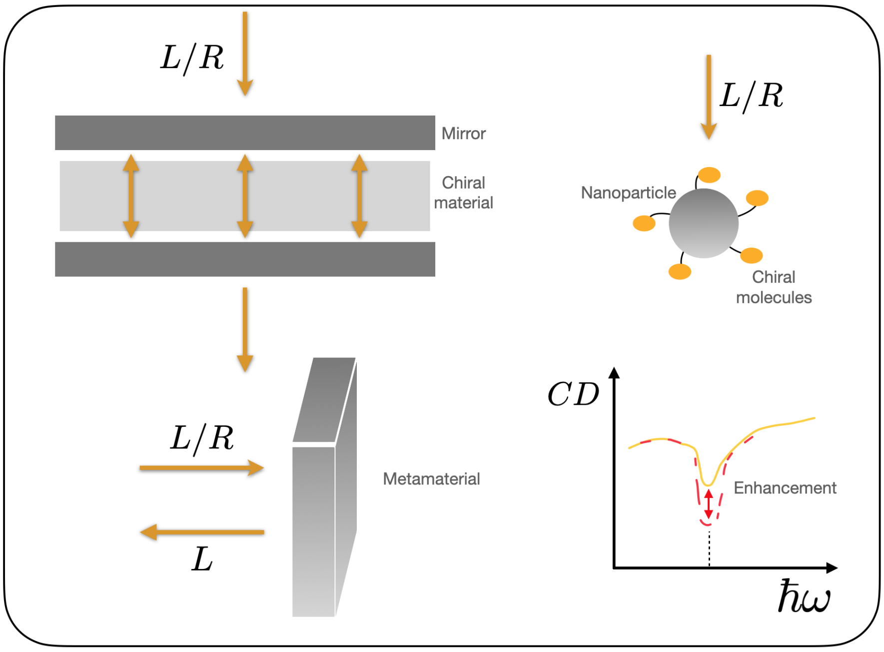

Figure 9.3: Some ways to try to enhance the Circular Dichroism response.

Today, improving natural chiroptical effects is still a goal of an active branch of research. One direction is related to the confinement of light at the nanoscale with the generation of localized surface plasmon resonances. Theory and experiments predict that nanoparticles capped with chiral molecules can have optically active plasmon resonances due to several modes of mutual interactions between the two partners that can doubly modify the chiral spectroscopic response [62, 45, 35]. The main chiral response is the *Circular Dichroism* (CD), that is the differential absorption of left and right-handed circularly polarized light. The CD signal is important to understand the conformation of biomolecules and their dynamics [163].
Another direction to increase the chiroptical response is with the fabrication of *chiral metamaterial*. These metasurfaces are artificial composite structures engineered to have innovative properties [118]. They are capable to display higher optical activity than natural materials and some even show a negative refractive index [32, 93, 123, 177, 23].
In the context of enhancing chiroptical effects, Fabry-Pérot (FP) cavities were recently adopted and engineered to *selectively probe* chiral matter with chiral light. A common property of a standard, and not engineered, FP cavity is that each time the circularly polarized light is reflected inside the cavity, the handedness is flipped [7]. Thus the reflections inside the cavity reduce a selective polarization in one handedness with a resulting small/negligible chiroptical effect in the transmission. Some theoretical investigations show that modifications at the level of the mirrors of the cavity reduce the destructive internal polarization conversion and enhance the chiral response in terms of CD [47, 9, 175]. An interesting example of a mirror that reflects only one handedness of circularly polarized light can be found in nature. In fact, *Chrysina Gloriosa*, a jeweled beetle, appears more brilliant under illumination of left-handed circularly polarized light (LHCP) than the right-handed polarization (RHCP). This means the beetle efficiently reflects LHCP and absorbs the RHCP [15]. This mechanism is due to the presence of helicoidal layers in its cuticle, making it a natural spin-preserving mirror.

Many theoretical proposals offered the perspective of a sort of spin-preserving mirror [130, 47, 9] and some experimental realizations are available right now. A spin-preserving chiral photonic crystal mirror has recently been designed and fabricated, exhibiting a large chiroptical effect [142]. This thin monolithic mirror

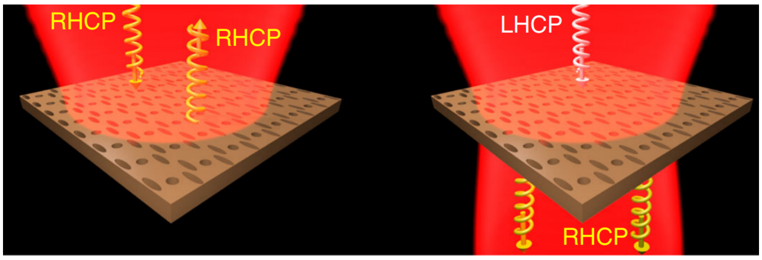

Figure 9.4: Illustration of the optical response of the experimentally realized spin-preserving chiral photonic crystal mirror at the designed wavelength of 870 nm. The structure reflects RHCP light while preserving its handedness. The LHCP is transmitted, and its handedness is reversed. Adapted from [142].

(thickness of 309 nm) outperforms most of the previous experimental devices, in fact, it is capable to reflect 80% of a chosen helicity of light, working at the wavelength of 870 nm, with an extinction ratio above 30:1. The ability of the mirror to preserve almost one handedness of the polarized light relies on the chiral unit elements, composed by a tripartite array of perforating holes, which covers the entire surface (see Figure 9.4). Instead, the strong chiroptical effect originates from the bi-modal interference of leaky TE with TM Bloch modes in the photonic crystal mirror.

A recent theoretical article concerns the proposition of a single-handedness chiral optical cavity (cavity thickness of 1724 nm), with the usage of the spin-preserving photonic mirror described above [156]. The authors show that the cavity supports only one mode of a given handedness and the other one is almost suppressed. Furthermore, adding a chiral emitter between the two mirrors it is predicted to enhance the spontaneous emission rate of one order of magnitude, at the wavelength of 798.2 nm, in one handedness respect to the other one. These results suggest a new path towards *"chiral vacuum quantum fluctuations"* and *"chiral Polaritonic states"*.

Schichao Sun *et al.* explored theoretically the effects of another kind of chiral cavity, composed by two normal mirrors with Faraday rotators and a sample plate of Mg-porphyrin molecules placed in the middle of cavity [154] (see Figure 9.5). The application of a static magnetic field breaks time reversal symmetry and a simultaneous pumping of circularly polarized light rays generate ring current in Mg-porphyrin. It follows a lift of the excited states degeneracy and the Polaritonic states generated with this mechanism affect the Circular Dichroism. The authors show that the Polaritonic CD signal is enhanced of one order of magnitude than in the bare molecular case.

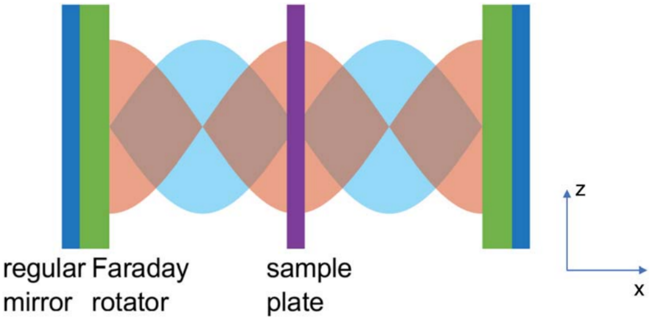

Figure 9.5: Optical chiral cavity created by Faraday rotator and regular mirrors. Two Faraday rotators (green) are placed on the interior side of the two mirrors (blue). A magnetic field is applied along the cavity x-axis. The left circularly polarized standing wave (light blue) and right circularly polarized standing wave (orange) have a phase difference. At the node of the left circularly polarized standing wave, the right circularly polarized wave dominates. A plate of sample molecules is placed in the plane at the peak of right circularly polarized standing wave. Adapted from [154].

Another more recent theoretical and experimental article paves the way to investigate chiral modes in the context of chiral cavity QED and Polaritonic Chemistry [59]. In this paper a chiral 2D layer of polystyrene (thickness of 150 nm) is sandwiched between two smooth metallic silver mirrors, forming a chiral FP cavity (see Figure 9.6). The total structure can be illuminated at oblique incidence, given the fact that the chiral layer is subjected to torsional stress in solution, and the resulting combination of 2D and 3D chirality (for the torsional angle) enables a spin-orbit coupling mechanism which preserves one helicity of light in cavity.

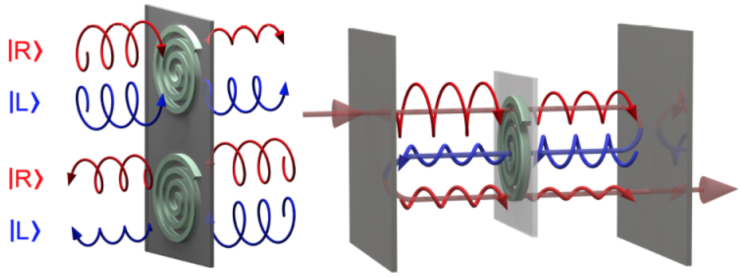

Figure 9.6: Breaking of left- vs right-handed polarization in a Fabry-Perot cavity composed of two usual metallic mirrors but enclosing a 2D chiral medium, here conceptually represented by a 2D spiral. Adapted from [59].

These studies hint at open questions for future investigations:

- What is the role of the presumed chiral vacuum quantum fluctuations?
- Do chiral Polaritonic states exist as the result of strong chiral light-matter interaction?
- Is it possible to enhance the response of chiral molecules which interact with chiral modes of the cavity-field?

These questions could lead to new ways of engineering, revealing, discovering chiral optical properties in the classical and quantum regime. Indeed, a chiral optical cavity constitutes an added value for an efficient and specific manipulation of chiral entities, highly desired in pharmaceutical industries, chemical applications, biological purposes and all the fields interested in separating chiral molecules among racemic mixtures.

The challenge to predict the existence of chiral Polaritons and to propose new setups that enhance the intrinsic chirality of molecules is the objective of our theoretical work in the framework of chiral light-matter interactions. We study in detail how a standard Fabry-Pérot cavity, probed by circularly polarized light rays, behaves when a macroscopic concentration of chiral molecules are confined inside. Eventually, we study another Fabry-Pérot cavity by adopting a novel and original modelling for the mirrors, that now are chiral. The modelling of the mirrors follows the operational function of the previously described spin-preserving chiral photonic crystal mirrors (see Figure 9.4). Amazingly, we reveal that the new system is capable to enhance the chirality of the inserted molecular layer and is the first setup (at our knoweldge) that clearly show the onset of chiral Polaritons.
The outline of the work is summarized in the following section.

9.1 Contents

The second part of the manuscript contains the macroscopic and the corresponding microscopic model of an isotropic chiral medium. The model's description is encoded in the constitutive relations of the Maxwell's equations, that is the starting point to understand how plane waves propagate in chiral media (first part of Chapter 10). By studying the boundary conditions at the interface of two different isotropic chiral media, it is possible to construct transfer matrices to propagate circularly polarized light through a multilayer system (second part of Chapter 10, see from Section 10.4). This approach enables the modelling of a Fabry-Pérot resonator filled with a chiral layer, which represents a macroscopic collection of chiral molecules of the same handedness (Chapter 11). The same device is also studied with the inclusion of metallic mirrors and an associated dispersive model (Chapter 12). A similar dispersive model is adopted for the chiral layer (see Section 12.2). The dispersive modelling can also be treated analytically to better characterize the chirality of the system, in a low and strong regime (see from Section 12.3 to the Section 12.7). The final Section of Chapter 12 describes the implication of Lorentz's reciprocity on transmission and reflection matrices.

The last part of this manuscript is devoted to model a chiral Fabry-Pérot cavity with spin (helicity)-preserving mirrors (Chapter 13). The chiral mirrors are modelized using reciprocity and time-reversal symmetry, essential aid to construct the correct transfer matrix in order to propagate the circularly polarized rays of light which accumulate particular phases in the multiple reflections. The usage of spin-preserving chiral mirrors add some effects that are not available for achiral metallic mirrors. In fact, the section 13.2 gradually presents the influence of the chiral mirrors on cavity-light modes, in the empty cavity. The same is done for the cavity filled with an isotropic chiral medium to finally reveal the interplay between the chirality of the mirrors and the chirality of the inserted medium (see from Section 13.5 to the end of the Chapter 13).

10

Plane waves in Chiral media

The propagation of light in a lossless homogeneous chiral medium extends the knowledge of the modern electromagnetism which describes the propagation of light in isotropic achiral media. Moving from achiral to chiral media, some generalizations are required. In fact, the constitutive relations have to be modified in order to get the correct optical rotatory response of the medium. The chiral Helmholtz equation, its eigenvectors and eigenvalues are derived. The connections between the resulting eigenvectors are explicitly explained. A chiral transfer matrix approach is directly obtained from studying the boundary conditions at interface of different chiral layers. The approach has the advantage to describe any layered system, chiral and achiral.

10.1 Chiral constitutive relations

The starting point to deal with classical electrodynamics is to consider the Maxwell's equations plus the associated constitutive relations [84]. Together they represent a self consistent set of equations [169]. For a linear isotropic achiral medium the space-time Maxwell's equations with electric and magnetic sources are given by

$$\begin{gathered}\nabla \wedge \vec{E} = -\frac{\partial \vec{B}}{\partial t}, \nabla \cdot \vec{B} = 0, \\ \nabla \wedge \vec{H} = \vec{J} + \frac{\partial \vec{D}}{\partial t}, \nabla \cdot \vec{D} = \rho.\end{gathered} \tag{10.1}$$

The associated constitutive relations are

$$\begin{gathered}\vec{D} = \varepsilon \vec{E} \text{ with } \varepsilon = \varepsilon_0 \left(1 + \chi_e\right), \\ \vec{B} = \mu \vec{H} \text{ with } \mu = \mu_0 \left(1 + \chi_m\right),\end{gathered} \tag{10.2}$$

where ε_0 is the vacuum dielectric constant, χ_e is the dielectric susceptibility, μ_0 is the vacuum magnetic permeability and χ_m is the magnetic susceptibility.
These relations can also be written with the usage of the macroscopic polarization $\vec{P}$ and magnetization $\vec{M}$ as it follows

$$\begin{gathered}\vec{D} = \varepsilon_0 \vec{E} + \vec{P} \text{ with } \vec{P} = \varepsilon_0 \chi_e \vec{E}, \\ \vec{B} = \mu_0 \vec{H} + \vec{M} \text{ with } \vec{M} = \mu_0 \chi_m \vec{H}.\end{gathered} \tag{10.3}$$

A chiral medium is the source of *optical activity* (rotatory power), *i.e.*, the property of some crystal, liquids and gases to rotate the plane of polarization of light that is transmitted through it [97]. In 1937, E. U. Condon proposed a theory of optical activity with the modification of the constitutive relations given by eqs. (10.2) and (10.3) [29]. The new relations are

$$\boxed{\begin{aligned}\vec{D} &= \varepsilon\vec{E} - \frac{g}{c}\frac{\partial\vec{H}}{\partial t},\\ \vec{B} &= \mu\vec{H} + \frac{g}{c}\frac{\partial\vec{E}}{\partial t},\end{aligned}} \tag{10.4}$$

where c is the velocity of light in free vacuum space and g is a pseudoscalar ($g \to -g$ when $\vec{r} \to -\vec{r}$) which represents a *magnetoelectric* coupling. In rationalized units g has the dimension of time. The coupling is a dynamic coupling for the presence of varying coupled fields in a chiral medium. The archetype of chiral medium is a medium composed by a large number of randomly oriented metallic helices, called *Pasteur medium* (see Figure 10.1). The magnetoelectric coupling can be intuitively grasped from the behaviour of a helix as it is exposed to the electromagnetic field. If an electric field excites the helix, it separates charges, creating an electric dipole moment $\hat{\vec{\mu}}$. This contributes to the permittivity of the medium, but the shape of the helix forces the charge to move along a circular route, in addition to the linear path. This electric current loop gives rise to a magnetic dipole $\hat{\vec{m}}$, and if all helices of the mixture have the same handedness, the magnetic polarization is enhanced [102, 85].

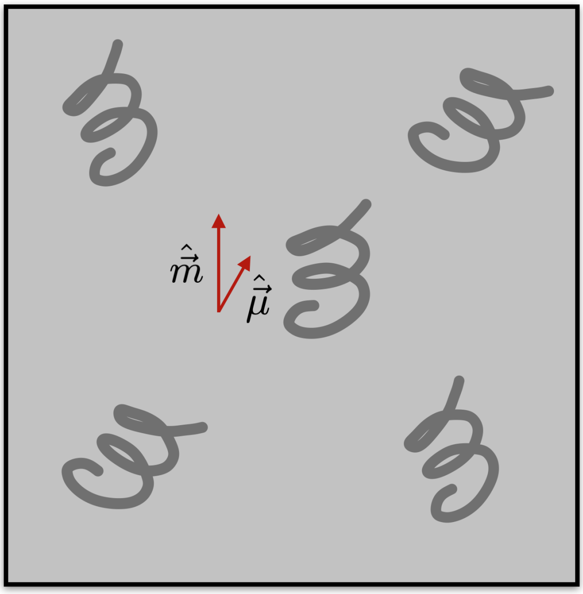

Figure 10.1: Sketch of a Pasteur Medium.

The coupling g is a pseudoscalar and it changes the sign under spatial inversion of the coordinate system. This aspect suggests to redefine g as g_p where g_p is equal to $+g$ or $-g$. In particular, the assumption is to use $g_p = +g$ when the wave is left-handed circularly (LHC) polarized with respect to the view of an observer looking at the oncoming wave; and $g_p = -g$ when the wave is right-handed circularly polarized (RHC). Using the redefinition of g and assuming monochromatic waves with a harmonic time-dependence $e^{-i\omega t}$, the chiral constitutive relations or also called *Condon relations* (CR) for a Pasteur medium get

$$\boxed{\begin{aligned}\vec{D} &= \varepsilon\vec{E} + i\frac{\kappa_p}{c}\vec{H},\\ \vec{B} &= \mu\vec{H} - i\frac{\kappa_p}{c}\vec{E},\end{aligned}} \tag{10.5}$$

where $\kappa_p \equiv \omega g_p$ and it becomes a dimensionless chiral parameter. It satisfies the same property of g_p, that is $\kappa_p = \kappa$ if the wave is LHC and $\kappa_p = -\kappa$ if the wave is RHC. Typical values of κ_p are between $10^{-5} - 10^{-3}$.

10.1.1 Post relations

Another set of constitutive relations has been deduced by E. J. Post, in 1962, making an explicit treatment of general covariance in electromagnetism [131]. The same set of equations was also obtained by Jaggard *et al.* [85], in 1978, considering the scattering of electromagnetic waves from a metallic single-turn helices. The Post and Jaggard relations are

$$\boxed{\begin{aligned} &\vec{D} = \varepsilon\vec{E} + i\xi_p\vec{B}, \\ &\vec{B} = \mu\left(\vec{H} - i\xi_p\vec{E}\right), \end{aligned}} \tag{10.6}$$

where ξ_p is a pseudoscalar and it has the dimension of an admittance ($\sqrt{\frac{\mu}{\epsilon}}$), the inverse of the impedance. In particular, from the constitutive relation for $\vec{B}$ it follows that $\xi_p = \kappa_p/c\mu$ with units $[\xi_p] = \sqrt{\mu_0\varepsilon_0}/\mu$. One more difference between the Post relations and the Condon relations is related to the dielectric constant. In fact,

$$\varepsilon_{Post} = \varepsilon\left(1 - \frac{\mu}{\varepsilon}\xi_p^2\right). \tag{10.7}$$

Indeed, the Condon and the Post relations are the same at first order in the chiral parameter but they are different at second order because they originate from distinct microscopic models.
From here to the end of the manuscript, Condon relations are chosen to describe the chirality of the medium.

10.2 Derivation of the Condon relations

10.2.1 Perturbed wave function

The Condon relations are derived by studying the interactions between the electric and magnetic dipoles in a molecular system induced by a classical electromagnetic field [29, 41].

In developing the radiation theory, the vector field $\vec{A}(\vec{r},t)$ is regarded as constant over the molecular dimension (dipole approximation). The corresponding Hamiltonian is

$$\hat{\mathrm{H}} = \frac{1}{2m}\|\vec{p} - q\vec{A}\|^2 \approx \hat{\mathrm{H}} + \hat{\mathrm{V}} = \frac{1}{m}\left(\frac{\|\vec{p}\|^2}{2} - q\vec{A}\cdot\vec{p}\right), \tag{10.8}$$

where the term proportional to $\|\vec{A}\|^2$ is neglected and the vector field $\vec{A}$ is written in Coulomb gauge ($\nabla \cdot \vec{A} = 0$).
For the discussion of optical activity this approximation is not sufficient and $\vec{A}$ has to be Taylor expanded around the origin of the coordinate systems fixed in the molecule:

$$\vec{A}(\vec{r},t) \approx \vec{A}(\vec{0},t) + \vec{x}\frac{\partial}{\partial\vec{x}}\vec{A}(\vec{r},t)\big|_{\vec{r}=\vec{0}} + \text{higher order terms}, \tag{10.9}$$

By replacing the Taylor expansion of $\vec{A}(\vec{r},t)$ in the right-hand side of eq. (10.8), the perturbation Hamiltonian $\hat{\mathrm{V}}$ may be written as

$$\hat{\mathrm{V}} = -q\frac{1}{m}\left[\vec{A}\cdot\vec{p} + \frac{1}{2}\left(\nabla\wedge\vec{A}\right)\cdot(\vec{r}\wedge\vec{p}) + \text{quadrupole moments}\right], \tag{10.10}$$

where the first term is the electric dipole moment and the second is the magnetic dipole moment. Here the terms corresponding to the quadrupole moments are neglected. For simplicity of writing the hat on the operators is omitted.

An unperturbed molecule, in the state a, is represented by the stationary wave function $\psi_a(\vec{r},t) = \phi_a(\vec{r})\,e^{-i\frac{E_a}{\hbar}t}$. In the presence of the electromagnetic field the wave function can be written in the following form

$$\psi(\vec{r},t) = \psi_a(\vec{r},t) + \sum_b c_b(t)\psi_b(\vec{r},t)\,, \text{ with } \frac{\partial c_b(t)}{\partial t} = -\frac{i}{\hbar}\left\langle\psi_b^*(\vec{r},t)\right| \hat{V} \left|\psi_a(\vec{r},t)\right\rangle, \tag{10.11}$$

where the perturbation $\hat{V}$ is reported in eq. (10.10).

The coefficents $c_b\left(t\right)$ are found inserting eq. (10.10) in the expression of $\frac{\partial c_b(t)}{\partial t}$, finding

$$\frac{\partial c_b\left(t\right)}{\partial t} = \frac{i}{2\hbar}\left[i\Omega_{ba}\left\langle b\right|\vec{\mu}\left|a\right\rangle \cdot \vec{A}_0 + \left\langle b\right|\vec{m}\left|a\right\rangle \cdot \left(\nabla \wedge \vec{A}_0\right)\right] e^{i\Omega_{ba}t}\left(e^{i\omega t} + e^{-i\omega t}\right), \tag{10.12}$$

where $\Omega_{ba} \equiv \left(E_b - E_a\right)/\hbar$, $\left\langle b\right|\vec{\mu}\left|a\right\rangle \equiv \left\langle \phi_b^\star\left(\vec{r}\right)\right| q\sum_j \vec{r}_j \left|\phi_a\left(\vec{r}\right)\right\rangle$ and $\left\langle b\right|\vec{m}\left|a\right\rangle \equiv \left\langle \phi_b^\star\left(\vec{r}\right)\right| \sum_j \frac{q}{2m_j}\left(\vec{r}_j \wedge \vec{p}_j\right)\left|\phi_a\left(\vec{r}\right)\right\rangle$. It has been introduced the time dependence of $\vec{A}$ as $\vec{A} = (1/2)\vec{A}_0\left[\exp\left(i\epsilon t/\hbar\right) + \exp\left(-i\epsilon t/\hbar\right)\right]$ with $\epsilon = \hbar\omega$ the energy of the electromagnetic field which is perturbing the molecule.

Integrating with respect to time eq. (10.12), the coefficients get

$$c_b\left(t\right) = \frac{1}{2\hbar}\left[i\Omega_{ba}\left\langle b\right|\vec{\mu}\left|a\right\rangle \cdot \vec{A} + \left\langle b\right|\vec{m}\left|a\right\rangle \cdot \left(\nabla \wedge \vec{A}\right)\right] \cdot \left[\frac{e^{i(\Omega_{ba}+\omega)t}}{\Omega_{ba}+\omega} + \frac{e^{i(\Omega_{ba}-\omega)t}}{\Omega_{ba}-\omega}\right], \tag{10.13}$$

10.2.2 Induced microscopic moments

The electric dipole moment associated with the transition between two states a and b is defined as

$$\begin{aligned} \vec{\mu}_{ab} &= \left\langle \psi_a^\star\left(\vec{r},t\right)\right| q\vec{r}\left|\psi_b\left(\vec{r},t\right)\right\rangle + \left\langle \psi_b^\star\left(\vec{r},t\right)\right| q\vec{r}\left|\psi_a\left(\vec{r},t\right)\right\rangle = \\ &= \left\langle a\right| q\vec{r}\left|b\right\rangle\left[e^{i\Omega_{ab}t} + e^{-i\Omega_{ab}t}\right] = 2\left\langle a\right| q\vec{r}\left|b\right\rangle \cos\left(\Omega_{ab}t\right) = \\ &= 2Re\{\left\langle \psi_a^\star\left(\vec{r},t\right)\right| q\vec{r}\left|\psi_b\left(\vec{r},t\right)\right\rangle\}, \end{aligned} \tag{10.14}$$

where it has been used the stationary wave function $\psi_a\left(\vec{r},t\right) = \phi_a\left(\vec{r}\right)e^{-i\frac{E_a}{\hbar}t}$ and $\Omega_{ab} \equiv \left(E_a - E_b\right)/\hbar$.

It follows that an electric dipole moment associated with a given wave function ψ is

$$\vec{\mu} = Re\{\left\langle \psi^\star\left(\vec{r},t\right)\right| q\vec{r}\left|\psi\left(\vec{r},t\right)\right\rangle\}. \tag{10.15}$$

Now let's consider the dipole moment in presence of an electromagnetic field. The perturbed wave function is given by eq. (10.11). Thus, combining eq. (10.11) and (10.15), the electric dipole may be written as

$$\vec{\mu}_a = Re\{\left\langle a\right|\vec{\mu}\left|a\right\rangle + 2\sum_b c_b\left(t\right)\left\langle a\right|\vec{\mu}\left|b\right\rangle e^{-i\Omega_{ba}t}\}, \tag{10.16}$$

where terms of order $\mathcal{O}(c^2)$ have been neglected. The resulting first term represents the permanent dipole of the unperturbed molecule; the second one represents the induced dipole moment by the interaction with the field.

The Condon relations are derived taking the induced electric and magnetic dipole moments:

$$\boxed{\begin{aligned} \vec{\mu}_a^i &= 2Re\{\sum_b c_b\left(t\right)\left\langle a\right|\vec{\mu}\left|b\right\rangle e^{-i\Omega_{ba}t}\}, \\ \vec{m}_a^i &= 2Re\{\sum_b c_b\left(t\right)\left\langle a\right|\vec{m}\left|b\right\rangle e^{-i\Omega_{ba}t}\}. \end{aligned}} \tag{10.17}$$

The calculation can be performed only for the induced electric dipole $\vec{\mu}_a^i$ (the superscript i means induced), then subtituting $\left\langle a\right|\vec{\mu}\left|b\right\rangle$ for $\left\langle a\right|\vec{m}\left|b\right\rangle$ the result for the induced magnetic dipole is obtained.

The first step consists in inserting the relation (10.13) in the expression of the induced electric dipole moment given by eq. (10.17). It reads

$$\begin{aligned} \vec{\mu}_a^i = \frac{1}{\hbar}Re\{&\sum_b \left\langle a\right|\mu_i\left|b\right\rangle\left\langle b\right|\mu_j\left|a\right\rangle\left[\frac{i\Omega_{ba}^2}{\Omega_{ba}^2-\omega^2}A_{0,j}\left(e^{i\omega t} + e^{-i\omega t}\right) - \frac{i\Omega_{ba}\omega}{\Omega_{ba}^2-\omega^2}A_{0,j}\left(e^{i\omega t} - e^{-i\omega t}\right)\right] + \\ &+\sum_b \left\langle a\right|\mu_i\left|b\right\rangle\left\langle b\right|m_j\left|a\right\rangle\left[\frac{\Omega_{ba}}{\Omega_{ba}^2-\omega^2}\left(\nabla \wedge \vec{A}_0\right)_j\left(e^{i\omega t} + e^{-i\omega t}\right) - \right. \\ &\left. + \frac{\omega}{\Omega_{ba}^2-\omega^2}\left(\nabla \wedge \vec{A}_0\right)_j\left(e^{i\omega t} - e^{-i\omega t}\right)\right]\}, \end{aligned} \tag{10.18}$$

where the vector arrow on the operators is replaced by the index notation.

The field $\vec{A}$ is related to the other fields $\vec{E}$ and $\vec{H}$, using $\vec{E} = -\frac{\partial \vec{A}}{\partial t}$ and $\vec{H} = \nabla \wedge \vec{A}$ (for a free field in Coulomb gauge), thereby (10.18) reduces to

$$\begin{aligned}\vec{\mu}^i_a = \frac{2}{\hbar} Re\{ \sum_b \langle a| \mu_i |b\rangle \langle b| \mu_j |a\rangle \left[\frac{i\Omega^2_{ba}}{\left(\Omega^2_{ba} - \omega^2\right)\omega^2} \frac{\partial E_{0,j}}{\partial t} + \frac{\Omega_{ba}}{\Omega^2_{ba} - \omega^2} E_{0,j} \right] + \\ + \sum_b \langle a| \mu_i |b\rangle \langle b| m_j |a\rangle \left[\frac{\Omega_{ba}}{\Omega^2_{ba} - \omega^2} H_{0,j} + \frac{i}{\Omega^2_{ba} - \omega^2} \frac{\partial H_{0,j}}{\partial t} \right] \},\end{aligned} \tag{10.19}$$

with the usage of the following relations

$$\begin{aligned} E_{0,j} &= -\frac{i\omega}{2} A_{0,j} \left(e^{i\omega t} - e^{-i\omega t}\right), \\ \frac{\partial E_{0,j}}{\partial t} &= \frac{\omega^2}{2} A_{0,j} \left(e^{i\omega t} + e^{-i\omega t}\right), \\ H_{0,j} &= \frac{1}{2} \left(\nabla \wedge \vec{A}_0\right)_j \left(e^{i\omega t} + e^{-i\omega t}\right), \\ \frac{\partial H_{0,j}}{\partial t} &= \frac{i\omega}{2} \left(\nabla \wedge \vec{A}_0\right)_j \left(e^{i\omega t} - e^{-i\omega t}\right). \end{aligned} \tag{10.20}$$

An analogous calculation can be performed for the induced magnetic dipole moment, with the mentioned substitutions, to get

$$\begin{aligned}\vec{m}^i_a = \frac{2}{\hbar} Re\{ \sum_b \langle a| m_i |b\rangle \langle b| \mu_j |a\rangle \left[\frac{i\Omega^2_{ba}}{\left(\Omega^2_{ba} - \omega^2\right)\omega^2} \frac{\partial E_{0,j}}{\partial t} + \frac{\Omega_{ba}}{\Omega^2_{ba} - \omega^2} E_{0,j} \right] + \\ + \sum_b \langle a| m_i |b\rangle \langle b| m_j |a\rangle \left[\frac{\Omega_{ba}}{\Omega^2_{ba} - \omega^2} H_{0,j} + \frac{i}{\Omega^2_{ba} - \omega^2} \frac{\partial H_{0,j}}{\partial t} \right] \}.\end{aligned} \tag{10.21}$$

In order to obtain the constitutive relations, it is necessary to average the vector quantities over all orientations of the system with respect to the fields, assuming all orientations to be equally probable. The result of the orientation average is

$$\begin{aligned}\langle \vec{\mu}^i_a \rangle &= \frac{2}{3\hbar} Re\{ \sum_b |\langle a| \vec{\mu} |b\rangle|^2 \left[\frac{i\Omega^2_{ba}}{\left(\Omega^2_{ba} - \omega^2\right)\omega^2} \frac{\partial \vec{E}_0}{\partial t} + \frac{\Omega_{ba}}{\Omega^2_{ba} - \omega^2} \vec{E}_0 \right] + \\ &\quad + \sum_b \langle a| \vec{\mu} |b\rangle \langle b| \vec{m} |a\rangle \left[\frac{\Omega_{ba}}{\Omega^2_{ba} - \omega^2} \vec{H}_0 + \frac{i}{\Omega^2_{ba} - \omega^2} \frac{\partial \vec{H}_0}{\partial t} \right] \}, \\ \langle \vec{m}^i_a \rangle &= \frac{2}{3\hbar} Re\{ \sum_b \langle a| \vec{m} |b\rangle \langle b| \vec{\mu} |a\rangle \left[\frac{i\Omega^2_{ba}}{\left(\Omega^2_{ba} - \omega^2\right)\omega^2} \frac{\partial \vec{E}_0}{\partial t} + \frac{\Omega_{ba}}{\Omega^2_{ba} - \omega^2} \vec{E}_0 \right] + \\ &\quad + \sum_b |\langle a| \vec{m} |b\rangle|^2 \left[\frac{\Omega_{ba}}{\Omega^2_{ba} - \omega^2} \vec{H}_0 + \frac{i}{\Omega^2_{ba} - \omega^2} \frac{\partial \vec{H}_0}{\partial t} \right] \},\end{aligned} \tag{10.22}$$

where the average is calculated as the following one

$$\langle \langle a| \mu_i |b\rangle \langle b| \mu_j |a\rangle E_{0,j} \rangle = \frac{|\langle a| \vec{\mu} |b\rangle|^2 \vec{E}_0}{8\pi^2} \int_0^{2\pi} \int_0^{\pi} \int_0^{2\pi} \cos^2\theta \sin\theta \, d\theta \, d\varphi \, d\psi = \frac{|\langle a| \vec{\mu} |b\rangle|^2 \vec{E}_0}{3}. \tag{10.23}$$

The last step for having the complete expressions for the induced dipoles consists in taking the real part of the equations above (see eq. (10.22)). Let's start for the induced electric dipole. The first term is purely imaginary and its real part is 0. The second is real and it remains as it is. The third and the fourth are proportional to a product of matrix elements which is in general complex. Thus, for the third it has to be taken the real part and for the fourth it is sufficient to use the fact that $Re(iz) = -Im(z)$, with $z \in \mathcal{C}$.

Similiar considerations can be applied to the real part of the induced magnetic dipole, but the first term of the magnetic dipole which can be decomposed in the following form

$$\begin{aligned}
&\frac{2}{3\hbar}Re\{\sum_b \langle a|\vec{m}\,|b\rangle\,\langle b|\,\vec{\mu}\,|a\rangle \left[\frac{i\Omega_{ba}^2}{\left(\Omega_{ba}^2-\omega^2\right)\omega^2}\frac{\partial\vec{E}_0}{\partial t}\right]\} = \\
&= \frac{2}{3\hbar}Re\{\sum_b \langle a|\vec{m}\,|b\rangle\,\langle b|\,\vec{\mu}\,|a\rangle \left[\frac{i}{\omega^2}+\frac{i}{\Omega_{ba}^2-\omega^2}\right]\frac{\partial\vec{E}_0}{\partial t}\} = \\
&= \frac{2}{3\hbar}Re\{\left[\frac{i}{\omega^2}\langle a|\vec{m}\cdot\vec{\mu}\,|a\rangle + \sum_b \langle a|\vec{m}\,|b\rangle\,\langle b|\,\vec{\mu}\,|a\rangle\frac{i}{\Omega_{ba}^2-\omega^2}\right]\frac{\partial\vec{E}_0}{\partial t}\}.
\end{aligned} \tag{10.24}$$

Indeed, the real part of the first term is 0, being purely imaginary, and for the second term follows another manipulation

$$Re\{i\,\langle a|\,\vec{m}\,|b\rangle\,\langle b|\,\vec{\mu}\,|a\rangle\} = Re\{i\,[\langle a|\,\vec{\mu}\,|b\rangle\,\langle b|\,\vec{m}\,|a\rangle]^\star\} = Im\{\langle a|\,\vec{\mu}\,|b\rangle\,\langle b|\,\vec{m}\,|a\rangle\}, \tag{10.25}$$

where the first equality takes into account the Hermitian character of $\vec{\mu}$ and $\vec{m}$.

Finally, the induced dipoles take the form:

$$\boxed{\begin{aligned}
\langle\vec{\mu}_a^i\rangle &= \alpha_a\vec{E}' + \beta_a\vec{H}' - \frac{g_a}{c}\frac{\partial\vec{H}'}{\partial t}, \\
\langle\vec{m}_a^i\rangle &= \chi_a\vec{H}' + \beta_a\vec{E}' + \frac{g_a}{c}\frac{\partial\vec{E}'}{\partial t},
\end{aligned}} \tag{10.26}$$

with

$$\begin{aligned}
\alpha_a &= \frac{2}{3\hbar}\sum_b\frac{\Omega_{ba}}{\Omega_{ba}^2-\omega^2}|\langle a|\,\vec{\mu}\,|b\rangle|^2, \\
\chi_a &= \frac{2}{3\hbar}\sum_b\frac{\Omega_{ba}}{\Omega_{ba}^2-\omega^2}|\langle a|\,\vec{m}\,|b\rangle|^2, \\
\beta_a &= \frac{2}{3\hbar}\sum_b\frac{\Omega_{ba}}{\Omega_{ba}^2-\omega^2}Re\{\langle a|\,\vec{\mu}\,|b\rangle\,\langle b|\,\vec{m}\,|a\rangle\}, \\
g_a &= \frac{2}{3\hbar}\sum_b\frac{Im\{\langle a|\,\vec{\mu}\,|b\rangle\,\langle b|\,\vec{m}\,|a\rangle\}}{\Omega_{ba}^2-\omega^2}.
\end{aligned} \tag{10.27}$$

The fields are written omitting the subscript 0 and adding a superscript, such as $\vec{E}'$, to denote the fact that they are total local fields at the molecule, which may not be the same as the external applied field.

The macroscopic relations are obtained considering a chiral isotropic medium which contains N molecules per cm^3 with an associated probability to be in the state a. Thereby, the macroscopic polarization and magnetization are

$$\begin{aligned}
\vec{P} &= \alpha\vec{E} - \frac{g}{c}\frac{\partial\vec{H}}{\partial t}, \\
\vec{M} &= \chi\vec{H} + \frac{g}{c}\frac{\partial\vec{E}}{\partial t},
\end{aligned} \tag{10.28}$$

where $\alpha = \sum_a p_a\alpha_a$, $g = \sum_a p_a g_a$, $\chi = \sum_a p_a\chi_a$ and p_a is the probability that the molecule goes to the state a. The terms proportional to β_a have been dropped because their inclusion would have only a second-order effect on the optical rotatory power g_a [29].

These last equations are the same relations given by eq. (10.5) with the usage of eq. (10.3) and the definitions $\alpha \equiv \varepsilon_0\chi_e$ and $\chi \equiv \mu_0\chi_m$.

10.3 Waves propagation

Let's retake the Maxwell's equations (10.1) but in the space-frequency domain, assuming as before a harmonic time-dependence $e^{-i\omega t}$. They read

$$\begin{aligned}\nabla\wedge\vec{E}=+i\omega\vec{B},\nabla\cdot\vec{B}=0,\\ \nabla\wedge\vec{H}=\vec{J}-i\omega\vec{D},\nabla\cdot\vec{D}=\rho.\end{aligned}\tag{10.29}$$

The governing chiral Helmholtz equation, which describes the wave propagation in a chiral medium, can be derived combining the Maxwell's equations (10.29) and the CR (10.5). In the following lines the main steps of the calculation are reported (using the Condon relations).

10.3.1 Main steps to get the chiral Helmholtz equation

Let's apply the curl to the Faraday's law replacing the vector field $\vec{B}$ with $\vec{B}=\mu\vec{H}-i\frac{\kappa_p}{c}\vec{E}$. The result is

$$\nabla\wedge\nabla\wedge\vec{E}=i\omega\mu\nabla\wedge\vec{H}+\omega\frac{\kappa_p}{c}\nabla\wedge\vec{E}.\tag{10.30}$$

Then $\nabla\wedge\vec{H}$ is substituted with the Ampère-Maxwell's law (AM) and $\vec{D}$ with the other constitutive relation $\vec{D}=\varepsilon\vec{E}+i\frac{\kappa_p}{c}\vec{H}$. Thus, eq. (10.30) gets

$$\nabla\wedge\nabla\wedge\vec{E}=i\omega\mu\vec{J}+\omega^2\mu\varepsilon\vec{E}+i\omega^2\mu\frac{\kappa_p}{c}\vec{H}+\omega\frac{\kappa_p}{c}\nabla\wedge\vec{E}.\tag{10.31}$$

Now it remains to eliminate the field $\vec{H}$ applying the following manipulation,

$$\vec{H}\overset{\text{CR}}{=}\frac{\vec{B}}{\mu}+i\frac{\kappa_p}{c\mu}\vec{E}\overset{\text{AM}}{=}\frac{1}{\mu}\left(\frac{\nabla\wedge\vec{E}}{i\omega}\right)+i\frac{\kappa_p}{c\mu}\vec{E}.\tag{10.32}$$

Finally, inserting eq. (10.32) in eq. (10.31) the chiral Helmholtz equation is obtained as it follows

$$\boxed{\Box^2_\kappa\vec{E}=i\omega\mu\vec{J},}\tag{10.33}$$

where the chiral differential operator $\Box^2_\kappa$ is given by

$$\Box^2_\kappa\{\}\equiv\nabla\wedge\nabla\wedge\{\}-2\omega\frac{\kappa_p}{c}\nabla\wedge\{\}-\omega^2\left(\mu\varepsilon-\frac{\kappa_p^2}{c^2}\right)\{\}.\tag{10.34}$$

The Helmholtz equations for the other fields are:

$$\boxed{\begin{aligned}&\Box^2_\kappa\vec{H}=-\frac{\omega\kappa_p}{c}\vec{J}+\nabla\wedge\vec{J},\\ &\Box^2_\kappa\vec{D}=i\omega\left(\mu\varepsilon-\frac{\kappa_p^2}{c^2}\right)\vec{J}+\frac{i\kappa_p}{c}\nabla\wedge\vec{J},\\ &\Box^2_\kappa\vec{B}=\mu\nabla\wedge\vec{J}.\end{aligned}}\tag{10.35}$$

Equivalently, using the relation $\nabla\wedge\left(\nabla\wedge\vec{F}\right)=\nabla\left(\nabla\cdot\vec{F}\right)-\Delta\vec{F}$, where $\vec{F}$ is a generic vector field, the equation for the field $\vec{D}$ (10.35) becomes

$$\nabla\left(\nabla\cdot\vec{D}\right)-\Delta\vec{D}-2\omega\frac{\kappa_p}{c}\nabla\wedge\vec{D}-\omega^2\left(\mu\varepsilon-\frac{\kappa_p^2}{c^2}\right)\vec{D}=i\omega\left(\mu\varepsilon-\frac{\kappa_p^2}{c^2}\right)\vec{J}+\frac{i\kappa_p}{c}\nabla\wedge\vec{J}.\tag{10.36}$$

If there are not sources, namely $\vec{J}=0$ and $\rho=0$, eq. (10.36) reads

$$\Delta\vec{D}+2\omega\frac{\kappa_p}{c}\nabla\wedge\vec{D}+\omega^2\left(\mu\varepsilon-\frac{\kappa_p^2}{c^2}\right)\vec{D}=0, \tag{10.37}$$

where it has been used the solenoidal property of the vector $\vec{D}$ ($\nabla\cdot\vec{D}=0$) in the absence of electric charges.

The chiral Helmholtz equation gets the usual Helmholtz equation for the propagation in a homogeneous achiral medium when $\kappa_p\to 0$.

10.3.2 Wavevectors in a homogeneous chiral medium

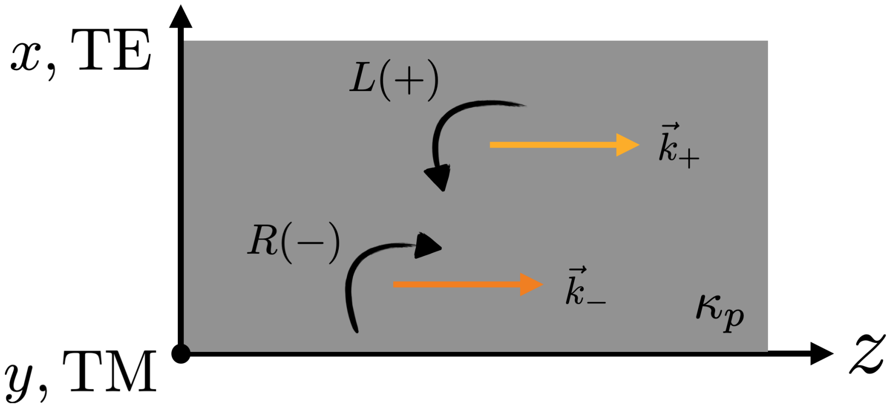

Figure 10.2: Propagating fields in a homogeneous chiral medium.

Let's consider a homogeneous chiral medium with the absence of charges and a plane wave decomposed in TE (x axis) and TM (y axis) components propagating along the z axis:

$$\vec{D}=\vec{D}_{0x}e^{ik_zz}+\vec{D}_{0y}e^{ik_zz}, \tag{10.38}$$

where $k_z=k\cos\theta$ (θ is the angle of incident) with $k=n\frac{\omega}{c}$.

Using the chosen form of plane wave, eq. (10.37) gives two scalar equations

$$\begin{aligned}&-k_z^2D_{0x}-2i\omega\frac{\kappa_p}{c}k_zD_{0y}+\omega^2\left(\mu\varepsilon-\frac{\kappa_p^2}{c^2}\right)D_{0x}=0,\\&-k_z^2D_{0y}+2i\omega\frac{\kappa_p}{c}k_zD_{0x}+\omega^2\left(\mu\varepsilon-\frac{\kappa_p^2}{c^2}\right)D_{0y}=0.\end{aligned} \tag{10.39}$$

A non-zero solution implies that the determinant of the coefficients of $\vec{D}$ has to be zero. Thus there are four possible plane waves in a homogeneous chiral medium: two propagating along the z direction and other two propagating in the opposite direction with the following wave numbers:

$$\boxed{|k_\pm|^2=\frac{\omega^2}{c^2}\left(\pm\kappa_p+c\sqrt{\mu\varepsilon}\right)^2=\frac{\omega^2}{c^2}n_\pm^2\text{ with }n_\pm=\pm\kappa_p+c\sqrt{\mu\varepsilon}.} \tag{10.40}$$

Two wave numbers $k_\pm$ correspond to two different dimensionless effective refractive indices $n_\pm$. An interesting aspect of $k_\pm$ is that the arithmetic mean of these two wave numbers is

$$\frac{k_++k_-}{2}=\omega\sqrt{\mu\varepsilon} \tag{10.41}$$

and it is not a function of κ_p, while their geometric mean,

$$\sqrt{k_+k_-} = \frac{\omega}{c}\sqrt{-k_p^2 + c^2\mu\varepsilon}, \tag{10.42}$$

is a function of κ_p but it does not depend on the handedness of light polarization.

10.3.3 Eigenfields in a homogeneous chiral medium

The eigenfields are obtained substituting the wavenumbers $k_\pm$ in eq. (10.39), and it results

$$\boxed{\vec{D}_{+R} = \vec{D}_+ e^{ik_+z},\ \vec{D}_{-R} = \vec{D}_- e^{ik_-z} \text{ with } \vec{D}_\pm = D_0\hat{e}_\pm = \frac{D_0}{\sqrt{2}}\left(\hat{e}_x \pm i\hat{e}_y\right),} \tag{10.43}$$

where the subscript R means a right-going wave propagating along the positive z direction.
It is important to notice that the propagating eigenfields are circularly polarized: $\vec{D}_{+R}$ is LHC polarized (+), and $\vec{D}_{-R}$ is RHC polarized (−) (see Figure 10.2). The left-going eigenfields are obtained subtituting $-k_\pm$ in eq. (10.39) and changing the sign of κ_p because $z \to -z$ and κ_p is a pseudoscalar. The left-going eigenfields get

$$\boxed{\vec{D}_{+L} = \vec{D}_+ e^{-ik_+z},\ \vec{D}_{-L} = \vec{D}_- e^{-ik_-z} \text{ with } \vec{D}_\pm = D_0\hat{e}_\pm = \frac{D_0}{\sqrt{2}}\left(\hat{e}_x \pm i\hat{e}_y\right),} \tag{10.44}$$

where the subscript L means a left-going wave propagating along the negative z direction.
The L propagating fields have the same polarization of the corresponding R fields. In fact, it is experimentally verified that light propagating in an isotropic chiral medium, once it is reflected, it propagates in the opposite direction and it arrives at the source with the same initial polarization (without an external magnetic field) [128, 114].

Let's restrict the discussion considering only the propagation along the positive z direction. The other eigenfields can be found using the Maxwell's equations (10.29) and the constitutive relations (10.5) to get

$$\begin{aligned}
\vec{B}_\pm &= \mp i\frac{n_\pm}{c}\vec{E}_\pm = \mu_\pm\vec{H}_\pm, \text{ with } \mu_\pm = \mu \pm \frac{\kappa_p}{c}\sqrt{\frac{\mu}{\varepsilon}},\\
\vec{H}_\pm &= \mp i\sqrt{\frac{\varepsilon}{\mu}}\vec{E}_\pm,\\
\vec{D}_\pm &= \frac{n_\pm}{c}\sqrt{\frac{\varepsilon}{\mu}}\vec{E}_\pm = \varepsilon_\pm\vec{E}_\pm, \text{ with } \varepsilon_\pm = \varepsilon \pm \frac{\kappa_p}{c}\sqrt{\frac{\varepsilon}{\mu}},
\end{aligned} \tag{10.45}$$

where $n_\pm$ are defined in eq. (10.40).

The general relations between the eigenfields propagating in a chiral medium are given by

$$\boxed{\begin{aligned}
\vec{B}_\pm &= \frac{1}{\omega}\vec{k}_\pm \wedge \vec{E}_\pm,\\
\vec{H}_\pm &= \frac{1}{\omega\mu}\vec{k}_\pm \wedge \vec{E}_\pm + i\frac{\kappa_p}{c\mu}\vec{E}_\pm,\\
\vec{D}_\pm &= \left(\varepsilon - \frac{\kappa_p^2}{c^2\mu}\right)\vec{E}_\pm + i\frac{\kappa_p}{c\,\omega\mu}\vec{k}_\pm \wedge \vec{E}_\pm.
\end{aligned}} \tag{10.46}$$

10.3.4 Spatial dependence of the propagating eigenfields

The spatial dependence of the eigenfields can be characterized supposing to have a plane wave polarized along the x-axis, at $z = 0$, propagating along the axis z. Then this wave can be written using the basis of circularly polarized states as it follows

$$\vec{D}\left(0\right) = D_0 \hat{e}_x = D_0 \frac{\hat{e}_+ + \hat{e}_-}{\sqrt{2}}, \text{ with } \hat{e}_\pm = \frac{1}{\sqrt{2}}\left(\hat{e}_x \pm i\hat{e}_y\right). \tag{10.47}$$

At position z the wave can be rewritten as

$$\vec{D}\left(z\right) = \frac{D_0}{\sqrt{2}}\left(\hat{e}_+ e^{ik_+ z} + \hat{e}_- e^{ik_- z}\right) = D_0 e^{ikz}\left[\hat{e}_x \cos\left(\frac{k\kappa_p z}{n}\right) + \hat{e}_y \sin\left(-\frac{k\kappa_p z}{n}\right)\right], \tag{10.48}$$

where the right-hand side of the equality is found using (10.40).
The field $\vec{D}\left(0\right)$ during the propagation undergoes a rotation in the left-hand direction, when the observer is looking in front of the propagating wave, by an angle $\theta = -\kappa_p kz/n = -\kappa kz/n$ ($\kappa_p = \kappa$ for a LHC polarized wave). Indeed, eq. (10.48) is cast in a more compact and general form:

$$\boxed{\vec{D}\left(z\right) = e^{ikz}\mathcal{R}\left(-\kappa kz\right)\vec{D}\left(0\right),} \tag{10.49}$$

where $\mathcal{R}\left(\theta\right) = \bar{\bar{I}}_t \cos\left(\theta\right) + \bar{\bar{J}}\sin\left(\theta\right) = e^{\bar{\bar{J}}\theta}$, with $\bar{\bar{I}}_t \equiv \hat{e}_x\hat{e}_x + \hat{e}_y\hat{e}_y$ and the $\pi/2$ rotator dyadic $\bar{\bar{J}} \equiv \hat{e}_z \wedge \bar{\bar{I}}_t$, is the rotation dyadic which rotates any two-dimensional vector by the angle θ in left-hand sense for an observer in front of the propagating wave. Or simply

$$\mathcal{R}\left(\theta\right) = \begin{pmatrix} \cos\theta & \sin\theta \\ -\sin\theta & \cos\theta \end{pmatrix}. \tag{10.50}$$

The propagating field rotates as an helix around the propagation axis z, in a lossless homogeneous chiral medium. The chirality parameter κ_p affects the polarization of the propagating field. The connection between the angle of rotation and the chiral parameter is given by $|\kappa_p| = n\theta/(kz)$. The equation (10.49) is also valid for any polarization of the field $\vec{D}\left(0\right)$.
In a lossy and bi-isotropic medium the phase of the propagating electric field is also affected and the field is attenuated [102]. Thus, in a lossy medium the two eigenfields are attenuated differently in a resulting modification of the helix.

10.3.5 Riemann-Silberstein vector approach

The wave propagation in a homogeneous chiral medium can be described by using the Riemann-Silberstein (RS) vector [10, 97], a linear combination of the electric and magnetic field:

$$\vec{F} = \vec{E} \pm i\eta\vec{H} \text{ with } \eta = \sqrt{\frac{\mu}{\varepsilon}}. \tag{10.51}$$

The RS vector was studied for the first time in 1907 by Silberstein [149] and it made its first appearance in the lectures on partial differential equations by Bernhard Riemann [168]. The RS vector is complex with a real part for the electric field and an imaginary part for the magnetic field. The use of such a complex representation can simplify the derivation of various solutions of Maxwell equations. For instance, taking the curl of the RS vector it follows

$$\boxed{\nabla \wedge \vec{F}_\pm = \pm k_\pm \vec{F}_\pm \text{ with } k_\pm = \frac{\omega}{c}\left(\pm\kappa_p + c\sqrt{\mu\varepsilon}\right),} \tag{10.52}$$

where the Maxwell's equations (10.29), with no sources, and the constitutive relations (10.5) have been used. This result implies that $\vec{F}_\pm$ are eigenstates of $\nabla\wedge$ with eigenvalues $\pm k_\pm$, a simple way with respect to the previous procedure to get eq. (10.40).

Another interesting connection is obtained substituting the eigenfields of eq. (10.45) in eq. (10.51) to get

$$\nabla \wedge \begin{pmatrix} \vec{E}_\pm \\ \vec{H}_\pm \end{pmatrix} = \pm k_\pm \begin{pmatrix} \vec{E}_\pm \\ \vec{H}_\pm \end{pmatrix} . \tag{10.53}$$

This last relation shows immediately the connections of the eigenfields with their polarizations.

10.3.6 Convention for circularly polarized light in relation to polarization and the observer

LHC or RHC

In order to describe the propagation of a circularly polarized light in a chiral medium, or the inverse propagation in the same medium, some conventions have to be established. Let's focus on a propagating LHC or RHC polarized wave to recall the relation between its polarization and rotation along the propagation, and to make the connection with a given observer. The eigenfield in a homogeneous chiral medium has the generic form

$$\vec{D}_\pm = Re\{\frac{D_0}{\sqrt{2}}\,(\hat{e}_x \pm i\hat{e}_y)\,e^{i(k_\pm z-\omega t)}\} = \frac{D_0}{\sqrt{2}}\,[\hat{e}_x\cos(k_\pm z-\omega t) \mp \hat{e}_y\sin(k_\pm z-\omega t)]\,. \tag{10.54}$$

The field along the propagation maintain the same amplitude and the vector direction rotates along the direction of $\vec{k}_\pm$. During the time evolution (considering a plane $z = 0$) the sign $+$ is connected to a counterclockwise rotation, if the observer is facing the source of the propagating field. Accordingly, the sign - stands for a clockwise rotation. The convention here is to associate a LHC (RHC) polarized wave to the sign $+$ (-), as in the optics convention. Importantly, this convention holds if the observer continue to stay in front of the light source also if the wave is reflected and it propagates in the opposite direction [152].

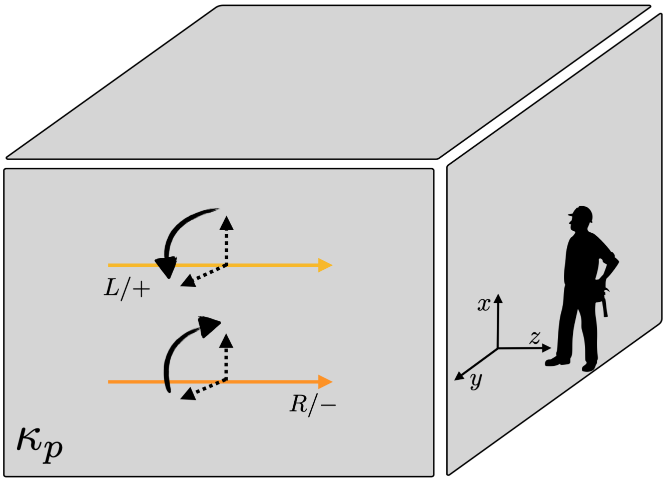

Figure 10.3: Sketch of LHC and RHC polarized waves propagating in a chiral medium.

Polarization of the reflected wave

To study the polarization of the reflected wave, it's covenient to consider a LHC (RHC) polarized wave propagating in achiral medium. The light wave encounters another achiral dielectric medium, characterized by an higher refractive index, and it is reflected back. The sign of the reflection coefficient determines the sign of the polarization for the reflected wave. At normal incidence the reflected wave has the form

$$\vec{D}_{\pm,r} = Re\{-r\frac{D_0}{\sqrt{2}}\left(\hat{e}_x \pm i\hat{e}_y\right)e^{i(-kz-\omega t)}\} = \frac{rD_0}{\sqrt{2}}\left[-\hat{e}_x\cos(-kz-\omega t) \pm \hat{e}_y\sin(-kz-\omega t)\right], \tag{10.55}$$

where r is the reflection coefficient.

The eq. (10.55) is the proof that an oncoming LHC/+ (RHC/-) polarized wave does not change its polarization upon reflection with respect to the propagating direction of $\vec{k}$. But an observer which remains in front of the light source see an opposite rotation of the polarization vectors and a polarization conversion (see Figure 10.4). If the fields are generated in the opposite direction, what is previously defined left-going propagation (see Section 10.3.3), the observer has to be put in front of the new source to distinguish the two polarizations with the same convention. From here to the end of the manuscript, the convention in which the observer is placed in front of the light source is adopted.

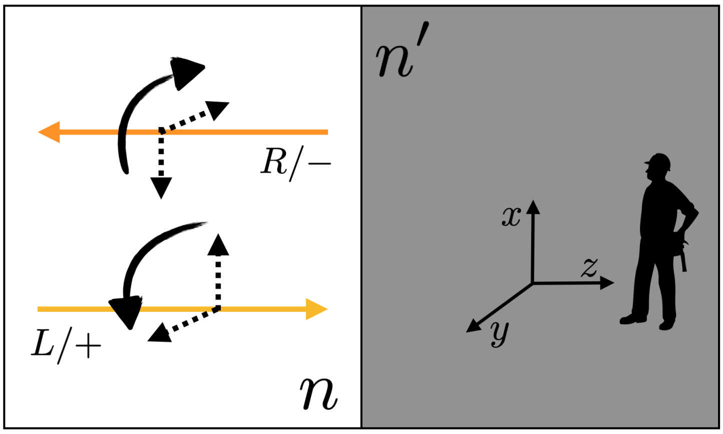

Figure 10.4: Sketch of LHC polarized wave propagating in an achiral medium and the effect of polarization conversion upon reflection.

10.4 Eigenfields at interface between two chiral media

The reflections and refractions of circularly polarized light, left-handed or right-handed, at interface between two chiral media generalize the similar familiar phenomenon between two non-chiral media of different dielectric properties. The idea is to consider two eigenfields, LHC and RHC, which are travelling in a chiral medium (characterized by κ_p, ε and μ) and they are refracted and reflected when they reach the surface of another chiral medium of different chiral and dielectric properties (κ_p', ε' and μ'). The waves are travelling at arbitrary angle along the positive direction of the z axis and also along the negative direction of the z axis. All the incident, refracted and reflected fields are given by:

$$\begin{aligned}
\underline{\text{Incident } R} \qquad & \vec{D}_{\pm R}\left(\vec{r}\right) = \vec{D}_{\pm R}e^{i\vec{k}_{\pm}\cdot\vec{r}}, \\
\underline{\text{Incident } L} \qquad & \vec{D}'_{\pm L}\left(\vec{r}\right) = \vec{D}'_{\pm L}e^{-i\vec{k}'_{\pm}\cdot\vec{r}}, \\
\underline{\text{Refracted } R} \qquad & \vec{D}'_{\pm R}\left(\vec{z}\right) = \vec{D}'_{\pm R}e^{i\vec{k}'_{\pm}\cdot\vec{r}}, \\
\underline{\text{Refracted } L} \qquad & \vec{D}_{\pm L}\left(\vec{r}\right) = \vec{D}_{\pm L}e^{-i\vec{k}_{\pm}\cdot\vec{r}}, \\
\underline{\text{Reflected } R} \qquad & \vec{D}_{\pm L}\left(\vec{r}\right) = \vec{D}_{\pm L}e^{-i\vec{k}_{\pm}\cdot\vec{r}}, \\
\underline{\text{Reflected } L} \qquad & \vec{D}'_{\pm L}\left(\vec{r}\right) = \vec{D}'_{\pm L}e^{i\vec{k}'_{\pm}\cdot\vec{r}}
\end{aligned} \tag{10.56}$$

where R and L denote a right-going and a left-going wave, respectively.

10.4.1 Kinematic properties

At the interface (at $z = 0$ for simplicity) between the two chiral media, the spatial variation of all the eigenfields must be the same, then

$$\begin{aligned} &\underline{\text{Incident } R} && \left(\vec{k}_\pm \cdot \vec{r}\right)\Big|_{z=0} = \left(-\vec{k}_\pm \cdot \vec{r}\right)\Big|_{z=0} = \left(\vec{k}'_\pm \cdot \vec{r}\right)\Big|_{z=0}, \\ &\underline{\text{Incident } L} && \left(-\vec{k}'_\pm \cdot \vec{r}\right)\Big|_{z=0} = \left(\vec{k}'_\pm \cdot \vec{r}\right)\Big|_{z=0} = \left(-\vec{k}_\pm \cdot \vec{r}\right)\Big|_{z=0}. \end{aligned} \tag{10.57}$$

These relations show that the vectors must lie in a plane and they produce the *chiro-Snell's law* [86] as it follows

$$\boxed{k_+ \sin\theta_+ = k_- \sin\theta_- = k'_+ \sin\theta'_+ = k'_- \sin\theta'_-.} \tag{10.58}$$

Figure 10.5 shows what is previously described.

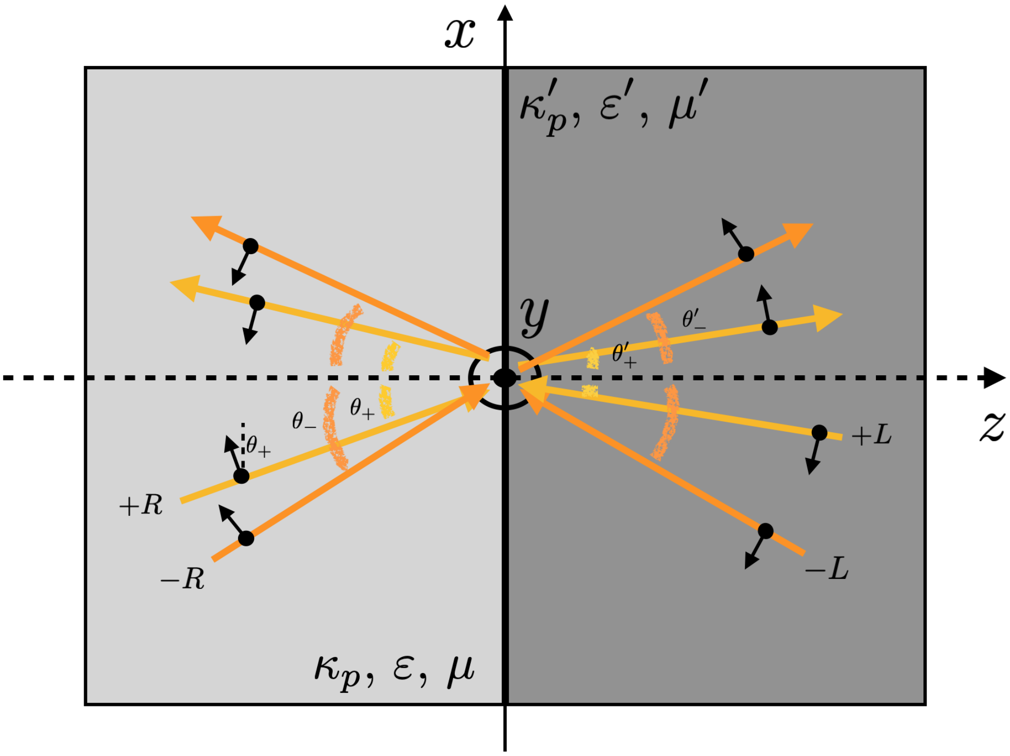

Figure 10.5: Sketch of reflections and refractions at interface between two different chiral media.

10.4.2 Dynamic properties

The dynamic properties are contained in the boundary conditions which are derived from the Maxwell's equations (10.1). The proper constitutive relations are crucial to derive the fields equations in a given medium. the Here it is considered the case with the absence of sources and the conditions get

$$\begin{aligned} &\underline{\text{Continuity of normal components of } \vec{D} \text{ and } \vec{B}} && \vec{n}\cdot\left(\vec{D}-\vec{D}'\right)=0,\ \ \vec{n}\cdot\left(\vec{B}-\vec{B}'\right)=0, \\ &\underline{\text{Continuity of tangential components of } \vec{E} \text{ and } \vec{H}} && \vec{n}\wedge\left(\vec{E}-\vec{E}'\right)=0,\ \ \vec{n}\wedge\left(\vec{H}-\vec{H}'\right)=0, \end{aligned} \tag{10.59}$$

where $\vec{n}$ is the unit vector normal to the interface between two chiral media.
The boundary conditions given by eq. (10.59) constitute the starting point to find relations of the complex amplitudes of a given eigenfield and moreover to find a general description of transfer and reflective mechanisms between the two chiral media.

Let's consider the electric eigenfields $\vec{E}_\pm$ and the relations connecting other eigenfields are given by eq. (10.46), using Condon relations (10.5). Indeed, the boundary conditions for $\vec{E}_\pm$ are derived from the usage of eqs. (10.56), (10.58) and eq. (10.59) to obtain

$$\begin{aligned}
&\underline{\text{TM for } \vec{E}} && E_{+R} - E_{-R} + E_{+L} - E_{-L} = E'_{+R} - E'_{-R} + E'_{+L} - E'_{-L}, \\
&\underline{\text{TM for } \vec{H}} && \frac{1}{\eta}\left(E_{+R} + E_{-R} + E_{+L} + E_{-L}\right) = \frac{1}{\eta'}\left(E'_{+R} + E'_{-R} + E'_{+L} + E'_{-L}\right), \\
&\underline{\text{TE for } \vec{E}} && E_{+R}\cos\theta_+ + E_{-R}\cos\theta_- - E_{+L}\cos\theta_+ - E_{-L}\cos\theta_- = \\
& && = E'_{+R}\cos\theta'_+ + E'_{-R}\cos\theta'_- - E'_{+L}\cos\theta'_+ - E'_{-L}\cos\theta'_-, \\
&\underline{\text{TE for } \vec{H}} && \frac{1}{\eta}\left(E_{+R}\cos\theta_+ - E_{-R}\cos\theta_- - E_{+L}\cos\theta_+ + E_{-L}\cos\theta_-\right) = \\
& && = \frac{1}{\eta'}\left(E'_{+R}\cos\theta'_+ - E'_{-R}\cos\theta'_- - E'_{+L}\cos\theta'_+ + E'_{-L}\cos\theta'_-\right),
\end{aligned} \tag{10.60}$$

where $\eta \equiv \sqrt{\frac{\mu}{\varepsilon}}$ and $\eta' \equiv \sqrt{\frac{\mu'}{\varepsilon'}}$. The equations (10.60) are obtained by imposing the continuity of tangential components of $\vec{E}$ and $\vec{H}$. The continuity of normal components of $\vec{D}$ and $\vec{B}$ gives redundant relations.

10.4.3 Transfer matrix

The reported boundary conditions contain all the necessary information to construct a 4×4 transfer matrix $\mathcal{T}$. All the coefficients of the matrix are found using the 4 obtained equations (10.60); the steps to get the coefficients involve calculations to express one unprimed amplitude as a function of other two primed amplitudes. One choice of the transfer matrix is the following

$$\boxed{\left(\begin{array}{c} \begin{pmatrix} E_{+R} \\ E_{-R} \end{pmatrix}_{in} \\ \begin{pmatrix} E_{+L} \\ E_{-L} \end{pmatrix}_{out} \end{array}\right) = \mathcal{T} \left(\begin{array}{c} \begin{pmatrix} E'_{+R} \\ E'_{-R} \end{pmatrix}_{out} \\ \begin{pmatrix} E'_{+L} \\ E'_{-L} \end{pmatrix}_{in} \end{array}\right) \text{ with } \mathcal{T} = \begin{pmatrix} \mathcal{M}_T & \mathcal{M}_R \\ \mathcal{M}_R & \mathcal{M}_T \end{pmatrix},} \tag{10.61}$$

where

$$\mathcal{M}_T = \begin{bmatrix} \frac{1}{4}\left(1 + \frac{\eta}{\eta'}\right)\left(1 + \frac{\cos\theta'_+}{\cos\theta_+}\right) & \frac{1}{4}\left(\frac{\eta}{\eta'} - 1\right)\left(1 - \frac{\cos\theta'_-}{\cos\theta_+}\right) \\ \frac{1}{4}\left(\frac{\eta}{\eta'} - 1\right)\left(1 - \frac{\cos\theta'_+}{\cos\theta_-}\right) & \frac{1}{4}\left(1 + \frac{\eta}{\eta'}\right)\left(1 + \frac{\cos\theta'_-}{\cos\theta_-}\right) \end{bmatrix}, \tag{10.62}$$

and

$$\mathcal{M}_R = \begin{bmatrix} \frac{1}{4}\left(1 + \frac{\eta}{\eta'}\right)\left(1 - \frac{\cos\theta'_+}{\cos\theta_+}\right) & \frac{1}{4}\left(\frac{\eta}{\eta'} - 1\right)\left(1 + \frac{\cos\theta'_-}{\cos\theta_+}\right) \\ \frac{1}{4}\left(\frac{\eta}{\eta'} - 1\right)\left(1 + \frac{\cos\theta'_+}{\cos\theta_-}\right) & \frac{1}{4}\left(1 + \frac{\eta}{\eta'}\right)\left(1 - \frac{\cos\theta'_-}{\cos\theta_-}\right) \end{bmatrix}. \tag{10.63}$$

The chiral signature is explicit using the chiro-Snell's law (see eq. (10.58)) to get $\cos\theta'_\pm = \sqrt{1 - \left(\frac{k_\pm}{k'_\pm}\right)^2 \sin^2\theta_\pm}$.

10.4.4 Reflection and transmission matrices

The transfer matrix given by eq. (10.61) represents the building block to extract transmission and reflection matrices. Considering the incident from the left, transmission and reflection can be derived setting $\left(E'_{+L}, E'_{-L}\right)_{in} = (0, 0)$. Thus, the transmission and reflection matrices are calculated as it follows

$$\begin{pmatrix} E_{+R} \\ E_{-R} \end{pmatrix}_{in} = \mathcal{M}_T \begin{pmatrix} E'_{+R} \\ E'_{-R} \end{pmatrix}_{out} \iff \begin{pmatrix} E'_{+R} \\ E'_{-R} \end{pmatrix}_{out} = \mathcal{M}_T^{-1} \begin{pmatrix} E_{+R} \\ E_{-R} \end{pmatrix}_{in}, \tag{10.64}$$

and for the reflection

$$\begin{pmatrix} E_{+L} \\ E_{-L} \end{pmatrix}_{out} = \mathcal{M}_R \begin{pmatrix} E'_{+R} \\ E'_{-R} \end{pmatrix}_{out} = \mathcal{M}_R \mathcal{M}_T^{-1} \begin{pmatrix} E_{+R} \\ E_{-R} \end{pmatrix}_{in}. \tag{10.65}$$

Finally the matrices are

$$\boxed{\begin{array}{l} \begin{pmatrix} E'_{+R} \\ E'_{-R} \end{pmatrix}_{out} = T_m \begin{pmatrix} E_{+R} \\ E_{-R} \end{pmatrix}_{in}, \text{with } T_m = \mathcal{M}_T^{-1}, \\ \begin{pmatrix} E_{+L} \\ E_{-L} \end{pmatrix}_{out} = R_m \begin{pmatrix} E_{+R} \\ E_{-R} \end{pmatrix}_{in}, \text{with } R_m = \mathcal{M}_R \mathcal{M}_T^{-1}. \end{array}} \tag{10.66}$$

10.4.5 Interfaces and homogeneous chiral slabs

The transfer matrix (see eq. (10.61)) contains all the information of transmissions and reflections at the interface between two chiral media. If a homogeneous slab of finite thickness is located between two interfaces, light undergoes multiple reflections in this slab before going out. Thus, to take into account the multiple reflection mechanism is necessary to add a so-called phase matrix:

$$\mathcal{P} = \begin{pmatrix} e^{-i\phi_+} & 0 & 0 & 0 \\ 0 & e^{-i\phi_-} & 0 & 0 \\ 0 & 0 & e^{i\phi_+} & 0 \\ 0 & 0 & 0 & e^{i\phi_-} \end{pmatrix}, \text{with } \phi_\pm = k_\pm d \cos\theta_\pm, \tag{10.67}$$

where $k_\pm = \frac{\omega}{c}\left(\pm\kappa_p + c\sqrt{\mu\varepsilon}\right)$, and d is the thickness of the homogeneous slab.

Hence, a total transfer matrix can be easily derived if there is one chiral interface, a homogeneous chiral slab and another chiral interface as it follows

$$\mathcal{T}_{tot} = \mathcal{T}_1 \mathcal{P}_{12} \mathcal{T}_2, \tag{10.68}$$

where the subscripts $_1$ and $_2$ indicate the first and the second interfaces, respectively.
It is important to note that the choice of matrix construction allows the multiplication of matrices from left to right, a convention opposite to the usual one of multiplying matrices from right to left. The advantage of this construction is that matrices multiplication follows the light propagation along the two interfaces and the slab. A generalization can be done if there are multiple chiral slabs and interfaces by simply multiplying phase and transfer matrices in the correct order.

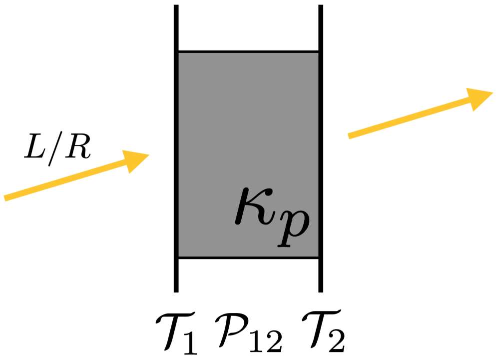

Figure 10.6: Convention of matrices multiplication that follows the light propagation.

The total transfer matrix $\mathcal{T}_{tot}$ is not in general symmetric but contains again submatrices that can be extracted to get reflection and transmission matrices for the incident from the left and from the right.

11

Chiral Fabry-Pérot Interferometer

A simple Fabry-Pérot interferometer (FPI) can be built by immersing a homogeneous chiral layer in a single host medium, as the sketch shown in Figure 11.1. The transfer and the phase matrices represent the building blocks to study how the light is transmitted out of this device.

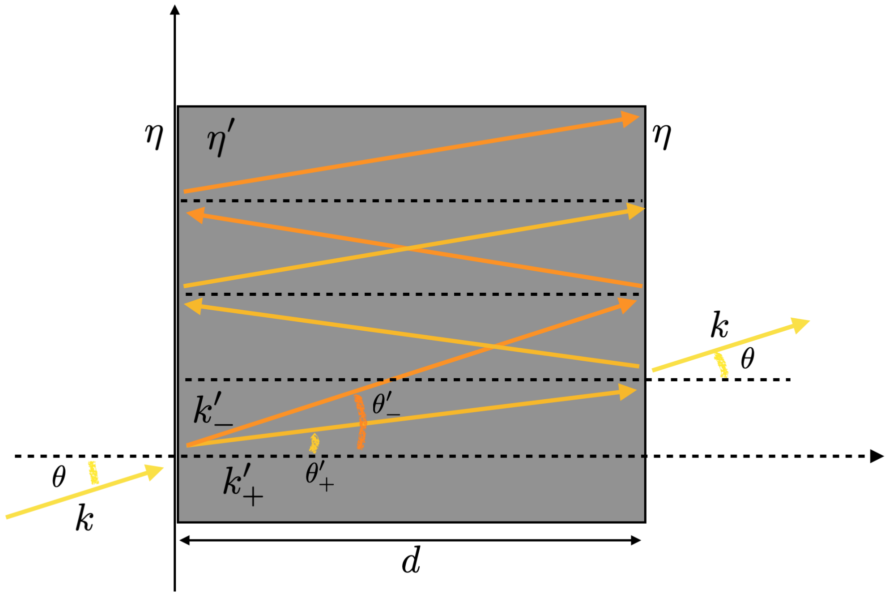

Figure 11.1: Sketch of a chiral Fabry-Pérot interferometer. Here the chiral medium is embedded in air. LHC (gold arrow inside the chiral material) and RHC (orange arrow) polarized light propagate inside the chiral medium, the rays undergo multiple reflections and they are transmitted out of the device.

Let's start writing the transfer matrix for the achiral-chiral interface, phase matrix of the chiral medium and the chiral-achiral interface:

$$\mathcal{T}_{12} = \begin{pmatrix} \frac{\bar\eta+1}{4}\left(1+\frac{\cos\theta'_+}{\cos\theta}\right) & \frac{\bar\eta-1}{4}\left(1-\frac{\cos\theta'_-}{\cos\theta}\right) & \frac{\bar\eta+1}{4}\left(1-\frac{\cos\theta'_+}{\cos\theta}\right) & \frac{\bar\eta-1}{4}\left(1+\frac{\cos\theta'_-}{\cos\theta}\right) \\ \frac{\bar\eta-1}{4}\left(1-\frac{\cos\theta'_+}{\cos\theta}\right) & \frac{\bar\eta+1}{4}\left(1+\frac{\cos\theta'_-}{\cos\theta}\right) & \frac{\bar\eta-1}{4}\left(1+\frac{\cos\theta'_+}{\cos\theta}\right) & \frac{\bar\eta+1}{4}\left(1-\frac{\cos\theta'_-}{\cos\theta}\right) \\ \frac{\bar\eta+1}{4}\left(1-\frac{\cos\theta'_+}{\cos\theta}\right) & \frac{\bar\eta-1}{4}\left(1+\frac{\cos\theta'_-}{\cos\theta}\right) & \frac{\bar\eta+1}{4}\left(1+\frac{\cos\theta'_+}{\cos\theta}\right) & \frac{\bar\eta-1}{4}\left(1-\frac{\cos\theta'_-}{\cos\theta}\right) \\ \frac{\bar\eta-1}{4}\left(1+\frac{\cos\theta'_+}{\cos\theta}\right) & \frac{\bar\eta+1}{4}\left(1-\frac{\cos\theta'_-}{\cos\theta}\right) & \frac{\bar\eta-1}{4}\left(1-\frac{\cos\theta'_+}{\cos\theta}\right) & \frac{\bar\eta+1}{4}\left(1+\frac{\cos\theta'_-}{\cos\theta}\right) \end{pmatrix}, \tag{11.1}$$

$$\mathcal{P} = \begin{pmatrix} e^{-i\phi_+} & 0 & 0 & 0 \\ 0 & e^{-i\phi_-} & 0 & 0 \\ 0 & 0 & e^{i\phi_+} & 0 \\ 0 & 0 & 0 & e^{i\phi_-} \end{pmatrix}, \tag{11.2}$$

$$\mathcal{T}_{21} = \begin{pmatrix} \frac{\bar{\eta}^{-1}+1}{4}\left(1+\frac{\cos\theta}{\cos\theta'_+}\right) & \frac{\bar{\eta}^{-1}-1}{4}\left(1-\frac{\cos\theta}{\cos\theta'_+}\right) & \frac{\bar{\eta}^{-1}+1}{4}\left(1-\frac{\cos\theta}{\cos\theta'_+}\right) & \frac{\bar{\eta}^{-1}-1}{4}\left(1+\frac{\cos\theta}{\cos\theta'_+}\right) \\ \frac{\bar{\eta}^{-1}-1}{4}\left(1-\frac{\cos\theta}{\cos\theta'_-}\right) & \frac{\bar{\eta}^{-1}+1}{4}\left(1+\frac{\cos\theta}{\cos\theta'_-}\right) & \frac{\bar{\eta}^{-1}-1}{4}\left(1+\frac{\cos\theta}{\cos\theta'_-}\right) & \frac{\bar{\eta}^{-1}+1}{4}\left(1-\frac{\cos\theta}{\cos\theta'_-}\right) \\ \frac{\bar{\eta}^{-1}+1}{4}\left(1-\frac{\cos\theta}{\cos\theta'_+}\right) & \frac{\bar{\eta}^{-1}-1}{4}\left(1+\frac{\cos\theta}{\cos\theta'_+}\right) & \frac{\bar{\eta}^{-1}+1}{4}\left(1+\frac{\cos\theta}{\cos\theta'_+}\right) & \frac{\bar{\eta}^{-1}-1}{4}\left(1-\frac{\cos\theta}{\cos\theta'_+}\right) \\ \frac{\bar{\eta}^{-1}-1}{4}\left(1+\frac{\cos\theta}{\cos\theta'_-}\right) & \frac{\bar{\eta}^{-1}+1}{4}\left(1-\frac{\cos\theta}{\cos\theta'_-}\right) & \frac{\bar{\eta}^{-1}-1}{4}\left(1-\frac{\cos\theta}{\cos\theta'_-}\right) & \frac{\bar{\eta}^{-1}+1}{4}\left(1+\frac{\cos\theta}{\cos\theta'_-}\right) \end{pmatrix}, \tag{11.3}$$

with

$$\begin{aligned} &\bar{\eta} \equiv \eta/\eta', \ \cos\theta'_\pm = \sqrt{1-\left(\frac{k}{k'_\pm}\right)^2 \sin^2\theta} \text{ or analogously } \theta'_\pm = \arcsin\left(\frac{k}{k'_\pm}\sin\theta\right) = \arcsin\left(\frac{n}{n'_\pm}\sin\theta\right), \\ &\phi_\pm = k'_\pm d\cos\theta'_\pm = \frac{2\pi n'\left(1\pm\kappa'_p\right)}{\lambda} d\cos\theta'_\pm = 2\pi n'_\pm \frac{d}{\lambda}\cos\theta'_\pm \text{ with } k = \frac{2\pi n}{\lambda}, \end{aligned} \tag{11.4}$$

where θ is the angle of incidence in the achiral medium and it varies from 0 to $\pi/2$.
Defining $\alpha \equiv d/\lambda$, the last eqs. (see (11.4)) can be rewritten as

$$\begin{aligned} &\theta'_\pm = \arcsin\left(\frac{n}{n'_\pm}\sin\theta\right) \text{ with } n'_\pm = n'\left(1\pm\kappa'_p\right), \\ &\phi_\pm = 2\pi n'_\pm \alpha \cos\theta'_\pm. \end{aligned} \tag{11.5}$$

The total transfer matrix is calculated multiplying the three matrices following the path of the incoming light, then:

$$\mathcal{T}_{FP} = \mathcal{T}_{12}\,\mathcal{P}\,\mathcal{T}_{21} = \begin{pmatrix} \mathcal{M}^l_{T,FP} & \mathcal{M}^r_{R,FP} \\ \mathcal{M}^l_{R,FP} & \mathcal{M}^r_{T,FP} \end{pmatrix}, \tag{11.6}$$

where the superscripts l, r mean incidence from the left or right, respectively.
To study the transmission from the left it remains to choose the submatrix $\mathcal{M}^l_{T,FP}$ and calculate its inverse, as it is explained in Section 10.4.4.

11.1 Normal incidence

At normal incidence, $\theta = 0$, the transmission matrix for incidence from the left has a particular simple form:

$$T_{m,FP} = \left(\mathcal{M}^l_{T,FP}\right)^{-1} = \begin{pmatrix} \frac{4}{e^{i\phi_-}(\bar{\eta}-1)(1/\bar{\eta}-1)+e^{-i\phi_+}(\bar{\eta}+1)(1/\bar{\eta}+1)} & 0 \\ 0 & \frac{4}{e^{i\phi_+}(\bar{\eta}-1)(1/\bar{\eta}-1)+e^{-i\phi_-}(\bar{\eta}+1)(1/\bar{\eta}+1)} \end{pmatrix}, \tag{11.7}$$

where $\phi_\pm = \frac{2\pi n'\left(1\pm\kappa'_p\right)}{\lambda} d$ and $\bar{\eta} \equiv \eta/\eta'$.

The non-vanishing matrix coefficients are the copolarized transmission coefficients t_{++} (the upper diagonal coefficient) and t_{--} (the lower diagonal coefficient), meaning that at normal incidence the polarization does not change in transmission. The matrices are written in the circular basis, that is an incoming ray of light LHC (+) polarized goes into the chiral medium, it propagates and at each internal reflection changes its polarization (the conversion of polarization in reflection is seen by an observer which is placed in front of the light source, as it is explained in Section 10.3.6) (the corresponding matrix $R_{m,FP}$ has non-vanishing matrix coefficients r_{-+} and r_{+-}) to be eventually transmitted out with the same initial handedness (+). An analogous explanation is valid for light RHC polarized (-).

The modulo squared of these coefficients is useful to investigate chiral effects as the Differential Circular Transmission [97, 152] (DCT) defined by

$$\mathrm{DCT} = \frac{2\left(T_+ - T_-\right)}{T_+ + T_-} \text{ with } T_+ = |t_{++}|^2 + |t_{+-}|^2, T_- = |t_{--}|^2 + |t_{-+}|^2. \tag{11.8}$$

This quantity, also called dissymetry factor, basically represents the manifestation of chiral asymmetry in the transmitted wave. At normal incidence, the transmittances ($|t|^2$) for a transparent chiral layer are

$$
\begin{aligned}
T_{\pm,\perp} &= \frac{8\bar{\eta}^2}{1+6\bar{\eta}^2+\bar{\eta}^4-\left(\bar{\eta}^2-1\right)^2\cos\left(\phi_+ + \phi_-\right)} = \\
&= \frac{8\bar{\eta}^2}{1+6\bar{\eta}^2+\bar{\eta}^4-\left(\bar{\eta}^2-1\right)^2\cos\left(4\pi n'\alpha\right)},
\end{aligned}
\tag{11.9}
$$

where $\alpha \equiv d/\lambda$.

Thus, the transmittances $T_{+,\perp}$ and $T_{-,\perp}$ are equal and there is no difference between an incoming ray of light LHC or RHC polarized. It follows that at normal incidence the dissymetry factor is 0. The transmittances, as a function of $\hbar\omega$[1], are shown in Figure 11.2 (the range of $\hbar\omega$ is chosen to visualize two periods of the oscillation). The media are assumed to be non-magnetic, so the ratio between the two impedances becomes

$$
\bar{\eta} \equiv \frac{\eta}{\eta'} = \frac{\sqrt{\frac{\mu_0\mu_r}{\varepsilon_0\varepsilon_r}}}{\sqrt{\frac{\mu_0\mu_r'}{\varepsilon_0\varepsilon_r'}}} = \frac{\mu_r}{n}\frac{n'}{\mu_r'} = \frac{n'}{n} \text{ if } \mu_r = \mu_r' = 1. \tag{11.10}
$$

Figure 11.2 shows the same behaviour of an a achiral Fabry-Pérot Étalon [94], in which the rays of light inside the interferometer can interfere constructively or not. The maxima are obtained (see eq. (11.9)) when

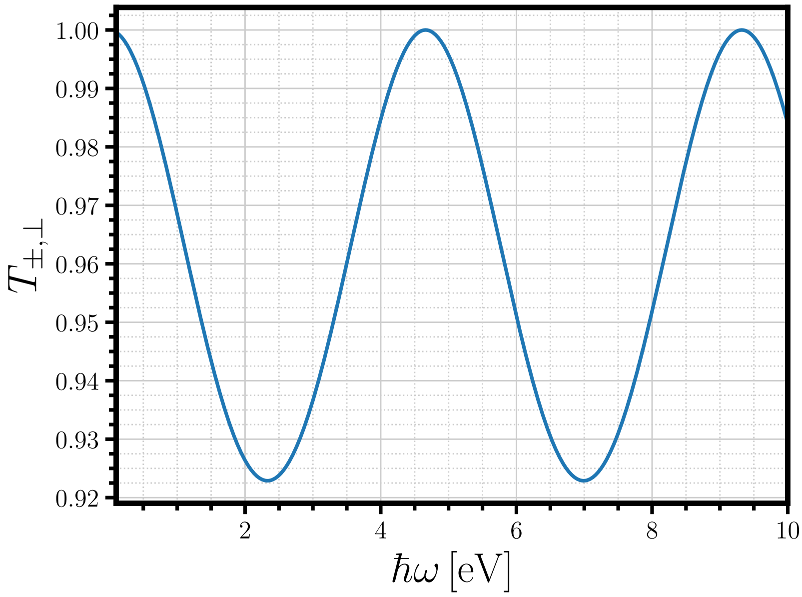

Figure 11.2: Transmittances $T_{+,\perp}$ and $T_{-,\perp}$ at normal incidence from a Fabry-Pérot interferometer, composed by air-chiral liquid-air, as a function of $\hbar\omega$. Parameters are as follows: $n = 1$, $n' = 1.33$, $\kappa_p' = 10^{-4}$, $d = 100\,\text{nm}$.

$$
4\pi n'\alpha = 2m\pi \iff \hbar\omega_m = \frac{m}{2n'd}1239.8 \text{ with } m = 0, 1, 2\ldots, \tag{11.11}
$$

then $\hbar\omega_0 = 0\,\text{eV}$, $\hbar\omega_1 \approx 4.7\,\text{eV}$, $\hbar\omega_2 \approx 9.3\,\text{eV}$ and so on. The amplitude of the transmittances oscillates between the approximated minimum value of 0.924 and 1.00.

If the media are linearly birefringent chiral asymmetries should persist [152] with a resulting DCT$\neq 0$.

---

[1] Here the conversion $\hbar\omega[\text{eV}] = 1239.8/\lambda[\text{nm}]$ is adopted.

11.2 Finite angle

11.2.1 Transmittances

At finite angle of incidence the transmission matrix has no vanishing transmission coefficients and the polarizations are mixture of both handedness. Light which is propagating into the chiral medium is not normally oriented and it may be visualized as a propagating helix with components of both handedness. The transmittances T_+ and T_- at finite angle produce a DCT$\neq$ 0, and they differ at the same order of the chiral quantity κ_p. Figure 11.3 shows the transmittances at finite angle as a function of $\hbar\omega$. T_+ and T_- for a given angle of incidence oscillate in the same manner of the transmittances at normal incidence. Differences in the position of maxima and minima are connected to the fact that the incident angle is not 0. This difference affects the transmission coefficients, which are functions of the incident angle, at the two achiral-chiral and chiral-achiral interfaces. Moreover a phase is acquired by the light rays which are reflected several times in the chiral material before going out of the chiral layer. The problem of determining the transmission from an achiral Fabry-Pérot interferometer is well-known [128] and the final result is the so-called Airy function given by

$$\tau = \frac{T_1\left(\theta, n, n'\right) T_2\left(\theta, n, n'\right)}{1 + R_1\left(\theta, n, n'\right) R_2\left(\theta, n, n'\right) - 2\sqrt{R_1\left(\theta, n, n'\right) R_2\left(\theta, n, n'\right)} \cos\psi}, \tag{11.12}$$

where $\{T, R\}_{1,2} = |\{t, r\}_{1,2}\left(\theta, n, n'\right)|^2$, $\psi = 2kd\cos\theta$ (k the wave number inside the cavity, d the thickness of the cavity and θ the incidence angle) and $\{t, r\}_{1,2}$ are the transmission coefficients of the first $_1$ and the second $_2$ interface of the Fabry-Pérot interferometer, respectively.
The Airy function τ, defined for $\kappa = 0$, reproduces very-well the oscillatory nature of the transmittances shown in Figure 11.3 (the Airy function is not displayed in Figure 11.3). The transmission and reflection coefficients for achiral-chiral and chiral-achiral interfaces [86] in case of positive or negative transmission can be derived using the matrices T_m and R_m (see eq. 10.66). The expressions, which are the Fresnel equations

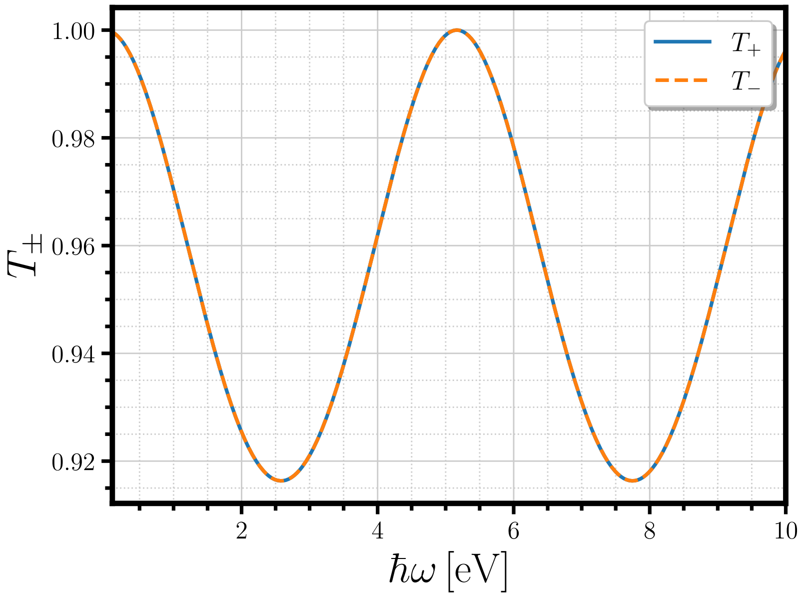

Figure 11.3: Transmittances T_+ (light-blue line) and T_- (orange dashed line) from a Fabry-Pérot interferometer, composed by air-chiral liquid-air, as a function of $\hbar\omega$ for a given value of θ. Parameters are as follows: $n = 1$, $n' = 1.33$, $\kappa_p = 10^{-4}$, $d = 100\,\text{nm}$ and $\theta = 0.61\,\text{rad} \approx 35°$.

at the interface of chiral media, at first interface are the following:

$$\begin{aligned} t_{\pm,TM} &= \frac{2\cos\theta}{\cos\theta + \bar{\eta}\cos\theta'_{\pm}}, \quad t_{\pm,TE} = \frac{2\cos\theta}{+\bar{\eta}\cos\theta + \cos\theta'_{\pm}}, \\ r_{\pm,TM} &= \frac{\cos\theta - \bar{\eta}\cos\theta'_{\pm}}{\cos\theta + \bar{\eta}\cos\theta'_{\pm}}, \quad r_{\pm,TE} = \frac{\bar{\eta}\cos\theta - \cos\theta'_{\pm}}{\bar{\eta}\cos\theta + \cos\theta'_{\pm}}. \end{aligned} \tag{11.13}$$

where TM means perpendicular polarization and TE means parallel polarization with respect to the plane of incidence. At second interface the expressions are modified sending $\theta \to \theta'_{\pm}$, $\theta'_{\pm} \to \theta$, and $\bar{\eta} \to 1/\bar{\eta}$. Consequently, all these coefficients can be used to define an approximate chiral Airy function τ_+ and τ_-. The definitions are

$$\tau_{\pm} = \frac{T_1(\theta,\theta_{\pm},n,n')\,T_2(\theta,\theta_{\pm},n,n')}{1 + R_1(\theta,\theta_{\pm},n,n')\,R_2(\theta,\theta_{\pm},n,n') - 2\sqrt{R_1(\theta,\theta_{\pm},n,n')\,R_2(\theta,\theta_{\pm},n,n')}\cos\psi_{\pm}}, \tag{11.14}$$

with

$$\begin{aligned} T_i(\theta,\theta_{\pm},n,n') &= \frac{|t_{i,\pm,TM}|^2 + |t_{i,\pm,TE}|^2}{2}, \\ R_i(\theta,\theta_{\pm},n,n') &= \frac{|r_{i,\pm,TM}|^2 + |r_{i,\pm,TE}|^2}{2}, \end{aligned} \tag{11.15}$$

where $\psi_{\pm} = 2k_{\pm}d\cos\theta'_{\pm}$ and $i = 1,2$ for the first or the second interface, respectively. The definitions for $k_{\pm}$ and $\cos\theta'_{\pm}$ are shown in eq. (11.4). The transmittances $\tau_{\pm}$ are an approximation of the light propagation in a chiral Fabry-Pérot resonator because the transmissions T_1, T_2 and the reflections R_1, R_2 are built by summing the modulo squared of the Fresnel coefficients for polarizations TM and TE. In fact, at finite angle of incidence the rays are combination of both handedness and they mix TM and TE components. By doing this, the pictorial idea is to reproduce the propagation of two independent rays: one polarized + and the other polarized - (see Figure 11.1). The transmittances $\tau_{\pm}$ are represented in Figure 11.4 as a function of the incident angle θ in the unit of $\pi/2$. The result of the matrix multiplication converges well to the result of the chiral Airy function. The curves, for a given value of λ, show an initial oscillation close to the maximum transmission of 1, a typical feature of a FPI, and two rapid changes in the neighborhood of the critical angles called Brewster angles θ_{B_1} and θ_{B_2}. At the Brewster angle the reflected wave becomes linearly polarized and for achiral layers it is defined as $\theta_B = \arctan(n_2/n_1)$ where the first medium has a refractive index n_1 and the second n_2. In the present discussion $\theta_{B_1} = \arctan(n'/n)$ and $\theta_{B_2} = \arctan(n/n')$. The corresponding chiral Brewster angles are the same at the scale of the plot and it is sufficient to plot the achiral ones. The transmissions go to 0 for $\theta = \pi/2$ because the *e.m* wave travels along the interface and it is not transmitted through the successive medium. The rapid change of the transmission near the Brewster angle is commonly observed at the interface between two different dielectric media.

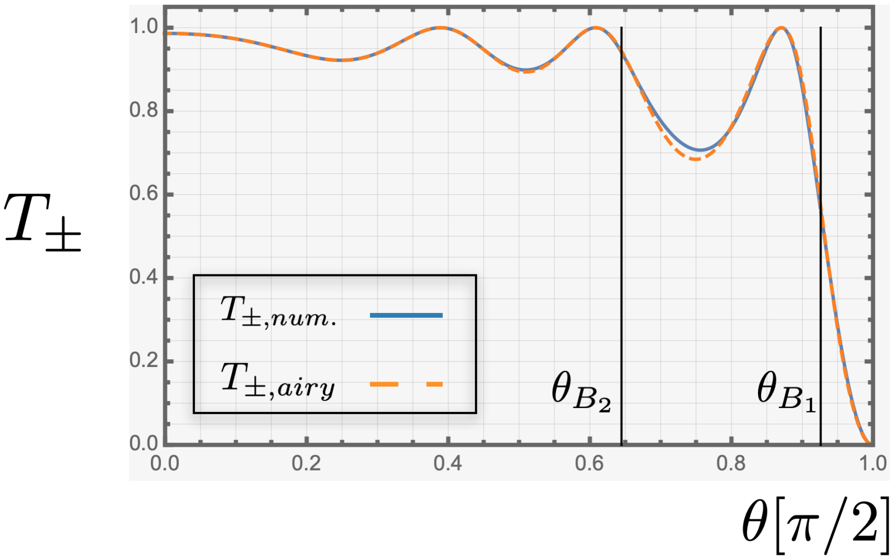

Figure 11.4: Transmittances $T_\pm$ for the numerical approach using the transfer matrices (light-blue line) and for the analytical one using the chiral Airy function (see eq. (11.14)) (orange dashed line) from a Fabry-Pérot interferometer, composed by air-chiral liquid-air, as a function of θ in the unit of $\pi/2$ for a given value of λ. Parameters are as follows: $n = 1$, $n' = 1.33$, $\kappa_p = 10^{-4}$, $d = 1.5\,\mu$m, $\lambda = 0.45\,\mu$m, $\theta_{B_1} \approx 0.93\,[\pi/2] \approx 83.7°$ and $\theta_{B_2} \approx 0.64\,[\pi/2] \approx 57.6°$.

11.2.2 Differential Circular Transmission

The Differential Circular Transmission, defined in eq. (11.8), evaluates the degree of asymmetry of a given medium under certain conditions. For instance, at normal incident the DCT is 0, that is the asymmetry is 0 and the isotropic chiral material shows no preferential handedness when the circularly polarized light is transmitted throught it. A different scenario occurs when the light creates a non-vanishing incident angle. Figure 11.5 and Figure 11.6 display DCT as a function of $\hbar\omega$ and θ in the unit of $\pi/2$, respectively. The observable DCT is an oscillatory function which changes sign (see Figure 11.5) and it grows in amplitude with $\hbar\omega$ (as the Figure 11.2, the range of $\hbar\omega$ is chosen to visualize more than one oscillation). The amplitude has the same scale of the chiral quantity κ_p, being a chiral effect. Both Figure 11.5 and Figure 11.6 show a qualitative match of the analytical DCT, $2\,(\tau_+ - \tau_-)\,/\,(\tau_+ + \tau_-)$, computed using eq. (11.14) and the numerical DCT using the transfer matrix approach as it is reported in eq. (11.6). By analogy with Figure 11.4, Figure 11.6 shows a change in the vicinity of the Brewster angles.

An interesting physical insight comes from Figure 11.7 which represents also ΔT and $\langle T\rangle$ defined as $\Delta T \equiv T_+ - T_-$ and $\langle T\rangle \equiv \frac{T_+ + T_-}{2}$, where $T_\pm$ are defined in eq. (11.8). The $\langle T\rangle$ is the achiral transmission output of the interferometer and it reaches its minimum value when the DCT is 0. This aspect may be interpreted as the relative phase of LHC (+) and RHC (-) polarized waves, for a given $\hbar\omega$, becomes equal and opposite producing a 0 DCT and this corresponds to a destructive interference in terms of wave packets.

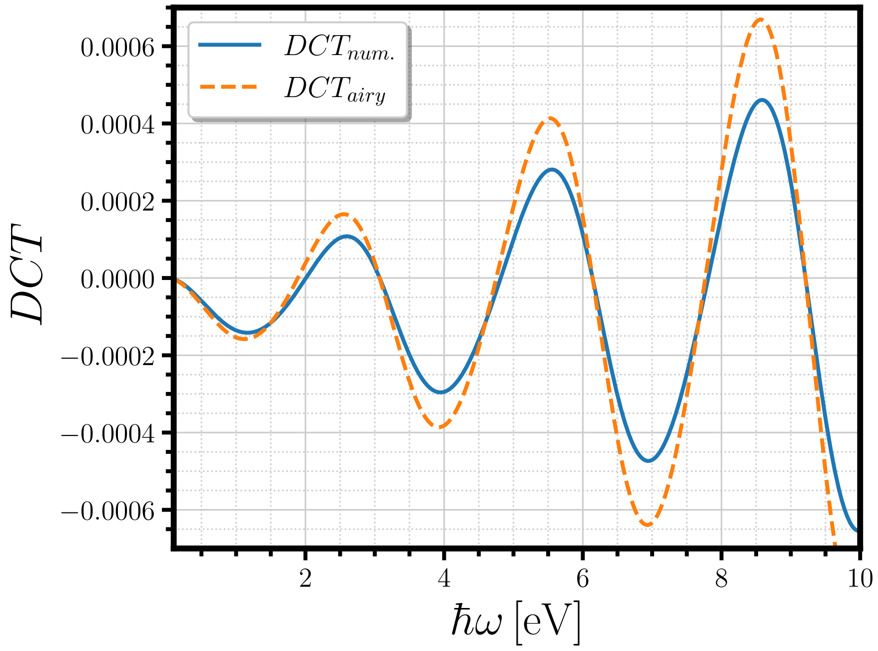

Figure 11.5: DCT for the numerical approach using the matrix multiplication (light-blue line) and for the analytical one using the chiral Airy function (see eq. (11.14)) (orange dashed line) from a Fabry-Pérot interferometer, composed by air-chiral liquid-air, as a function of α for a given value of θ. Parameters are as follows: $n = 1$, $n' = 1.33$, $\kappa_p = 10^{-4}$, $d = 200\,\text{nm}$ and $\theta = \pi/3$.

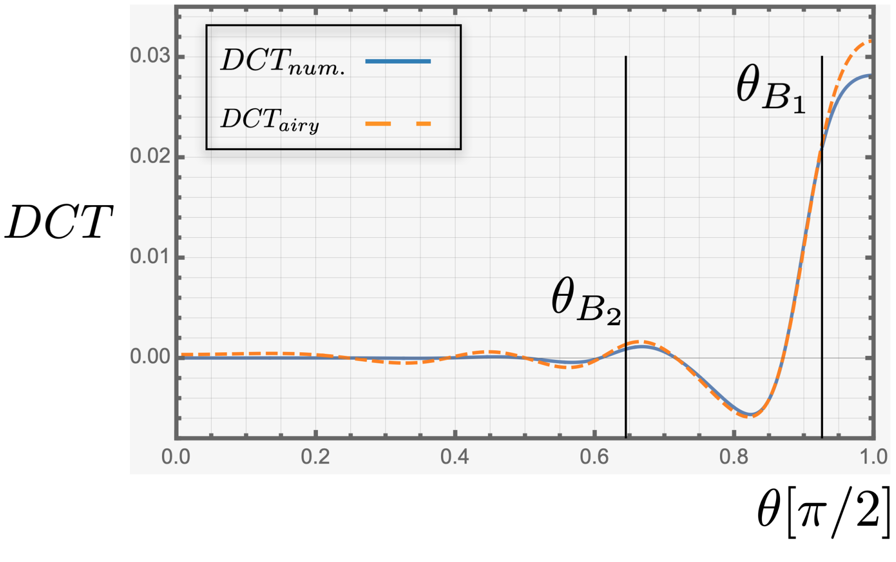

Figure 11.6: DCT for the numerical approach using the matrix multiplication (light-blue line) and for the analytical one using the chiral Airy function (see eq. (11.14)) (orange dashed line) from a Fabry-Pérot interferometer, composed by air-chiral liquid-air, as a function of θ in the unit of $\pi/2$ for different values of λ. Parameters are as follows: $n = 1$, $n' = 1.33$, $\kappa_p = 10^{-4}$, and $d = 1.5\,\mu\text{m}$, $\lambda = 0.45\,\mu\text{m}$, $\theta_{B_1} \approx 0.93\,[\pi/2] \approx 83.7°$, $\theta_{B_2} \approx 0.64\,[\pi/2] \approx 57.6°$.

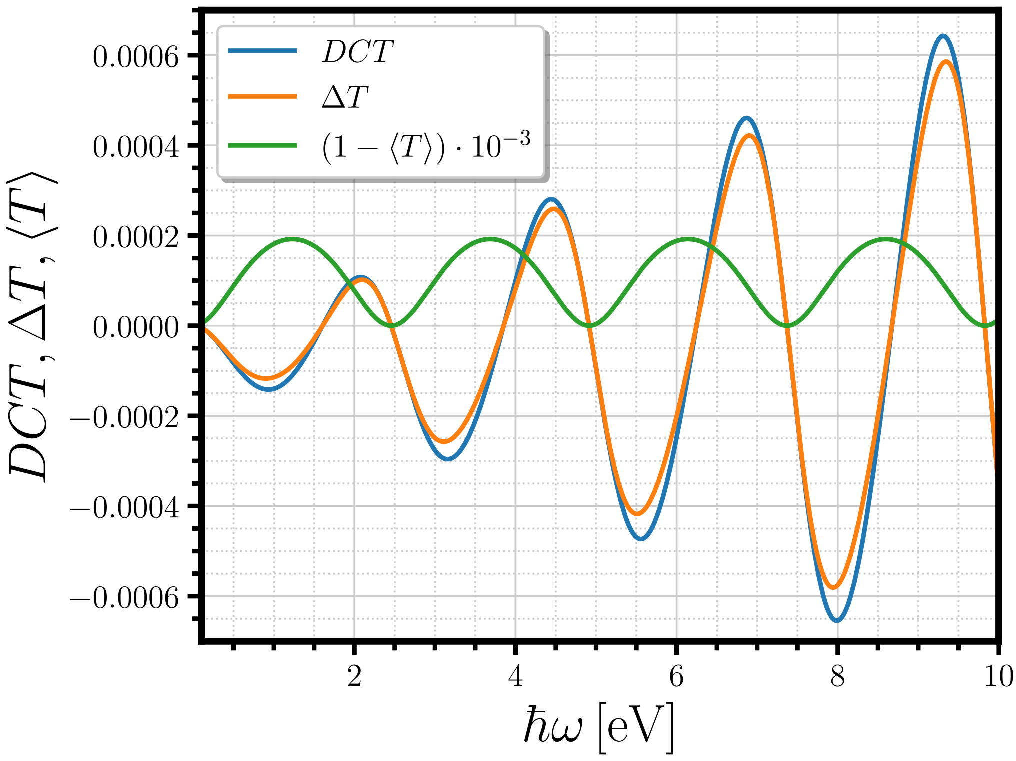

Figure 11.7: ΔT, $\langle T \rangle$ and DCT from a Fabry-Pérot interferometer, composed by air-chiral liquid-air, as a function of $\hbar\omega$ for a given value of θ. $\langle T \rangle$ is rescaled as $(1 - \langle T \rangle) \cdot 10^{-3.0}$. Parameters are as follows: $n = 1$, $n' = 1.33$, $\kappa_p = 10^{-4}$, $d = 250\,\mathrm{nm}$ and $\theta = \pi/3$.

12

Chiral Fabry-Pérot interferometer with mirrors

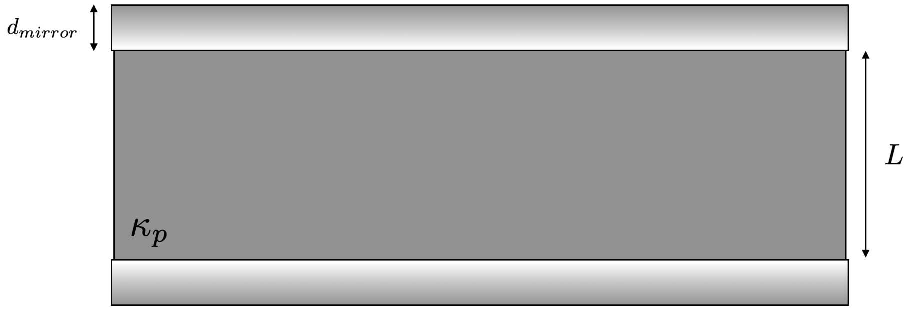

Figure 12.1: Sketch of a chiral Fabry-Pérot interferometer made by two metallic mirrors of length d_{mirror} and a chiral layer of length L.

In this Chapter, the system under investigation is composed by a thin metallic layer (called mirror) an isotropic chiral layer, and another thin metallic layer (see Figure 12.1). Before studying the interferometer, a review on the dispersive properties of dielectrics and metals is presented in the next Section.

12.1 Electromagnetic wave in a dispersive achiral medium

A simple classical description of the pertubation of an oscillating electron, in a dielectric medium, produced by an electromagnetic wave can be done assuming the following equation of motion [29, 114, 84]

$$\frac{d^2\vec{r}}{dt^2}+\gamma\frac{d\vec{r}}{dt}+\omega_0^2\vec{r}=\frac{q}{m}\vec{E}\ \text{ with } \vec{E}=\vec{E}_0e^{-i\omega t}, \tag{12.1}$$

where γ is a damping term connected to irradiation or interaction with the surrounding ions, ω_0 is the natural pulsation of the oscillator, q the charge of the electron, and m its mass.
The solution of the previous equation is

$$\vec{r}(t)=\frac{q\vec{E}_0}{m\left[\left(\omega_0^2-\omega^2\right)-i\gamma\omega\right]}e^{-i\omega t}. \tag{12.2}$$

The macroscopic polarization $\vec{P}$ as a function of ω is directly calculated from the induced electric dipole $\vec{p}=q\vec{r}\,(t)$ to get

$$\begin{aligned}\vec{P}\,(\omega)=Nq\vec{r}\,(t)&=\frac{Nq^2}{m}\frac{e^{-i\omega t}}{\left(\omega_0^2-\omega^2\right)-i\gamma\omega}\vec{E}_0=\varepsilon_0N\alpha_{1e}\,(\omega)\,\vec{E}\\ \text{with }\alpha_{1e}\,(\omega)&=\frac{q^2}{\varepsilon_0m}\frac{1}{\left(\omega_0^2-\omega^2\right)-i\gamma\omega},\end{aligned} \tag{12.3}$$

where N is the number of electrons per unit volume, $\alpha_{1e}(\omega)$ is the electronic polarizability and it is related to the electric susceptibility as $\alpha_{1e}(\omega) \equiv \varepsilon_0 \chi_{1e}(\omega)$.

The connection between the dispersive refractive index $n(\omega)$ and the polarizability $\alpha_{1e}(\omega)$ is obtained using eq. (10.3) and (12.3) as it follows

$$\varepsilon(\omega)\vec{E} = \varepsilon_0\vec{E} + \varepsilon_0 N\alpha_{1e}(\omega)\vec{E} \iff \frac{\varepsilon(\omega)}{\varepsilon_0} = n^2(\omega) = 1 + N\alpha_{1e}(\omega) \ \text{ if } \mu_r = 1. \tag{12.4}$$

The last equation on the right hand side implies that

$$\boxed{n^2(\omega) = 1 + N\alpha_{1e}(\omega) = 1 + \frac{Nq^2}{\varepsilon_0 m}\frac{1}{\left(\omega_0^2 - \omega^2\right) - i\gamma\omega}.} \tag{12.5}$$

Dispersive achiral medium in the visible range

The refractive index given by (12.5) has a more simple relation in the visible range, $2.4 \cdot 10^{15}\,\text{rad/s} \le \omega \le 5 \cdot 10^{15}\,\text{rad/s}$. In fact, the natural atomic pulsation ω_0 has a typical scale of 10^{16}rad/s and $\left(\omega_0^2 - \omega^2\right) \gg \gamma\omega$. Then the dispersive refractive index gets

$$n_{vis}^2(\omega) = 1 + \frac{Nq^2}{\varepsilon_0 m}\frac{1}{\omega_0^2 - \omega^2}. \tag{12.6}$$

In addition, the correction term is smaller than 1 and eq. (12.6) can be further simplified getting

$$n_{vis}(\omega) = \sqrt{1 + N\alpha(\omega)} \sim 1 + \frac{N\alpha(\omega)}{2} = 1 + \frac{Nq^2}{2\varepsilon_0 m}\frac{1}{\omega_0^2 - \omega^2} = 1 + \frac{Nq^2}{2\varepsilon_0 m\omega_0^2}\frac{1}{1 - (\omega/\omega_0)^2}. \tag{12.7}$$

Finally, the last approximation consists in expanding $1/\left[1 - (\omega/\omega_0)^2\right]$ as $1 + (\omega/\omega_0)^2$ because $(\omega/\omega_0)^2 \ll 1$. Consequently, the dispersive refractive index for an achiral medium in the visible range is given by

$$n_{vis}(\omega) = 1 + \frac{Nq^2}{2\varepsilon_0 m\omega_0^2} + \frac{Nq^2}{2\varepsilon_0 m}\frac{\omega^2}{\omega_0^4}. \tag{12.8}$$

Case of a conductor

In a conductor electrons move freely and they interact with the fixed ions in the material. Then the eq. (12.5) is still valid for a conductor but sending $\omega_0 \to 0$. Thus, the dispersive refractive index in a conductor is given by

$$n_{co}^2(\omega) = 1 - \frac{Nq^2}{\varepsilon_0 m}\frac{1}{\omega(\omega + i\gamma)}. \tag{12.9}$$

The damping term γ can be determined knowing that each electron has an average velocity $v_d = qEm/\tau$ for the presence of an electric field, where τ is the average time between two successive collisions of the electron with the ions. Moreover, the damping makes the equation of motion (12.1) (with $\omega_0 = 0$) stationary ($d^2\vec{r}/dt^2 = 0$) to find

$$\gamma = \frac{1}{\tau}. \tag{12.10}$$

Another quantity with an explicit dependence of the average time τ of electron collisions is the conductivity $\sigma = Nq^2\tau/m$. Using eq. (12.10) and the conductivity σ the refractive index n_{co} can be rewritten as

$$n_{co}^2(\omega) = 1 - \frac{\sigma}{\varepsilon_0}\frac{1}{\omega(\omega\tau + i)}. \tag{12.11}$$

This formula can be further simplified for cases of low frequency (antenna's waves) or high frequency (from visible light to UV light). Let's consider the case of high frequency and in particular the case of visible

light.
The wavelength spectrum of visible light has approximately a range of 0.4-0.8 μm and the product for the Ag ($N_{Ag} \approx 5.86 \cdot 10^{28}\,\mathrm{e/m^3}$) $\omega\tau \approx$ 180-90, so $\omega\tau \gg 1$. Applying the approximation $\omega\tau \gg 1$ for the visible range to eq. (12.11) it follows

$$n_{co}^2(\omega) = 1 - \frac{\omega_p^2}{\omega^2} \text{ with } \omega_p = \sqrt{\frac{Nq^2}{\varepsilon_0 m}}, \tag{12.12}$$

where ω_p is the well-known plasma pulsation.
The plasma pulsation for Ag is approximately equal to $1.36 \cdot 10^{16}$ rad/s and it is larger than the visible pulsation range of the order $2\text{-}6 \cdot 10^{15}$ rad/s. The consequence is that in the visible range $n_{co}^2 < 1$ and n_{co} is purely imaginary. Physically the light wave is absorbed in Ag. For frequencies higher than the plasma frequency (UV is one case) the metal becomes transparent.

12.2 Electromagnetic wave in a dispersive chiral medium

The inclusion of a damping term in the quantum theory of optical activity was made by Condon [29], alterating correctly the denominator of eqs. (10.27) by analogy with the classical theory of dispersion (see Section 12.1). The microscopic polarization and chiral coupling become

$$\begin{aligned} \alpha_a &= \frac{2}{3\hbar}\sum_b \frac{\Omega_{ba}}{\Omega_{ba}^2 - \omega^2 - i\Gamma_{ba}\omega}|\langle a|\,\vec{\mu}\,|b\rangle|^2, \\ g_a &= \frac{2}{3\hbar}\sum_b \frac{Im\{\langle a|\,\vec{\mu}\,|b\rangle\,\langle b|\,\vec{m}\,|a\rangle\}}{\Omega_{ba}^2 - \omega^2 - i\Gamma_{ba}\omega}, \end{aligned} \tag{12.13}$$

where a represents a given state of the molecule.

The polarization α_a can be directly linked to the dimensionless oscillator strength defined by

$$f_{ba} = \frac{2m}{3q^2\hbar}\Omega_{ba}|\langle a|\,\vec{\mu}\,|b\rangle|^2 \text{ with } \sum_b f_{ba} = \text{number of electrons in the molecule}, \tag{12.14}$$

where m is the mass of the electron and q the electric charge. Thus, the microscopic polarization in terms of the oscillator strength reads

$$\alpha_a = \frac{q^2}{m}\sum_b \frac{f_{ba}}{\Omega_{ba}^2 - \omega^2 - i\Gamma_{ba}\omega}. \tag{12.15}$$

This formula provides an interpretation on polarizability of molecules: if a molecule has an intense, low-frequency transitions in its absorption spectrum, then it is highly polarizable [4].

The macroscopic polarization can be deduced summing over the states a as it follows

$$\alpha(\omega) = \sum_a p_a \alpha_a(\omega) = \frac{Nq^2}{m}\frac{f_0}{\left(\omega_0^2 - \omega^2\right) - i\gamma\omega}, \tag{12.16}$$

where p_a is the probability of the molecule to be in the state a, N is the number of molecules per unit volume, and f_0 is the dimensionless oscillator strength ($0 \leq f_0 \leq 1$). It is assumed that $\Omega_{ba} \to \omega_0$ and $\Gamma_{ba} \to \gamma$. In this way the macroscopic polarizability α is equal to $\varepsilon_0 N\alpha_{1e}(\omega)$, reported in eq. (12.3).

Similar arguments used to get a macroscopic polarization can be applied to find a dispersive macroscopic chiral coupling $\kappa_p(\omega)$.
First of all, the term $Im\{\langle a|\,\vec{\mu}\,|b\rangle\,\langle b|\,\vec{m}\,|a\rangle\}$ is known as the rotational strength of a given absorbed line and it is generically called R_{ba} . It has the following properties

$$\begin{aligned} R_{ba} &= -R_{ab}, \\ \sum_b R_{ba} &= 0, \end{aligned} \tag{12.17}$$

where the first one follows from the interchange of a and b and the second from the fact that any diagonal matrix element of a real observable is real and therefore its imaginary part vanishes. The rotatory strength has been related to another quantity, the anisotropy factor κ_{ba} for a given line as

$$R_{ba} = \kappa_{ba} |\langle a| \vec{\mu} |b\rangle|^2 = \kappa_{ba} \frac{3q^2 \hbar f_{ba}}{2m\Omega_{ba}}, \tag{12.18}$$

where κ_{ba} is a pure number, and the second equality comes from the application of eq. (12.14). Some typical values [29] for κ_{ba} and R_{ba} on d-sec octyl alcohol in the case of strong absorption bands, for which f_{ba} is of order of unity, (for UV bands lumped at 1700 A) are 10^{-6} and 10^{-40}, respectively.
Hence, inserting the relation given by eq. (12.18) in the microscopic chiral coupling g_a and summing over the states a with the definition $\kappa_p(\omega) = \omega g_p(\omega)$, the macroscopic dispersive chiral coupling can be found as

$$\boxed{\kappa_p(\omega) = \omega \sum_a p_a g_a = \kappa_{p,0} \frac{Nq^2}{\varepsilon_0 m} \frac{\omega f_0}{\omega_0 \left[\left(\omega_0^2 - \omega^2\right) - i\gamma\omega\right]} = \kappa_{p,0} \frac{\omega_p^2 \omega f_0}{\omega_0 \left[\left(\omega_0^2 - \omega^2\right) - i\gamma\omega\right]},} \tag{12.19}$$

where $\kappa_{p,0}$ is a pure number maintaining the pseudoscalar nature, ω_p is the plasma pulsation, and it is assumed that $\kappa_{ba} \to \kappa_{p,0}$, $\Omega_{ba} \to \omega_0$, $\Gamma_{ba} \to \gamma$. The vacuum dielectric constant ε_0 makes $\kappa_p(\omega)$ dimensionless. The inclusion of $1/\varepsilon_0$ is consistent to replace the cgs units (adopted by Condon) with rationalized units (mks).

Now all the elements to study a dispersive chiral interferometers are explained. The next section contains an analytical approach to study the transmission of light rays in a Fabry-Pérot interferometer. This time the interferometer is dispersive and it is lossy.

12.3 Analytical treatment of a achiral dispersive Fabry-Pérot interferometer

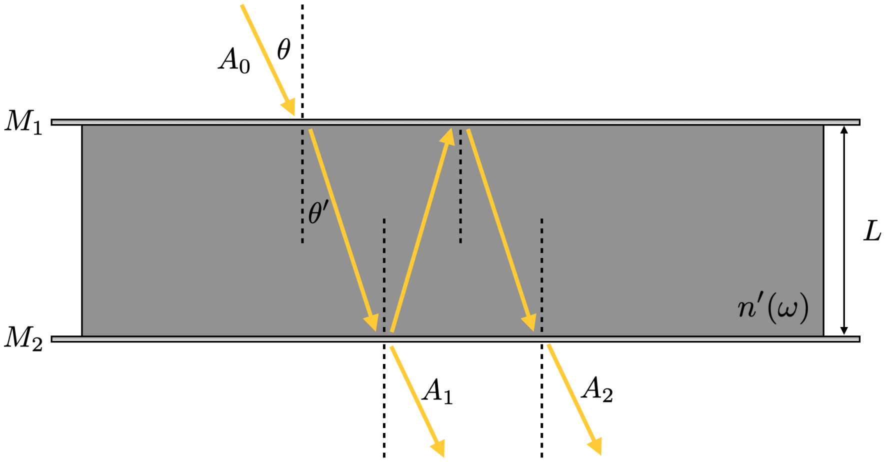

Figure 12.2: Sketch of the accumulation of transmitted amplitudes in a achiral dispersive Fabry-Pérot interferometer.

The analytical derivation of the dispersive Airy function (the Airy function without dispersion is presented in Section 11.2) consists in following the path of a given ray of light, whatever polarization is initially chosen, during its "trip" inside the Fabry-Pérot (FP) interferometer [13, 83].

Let's call A_0 the complex amplitude of the incoming ray, r the reflection coefficient of the mirrors (it is supposed that they are equal), t' the transmission coefficient at the interface of the first mirror M_1, and t the transmission coefficient at the interface of the second mirror M_2. When the light illuminates M_1 it is partially transmitted into the dielectric layer, it propagates to reach M_2 and it is partially transmitted out from M_2 (see Figure 12.2). Thus, the first complex transmitted amplitude is

$$A_1 = tt' A_0 e^{i\phi} \quad \text{with } \phi \equiv kn'(\omega) L \cos\theta', \tag{12.20}$$

where $k = 2\pi/\lambda$ is the wave number of the ray of light, $n'(\omega)$ is the dispersive refractive index of the dielectric layer, L is the length of the cavity supposing that the mirrors have no thickness, and θ' is the angle at which the incoming ray is refracted inside the dispersive dielectric layer.

The phase ϕ acquired by the light wave, along the propagation inside the dielectric, is a function of ω because the refractive index is dispersive and is complex because it has a real $n'_{re}(\omega)$ and an imaginary part $n'_{im}(\omega)$:

$$\begin{aligned} n'(\omega) &= 1 + \frac{Nq^2}{2\varepsilon_0 m} \frac{f_0}{\left(\omega_0^2 - \omega^2\right) - i\gamma\omega} = 1 + \frac{1}{2} \frac{\omega_p^2 f_0 \left(\omega_0^2 - \omega^2\right)}{\left(\omega_0^2 - \omega^2\right)^2 + (\gamma\omega)^2} + \frac{i}{2} \frac{\omega_p^2 f_0 \gamma\omega}{\left(\omega_0^2 - \omega^2\right)^2 + (\gamma\omega)^2}, \\ \text{with } n'_{re}(\omega) &= 1 + \frac{1}{2} \frac{\omega_p^2 f_0 \left(\omega_0^2 - \omega^2\right)}{\left(\omega_0^2 - \omega^2\right)^2 + (\gamma\omega)^2}, \quad n'_{im}(\omega) = \frac{1}{2} \frac{\omega_p^2 f_0 \gamma\omega}{\left(\omega_0^2 - \omega^2\right)^2 + (\gamma\omega)^2}, \end{aligned} \tag{12.21}$$

where N is number of molecules per unit volume, q is the electric charge, ε_0 is the vacuum dielectric constant, m is the mass of the electron, f_0 is the dimensionless oscillator strength for a single electronic transition ($0 \leq f_0 \leq 1$), ω_0 is the natural atomic pulsation, γ is the damping term connected to irradiation or interaction with the surrounding ions, and $\omega_p^2 \equiv Nq^2/\varepsilon_0 m$. The refractive index n' is calculated bearing in mind that its value is close to 1, so the correction term is smaller than 1 (see eqs. (12.6) and (12.7)).

Hence, it is convenient to express ϕ as $\phi = kn'_{re} L \cos\theta' + i\, kn'_{im} L \cos\theta' \equiv \beta + i\, \alpha L/2$ where α is the absorption coefficient [84]. It follows that the first transmitted amplitude out of the cavity can be rewritten as

$$A_1 = tt' A_0 e^{i\beta - \frac{\alpha L}{2}}. \tag{12.22}$$

Coming back to the propagation of the ray of light, when it is travelling towards M_2, it happens that the ray is partially reflected from M_2 and it arrives at M_1 where it is again partially reflected. Afterwards, it propagates inside the dielectric medium reaching for the second time M_2 where it is transmitted out from the interferometer. Then, the second transmitted amplitude has the form

$$A_2 = tt'(r')^2 A_0 e^{i3\beta - \frac{3}{2}\alpha L}, \tag{12.23}$$

where 2ϕ is commonly called *round-trip phase* because light has completed a round-trip through the cavity [13].

The pth transmitted amplitude is

$$A_p = tt'(r')^{2(p-1)} A_0 e^{i(2p-1)\beta - \frac{2p-1}{2}\alpha L}. \tag{12.24}$$

Now to calculate the total transmission, supposing that the cavity is sufficiently extended to send $p \to \infty$, it remains to sum all the complex amplitudes by sending $p \to \infty$ to get

$$A_t = \lim_{p\to\infty} \left(E_1 + E_2 + \cdots E_p\right) = \frac{tt' e^{i\beta - \frac{\alpha L}{2}}}{1 - (r')^2 e^{i2\beta - \alpha L}} A_0 \quad \text{if } (r')^2 < 1, \tag{12.25}$$

where the geometric series has been used.

The corresponding transmitted intensity (transmittance), represented by the dispersive Airy function [181], is

$$\boxed{\tau(\omega) = \left|\frac{A_t}{A_0}\right|^2 = \frac{T^2 e^{-\alpha L}}{\left(1 - Re^{-\alpha L}\right)^2 + 4Re^{-\alpha L}\sin^2\beta} \quad \text{with } \beta = kn'_{re} L \cos\theta',} \tag{12.26}$$

where $T \equiv tt'$, $R \equiv (r')^2$ and the identity $\cos 2\beta = 1 - 2\sin^2\beta$ has been used.

12.4 Analytical treatment of a chiral dispersive Fabry-Pérot interferometer

A similar analysis to the case of a chiral dielectric layer can be done by replacing the refractive index $n'(\omega)$ by $n'_{\pm}(\omega)$ to get

$$\begin{aligned} n'_{\pm}(\omega) = n'(\omega)\left[1 \pm \kappa'_p(\omega)\right] &= \left[n'_{re} \pm \left(n'_{re}\kappa'_{re} - n'_{im}\kappa'_{im}\right)\right](\omega) + i\left[n'_{im} \pm \left(n'_{re}\kappa'_{im} + n'_{im}\kappa'_{re}\right)\right](\omega) = \\ &= n'_{\pm,re}(\omega) + in'_{\pm,im}(\omega), \\ \text{with} \quad \kappa'_p(\omega) = \kappa_{p,0}\frac{\omega_p^2\omega f_0}{\omega_0\left[\left(\omega_0^2 - \omega^2\right) - i\gamma\omega\right]} &= \kappa'_{re}(\omega) + i\kappa'_{im}(\omega) = \\ &= \kappa_{p,0}\frac{\omega_p^2\omega f_0\left(\omega_0^2 - \omega^2\right)}{\omega_0\left[\left(\omega_0^2 - \omega^2\right)^2 + (\gamma\omega)^2\right]} + i\kappa_{p,0}\frac{\omega_p^2\omega^2 f_0\gamma}{\omega_0\left[\left(\omega_0^2 - \omega^2\right)^2 + (\gamma\omega)^2\right]}, \end{aligned} \tag{12.27}$$

where on the right hand side, of the first equality, the real and the imaginary part of the chiral refractive indeces have been collected.

Now let's focus on the construction of the chiral dispersive Airy function for the case of normal incidence. The incoming ray of light is LHC (+) or RHC (-) polarized, to be also consistent with the formalism of transfer matrices developed in the previous sections.

Normal incidence

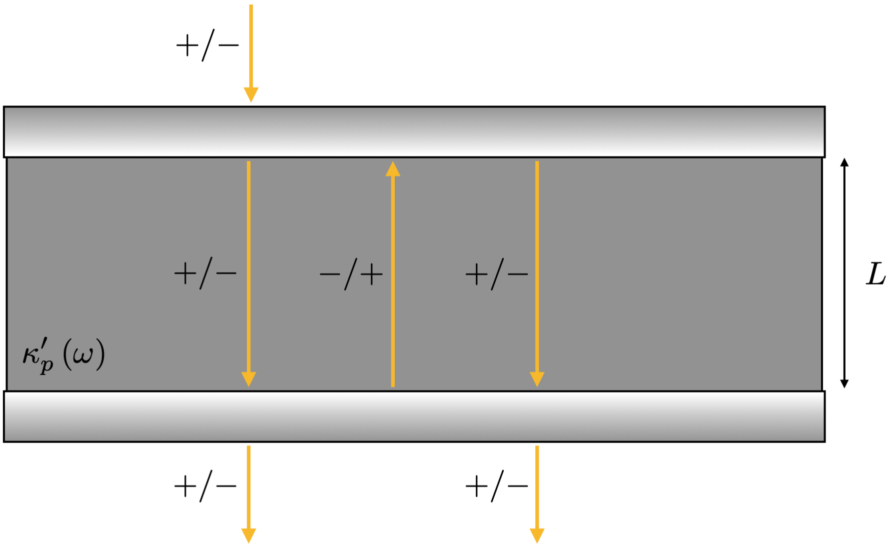

Figure 12.3: Sketch of transmission and reflection of circularly polarized light rays in a chiral dispersive Fabry-Pérot interferometer.

At normal incidence a ray of LHC or RHC polarized light is transmitted inside the finite chiral layer, as for the achiral case, and it undergoes the multiple reflection process. The main difference with respect to the achiral interferometer consists in the explicit change of polarization at each reflection, producing a consequential accumulation of phases of opposite sign. The visualization of this phenomenon becomes clear by starting to count all the transmitted complex amplitudes, in the same way of the achiral dispersive interferometer (see Figure 12.3). The first two transmitted amplitudes are

$$A_{1,\perp} = T^2A_0e^{i\phi_{+/-}}, A_{2,\perp} = T^2RA_0e^{i\left(2\phi_{+/-}+\phi_{-/+}\right)}, \tag{12.28}$$

where the sign +/- means an incoming LHC/RHC polarized ray, T and R are respectively the transmittance and the reflectance of the metallic mirror. In particular, T is $te^{i\phi_{M1}}t'$ and R is $r_{M1}r_{M2} = r_{M1}^2$ where ϕ_{M1}

is the phase accumulated along the propagation inside the metallic mirror $M1$, which is equal to the phase accumulated inside the metallic mirror $M2$, being $M1 = M2$. It follows that the total transmission is given by

$$A_{t,\perp} = \frac{T^2 e^{i\phi_{+/-}}}{1 - Re^{i(\phi_+ + \phi_-)}} A_0 \quad \text{with } \phi_\pm \equiv \beta_\pm + i\,\alpha_\pm L/2. \tag{12.29}$$

The corresponding transmittances are

$$\tau_{\pm,\perp}(\omega) = \frac{T^4 e^{-\alpha_\pm L}}{1 + R^2 e^{-(\alpha_+ + \alpha_-)L} - 2Re^{-\frac{(\alpha_+ + \alpha_-)L}{2}} \cos(\beta_+ + \beta_-)}. \tag{12.30}$$

These transmittances can be furthermore simplified evaluating explicitly $\alpha_+ + \alpha_-$ and $\beta_+ + \beta_-$ as follows

$$\begin{aligned} \alpha_+ + \alpha_- &= 2k\left(n'_{+,im}(\omega) + n'_{-,im}(\omega)\right) = 4kn'_{im}(\omega) = 2\alpha, \\ \beta_+ + \beta_- &= k\left(n'_{+,re}(\omega) + n'_{-,re}(\omega)\right) L = 2kn'_{re}(\omega) L = 2\beta, \end{aligned} \tag{12.31}$$

where $n'_{\pm,\{re,im\}}$ are defined in eq. (12.27), β and α are the real and the imaginary part of the achiral phase, respectively. Thus, the chiral transmittances at normal incidence become

$$\boxed{\tau_{\pm,\perp}(\omega) = \frac{T^4 e^{-\alpha_\pm L}}{\left(1 - Re^{-\alpha L}\right)^2 + 4Re^{-\alpha L}\sin^2\beta} \equiv \tau_\perp(\omega)\, e^{-\alpha_\pm L},} \tag{12.32}$$

where $\alpha_\pm = 2kn'_{\pm,im}(\omega)$ and $\beta = kn'_{re}(\omega)L$.

For the propagation in a transparent medium $\alpha_\pm = \alpha = 0$, then $\tau_{\pm,\perp} = \tau_\perp$ and the eq. (11.9) is recovered. The chiral transmittances in a dispersive medium show that the LHC and RHC polarized waves are transmitted with the associated absorption factor $\mathcal{A}_\pm \equiv e^{-\alpha_\pm L}$, meaning that the LHC polarized wave is attenuated by α_+ and the RHC polarized wave is attenuated by α_-. ***The eq.*** (12.32) ***is the chiral version of the famous Beer-Lambert Law for a homogeneous isotropic chiral medium.***

12.5 Transmittance

In this paragraph, the Figures 12.4, 12.5 and the Figures 12.8, 12.9 show the transmittance for two regimes: a weak coupling regime and a strong coupling regime, respectively. In the weak coupling regime the transmission has only one peak for a chosen cavity mode in the optical range. In this case the peak is at the same energy of the electronic mode (approximately 2.4 eV) of P3HT, the polymer inside the cavity. The polymer P3HT is a typical polymer which is inserted in optical cavities to study the property of the system in the strong coupling regime [33]. When the oscillator strength, defined as $(\hbar\omega_p\sqrt{f_0})_{P3HT}$, becomes of the same order or larger than the damping of the polymer γ_{P3HT} the previous peak is splitted in two peaks: one at lower energy, the Lower Polariton, and the other at higher energy, the Upper Polariton [33, 111]. The splitting takes place at resonance, when the cavity mode frequency is the same as the transition frequency of the polymer. The onset of Polaritons is well-resolved in Figure 12.10. By increasing the oscillator strength, directly related to the concentration of the molecules in the polymer, the Polaritonic splitting increases and it is proportional to $(\hbar\omega_p\sqrt{f_0})_{P3HT}/2$. The peaks are also well-resolved by varying the parallel component of the wave vector $k_\parallel$ (see Figure 12.5 and Figure 12.9). The parallel component $k_\parallel$ is defined as $k_\parallel = k\sin\theta$. The range of $k_\parallel$ (between -4 to 4) is chosen to vary the incident angle θ from $-17°$ to $17°$.

In the strong regime, Figure 12.6 and Figure 12.7 display the dispersive refractive index of P3HT and the dispersive chiral coupling, respectively. The general dispersive expressions for the refractive index and the chiral coupling are given by

$$\begin{aligned} n(\omega) &= \sqrt{\varepsilon_\infty + \frac{\omega_p^2 f_0}{\left(\omega_0^2 - \omega^2\right) - i\gamma\omega}}, \\ \kappa_p(\omega) &= \kappa_{p,0}\frac{\omega_p^2\,\omega f_0}{\omega_0\left[\left(\omega_0^2 - \omega^2\right) - i\gamma\omega\right]}, \end{aligned} \tag{12.33}$$

where ε_∞ is the background dielectric constant, $\omega_p^2 \equiv \frac{Nq^2}{\varepsilon_0 m}$, f_0 is the dimensionless oscillator strength, ω_0 is the resonant pulsation, γ is the damping factor, and $\kappa_{p,0}$ the dimensionless chiral parameter. They are essentially describing the same dispersive feature of the polymer but at different scales.

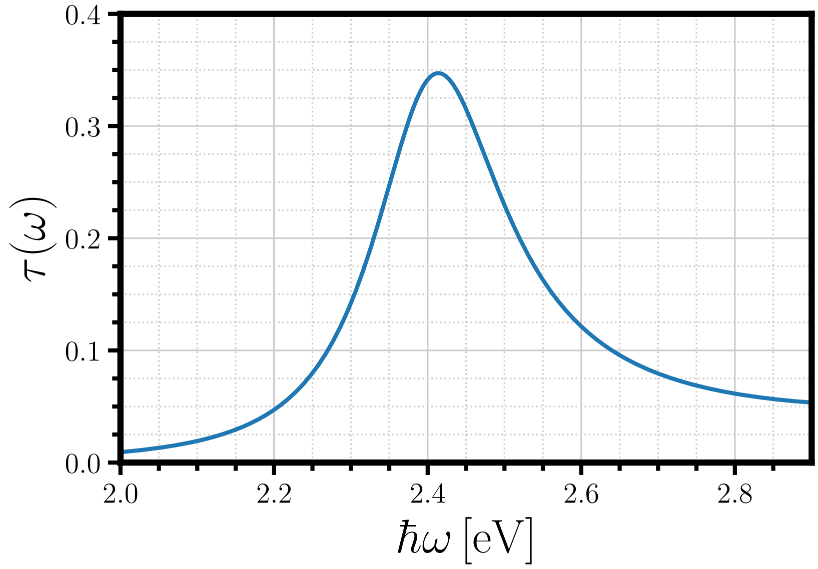

Figure 12.4: Transmittance $\tau(\omega)$ at normal incidence from a Fabry-Pérot interferometer, composed by air-P3HT-air, as a function of $\hbar\omega$ in the unit of eV. Parameters are as follows: $n = 1$, $d_{mirror} = 30\,\text{nm}$, $\varepsilon_{\infty,Ag} = 4.8$, $\hbar\omega_{p,Ag} = 9.5\,\text{eV}$, $\hbar\gamma_{Ag} = 0.17\,\text{eV}$, $L_{P3HT} = 100\,\text{nm}$, $\varepsilon_{\infty,P3HT} = 2.89$, $(\hbar^2\omega_p^2 f_0)_{P3HT} = 0.01\,\text{eV}^2$, $\hbar\omega_{0,P3HT} = 2.407\,\text{eV}$, $\hbar\gamma_{P3HT} = 0.28\,\text{eV}$ and $\theta = 0$.

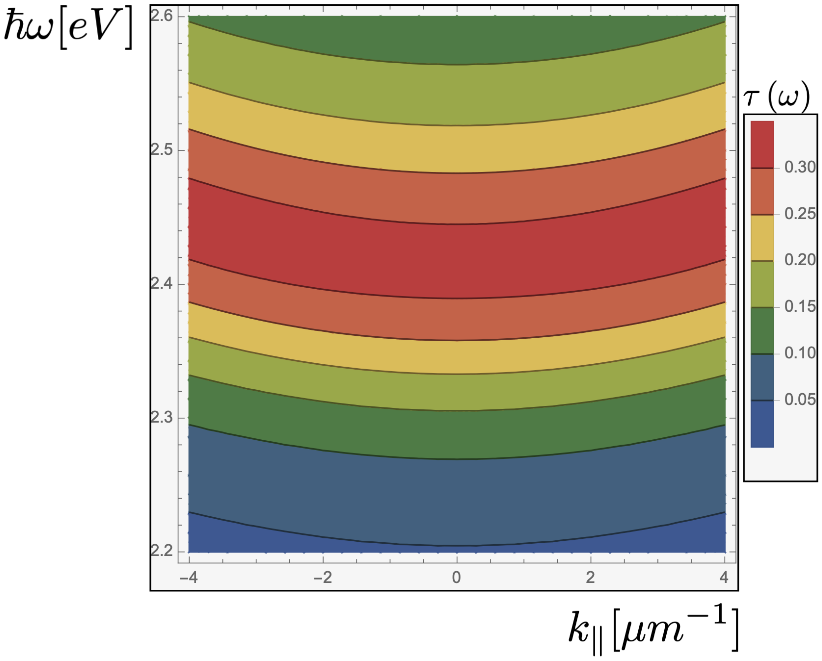

Figure 12.5: Transmittance $\tau(\omega)$ from a Fabry-Pérot interferometer, composed by air-P3HT-air, as a function of $k_{||}$ in the unit of μm^{-1} and as a function of $\hbar\omega$ in the unit of eV. Parameters are those of Figure 12.4, except that θ is varied from −17° to 17°.

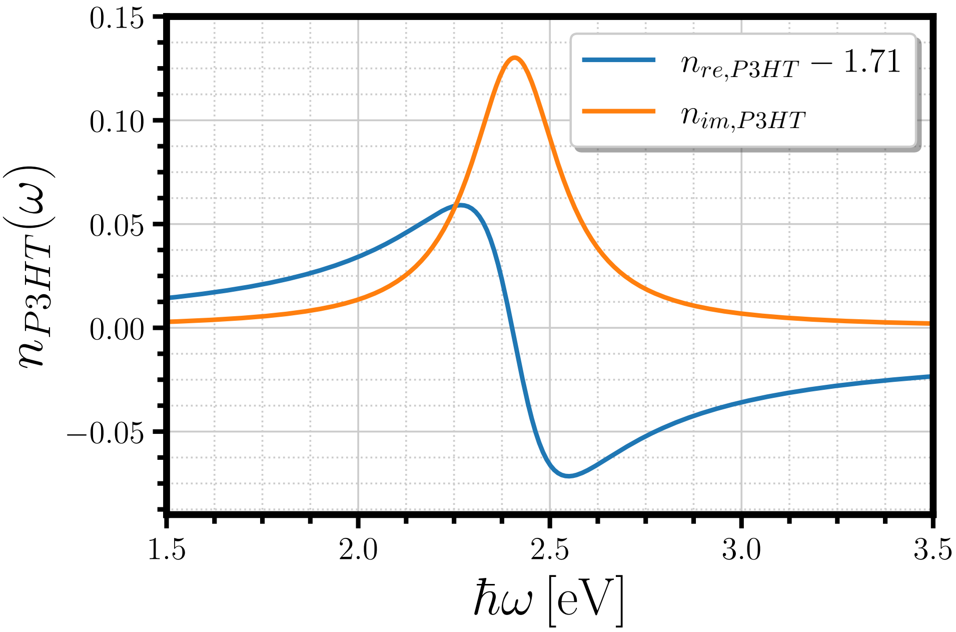

Figure 12.6: Real part (light-blue line) and imaginary part (orange line) for the refractive index of P3HT as a function of $\hbar\omega$ in the unit of eV. Parameters are as follows: $\varepsilon_{\infty,P3HT} = 2.89$, $(\hbar^2\omega_p^2 f_0)_{P3HT} = 0.3\,\mathrm{eV}^2$, $\hbar\omega_{0,P3HT} = 2.407\,\mathrm{eV}$, and $\hbar\gamma_{P3HT} = 0.28\,\mathrm{eV}$.

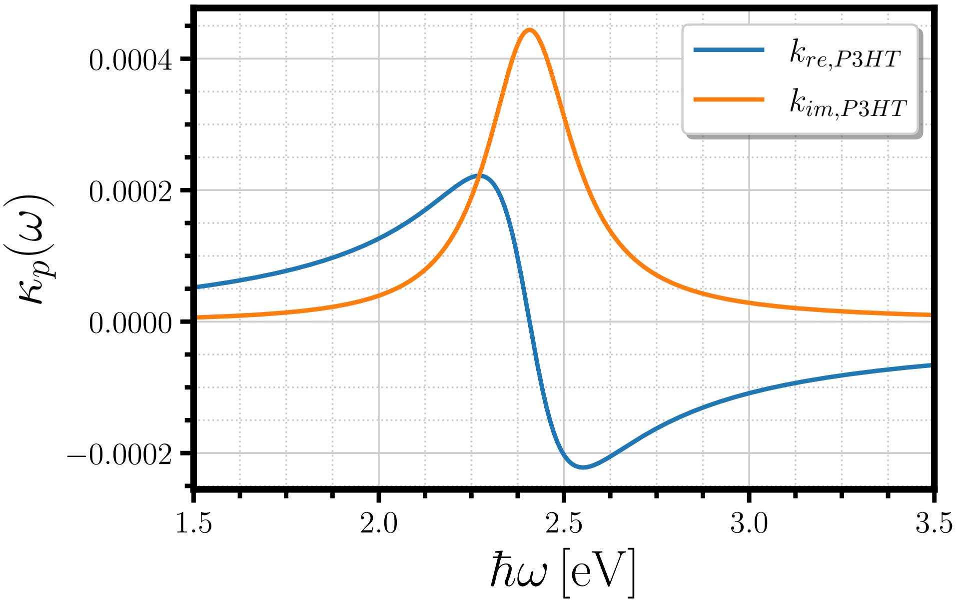

Figure 12.7: Real part (light-blue line) and imaginary part (orange line) for the chiral parameter κ_p, using the dispersive feature of P3HT, as a function of $\hbar\omega$ in the unit of eV. Parameters are as follows: $(\hbar^2\omega_p^2 f_0)_{P3HT} = 0.3\,\mathrm{eV}^2$, $\hbar\omega_{0,P3HT} = 2.407\,\mathrm{eV}$, $\hbar\gamma_{P3HT} = 0.28\,\mathrm{eV}$, and $\kappa_{p,0} = 10^{-3}$.

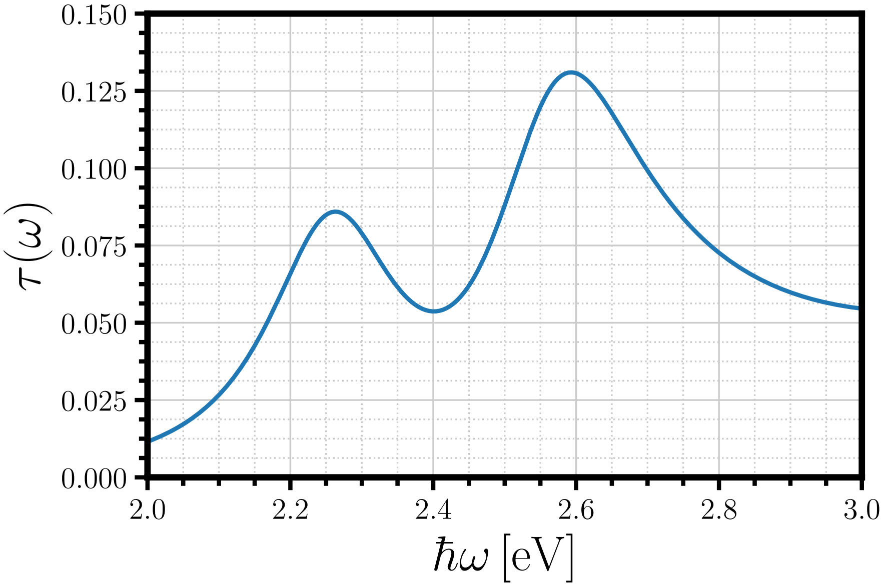

Figure 12.8: Transmittance $\tau(\omega)$ at normal incidence from a Fabry-Pérot interferometer, composed by air-P3HT-air, as a function of $\hbar\omega$ in the unit of eV. Parameters are as follows: $n = 1$, $d_{mirror} = 30\,\text{nm}$, $\varepsilon_{\infty,Ag} = 4.8$, $\hbar\omega_{p,Ag} = 9.5\,\text{eV}$, $\hbar\gamma_{Ag} = 0.17\,\text{eV}$, $L_{P3HT} = 100\,\text{nm}$, $\varepsilon_{\infty,P3HT} = 2.89$, $(\hbar^2\omega_p^2 f_0)_{P3HT} = 0.3\,\text{eV}^2$, $\hbar\omega_{0,P3HT} = 2.407\,\text{eV}$, $\hbar\gamma_{P3HT} = 0.28\,\text{eV}$ and $\theta = 0$.

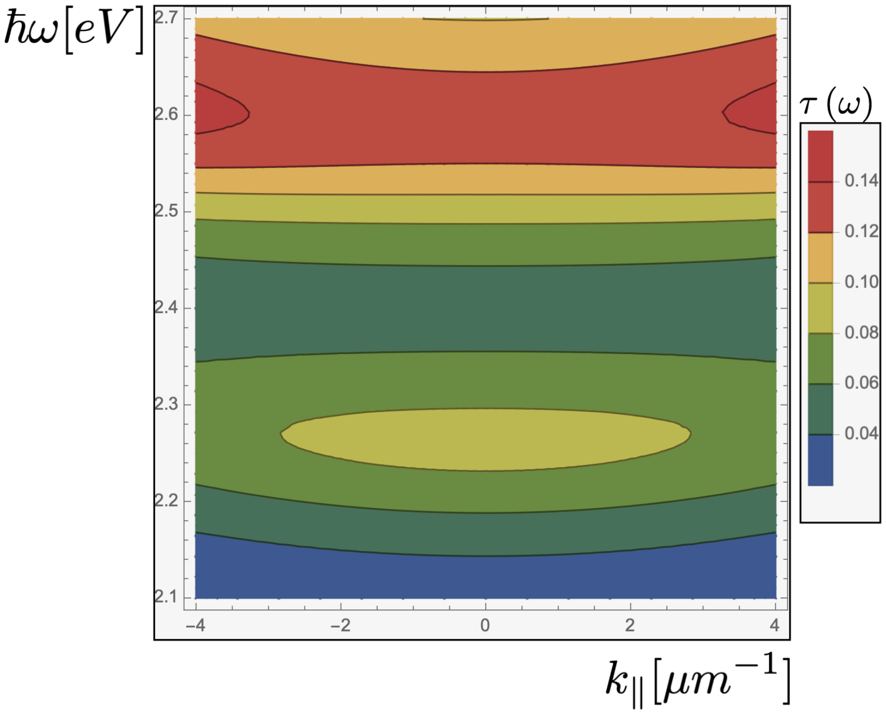

Figure 12.9: Transmittance $\tau(\omega)$ from a Fabry-Pérot interferometer, composed by air-P3HT-air, as a function of $k_{||}$ in the unit of μm^{-1} and as a function of $\hbar\omega$ in the unit of eV. Parameters are those of Figure 12.8, except that θ is varied from −17° to 17°.

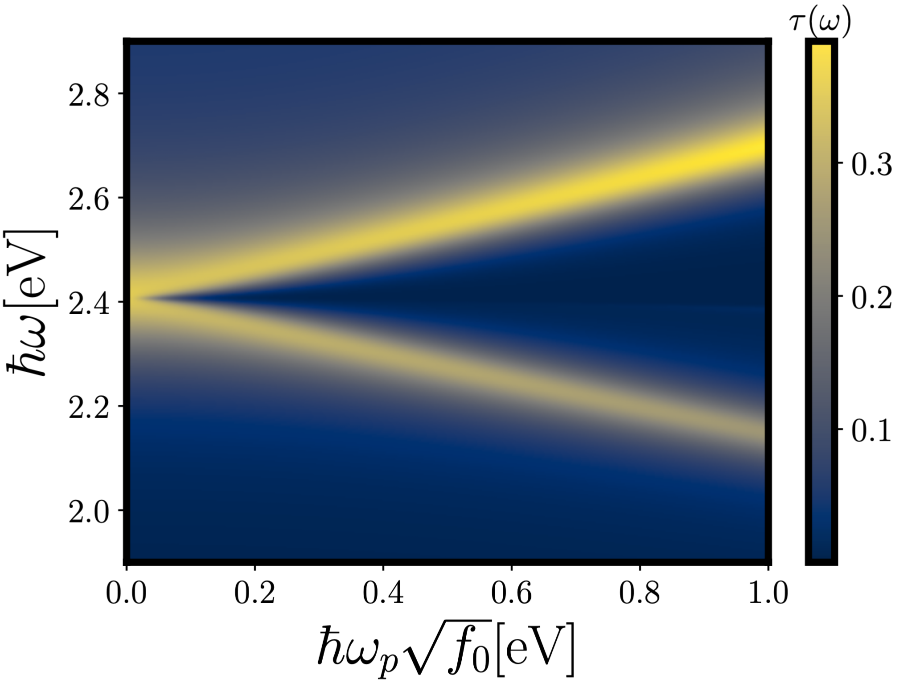

Figure 12.10: Transmittance $\tau(\omega)$ at normal incidence from a Fabry-Pérot interferometer, composed by air-P3HT-air, as a function of $\omega_p\sqrt{f_0}$ in unit of eV and as a function of $\hbar\omega$. Parameters are those of Figure 12.8.

12.6 DCT at normal incidence

The DCT is defined as twice the difference between the transmittances $\tau_{+,\perp}(\omega)$ and $\tau_{-,\perp}(\omega)$ (see eq. (12.32)) divided by their sum, and at normal incidence for this dispersive case is simply

$$DCT_{\perp} = \frac{2\left(e^{-\alpha_+ L} - e^{-\alpha_- L}\right)}{e^{-\alpha_+ L} + e^{-\alpha_- L}} \equiv \frac{2\left(\mathcal{A}_+ - \mathcal{A}_-\right)}{\mathcal{A}_+ + \mathcal{A}_-}, \tag{12.34}$$

where $\alpha_\pm = 2kn'_{\pm,im}(\omega)$ and L is the length of the chiral medium.
If $\alpha_\pm = 0$ the $DCT_\perp$ becomes 0 as it is shown in Section 11.1. ***At normal incidence DCT is a function of the absorption coefficients and of the length of the cavity.***
Figure 12.11 shows the DCT at normal incidence for a chiral dispersive Fabry-Pérot interferometer. The interferometer is composed by two thin Ag mirrors of 30 nm which cover a dispersive chiral layer, made by P3HT [33], of 100 nm. These kind of chiral polymers are versatile since they allow to tune the optical response in the visible by functionalising the side chains. The functionalisation can be realised such that their 3-dimensional arrangement results in intrinsically chiral helices of one handedness that exhibit high intrinsic chirality ($\kappa_p \approx 10^{-3}$) [81]. The DCT has a negative peak around 2.4 eV where the cavity light mode is at resonance with the electronic transition of the chosen chiral P3HT layer. The transfer matrix approach matches perfectly the analytical formula given by eq. (12.34) (see Figure 12.11). The shape of DCT is maintained by removing the mirrors as it encoded in eq. (12.34) and shown in Figure 12.12. In contrast to the DCT signal, the difference in transmission, defined as $\Delta\tau_\perp \equiv \tau_{+,\perp} - \tau_{-,\perp}$, is affected by the presence of the mirrors which reduce the signal (being lossy) with respect to bare signal out of cavity (see Figure 12.12). DCT increases almost linearly by varying the oscillator strength as it is shown in Figure 12.13. This is due to the dispersive modelling of $\kappa_p(\omega)$ given by eq. (12.33).

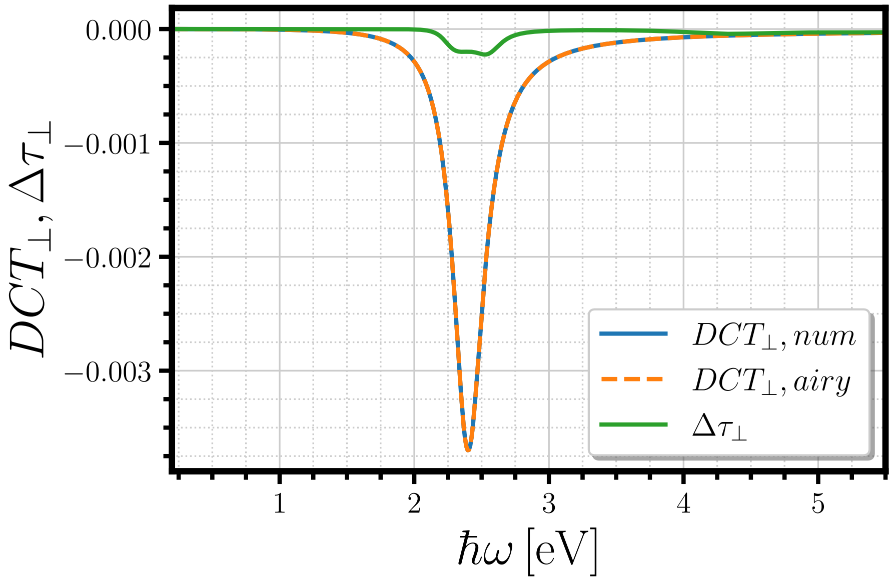

Figure 12.11: $DCT_\perp$ for the numerical approach using the transfer matrices (light-blue line), $DCT_\perp$ for the analytical approach (see eq. (12.34)) (orange dashed line), and $\Delta\tau_\perp \equiv \tau_{+,\perp} - \tau_{-,\perp}$ (green line) (see (12.32)) from a Fabry-Pérot interferometer, composed by air-chiral P3HT-air, as a function of $\hbar\omega$ in unit of eV. Parameters are as follows: $n = 1$, $d_{mirror} = 30\,\text{nm}$, $\varepsilon_{\infty,Ag} = 4.8$, $\hbar\omega_{p,Ag} = 9.5\,\text{eV}$, $\hbar\gamma_{Ag} = 0.17\,\text{eV}$, $L_{P3HT} = 100\,\text{nm}$, $\varepsilon_{\infty,P3HT} = 2.89$, $(\hbar^2\omega_p^2 f_0)_{P3HT} = 0.3\,\text{eV}^2$, $\hbar\omega_{0,P3HT} = 2.407\,\text{eV}$, $\hbar\gamma_{P3HT} = 0.28\,\text{eV}$, and $\kappa_p = 10^{-3}$.

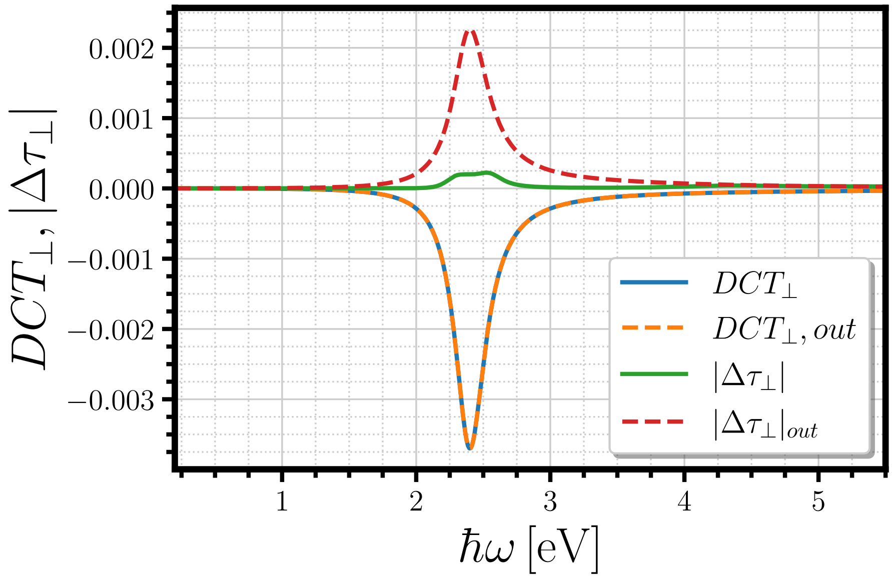

Figure 12.12: $DCT_\perp$ (light-blue line), $DCT_{\perp,out}$ (without mirrors) (orange dashed line), $|\Delta\tau_\perp \equiv \tau_{+,\perp} - \tau_{-,\perp}|$ (green line) (see eq. (12.32)), $|\Delta\tau_\perp \equiv \tau_{+,\perp} - \tau_{-,\perp}|_{out}$ (red dashed line) from a Fabry-Pérot interferometer, composed by air-chiral P3HT-air, as a function of $\hbar\omega$ in unit of eV. Parameters are those of Figure 12.11.

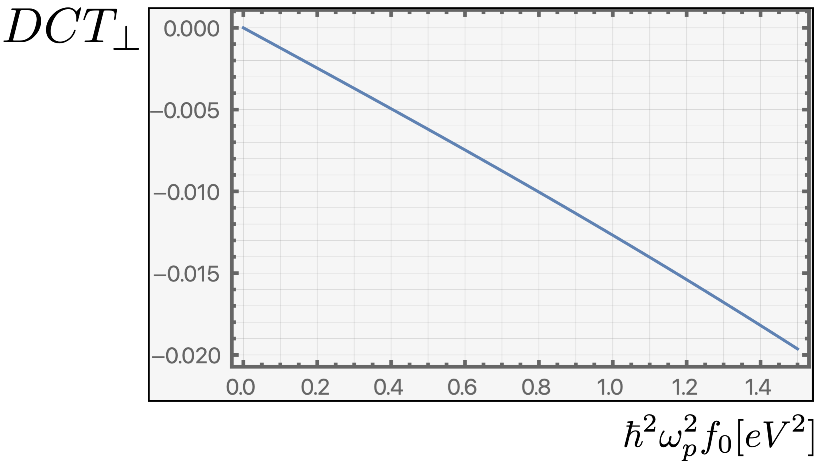

Figure 12.13: DCT from a Fabry-Pérot interferometer, composed by air-chiral P3HT-air, as a function of $\hbar^2\omega_p^2 f_0$ in the unit of eV^2 at resonance. Parameters are those of Figure 12.11.

12.7 DCT at finite angle

Using the transfer matrix approach (see Section 10.4.3), it is possible to discover that the ***Differential Circular Transmission has a maximum intensity for a given angle***. In particular, for the chiral P3HT ***the maximum is around 20°*** as it is shown in Figure 12.14. Figure 12.15 and Figure 12.16 show clearly that the maximum in intensity is attained at resonance and it covers a region between −30° to 30°, approximately. The intensity from −30° to 30° varies slightly. Figure 12.16 shows the DCT for an higher oscillator strength with respect to Figure 12.15. The increasing of the oscillator strength makes the region of maximum DCT more sharp and the intensity increases accordingly to Figure 12.13. In contrast to the case at normal incidence (see Figure 12.12), DCT in cavity and outside cavity have not the same shape for a given finite angle. This aspect is shown in Figure 12.14. In fact, at finite angle of incidence, the light inside the cavity no longer has a well-defined handedness (left or right). It is a mixture of two polarizations and the consequence is that DCT is now a function of the reflections and transmissions of the given system (the transmittances cannot factorized as in eq. (12.32)).

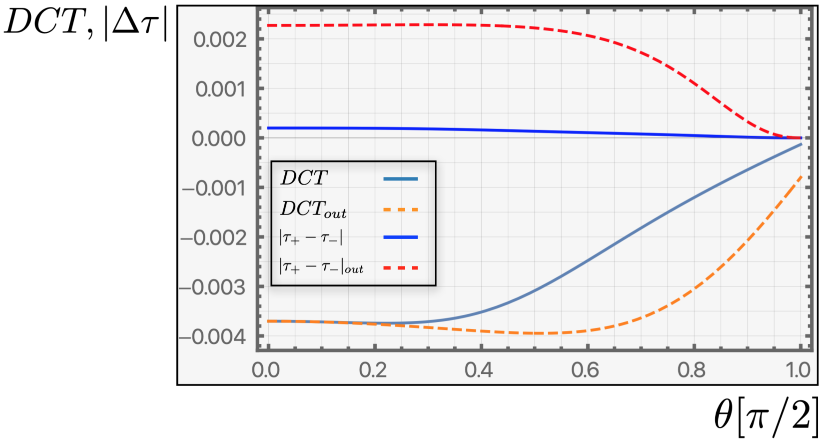

Figure 12.14: DCT for the numerical approach using the transfer matrices from a Fabry-Pérot interferometer, composed by air-chiral P3HT-air, as a function of θ in the unit of $\pi/2$ at resonance. Parameters are as follows: $n = 1$, $d_{mirror} = 30\,\mathrm{nm}$, $\varepsilon_{\infty,Ag} = 4.8$, $\hbar\omega_{p,Ag} = 9.5\,\mathrm{eV}$, $\hbar\gamma_{Ag} = 0.17\,\mathrm{eV}$, $L_{P3HT} = 100\,\mathrm{nm}$, $\varepsilon_{\infty,P3HT} = 2.89$, $(\hbar^2\omega_p^2 f_0)_{P3HT} = 0.3\,\mathrm{eV}^2$, $\hbar\omega = \hbar\omega_{0,P3HT} = 2.407\,\mathrm{eV}$, $\hbar\gamma_{P3HT} = 0.28\,\mathrm{eV}$, and $\kappa_p = 10^{-3}$.

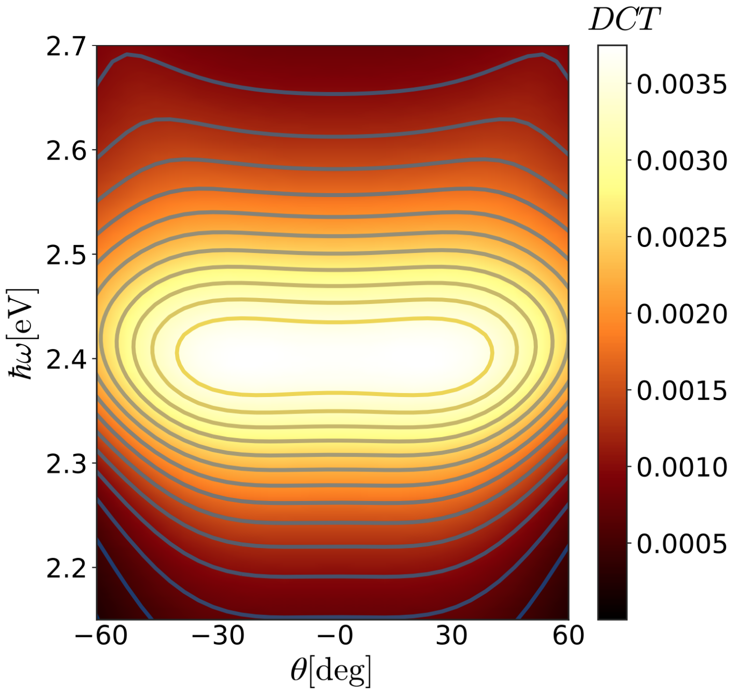

Figure 12.15: DCT for the numerical approach using the transfer matrices from a Fabry-Pérot interferometer, composed by air-chiral P3HT-air, as a function of θ in the unit of deg and as a function of $\hbar\omega$ in the unit of eV. Parameters are those of Figure 12.14.

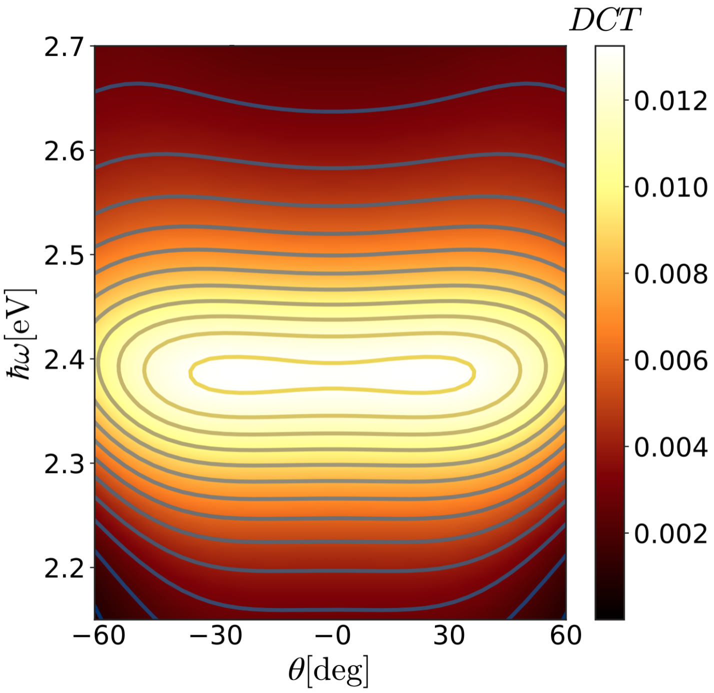

Figure 12.16: DCT for the numerical approach using the transfer matrices from a Fabry-Pérot interferometer, composed by air-chiral P3HT-air, as a function of θ in the unit of deg and as a function of $\hbar\omega$ in the unit of eV. Parameters are those of Figure 12.14, except that $(\hbar^2\omega_p^2 f_0)_{P3HT} = 1.0\,\mathrm{eV}^2$.

12.8 Lorentz's reciprocity applied to Transmission and Reflection

The transmission matrix, at normal incidence, (see eq. (11.7)) for the light propagation in an isotropic chiral medium has a particular form: two different diagonal elements and 0s for the off-diagonal elements. The 0s are connected to the fact that an isotropic chiral material does not convert the polarization in transmission. The two different diagonal terms, t_{++} and t_{--}, are the source of the chiral discrimination in an isotropic *Pasteur medium*. The form of the transmission matrix for the opposite propagation is the same for this kind of chiral medium. Thus, exchanging the source with the detector the same signal is recovered for the reverse light propagation. This section has the aim to find relations which connect the transmission (and the reflection) for the forward and the backward light propagation through a linear system.

Lorentz's reciprocity is a fundamental property of *microscopic reversibility* of field distributions and their sources [21]. In particular, for a scattering process reciprocity adds some constraints on transmission and reflection tensors [137, 20]. Let's start to introduce the Lorentz's reciprocity theorem.

12.8.1 Lorentz's reciprocity theorem

The physical situation is to consider a finite volume V_1 of sources ρ_1 and $\vec{J}_1$. The sources generate the fields $\vec{E}_1$, $\vec{B}_1$, $\vec{D}_1$, and $\vec{H}_1$ in the presence of a scatterer characterized by the dielectric and magnetic tensors $\overleftrightarrow{\varepsilon}(\vec{r},\omega)$, $\overleftrightarrow{\mu}(\vec{r},\omega)$, respectively. Analogously, the fields can be generated by another different source of finite volume V_2 without considering the presence of the first source. All the fields satisfy the Maxwell's equations and by assuming a harmonic time-dependence $e^{-i\omega t}$ they get

$$\begin{gathered}
\nabla \wedge \vec{E}_i = +i\omega \vec{B}_i, \nabla \cdot \vec{B}_i = 0, \\
\nabla \wedge \vec{H}_i = \vec{J}_i - i\omega \vec{D}_i, \nabla \cdot \vec{D}_i = \rho_i \,\text{with}\, i = 1, 2.
\end{gathered} \tag{12.35}$$

The fields generated by the first source can be associated to the fields of the second source making some manipulations on the Maxwell's equations to get the following equation

$$\begin{aligned}
\left(\vec{H}_2 \nabla \wedge \vec{E}_1 - \vec{E}_1 \nabla \wedge \vec{H}_2\right) + \left(\vec{E}_2 \nabla \wedge \vec{H}_1 - \vec{H}_1 \nabla \wedge \vec{E}_2\right) = i\omega \left(\vec{H}_2 \vec{B}_1 - \vec{H}_1 \vec{B}_2\right) - \\
+ i\omega \left(\vec{E}_2 \vec{D}_1 - \vec{E}_1 \vec{D}_2\right) + \\
+ \vec{E}_2 \vec{J}_1 - \vec{E}_1 \vec{J}_2.
\end{aligned} \tag{12.36}$$

The left-hand side of eq. (12.36) can be rewritten using the vector identity $\vec{F} \cdot \left(\nabla \wedge \vec{G}\right) = \nabla \cdot \left(\vec{G} \wedge \vec{F}\right) + \vec{G} \cdot \left(\nabla \wedge \vec{F}\right)$, where $\vec{F}$ and $\vec{G}$ are two generic vector fields. Using the identity, the result is

$$\nabla \left(\vec{E}_1 \wedge \vec{H}_2 - \vec{E}_2 \wedge \vec{H}_1\right) = i\omega \left(\vec{H}_2 \vec{B}_1 - \vec{H}_1 \vec{B}_2\right) - i\omega \left(\vec{E}_2 \vec{D}_1 - \vec{E}_1 \vec{D}_2\right) + \vec{E}_2 \vec{J}_1 - \vec{E}_1 \vec{J}_2. \tag{12.37}$$

On the right-hand side the constitutive relations can be included to simplify the total expression. Here two cases are considered: a case in which the scatterer is an inhomogeneous, anisotropic and achiral medium characterized by linear constitutive relations $\vec{D} = \overleftrightarrow{\varepsilon}\, \vec{E}$, $\vec{B} = \overleftrightarrow{\mu}\, \vec{H}$ and another case where the medium is homogeneous, isotropic and chiral described by the Condon relations (see eq. (10.5)).

Case of inhomogeneous, anisotropic and achiral medium

Inserting the constitutive relations $D_i = \varepsilon_{ij} E_j$ and $B_i = \mu_{ij} H_j$ in the right-hand side of eq. (12.37), it follows that

$$\nabla \left(\vec{E}_1 \wedge \vec{H}_2 - \vec{E}_2 \wedge \vec{H}_1\right) = i\omega \left(\vec{H}_2 \mu_{21} \vec{B}_1 - \vec{H}_1 \mu_{12} \vec{B}_2\right) - i\omega \left(\vec{E}_2 \varepsilon_{21} \vec{D}_1 - \vec{E}_1 \varepsilon_{12} \vec{D}_2\right) + \vec{E}_2 \vec{J}_1 - \vec{E}_1 \vec{J}_2. \tag{12.38}$$

The first two terms in parenthesis, on the right-hand side, vanish if and only if $\mu_{12} = \mu_{21}$ and $\varepsilon_{12} = \varepsilon_{21}$. The symmetry of tensors is one of the general class of reciprocal relations studied by L. Onsager [21] which can be derived using the principle of microscopic reversibility (without the presence of a static magnetic field). At microscopic level physics is symmetric interchanging the sources and the generated fields. Thus, the Lorentz's reciprocity theorem with sources is given by

$$\nabla\left(\vec{E}_1 \wedge \vec{H}_2 - \vec{E}_2 \wedge \vec{H}_1\right) = \vec{E}_2\vec{J}_1 - \vec{E}_1\vec{J}_2. \tag{12.39}$$

The theorem has its integral form upon integration over all space. Integrating the left-hand side a surface integral over a sphere with an infinite radius is obtained. This integral vanishes, and this can be shown replacing the fields in the far-region. The asymptotic expressions of the scattered fields propagating along a given direction of the wave vector $\vec{k}$ are

$$\begin{aligned}\vec{E}\,(kr \to +\infty) &\sim 2\pi i\,\gamma_k \hat{e}_k \frac{e^{ikr}}{r},\\ \vec{H}\,(kr \to +\infty) &\sim 2\pi i\,\gamma_k \hat{h}_k \frac{e^{ikr}}{r},\end{aligned} \tag{12.40}$$

where $\gamma_k = \sqrt{k^2 - |\vec{k}|^2}$ with $|\vec{k}| \le k$ for plane waves, $\hat{e}_k$ and $\hat{h}_k$ are the transverse Fourier transforms of the fields projected on a plane at infinity. They are transverse, in fact $\vec{k} \wedge \hat{e}_k = \omega\mu_0\hat{h}_k$. Subtituting these fields in eq. (12.39) and integrating over all space the theorem gets

$$\int \vec{J}_1 \cdot \vec{E}_2\, dV_1 = \int \vec{J}_2 \cdot \vec{E}_1\, dV_2, \tag{12.41}$$

where it remains only an integral over the volume V_1 on the left-hand side, where $\vec{J}_1$ is not 0, and an integral over the volume V_2 on the right-hand side.

The integral form of the Lorentz's reciprocity theorem is further simplified assuming the sources as dipole sources, $\vec{J}_i(\vec{r}) = -i\omega\vec{p}_i\delta(\vec{r} - \vec{r}_i)$, to obtain

$$\boxed{\vec{p}_1 \cdot \vec{E}_2(\vec{r}_1) = \vec{p}_2 \cdot \vec{E}_1(\vec{r}_2).} \tag{12.42}$$

The last equation is usually called the *customary statement* of the reciprocity theorem and it is widely applied in antenna theory.

Case of homogeneous, isotropic and chiral medium

In a homogeneous, isotropic and chiral medium the constitutive relations are the Condon constitutive relations: $\vec{D} = \varepsilon\vec{E} + i\frac{\kappa_p}{c}\vec{H}$ and $\vec{B} = \mu\vec{H} - i\frac{\kappa_p}{c}\vec{E}$. Now by inserting these relations in the right-hand side of eq. (12.37) it results

$$\begin{aligned}\nabla\left(\vec{E}_1 \wedge \vec{H}_2 - \vec{E}_2 \wedge \vec{H}_1\right) &= i\omega\left(\vec{H}_2\mu\vec{H}_1 - i\frac{\kappa_p}{c}\vec{H}_2\vec{E}_1 - \vec{H}_1\mu\vec{H}_2 + i\frac{\kappa_p}{c}\vec{H}_1\vec{E}_2\right)\\ &- i\omega\left(\vec{H} \leftrightarrow \vec{E},\ \mu \to \varepsilon \text{ and } \kappa_p \to -\kappa_p\right) +\\ &+ \vec{E}_2\vec{J}_1 - \vec{E}_1\vec{J}_2,\end{aligned} \tag{12.43}$$

where in the second parenthesis on the right-hand side the expression is the same as the first one sending $\vec{H} \leftrightarrow \vec{E}$, $\mu \to \varepsilon$, and $\kappa_p \to -\kappa_p$. By doing these substitutions the terms without the sources, on the right-hand side, cancels out and also in this case the eq. (12.39) is retrieved.

In chiral media the dipole approximation is not sufficient (see Section 10.2.1), thus by including the first order correction of the space variation of the electric field (see eq. (10.9)) the customary statement of the reciprocity theorem gets

$$\boxed{\vec{p}_1 \cdot \vec{E}_2(\vec{r}_1) - \vec{m}_1 \cdot \vec{B}_2(\vec{r}_1) = \vec{p}_2 \cdot \vec{E}_1(\vec{r}_2) - \vec{m}_2 \cdot \vec{B}_1(\vec{r}_2),} \tag{12.44}$$

where the quadrupole terms are neglected and $\vec{m} \equiv \frac{1}{2}\int \left(\vec{r} \wedge \vec{J}\right) dV$ is the magnetic moment.

The conclusion is that the concept of Lorentz reciprocity is the same for isotropic chiral media as for isotropic achiral media.

12.8.2 Transmission and reflection under reciprocity

Lorentz's reciprocity states that an interchange of sources and field distributions does not affect the physical result (without the presence of a static magnetic field). The theorem can be directly extended to the case of transmission and reflection tensors in a scattering problem [20]. Let's consider the application of reciprocity on transmission and afterwards on reflection tensors.

Reciprocity on transmission tensors

At -∞ a source generates a field $\vec{E}_{\pm}(-\infty, \vec{k})$ which propagates towards a given scatterer, characterized by linear constitutive relations. A detector captures the scattered field at $+\infty$, $\vec{E}_{\pm}(+\infty, \vec{k}')$. The action of the scatterer on the field is expressed by a generic transmission tensor which relates the generated field at -∞ to the scattered field at $+\infty$:

$$\vec{E}_{\pm}(+\infty, \vec{k}') = \overset{\leftrightarrow}{T}_{\rightarrow} \vec{E}_{\pm}(-\infty, \vec{k}). \tag{12.45}$$

A similar relation can be found exchanging the source with the detector to find

$$\vec{E}_{\pm}(-\infty, -\vec{k}) = \overset{\leftrightarrow}{T}_{\leftarrow} \vec{E}_{\pm}(+\infty, -\vec{k}'). \tag{12.46}$$

Under reciprocity the physical result has to remain unchanged, thus

$$\overset{\leftrightarrow}{T}_{\rightarrow} \vec{E}_{\pm}(-\infty, \vec{k}) = \overset{\leftrightarrow}{T}_{\leftarrow} \vec{E}_{\pm}(+\infty, -\vec{k}'). \tag{12.47}$$

The equality is satisfied if $\vec{k} \rightarrow -\vec{k}'$ on the left-hand side and this implies that the tensor has to exchange its indeces or analogously it has to be transposed. Reciprocity constraints the transmission tensors to satisfy

$$\boxed{\overset{\leftrightarrow}{T}_{\rightarrow} = \left(\overset{\leftrightarrow}{T}_{\leftarrow}\right)^{\mathrm{T}}.} \tag{12.48}$$

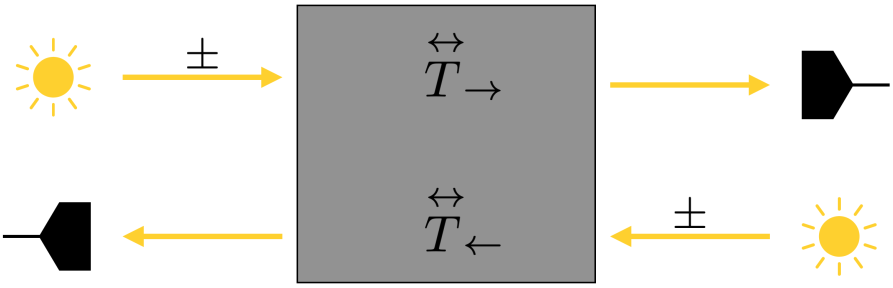

Figure 12.17: Schematic draw of the application of reciprocity on transmission tensors.

Reciprocity on reflection tensors

The reciprocity argument to deal with reflection tensors follows the same lines of the reasoning discussed for transmission tensors. The main difference concerns the application of the reciprocity's theorem only on the left of the scatterer for the reflection tensor $\overset{\leftrightarrow}{R}_{\leftarrow}$ and only on the right for the reflection tensor $\overset{\leftrightarrow}{R}_{\rightarrow}$. If the source is on the left of the scatterer the reciprocity theorem gives

$$\boxed{\overset{\leftrightarrow}{R}_{\leftarrow}=\left(\overset{\leftrightarrow}{R}_{\leftarrow}\right)^{\mathrm{T}}.} \tag{12.49}$$

Accordingly, the application of the reciprocity theorem for a source located on the right with respect to the position of the scatterer produces

$$\boxed{\overset{\leftrightarrow}{R}_{\rightarrow}=\left(\overset{\leftrightarrow}{R}_{\rightarrow}\right)^{\mathrm{T}}.} \tag{12.50}$$

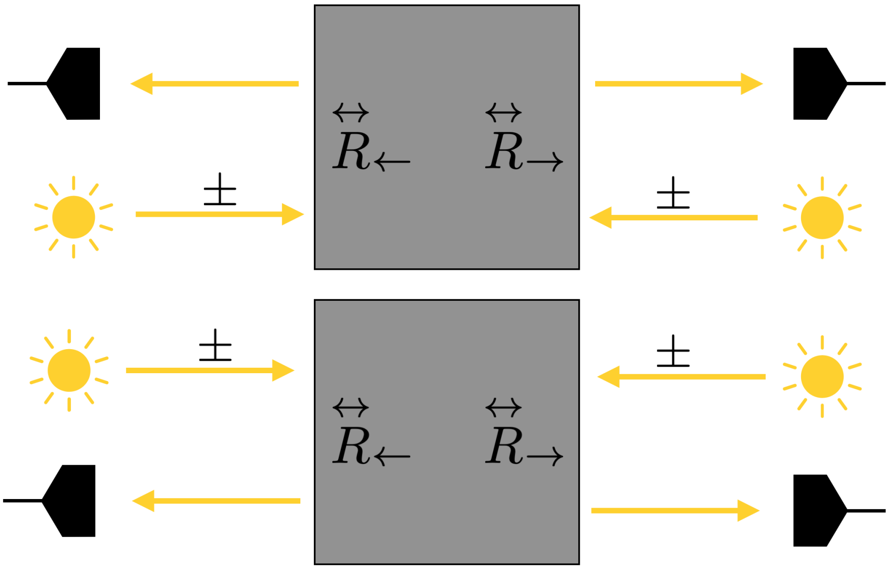

Figure 12.18: Schematic draw of the application of reciprocity on reflection tensors.

Reciprocity and time-reversal symmetry on the scattering matrix

A scattering matrix S connects the amplitudes of the fields approching to the scatterer with the scattered amplitudes of fields by the same scatterer. Under reciprocity the matrix S has particular properties that can be revealed knowing the properties of the transmission and reflection matrices. Using the relations given by eqs. (12.48), (12.49) and eq. (12.50) the reciprocal scattering matrix has the form

$$S=\begin{pmatrix} \overset{\leftrightarrow}{R}_{\leftarrow} & \overset{\leftrightarrow}{T}_{\leftarrow} \\ \overset{\leftrightarrow}{T}_{\rightarrow} & \overset{\leftrightarrow}{R}_{\rightarrow} \end{pmatrix}=S^{\mathrm{T}}, \tag{12.51}$$

with

$$\overset{\leftrightarrow}{R}_{\leftarrow}=\begin{pmatrix} r^{\leftarrow}_{++} & r^{\leftarrow}_{conv} \\ r^{\leftarrow}_{conv} & r^{\leftarrow}_{--} \end{pmatrix}, \quad \overset{\leftrightarrow}{R}_{\rightarrow}=\begin{pmatrix} r^{\rightarrow}_{++} & r^{\rightarrow}_{conv} \\ r^{\rightarrow}_{conv} & r^{\rightarrow}_{--} \end{pmatrix}, \tag{12.52}$$

$$\overset{\leftrightarrow}{T}_{\leftarrow}=\begin{pmatrix} t_{++} & t_1 \\ t_2 & t_{--} \end{pmatrix}, \quad \overset{\leftrightarrow}{T}_{\rightarrow}=\begin{pmatrix} t_{++} & t_2 \\ t_1 & t_{--} \end{pmatrix}. \tag{12.53}$$

The scattering matrix S is symmetric under reciprocity and the same symmetry is maintained under time-reversal in which the fields transform as $\vec{E}_{\pm}(\pm\infty,\pm\{\vec{k},\vec{k}'\}) \rightarrow \vec{E}^{\star}_{\mp}(\pm\infty,\mp\{\vec{k},\vec{k}'\})$ where $t \rightarrow -t$, and the complex amplitude is complex conjugated. The relations that are fulfilled by the sattering matrix under time-reversal symmetry are

$$S^{\dagger}S = I,\ SS^{\star} = I \Longleftrightarrow S = S^{\mathrm{T}} \quad \text{with } |\mathrm{DetS}| = 1, \tag{12.54}$$

where the relation $S^{\dagger}S = I$ is the conservation of the current density and $SS^{\star}$ is the consequence of $t \rightarrow -t$ and complex conjugation of the fields. Time-reversal symmetry is broken if there are losses and the scatterer dissipates energy. Reciprocity, instead of time-reversal, is conserved for processes in which energy is not conserved.

13

Chiral Fabry-Pérot with chiral mirrors

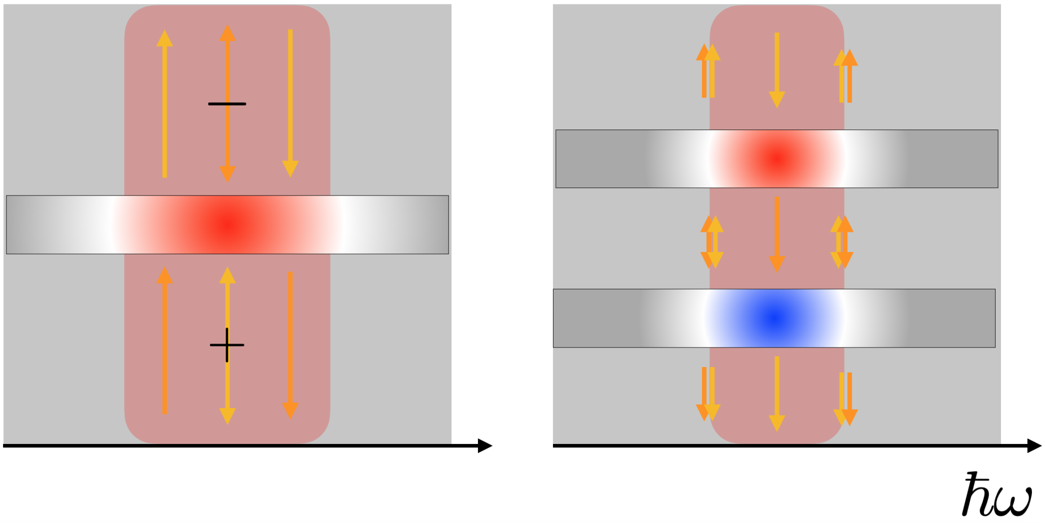

Figure 13.1: Sketch of a chiral mirror as the type of ref. [142], and a cavity made by the chiral mirror and its enantiomer. The mirror almost perfectly reflects RHC (-) (orange arrow) polarized light from one side and LHC (+) (yellow arrow) from the opposite side (the double arrow means that the ray arrives on the surface and it is reflected back). It also converts LHC (RHC) polarized light in transmission for the downward (upward) propagation. The preserving behaviour is confined in a narrow region (red shaded region) in energy; the same region appears in the enantiomer with a consequential flip of the polarization (in blue). Out of the preserving region the device works as a standard mirror. The cavity, made by the chiral mirror and its enantiomer (the right-hand side of the Figure), can internally reflect and discriminate one of the polarization in the proximity of the helicity-preserving region.

In this Chapter, the objective is to model and simulate the behaviour of a chiral Fabry-Pérot interferometer made by two chiral helicity-preserving mirrors, illustrated in ref. [142]. The single mirror (see Figure 13.1 on the left-hand side) is a lossless chiral photonic crystal mirror that reflects, upon normal illumination, RHC (-) polarized light without reversing its handedness. Moreover, it converts the polarization of the opposite handedness, LHC polarized light, upon transmission. The mirror acts as an helicity-preserving mirror (and transmission converter) in a small window in frequency (the experimental realization has the target energy, where the preservation is maximal, at 1.43 eV, approximately). Out of the "maximal preserving region" it behaves as a common mirror, that is it reflects the opposite polarization and it transmits without conversion of polarization.

The chirality of the mirror consists in a specific pattern of the two surfaces, which exhibits opposite chirality. The structure belongs to the class of 2D chirality [59], and it means that the oncoming circularly polarized light is scattered differently if it encounters one side or the opposite side of the mirror. In addition, the mirror is almost perfectly lossless and it fullfills time-reversal symmetry (see Section 12.8.2). In conjuction with the 2D chirality, the maximal preservation in reflection (and conversion in transmission) is acquired by the opposite polarization for the opposite side of the structure.

The construction of the Fabry-Pérot interferometer with this kind of chiral mirror is made by positioning the single mirror, as the first mirror, and subsequently the associated enantiomer, *i.e.*, the mirror image. In this way, the cavity perfectly transmits the LHC (RHC) polarized light (see Figure 13.1 on the right-hand side) at the center of the preserving-helicity energy region, for the downward (upward) light propagation. The most interesting region is in the close proximity to the helicity-preserving region where the LHC and RHC polarized light are partially transmitted and partially reflected. The advantage of this new setup is that it can discriminate and partially reflect, inside the structure, one polarization with respect to the other one close to the energy of the preserving region. This device has this additional and special property which is not available for a chiral Fabry-Pérot interferometer made by "normal" Ag mirrors (see Section 12).

The next section contains the modelling of the single mirror and its enantiomer, at the level of the scattering matrix.

13.1 Modelling of the chiral mirrors

The transmission and reflection properties of a given layer, chiral or achiral, are generically expressed with the corresponding transmission and reflection matrices, also called Jones matrices [87]. At normal incidence, an achiral material is represented by Jones matrices for the transmission or reflection with 0s in the off-diagonal or in the diagonal terms, respectively (see eq. (11.7)). This means that the achiral material does not covert the polarization in transmission and it does not preserve the same polarization in reflection. A chiral layer, as the chiral mirror, can have all the transmission and reflection coefficients different from 0. In the present case, the transmission and the reflection Jones matrices are built by considering only the shaded region of Fig. 2 of the reference [142]. That shaded region contains the transmissions and reflections of the preserving part and the background around it (see Figure 13.2). Thus, that small region is sufficient to study the interesting and unexplored behaviour close to the helicity-preserving region.

13.1.1 Single mirror

The single chiral mirror is modelled by assuming the following transmission and reflection matrices, for the downward light propagation (see Figure 13.1 on the left) or analogously for the propagation from left to right by using the convention of Section 12.8:

$$\begin{aligned} T_{\rightarrow} &= \begin{pmatrix} t & 0 \\ t_{+-} & t \end{pmatrix} = \begin{pmatrix} |t| \cdot e^{i\phi_t} & 0 \\ |t_{+-}| \cdot e^{i\psi} & |t| \cdot e^{i\phi_t} \end{pmatrix} \\ R_{\leftarrow} &= \begin{pmatrix} 0 & r \\ r & r_{--} \end{pmatrix} = \begin{pmatrix} 0 & |r| \cdot e^{i\phi_r} \\ |r| \cdot e^{i\phi_r} & |r_{--}| \cdot e^{i\xi} \end{pmatrix}, \end{aligned} \tag{13.1}$$

where the second equality separates the modulo and the complex phase of the transmission and reflection coefficients.

A minimal model is used to reproduce the transmissions and reflections shown in Figure 13.2. The elements $t_{-+} = r_{++}$ are chosen to be equal to 0 because their modulo squared is 0, in the ref. [142]. The diagonal transmission coefficients (the same for the off-diagonal reflection coefficients) are chosen to be equal as it is the case in achiral layer. These elements reproduce the "normal" operative behaviour of achiral mirrors. The modulo squared of the element t_{+-} should reproduce a resonant plasmonic mode of the mirror which tends to 1 at the resonant frequency (the frequency of the maximal conversion in transmission). Thus, the *coupled-mode theory* [44, 91, 43, 61] for a single mode, for a time-reversible system, offers the explicit form of the transmission coefficient:

$$|t_{+-}| \cdot e^{i\psi} = \frac{\gamma_{pr}}{i(\omega - \omega_{pr}) + \gamma_{pr}} \quad \text{with } \omega_{pr} \gg \gamma_{pr}, \tag{13.2}$$

where γ_{pr} is the linewidth of the mode and ω_{pr} is the resonant frequency of the preserving region.

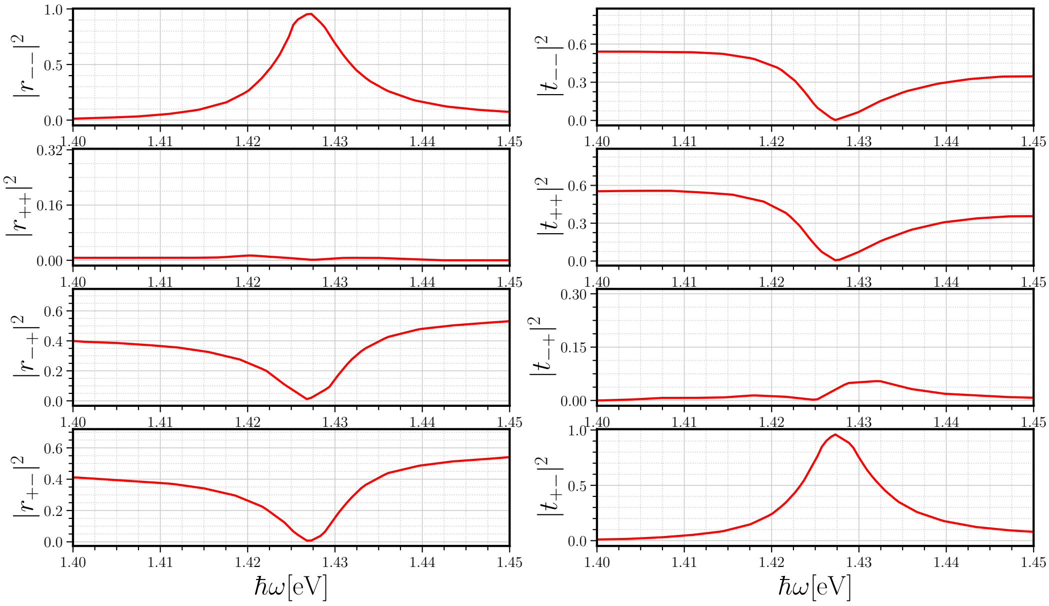

Figure 13.2: Transmissions and reflections of the chiral mirror of ref. [142] (see Fig. 2). Only the shaded preserving region is digitalized and shown. Note that the convention of the reference is translated into the convention adopted here[1].

The scattering matrix of the single chiral mirror is obtained by applying the conservation of energy and the condition of time-reversibility (see eq. (12.54)), being the chiral mirror lossless and invariant under time-reversal. The resulting scattering matrix is

$$S_{Cm} = \begin{pmatrix} R_{\leftarrow} & T_{\leftarrow} \\ T_{\rightarrow} & R_{\rightarrow} \end{pmatrix} = \begin{pmatrix} 0 & -|t|\cdot e^{i\psi} & |t| & |t_{+-}|\cdot e^{i\psi} \\ -|t|\cdot e^{i\psi} & |t_{+-}| & 0 & |t| \\ |t| & 0 & -|t_{+-}|\cdot e^{-2i\psi} & |t|\cdot e^{-i\psi} \\ |t_{+-}|\cdot e^{i\psi} & |t| & |t|\cdot e^{-i\psi} & 0 \end{pmatrix}, \tag{13.3}$$

with

$$\begin{aligned} &|t_{+-}|^2 + 2|r|^2 = 1, \\ &|t_{+-}| = |r_{--}| = \frac{\gamma_{pr}}{\sqrt{(\omega-\omega_{pr})^2+\gamma_{pr}^2}} \in [0,1]\,, \\ &|t| = |r| = \sqrt{\frac{1-|t_{+-}|^2}{2}} = \frac{(\omega-\omega_{pr})}{\sqrt{2\left[(\omega-\omega_{pr})^2+\gamma_{pr}^2\right]}} \in \left[0,\frac{1}{\sqrt{2}}\right], \end{aligned} \tag{13.4}$$

where $\xi = \psi$ and the phases ϕ_t and ϕ_r can be arbitrarily chosen to be 0.

The scattering matrix S_{Cm} of the single mirror is symmetric and it is automatically reciprocal, a property of any linear scatterer (see Section 12.8). The time-reversal symmetry implies strict constraints to all coefficients of transmission and reflection matrices. In particular, the symmetry reveals the form of the reflection matrix $R_{\rightarrow}$ which is not directly given by Figure 13.2.

---

[1] The LHC (RHC) polarized light is associated to the sign $-$ ($+$), in the ref. [142]. Here the convention is opposite: a LHC (RHC) polarized light ray is associated to the sign $+$ ($-$). It follows that the co-polarized transmission and reflection coefficients change their sign (for instance $t_{++} \rightarrow t_{--}$, here). The cross-polarized coefficients remain unchanged, because in the ref. the conversion of polarization is read from right to left. Here the conversion is read from left to right.

Once the Jones matrices for both light propagations (for transmission and reflection) are known, the corresponding transfer matrix is built with other small manipulations. The construction is analogous to what is discussed in Sections 10.4.3 and 10.4.4, and extended to the case of the chiral mirror; where the transmission and reflection for the light propagation from left to the right side of the structure do not coincide with the transmission and reflection for the opposite light propagation. Therefore, the transfer matrix of the single chiral mirror has the following form:

$$\boxed{\mathcal{T}_{CHP} = \begin{pmatrix} \mathcal{M}_{T_{\rightarrow}} & \mathcal{M}_{R_{\rightarrow}} \\ \mathcal{M}_{R_{\leftarrow}} & \mathcal{M}_{T_{\leftarrow}} \end{pmatrix},} \tag{13.5}$$

with

$$\begin{aligned} &\mathcal{M}_{T_{\rightarrow}} = (T_{\rightarrow})^{-1}, \quad \mathcal{M}_{R_{\leftarrow}} = R_{\leftarrow} (T_{\rightarrow})^{-1} \\ &\mathcal{M}_{T_{\leftarrow}} = T_{\leftarrow} - R_{\leftarrow} (T_{\rightarrow})^{-1} R_{\rightarrow}, \quad \mathcal{M}_{R_{\rightarrow}} = -(T_{\rightarrow})^{-1} R_{\rightarrow}. \end{aligned} \tag{13.6}$$

Figure 13.2 shows the transmittances $T_{\pm}$ ($T_{+} \equiv |t_{+-}|^2 + |t|^2$ and $T_{-} \equiv |t|^2$) (see their definition in eq. (13.1)) for the light propagation from the left to the right side of the single chiral mirror. The resonant energy of the preserving region, $\hbar\omega_{pr}$, is set to 1.6 eV and there the LHC (+) polarized light is fully transmitted and RHC (-) is fully reflected back (see the left-hand side of Figure 13.1). Going away from the maximal preserving region the signal saturates to 0.5 eV. This saturation is also visible in Figure 13.2 for the elements which convert the polarization in reflection and for the elements which preserve the polarization in transmission. They have asymmetric shapes for the presence of other modes out of the preserving region (see Fig. 2 in [142]). The saturation is a natural consequence of the application of time-reversal symmetry (see eq. (13.4) when t_{+-} goes to 0, *i.e.* out of the preserving region). The transmitted signal of the two polarizations is reversed by sending the light from the opposite side of the chiral mirror.

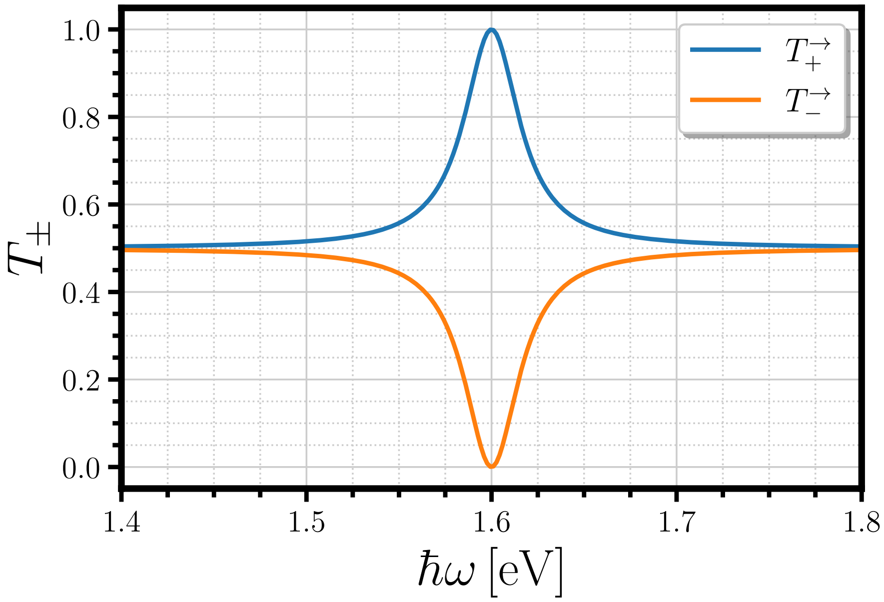

Figure 13.3: Transmittances $T_{\pm}$ at normal incidence from the single chiral mirror as a function of $\hbar\omega$ in the unit of eV. Parameters are as follows: $\hbar\omega_{pr} = 1.6\,\text{eV}$, $\hbar\gamma_{pr} = 0.02\,\text{eV}$ and $\theta = 0$.

13.1.2 Enantiomer of the single mirror

The enantiomer of the chiral mirror is obtained under a π-rotation along one of the polarization axis, x or y to be in agreement with the choice that z is the light propagation axis. This implies an application of one of these rotations on the scattering matrix S_{Cm} (see eq. (13.3)).

The scattering matrix S_{Cm} connects outgoing circularly polarized light rays with the incoming ones as it follows

$$\begin{pmatrix} \hat{e}_+ \\ \hat{e}_- \\ \hat{e}'_+ \\ \hat{e}'_- \end{pmatrix}_{out} = S_{Cm} \begin{pmatrix} \hat{e}_+ \\ \hat{e}_- \\ \hat{e}'_+ \\ \hat{e}'_- \end{pmatrix}_{in} , \tag{13.7}$$

where $\hat{e}_\pm \equiv \frac{1}{\sqrt{2}}(\hat{e}_x \pm i\hat{e}_y)$ (see also Section 10.3.3) are the unit vectors on the left-hand side of the chiral mirror and the primed unit vectors are the vectors on the right-hand side of the single chiral mirror.
The unit vectors in the circular basis, $\hat{e}_\pm$, are directly linked to the unit vectors in the linear basis, $\hat{e}_{x,y}$, through a linear transformation:

$$\begin{pmatrix} \hat{e}_+ \\ \hat{e}_- \\ \hat{e}'_+ \\ \hat{e}'_- \end{pmatrix} = U_{x,y\to\pm} \begin{pmatrix} \hat{e}_x \\ \hat{e}_y \\ \hat{e}'_x \\ \hat{e}'_y \end{pmatrix} \quad \text{with } U_{x,y\to\pm} = \frac{1}{\sqrt{2}} \begin{pmatrix} 1 & i & 0 & 0 \\ 1 & -i & 0 & 0 \\ 0 & 0 & 1 & i \\ 0 & 0 & 1 & -i \end{pmatrix} . \tag{13.8}$$

The π-rotations along the linear polarization axis x and y send $\hat{e}_x \to \hat{e}_x$, $\hat{e}_y \to -\hat{e}_y$ and $\hat{e}_x \to -\hat{e}_x$, $\hat{e}_y \to \hat{e}_y$, respectively. Their application at the matrix level is the following

$$\begin{gathered} \begin{pmatrix} \hat{e}_x \\ -\hat{e}_y \\ \hat{e}'_x \\ -\hat{e}'_y \end{pmatrix} = R_x(\pi) \begin{pmatrix} \hat{e}_x \\ \hat{e}_y \\ \hat{e}'_x \\ \hat{e}'_y \end{pmatrix} \text{with } R_x(\pi) = \begin{pmatrix} 1 & 0 & 0 & 0 \\ 0 & -1 & 0 & 0 \\ 0 & 0 & 1 & 0 \\ 0 & 0 & 0 & -1 \end{pmatrix} , \\ \begin{pmatrix} -\hat{e}_x \\ \hat{e}_y \\ -\hat{e}'_x \\ \hat{e}'_y \end{pmatrix} = R_y(\pi) \begin{pmatrix} \hat{e}_x \\ \hat{e}_y \\ \hat{e}'_x \\ \hat{e}'_y \end{pmatrix} \text{with } R_y(\pi) = \begin{pmatrix} -1 & 0 & 0 & 0 \\ 0 & 1 & 0 & 0 \\ 0 & 0 & -1 & 0 \\ 0 & 0 & 0 & 1 \end{pmatrix} . \end{gathered} \tag{13.9}$$

Now the matrices $R_x(\pi)$ and $R_y(\pi)$ can be adpated for the circular basis using $U_{x,y\to\pm}$:

$$\begin{gathered} \bar{R}_x(\pi) \equiv U_{x,y\to\pm} R_x(\pi) U^{-1}_{x,y\to\pm} = \begin{pmatrix} 0 & 1 & 0 & 0 \\ 1 & 0 & 0 & 0 \\ 0 & 0 & 0 & 1 \\ 0 & 0 & 1 & 0 \end{pmatrix} \\ \bar{R}_y(\pi) \equiv U_{x,y\to\pm} R_y(\pi) U^{-1}_{x,y\to\pm} = \begin{pmatrix} 0 & -1 & 0 & 0 \\ -1 & 0 & 0 & 0 \\ 0 & 0 & 0 & -1 \\ 0 & 0 & -1 & 0 \end{pmatrix} . \end{gathered} \tag{13.10}$$

Finally, the enantiomeric scattering matrix of S_{Cm} is found by applying the π-rotations in the circular basis. The form of the matrix is

$$\boxed{S_{ECm} = \bar{R}_{x,y}(\pi) S_{Cm} \bar{R}^{-1}_{x,y}(\pi) = \begin{pmatrix} |t_{+-}| & -|t| \cdot e^{i\psi} & |t| & 0 \\ -|t| \cdot e^{i\psi} & 0 & |t_{+-}| \cdot e^{i\psi} & |t| \\ |t| & |t_{+-}| \cdot e^{i\psi} & 0 & |t| \cdot e^{-i\psi} \\ 0 & |t| & |t| \cdot e^{-i\psi} & -|t_{+-}| \cdot e^{-2i\psi} \end{pmatrix} , \quad (13.11)}$$

where $\bar{R}_{x,y}(\pi)$ denotes the application of $\bar{R}_x(\pi)$ or $\bar{R}_y(\pi)$.

The matrix S_{ECm} is equal to S_{Cm} sending $+ \to -$, or viceversa, in the elements of Jones matrices. The enantiomer of the chiral mirror acts in the opposite way regarding the polarizations. Figure 13.4 shows the transmittances $T_\pm$, by using the transfer matrix approach already explained in the previous Subsection, for the light propagation from the left to the right side of the enantiomer. The transmittances are exactly reversed with respect to the previous Figure 13.3 of the chiral mirror. If the light is propagating from the opposite side of the enantiomer the signal is the same as the Figure 13.3 shows.

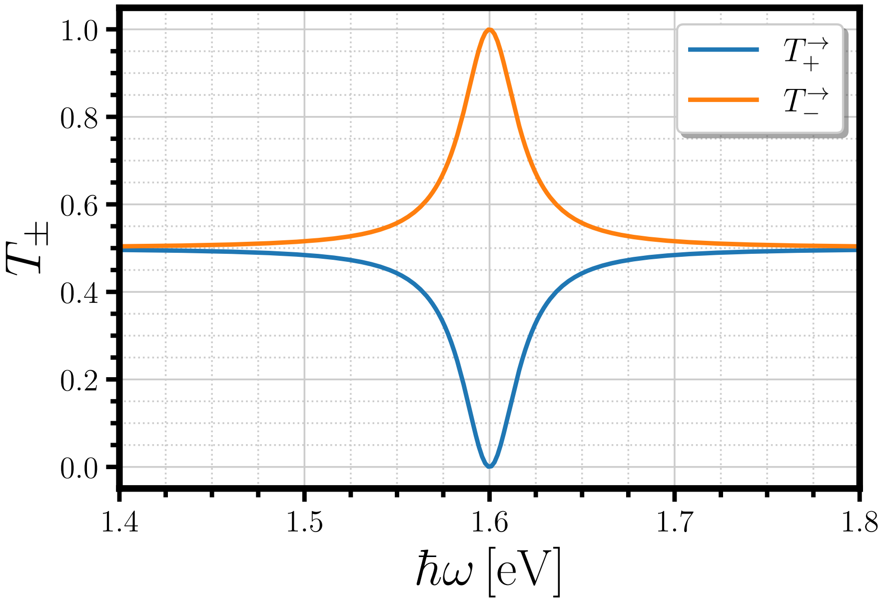

Figure 13.4: Transmittances $T_\pm$ at normal incidence from the enantiomer of the chiral mirror as a function of $\hbar\omega$ in the unit of eV. Parameters are as follows: $\hbar\omega_{pr} = 1.6\,\mathrm{eV}$, $\hbar\gamma_{pr} = 0.02\,\mathrm{eV}$ and $\theta = 0$.

13.2 Fabry-Pérot interferometer with chiral mirrors

The construction of the Fabry-Pérot interferometer, using the modelled chiral mirrors, is the subject of this Section. The interferometer contains the preserving region and this region has an effect on the standing light modes in cavity. The transmittance ($+$ or $-$) and the DCT signal can provide enough information to explain the effect of the preserving region inherited by the chiral mirror and its enantiomer.

13.3 Transmittance

The transmittance T_+ as a function of $\hbar\omega$ and d is shown in Figure 13.5. In this Figure the helicity-preserving region is chosen to be detuned with respect to the energy scale of the Figure ($\hbar\omega_{pr} = 3.0\,\mathrm{eV}$). Thus, the "normal" cavity light modes are recovered. In particular, the Figure focuses on two of them. Using eq. (11.11), the distance where one mode has the maximum transmission can be calculated. For instance, for $d = 200\,\mathrm{nm}$ and $\hbar\omega = 1.6\,\mathrm{eV}$ the m value is approximately 0.5. Then, the next maximum (of the second mode in Figure 13.5) is located at distance

$$d = \frac{m+1}{2\hbar\omega} 1239.8 \approx 581\,\mathrm{nm}. \tag{13.12}$$

The inclusion and the effect of the preserving region on one of the light modes is shown in Figure 13.6. The helicity-preserving region acts as a perfect converter in transmission. It fully transmits and converts LHC polarized light into RHC polarized light through the first chiral mirror and it again fully transmits and reconverts RHC into LHC polarized light through the chiral enantiomer (see the right-hand side of Figure 13.1).

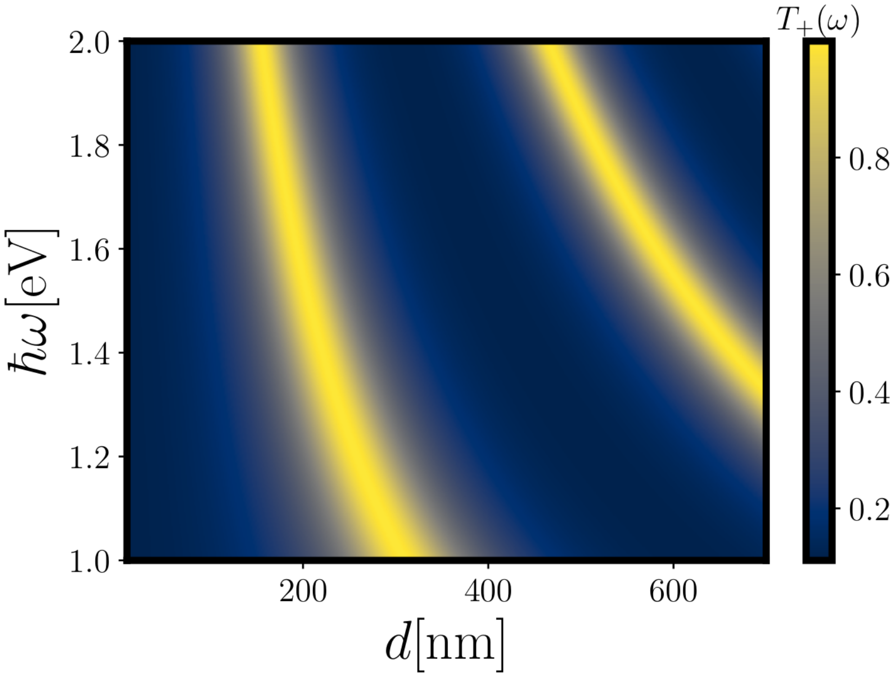

Figure 13.5: Transmittance T_+ at normal incidence from a Fabry-Pérot interferometer, composed by air-chiral mirror-air-chiral enantiomer of the mirror-air, as a function of the length d of the internal layer of air in the unit of nm and as a function of $\hbar\omega$ in the unit of eV. Parameters are as follows: $\hbar\omega_{pr} = 3.0\,\text{eV}$, $\hbar\gamma_{pr} = 0.02\,\text{eV}$ and $\theta = 0$.

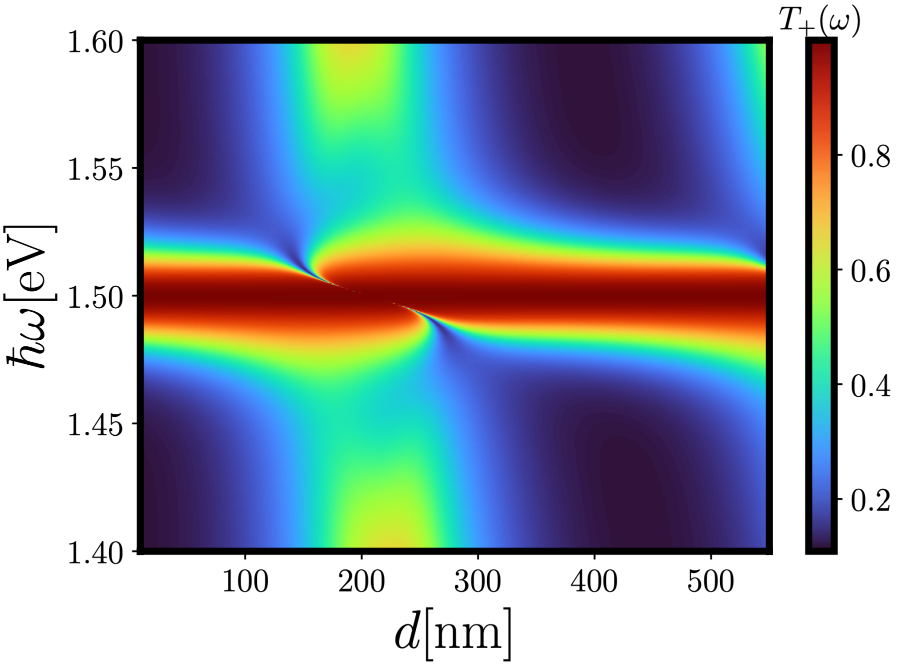

Figure 13.6: Transmittance T_+ at normal incidence from a Fabry-Pérot interferometer, composed by air-chiral mirror-air-chiral enantiomer of the mirror-air, as a function of the length d of the internal layer of air in the unit of nm and as a function of $\hbar\omega$ in the unit of eV. Parameters are as follows: $\hbar\omega_{pr} = 1.5\,\text{eV}$, $\hbar\gamma_{pr} = 0.02\,\text{eV}$ and $\theta = 0$.

The consequence of this process is visible in Figure 13.6 as a straight red line, distance independent, of maximum transmission. The light mode which encounters that region is subjected to a filtering effect, in such a way the energy is conserved without any presence of losses. This occurs at the center of the lineshape. The interaction of the cavity mode and the preserving region generates also an asymmetric feature around the center of maximum transmission. This asymmetric feature is commonly known as a Fano resonance which appears for the interaction of background radiation and a narrow discrete state (the lineshape of the preserving region) [44]. The generation of the asymmetry comes from the usage of the coupled-mode theory to model the response of the chiral mirror and its enantiomer.

13.4 DCT

The Differential Circular Transmission, defined as $2(T_+ - T_-)/(T_+ + T_-)$ takes into account the discrimination of one of the two polarizations over the transmitted signal. It reaches the maximum value of 2 at the center of the preserving region where T_+ is 1 and T_- is 0 (see Figure 13.7). The minimum value of 0 is attained "away" (fractions of eV in energy) from the helicity-preserving region where there is not any distinction of the two polarizations. The interesting behaviour is in the close proximity to the preserving region. There, as it is shown at the beginning of the present Chapter (see the right-hand side of Figure 13.1), an intermediate behaviour between a normal mirror and a fully transmitting region occurs. The result is a visible discrimination in Figure 13.7 where DCT tends to be negative, close to the maximal value of 2, and the opposite polarization ($-$) of the preserving region ($+$) is more transmitted out of the interferometer.

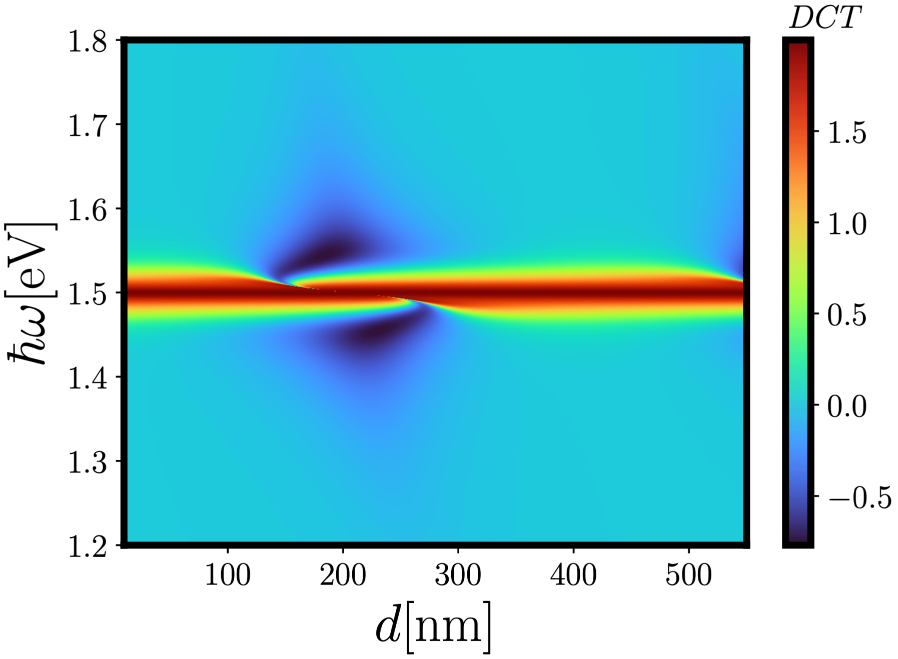

Figure 13.7: DCT at normal incidence from a Fabry-Pérot interferometer, composed by air-chiral mirror-air-chiral enantiomer of the mirror-air, as a function of the length d of the internal layer of air in the unit of nm and as a function of $\hbar\omega$ in the unit of eV. Parameters are as follows: $\hbar\omega_{pr} = 1.5\,\text{eV}$, $\hbar\gamma_{pr} = 0.02\,\text{eV}$ and $\theta = 0$.

This scenario is reversed if the cavity is composed by the chiral enantiomeric mirror-air-chiral mirror (see Figure 13.8). In this last case the center of preserving region has a DCT value of -2, as maximum, and the intermediate region reaches a positive discrimination.

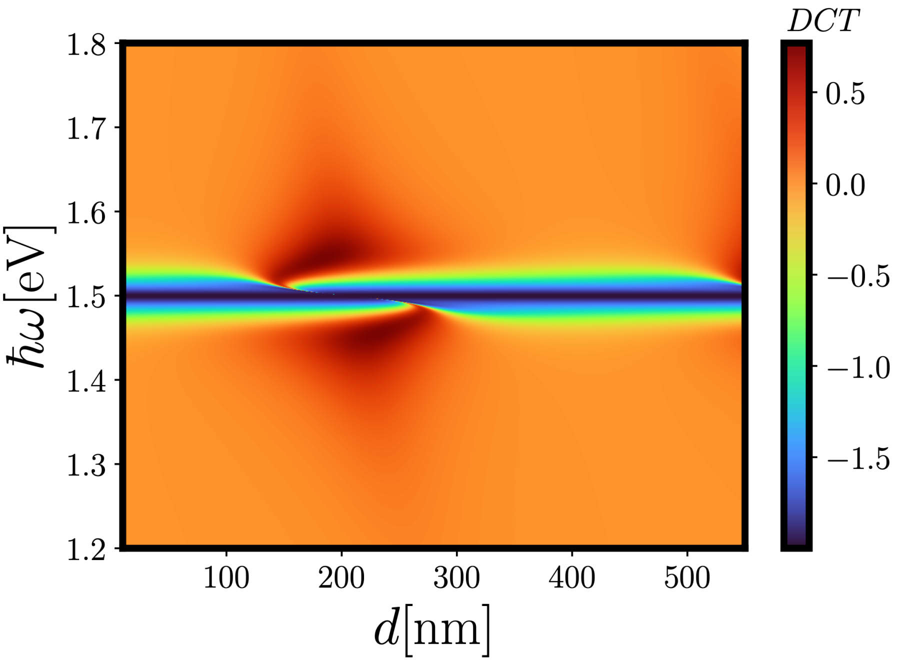

Figure 13.8: DCT at normal incidence from a Fabry-Pérot interferometer, composed by air-chiral enantiomer of the mirror-air-chiral mirror-air, as a function of the length d of the internal layer of air in the unit of nm and as a function of $\hbar\omega$ in the unit of eV. Parameters are as follows: $\hbar\omega_{pr} = 1.5\,\mathrm{eV}$, $\hbar\gamma_{pr} = 0.02\,\mathrm{eV}$ and $\theta = 0$.

An additional qualitative understanding of the DCT signal, of an empty cavity made by chiral mirrors, can be developed using the same analytical approach of the Section 12.4. The calculation is done with the presence of the chiral material inside the cavity. The limiting case for the empty cavity can be obtained from this more general derivation.

13.4.1 Normal incidence with perfect helicity preserving mirrors (analytical approach)

Now let's suppose that the mirrors have the property to preserve the handedness of the incoming circularly polarized light at each reflections inside the cavity. Then the analytical calculation is very similar to the case of the achiral interferometer (see section 12.3) at normal incidence, but the accumulation of phases inside the cavity has a sign, $+$ for the preserved LHC polarized light and - for the RHC polarized light. Another difference is that now the mirrors are chiral, so the first mirror is not equal to the second one to obtain the conservation of the helicity inside the cavity.

By redoing the calculation of section 12.4, and taking into account the difference in the sign of the accumulated phase, the transmittance of a preserving chiral Fabry-Pérot is

$$\tau^{hp}_{\pm,\perp}(\omega) = \frac{T^2_{1,\pm,hp} T^2_{2,\pm,hp} e^{-\alpha_\pm L}}{\left(1-\sqrt{R_{1,\pm,hp}R_{2,\pm,hp}}e^{-\alpha_\pm L}\right)^2 + 4\sqrt{R_{1,\pm,hp}R_{2,\pm,hp}}e^{-\alpha_\pm L}\sin^2\beta_\pm}, \tag{13.13}$$

where $\alpha_\pm = 2kn'_{\pm,im}(\omega)$, $\beta_\pm = kn'_{\pm,re}(\omega)L$, $T_{i,\pm,hp} \equiv |t_{i,\pm\pm}|^2$ and $R_{i,\pm,hp} \equiv |r_{i,\pm\pm}|^2$, with $i = 1, 2$, are the transmittances and the reflectances of the first and second helicity preserving mirror, respectively.

Using perfect helicity preserving mirrors, the DCT at normal incidence has not anymore a simple expression as the formula (12.34). In this case, the DCT obtained by eq. (13.13) gives

$$DCT^{hp}_{\perp} = 2\frac{\mathcal{T}_+e^{-\alpha_+L} - \mathcal{T}_-e^{-\alpha_-L} + \mathcal{T}_+e^{-2\alpha L}\left(\mathcal{R}_-e^{-\alpha_-L} - 2\sqrt{\mathcal{R}_-}\cos 2\beta_-\right) - \mathcal{T}_-e^{-2\alpha L}\left(\mathcal{R}_+e^{-\alpha_+L} - 2\sqrt{\mathcal{R}_+}\cos 2\beta_+\right)}{\mathcal{T}_+e^{-\alpha_+L} + \mathcal{T}_-e^{-\alpha_-L} + \mathcal{T}_+e^{-2\alpha L}\left(\mathcal{R}_-e^{-\alpha_-L} - 2\sqrt{\mathcal{R}_-}\cos 2\beta_-\right) + \mathcal{T}_-e^{-2\alpha L}\left(\mathcal{R}_+e^{-\alpha_+L} - 2\sqrt{\mathcal{R}_+}\cos 2\beta_+\right)}, \tag{13.14}$$

where $\mathcal{T}_\pm \equiv T^2_{1,\pm,hp} T^2_{2,\pm,hp}$, $\mathcal{R}_\pm \equiv R_{1,\pm,hp} R_{2,\pm,hp}$.
It is interesting to note that $DCT^{hp}_\perp$ is not 0 if $\alpha_\pm = 0$ and it becomes

$$DCT^{hp}_\perp(\alpha_\pm = 0) = 2\frac{\mathcal{T}_+ - \mathcal{T}_- + \mathcal{T}_+\left(\mathcal{R}_- - 2\sqrt{\mathcal{R}_-}\cos 2\beta_-\right) - \mathcal{T}_-\left(\mathcal{R}_+ - 2\sqrt{\mathcal{R}_+}\cos 2\beta_+\right)}{\mathcal{T}_+ + \mathcal{T}_- + \mathcal{T}_+\left(\mathcal{R}_- - 2\sqrt{\mathcal{R}_-}\cos 2\beta_-\right) + \mathcal{T}_-\left(\mathcal{R}_+ - 2\sqrt{\mathcal{R}_+}\cos 2\beta_+\right)}. \tag{13.15}$$

The mirrors are chiral, thus they produce asymmetries in transmission without having absorption inside the chiral layer in contrast to the case with “normal” mirrors.

Figure 13.9 shows the DCT signal of the Fabry-Pérot interferometer with chiral mirrors for $d = 200\,\text{nm}$ (the thickness of the internal layer of air). The shape of the DCT is well-reproduced by the eq. (13.15) if $\mathcal{T}_\pm$ are promoted to be the transmittances + and − of the interferometer. The promotion of these quantities to be transmittances is done to include the missing elements (off-diagonal elements) of the transmission or reflection matrices of the analytical approach, which takes into account only diagonal elements. In fact, the Jones matrices of the chiral mirrors have the form of eq. (13.1).
The added value of this qualitative approach is that it offers a way to understand the DCT signal close to its maximum intensity. The negative discrimination, shown in Figure 13.7 and Figure 13.9, is due to the increasement of $\mathcal{R}_+$ (it is 1 at $\hbar\omega_{pr} = 1.5\,\text{eV}$) and to the fact that $\mathcal{T}_- > \mathcal{T}_+$ near the preserving region. The imbalance between the internal reflectances (in cavity) of the chiral mirrors and the transmittances generate a total negative discrimination in the DCT signal.

13.4.2 Green function approach

A different approach to study the DCT of the empty cavity is based on the propagation of the Jones matrices through the overall system. The method of collecting the matrices is similar to the scalar case of Section 12.3, with the difference that now all the elements are matrices and they are multiplied from the right to the left (opposite convention of the transfer matrix approach described in Section 10.4.5). Here the calculation to get the matrix for the downward (or from the left to the right-hand side of the interferometer) propagation is shown.

The first transmitted matrix amplitude through the first chiral mirror (1) and the enantiomer (2) is

$$A_{1,\rightarrow} = T_2 P T_1 A_0, \tag{13.16}$$

where P is the matrix for the phase propagation and, for simplicity, the arrow of the propagating wave is added only on the total amplitude $A_{1,\rightarrow}$.
The second amplitude contains the reflection matrices of the internal side of the chiral mirrors:

$$A_{2,\rightarrow} = T_2 P R_1 P R_2 P T_1 A_0. \tag{13.17}$$

The same calculation can be done for the amplitude $A_{p,\rightarrow}$. The final total amplitude is obtained summing all the amplitudes and sending p to infinity as it is done for the eq. (12.25). The final result is a transmittance in a matrix form:

$$\boxed{T_{GF,\rightarrow} = T_2 G T_1 \quad \text{with } G = \frac{1}{P^{-1} - \Sigma}} \tag{13.18}$$

where G can be seen as the Green function or a free propagator and $\Sigma \equiv R_1 P R_2$ the self-energy of a scattering problem.

The transmittance $T_{GF,\rightarrow}$ can be evaluated by using the Jones matrices of the chiral mirrors (see the eqs. (13.3) and (13.11)) and a phase matrix P, which is a diagonal matrix with elements $e^{i\phi}$ where $\phi \equiv 2\pi d/\lambda$. The scalar transmittances T_+ and T_- are the diagonal elements of the matrix $T^\dagger_{GF,\rightarrow} T_{GF,\rightarrow}$ because

$$T^\dagger_{GF,\rightarrow} T_{GF,\rightarrow} = \begin{pmatrix} |t_{++}|^2 + |t_{+-}|^2 & t^\star_{++} t_{-+} + t^\star_{+-} t_{--} \\ t^\star_{-+} t_{++} + t^\star_{--} t_{+-} & |t_{--}|^2 + |t_{-+}|^2 \end{pmatrix}. \tag{13.19}$$

Thus the DCT, at normal incidence, can be computed as the usual way as the ratio between ΔT and the average of T. A very simple formula can be obtained at the correspondance of the light mode. The expression of this formula is

$$DCT_{\perp,GF} = \frac{16(4-\delta^4)}{32(1+\delta^2)+8\delta^4+\delta^6} \quad \text{with } \delta \equiv \frac{\omega-\omega_{pr}}{\gamma_{pr}}, \tag{13.20}$$

where the phase of propagation is $\phi = \pi/2$ (analogously $d = \lambda/4$), ω_{pr} is frequency of the preserving region and γ_{pr} its linewidth.

Figure 13.10 shows DCT evaluated along one of the cavity light mode, the case $d = \lambda/4$. The associated m value (see eq. 13.12) is $1/2$, which corresponds to a distance of about 207 nm for $\hbar\omega = 1.5\,\text{eV}$. Figure 13.5 or Figure 13.7 shows indeed that at the coordinates $d \approx 207\,\text{nm}$ and $\hbar\omega = 1.5\,\text{eV}$ DCT has the maximum value of 2, the center of the intersection of the light mode and the preserving region. Varying the energy, d varies accordingly to mantain the trajectory of DCT along the light mode (for $\hbar\omega = 1.8\,\text{eV}$ the distance $d \approx 172.2\,\text{nm}$). On the light mode, the numerical approach and the derived formulas show the same behaviour in the two limiting cases, that is the center of the preserving band and far away from it. The Green function approach, based on the propagation of the Jones matrices, matches perfectly the DCT of the transfer matrix approach. All the three approaches show that indeed the shape of DCT along the light mode is symmetric. The Fano resonances are generated around the center of the intersection of the two modes, where the background radiation can interact with the less intense part of the preserving region. Consequently, the Fano resonances do not unsymmetrize the DCT signal at the center of the cavity light mode, with the presence of the preserving region.

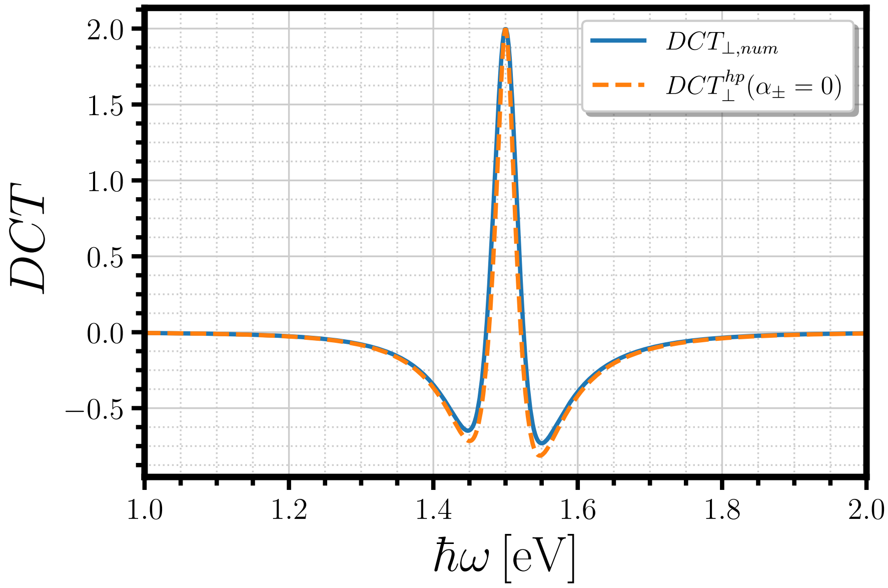

Figure 13.9: $DCT_\perp$ for the numerical approach using the transfer matrices (light-blue line), $DCT_\perp$ for the analytical approach (see eq. (13.15)) (orange dashed line) from a Fabry-Pérot interferometer, composed by air-chiral mirror-air-chiral enantiomer of the mirror-air, as a function of $\hbar\omega$ in the unit of eV. Parameters are as follows: $\hbar\omega_{pr} = 1.5\,\text{eV}$, $\hbar\gamma_{pr} = 0.02\,\text{eV}$, $d = 200\,\text{nm}$ and $\theta = 0$.

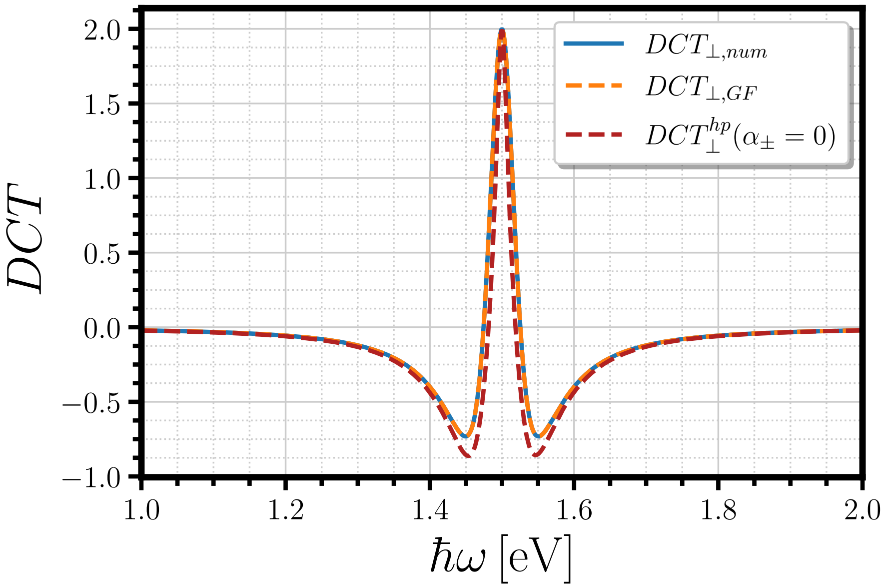

Figure 13.10: $DCT_{\perp}$, along the cavity light mode, for the numerical approach using the transfer matrices (light-blue line), $DCT_{\perp}$ for the Green function approach (orange dashed line) and $DCT_{\perp}$ for the analytical approach (see eq. (13.15)) (red dashed line) from a Fabry-Pérot interferometer, composed by air-chiral mirror-air-chiral enantiomer of the mirror-air, as a function of $\hbar\omega$ in the unit of eV. Parameters are as follows: $\hbar\omega_{pr} = 1.5\,\text{eV}$, $\hbar\gamma_{pr} = 0.02\,\text{eV}$, $d = \lambda/4$ and $\theta = 0$.

The Fabry-Pérot interferometer, with the previous modelized chiral mirrors, is now filled with a chiral layer, the same chiral layer (or Pasteur medium) described in Chapter 11.
The essence of the next sections is to understand which role plays the optical activity of the material with the presence of the "intrinsic" chirality injected by the chiral mirrors. Moreover, what is the influence of the preserving region on the DCT signal of the new entire system and the effect of the "bare" material properties, such as the refractive index or the oscillator strength, on the light modes are thematics addressed along the next sections.

13.5 Influence of the bare material on the light modes for a low oscillator strength

The presence of a medium inside the interferometer, which is not air, has an effect on the cavity light modes. In particular, here the interest is to monitor the change close to the preserving region in a low coupling regime, that is when the strength of the material, defined as $(\hbar\omega_p\sqrt{f_0})_{Pasteur}$, is lower or comparable to the damping $\gamma_{Pasteur}$ (in section 12.5 this distinction is explained).

13.5.1 Transmittance

The transmittance T_+, shown in Figure 13.11, contains the information about how the cavity light modes are altered by the inclusion of a Pasteur medium. In a low coupling regime, the chirality of the Pasteur medium is negligible (see eq. (12.19)), for a low value of γ (for $\hbar\omega_p\sqrt{f_0} = \hbar\gamma \approx 0.01\,\text{eV}$ the chiral parameter $\kappa_p \approx 10^{-6}$), and the material mantains only its bare properties ($n > 1$ with a low dispersive part). Thus, the bare material generates an impedance mismatch across the preserving region which is visible as a misalignement and a disconnection of the light modes. The Fano resonances become clearly distinguishable as thin lines which "cut" the helicity-preserving region. By increasing the refractive index of the material, the impedance mismatch increases and the light modes become more dense. The thin lines of the Fano resonances become thicker. The effect of the increasing of refractive index is shown in Figure 13.12.

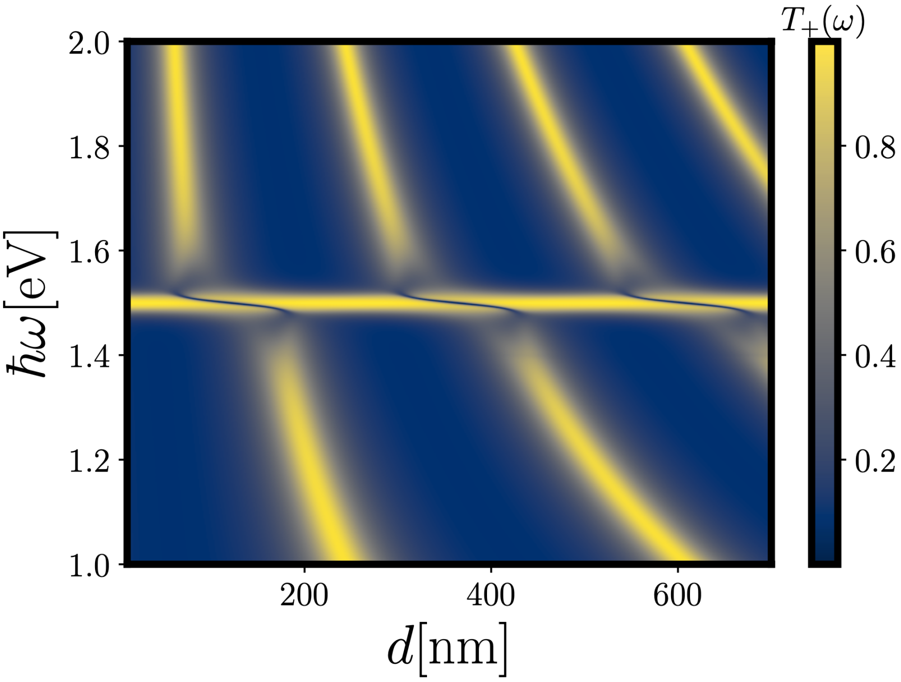

Figure 13.11: Transmittance T_+ at normal incidence from a Fabry-Pérot interferometer, composed by air-chiral mirror-Pasteur medium-chiral enantiomer of the mirror-air, as a function of the length d of the Pasteur medium in the unit of nm and as a function of $\hbar\omega$ in the unit of eV. Parameters are as follows: $\hbar\omega_{pr} = 1.5\,\mathrm{eV}$, $\hbar\gamma_{pr} = 0.02\,\mathrm{eV}$, $\varepsilon_{\infty,Pasteur} = 2.89$, $(\hbar\omega_p\sqrt{f_0})_{Pasteur} = \hbar\gamma_{Pasteur} = 0.01\,\mathrm{eV}$, $\hbar\omega_{0,Pasteur} = 1.4\,\mathrm{eV}$, $\kappa_p = 10^{-3}$ and $\theta = 0$.

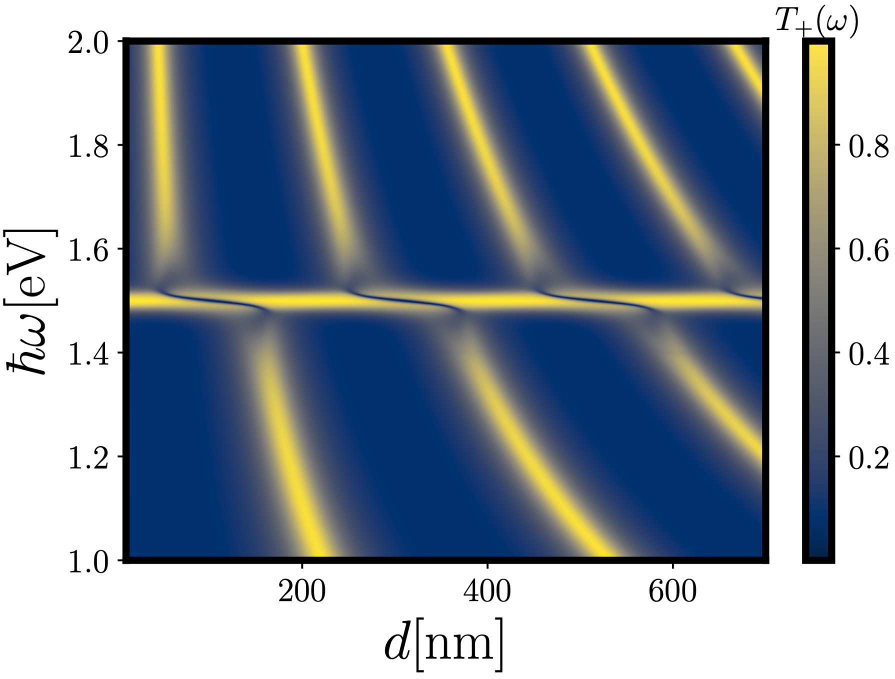

Figure 13.12: Transmittance T_+ at normal incidence from a Fabry-Pérot interferometer, composed by air-chiral mirror-Pasteur medium-chiral enantiomer of the mirror-air, as a function of the length d of the Pasteur medium in the unit of nm and as a function of $\hbar\omega$ in the unit of eV. Parameters are those of Figure 13.11, except that $\varepsilon_{\infty,Pasteur} = 4$.

13.5.2 DCT

The DCT of the interferometer, filled with the Pasteur medium, has the same peculiarities of the empty system (see Section 13.4). The substantial difference is that the negative discrimination (the region in close proximity to the preserving region) is asymmetric with respect to the preserving region. Figure 13.13 shows this asymmetric discrimination. Thus, in the low coupling regime the DCT of the full system differs from the DCT of the empty cavity in these differently unsymmetrized regions. Figure 13.15 shows a case where in one of the regions close to the maximal DCT signal, the full system has a negative DCT signal higher than the empty system. The negative peak has, as the upper bound, the value of -1 for the DCT. This value is exactly half of the maximal DCT signal reached at the center of the preserving region. The upper bound can be understood using the eq. (13.15). In fact, one of the best scenarios for the maximal negative DCT is with $\mathcal{T}_+ \approx 0.3$, $\mathcal{T}_- \approx 0.7$, $\mathcal{R}_+ \approx 0.3$, $\mathcal{R}_- \approx 0.1$, $\cos 2\beta \approx 0.2$ that produces a $DCT \to -1$.

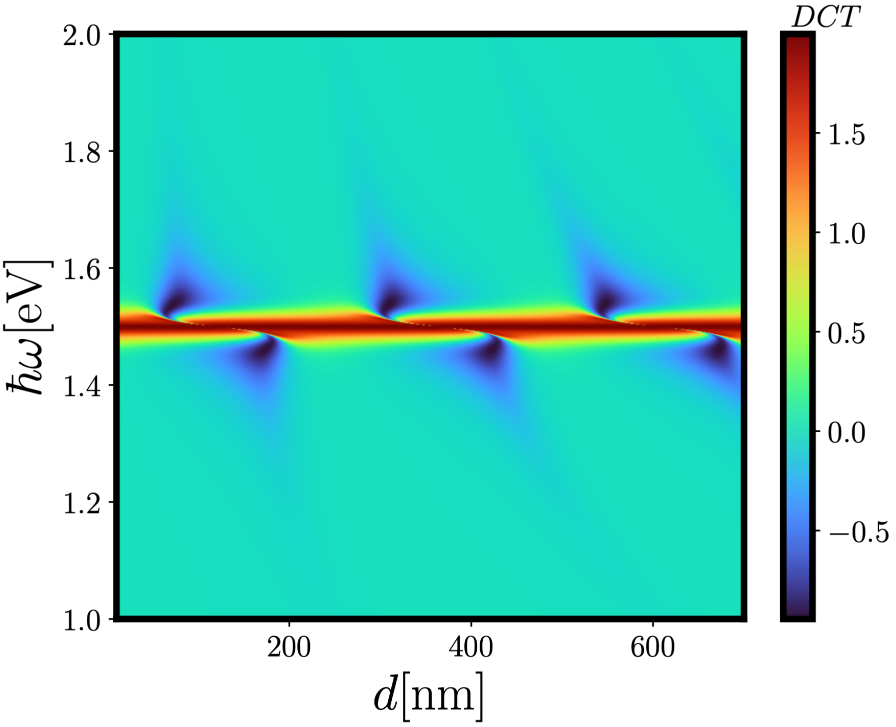

Figure 13.13: DCT at normal incidence from a Fabry-Pérot interferometer, composed by air-chiral mirror-Pasteur medium-chiral enantiomer of the mirror-air, as a function of the length d of the Pasteur medium in the unit of nm and as a function of $\hbar\omega$ in the unit of eV. Parameters are as follows: $\hbar\omega_{pr} = 1.5\,\text{eV}$, $\hbar\gamma_{pr} = 0.02\,\text{eV}$, $\varepsilon_{\infty,Pasteur} = 2.89$, $(\hbar\omega_p f_0)_{Pasteur} = \hbar\gamma_{Pasteur} = 0.01\,\text{eV}$, $\hbar\omega_{0,Pasteur} = 1.4\,\text{eV}$, $\kappa_p = 10^{-3}$ and $\theta = 0$.

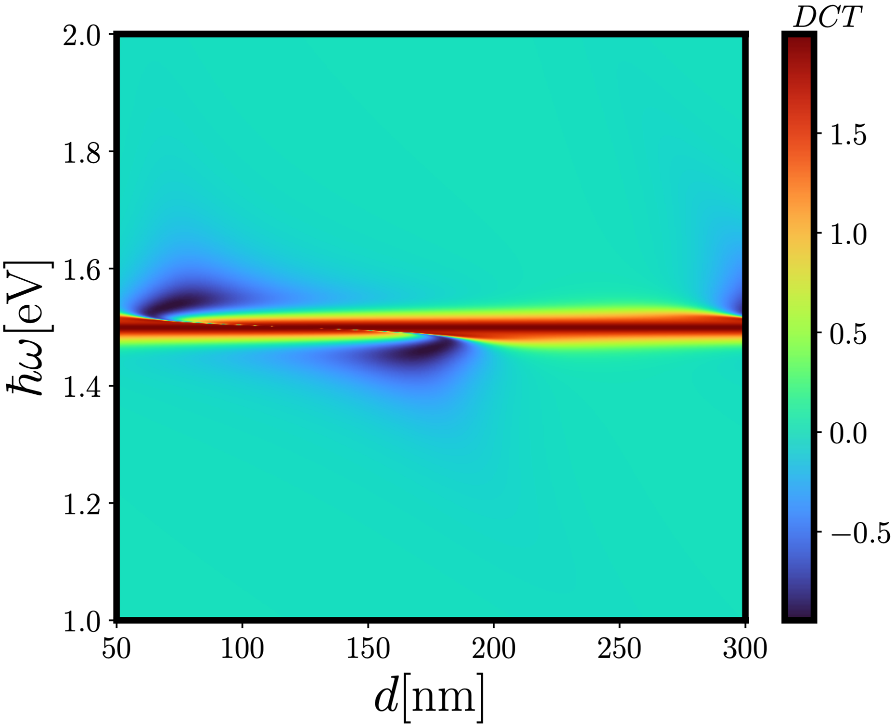

Figure 13.14: DCT at normal incidence from a Fabry-Pérot interferometer, composed by air-chiral mirror-Pasteur medium-chiral enantiomer of the mirror-air, as a function of the length d of the Pasteur medium in the unit of nm and as a function of $\hbar\omega$ in the unit of eV. Parameters are those of Figure 13.13.

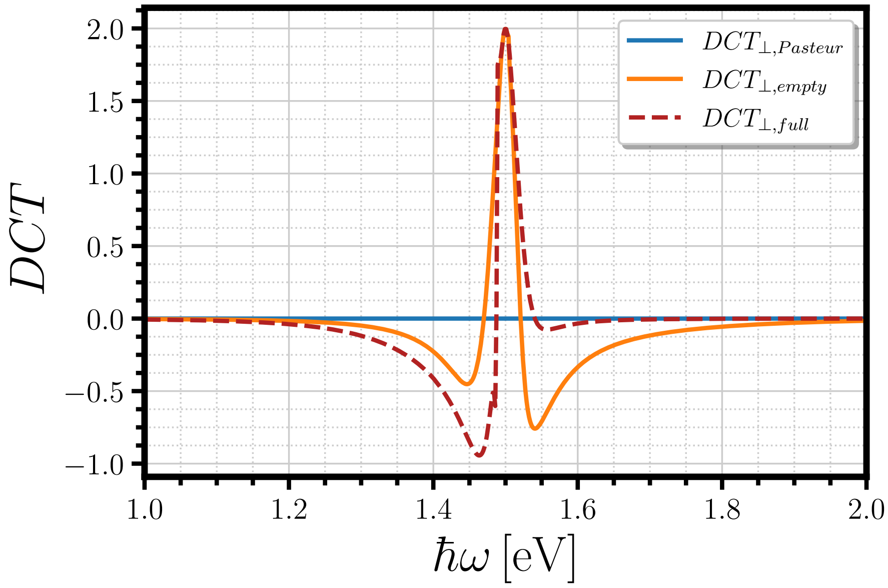

Figure 13.15: $DCT_{\perp}$ for the Pasteur medium (without the mirrors) (light-blue line), $DCT_{\perp}$ for the empty cavity made by chiral mirrors (orange line) and $DCT_{\perp}$ for the full system (red dashed line) as a function of $\hbar\omega$ in the unit of eV. Parameters are those of Figure 13.13, except that $d_{Pasteur} = 175\,\text{nm}$.

13.6 Transition to the strong coupling regime and discrimination of Polaritonic branches

13.6.1 Transmittance

The transition from the low coupling regime to the strong coupling regime occurs when the oscillator strength of the material, inside the cavity, is large enough to create a splitting of the light modes. The splitting is generated at resonance between the cavity mode and material resonance defined as $\omega_{0,Pasteur}$ (see Section 12.5). Figure 13.16 shows the case of the strong regime for only one mode, by varying the length of the material, without the inclusion of the preserving region (the same splitting obtained with "normal" mirrors). The two Polaritonic branches are clearly visible with the two yellow lines.
The inclusion of the preserving region generates the same asymmetric misalignement of the light modes, analyzed in Figure 13.11. In particular, this happens when the preserving region crosses the Polaritonic branches. The Figure 13.17 show the crossing of the preserving region through the lower Polaritonic branch.

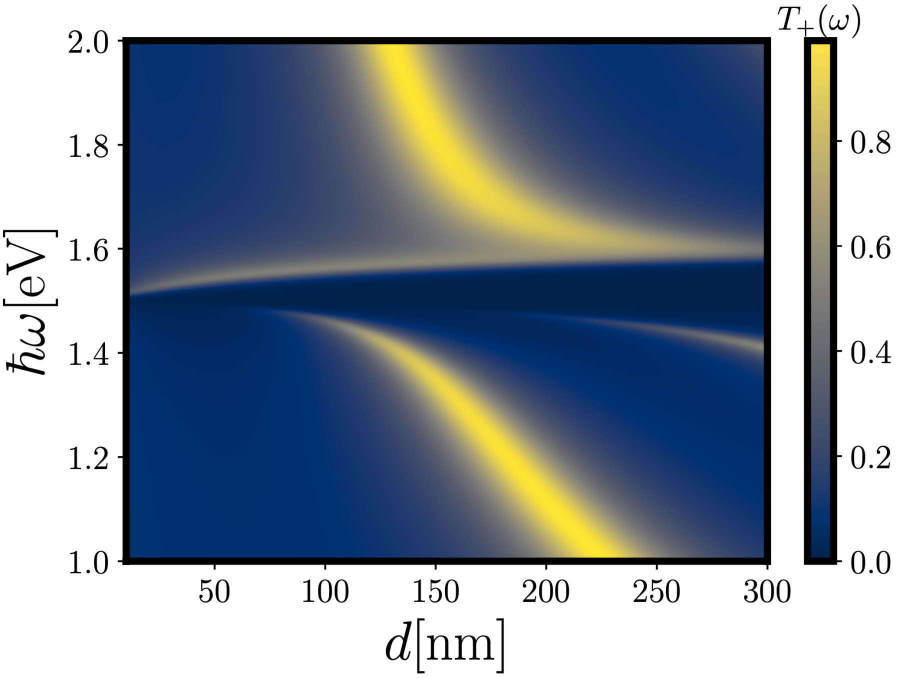

Figure 13.16: Transmittance T_+ and onset of Polaritons at normal incidence from a Fabry-Pérot interferometer, composed by air-chiral mirror-Pasteur medium-chiral enantiomer of the mirror-air, as a function of the length d of the Pasteur medium in the unit of nm and as a function of $\hbar\omega$ in the unit of eV. Parameters are as follows: $\hbar\omega_{pr} = 3.0\,\text{eV}$, $\hbar\gamma_{pr} = 0.02\,\text{eV}$, $\varepsilon_{\infty,Pasteur} = 2.89$, $(\hbar\omega_p\sqrt{f_0})_{Pasteur} = 1.0\,\text{eV}$, $\hbar\gamma_{Pasteur} = 0.01\,\text{eV}$, $\hbar\omega_{0,Pasteur} = 1.5\,\text{eV}$, $\kappa_p = 10^{-3}$ and $\theta = 0$.

13.6.2 DCT

The DCT signal, in the strong coupling regime, comes from the chirality of the mirrors, which induces a discrimination similar to the case of the empty cavity, and from the chirality of the Pasteur medium. The two types of chirality are clearly visible in Figure 13.18, the DCT signal of Figure 13.17. The DCT of the chiral material, studied in Section 12.6, is confined around its resonance frequency, $\omega_{0,Pasteur}$. It increases with the oscillator strength and with the thickness. In particular, if the $(\hbar\omega_p f_0)_{Pasteur} \approx 100 \cdot \hbar\gamma_{Pasteur}$, the strong regime, DCT reaches values of the order $10^3 \cdot \kappa_p$. This strong signal modifies the discrimination of the total DCT (chiral mirrors plus Pasteur medium), close to the resonance of the chiral material. Varying the

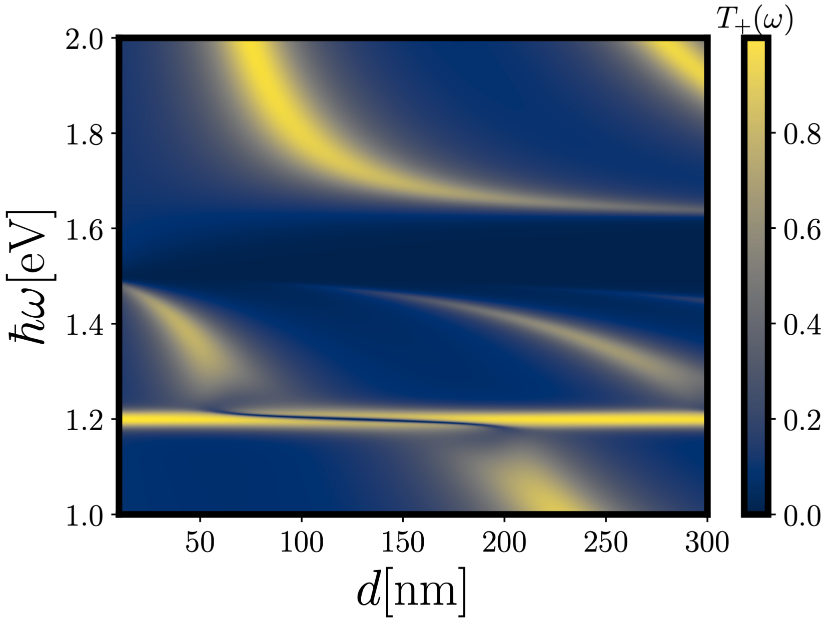

Figure 13.17: Transmittance T_+ at normal incidence from a Fabry-Pérot interferometer, composed by air-chiral mirror-Pasteur medium-chiral enantiomer of the mirror-air, as a function of the length d of the Pasteur medium in the unit of nm and as a function of $\hbar\omega$ in the unit of eV. Parameters are those of Figure 13.16, except that $\hbar\omega_{pr} = 1.2\,\text{eV}$.

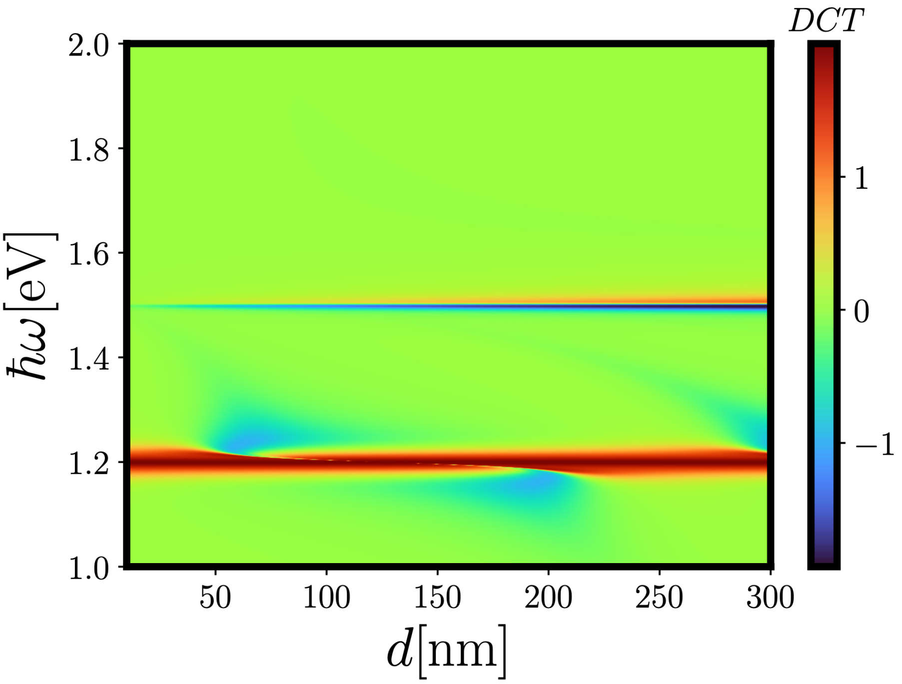

Figure 13.18: DCT at normal incidence from a Fabry-Pérot interferometer, composed by air-chiral mirror-Pasteur medium-chiral enantiomer of the mirror-air, as a function of the length d of the Pasteur medium in the unit of nm and as a function of $\hbar\omega$ in the unit of eV. Parameters are as follows: $\hbar\omega_{pr} = 1.2\,\text{eV}$, $\hbar\gamma_{pr} = 0.02\,\text{eV}$, $\varepsilon_{\infty,Pasteur} = 2.89$, $(\hbar\omega_p\sqrt{f_0})_{Pasteur} = 1.0\,\text{eV}$, $\hbar\gamma_{Pasteur} = 0.01\,\text{eV}$, $\hbar\omega_{0,Pasteur} = 1.5\,\text{eV}$, $\kappa_p = 10^{-3}$ and $\theta = 0$.

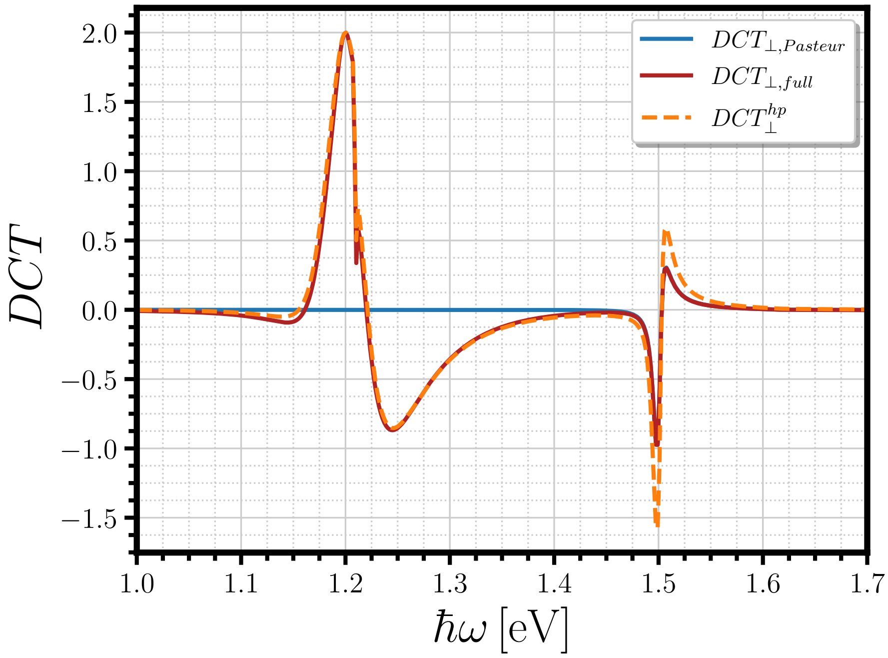

Figure 13.19: $DCT_{\perp}$ for the Pasteur medium (without the mirrors) (light-blue line), $DCT_{\perp}$ for the full system (red line) and $DCT_{\perp}$ for the analytical approach (see eq. (13.14)) (orange dashed line) as a function of $\hbar\omega$ in the unit of eV. Parameters are those of Figure 13.18, except that $d_{Pasteur} = 75\,\text{nm}$.

resonance of the material, the chirality of the Pasteur medium continues to modify, locally, the total DCT. This modification decreases and finally it is suppressed when $\omega_{0,Pasteur} = \omega_{pr}$, there the DCT signal is totally ruled by the preserving region. Figures 13.21, 13.22 and 13.23 show the decreasement of the discrimination produced by the Pasteur medium on the total DCT signal when $\omega_{0,Pasteur} \to \omega_{pr}$.

The total DCT of the mirrors and the Pasteur medium is qualitatively described, with a good approximation, by the formula in eq. (13.14). The formula works using the same "dressing" of its particular case for the empty cavity (see eq. (13.15)), that is the quantities $\mathcal{T}_{\pm}$ are promoted to be transmittances of the interferometer filled with the Pasteur medium. It describes quite well all the DCT shape but the maxima reached by the DCT of chiral material. This is mostly due to the fact that the formula is derived for the case of perfect helicity preservation. Furthermore, for a given polarization the propagating phase inside the Pasteur medium maintains the same sign. In the present chiral cavity, out and "far away" from the preserving region the mirrors behave as normal lossless mirrors and they do not preserve the helicity at each internal reflections.
Sending κ_p to $-\kappa_p$, the DCT signal reverses its sign only in the region where the chirality is due to the chiral Pasteur medium. Figure 13.20 shows the result of reversing the sign of κ_p compared to Figure 13.19.

The DCT signal at $\omega_{pr} = \omega_{0,Pasteur}$ is "imposed" by the preserving region and the chirality of the material has no effect on the total signal. Nevertheless, that resonance condition has an interesting effect on the Polaritonic branches (see Figure 13.24). ***When the preserving region is at the same frequency of the material resonance, the Polaritonic branches undergo the discrimination of the chiral mirrors and they acquire a polarized component along their formation. This means that the inclusion of the helicity-preserving region makes the Polaritonic branches chiral, in close proximity of that region***. Away from the preserving region, as the previous discussed cases, the discrimination is reduced until it becomes 0.

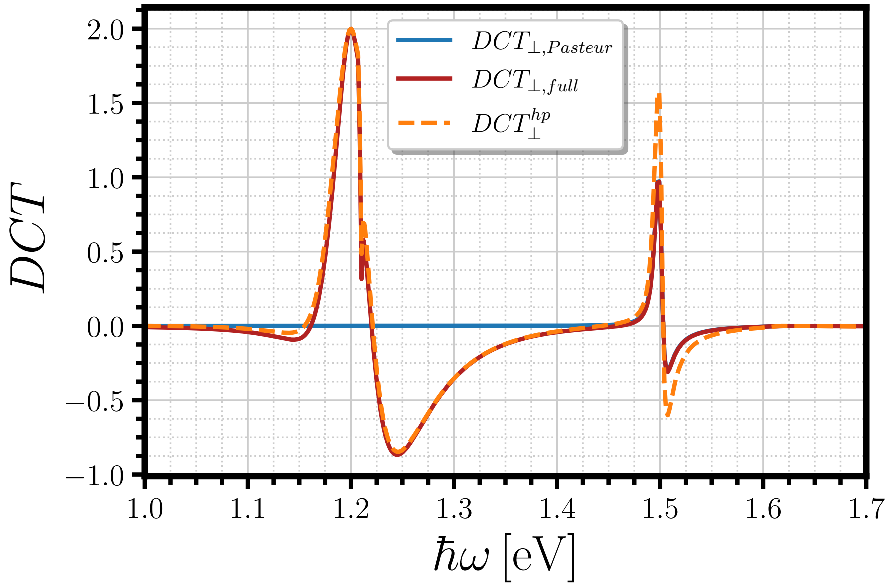

Figure 13.20: $DCT_\perp$ for the Pasteur medium (without the mirrors) (light-blue line), $DCT_\perp$ for the full system (red line) and $DCT_\perp$ for the analytical approach (see eq. (13.14)) (orange dashed line) as a function of $\hbar\omega$ in the unit of eV. Parameters are those of Figure 13.19, except that $\kappa_p = -10^{-3}$.

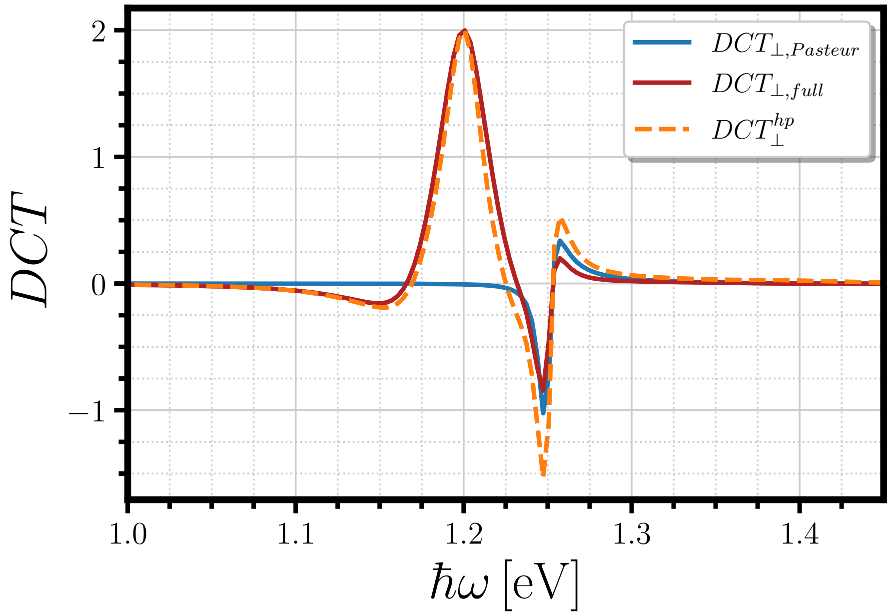

Figure 13.21: $DCT_\perp$ for the Pasteur medium (without the mirrors) (light-blue line), $DCT_\perp$ for the full system (red line) and $DCT_\perp$ for the analytical approach (see eq. (13.14)) (orange dashed line) as a function of $\hbar\omega$ in the unit of eV. Parameters are those of Figure 13.19, except that $\hbar\omega_{0,Pasteur} = 1.25\,\text{eV}$.

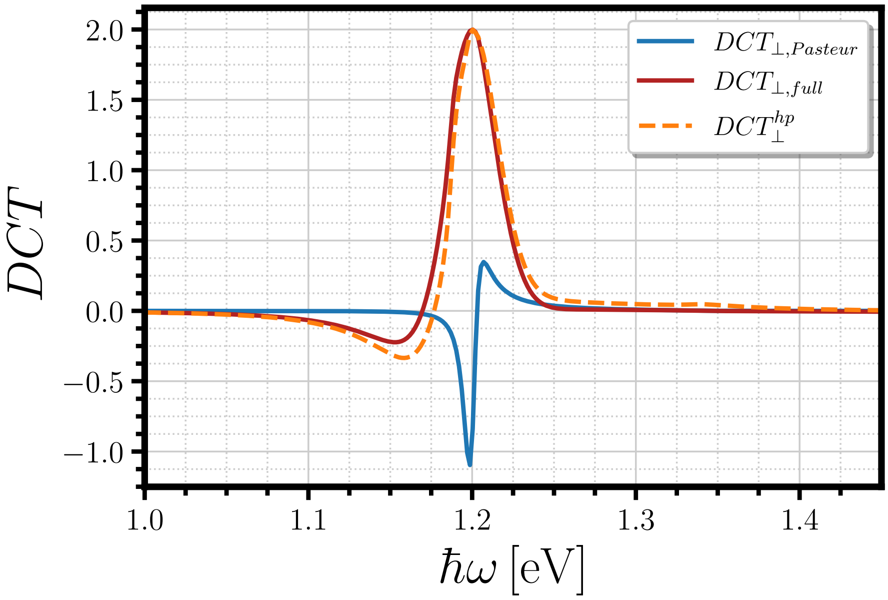

Figure 13.22: $DCT_\perp$ for the Pasteur medium (without the mirrors) (light-blue line), $DCT_\perp$ for the full system (red line) and $DCT_\perp$ for the analytical approach (see eq. (13.14)) (orange dashed line) as a function of $\hbar\omega$ in the unit of eV. Parameters are those of Figure 13.19, except that $\hbar\omega_{0,Pasteur} = 1.2\,\text{eV}$.

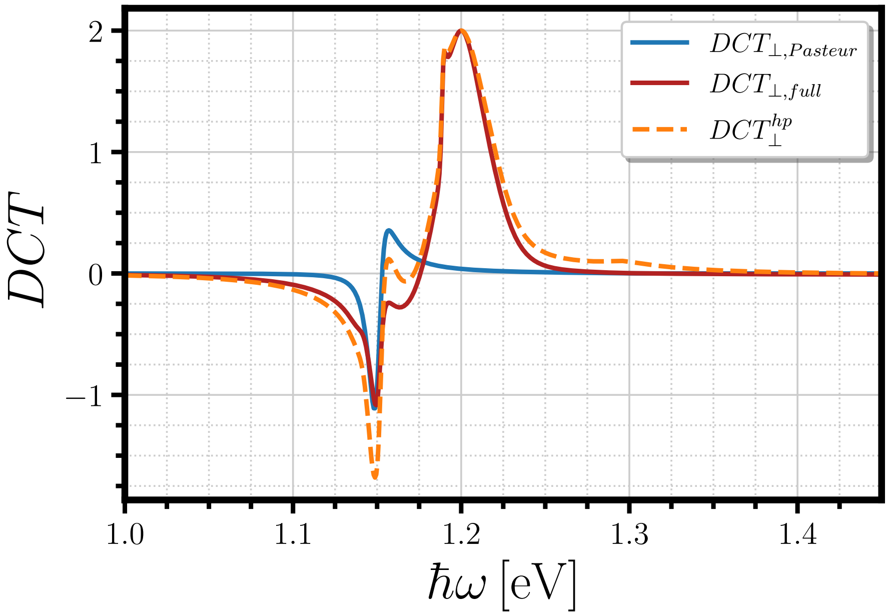

Figure 13.23: $DCT_\perp$ for the Pasteur medium (without the mirrors) (light-blue line), $DCT_\perp$ for the full system (red line) and $DCT_\perp$ for the analytical approach (see eq. (13.14)) (orange dashed line) as a function of $\hbar\omega$ in the unit of eV. Parameters are those of Figure 13.19, except that $\hbar\omega_{0,Pasteur} = 1.15\,\text{eV}$.

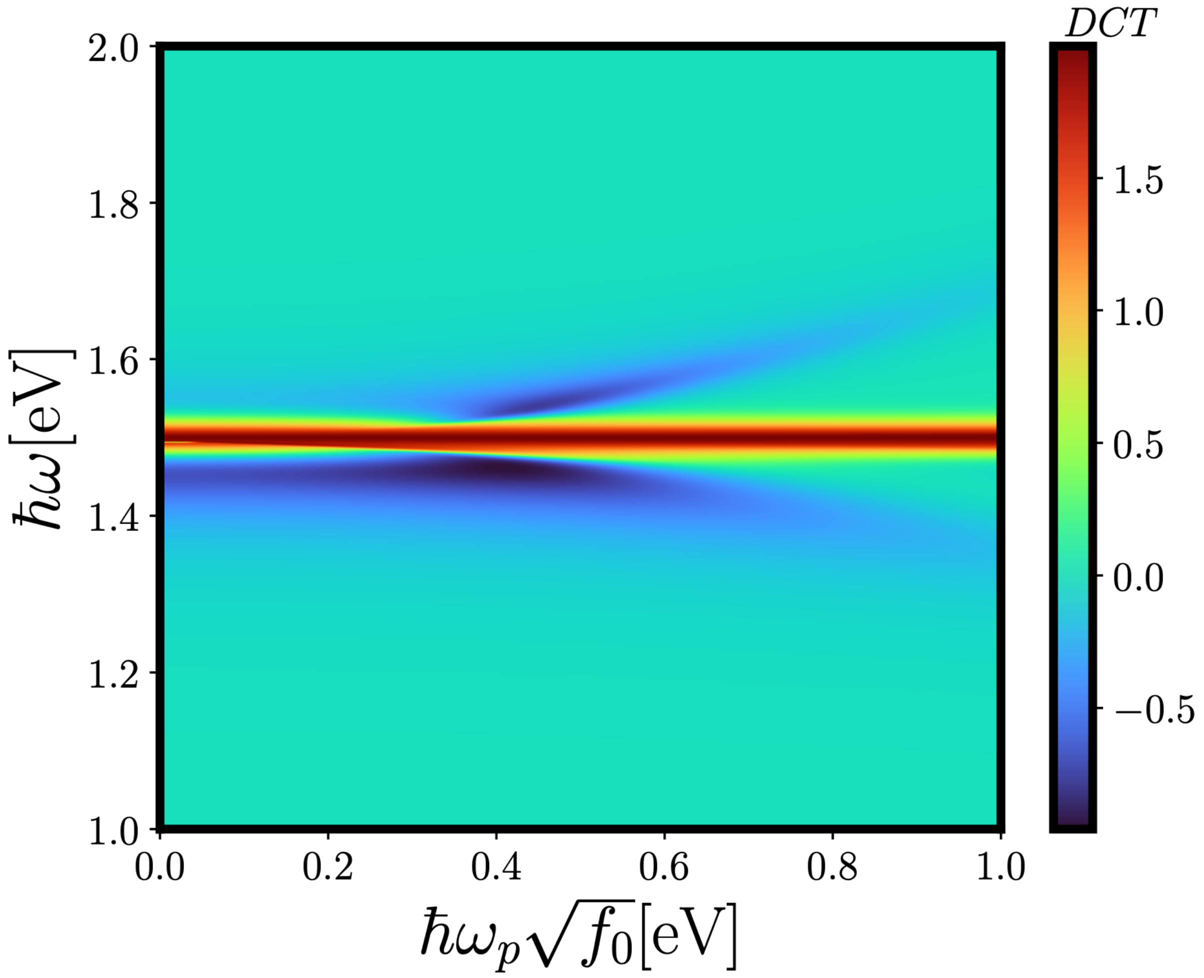

Figure 13.24: DCT at normal incidence from a Fabry-Pérot interferometer, composed by air-chiral mirror-Pasteur medium-chiral enantiomer of the mirror-air, as a function of the oscillator strength of the Pasteur medium in the unit of eV and as a function of $\hbar\omega$ in the unit of eV. Parameters are as follows: $\hbar\omega_{pr} = 1.5\,\text{eV}$, $\hbar\gamma_{pr} = 0.02\,\text{eV}$, $\varepsilon_{\infty,Pasteur} = 2.89$, $\hbar\gamma_{Pasteur} = 0.01\,\text{eV}$, $\hbar\omega_{0,Pasteur} = 1.5\,\text{eV}$, $\kappa_p = 10^{-3}$, $d_{Pasteur} = 150\,\text{nm}$ and $\theta = 0$.

13.7 Enhancement of optical activity of the Pasteur medium by spectral proximity of the helicity-preserving region

The previous Section shows that DCT is ruled by the preserving region. Its strong signal dominates the signal of the Pasteur medium. However, there is an observable that can quantify whether and how much the chirality of chiral mirrors alters the optical activity (chirality) of the Pasteur medium. The observable is ΔDCT, given by

$$\Delta DCT \equiv DCT(\kappa_p) - DCT(0), \tag{13.21}$$

where $DCT(\kappa_p)$ is the full signal (chiral mirrors plus Pasteur medium) and $DCT(0)$ is the full signal with $\kappa_p = 0$. ΔDCT does not contain the strong signal of the helicity-preserving region, and it reveals a net enhancement of the chirality of Pasteur medium (when the $\omega_{0,Pasteur} \rightarrow \omega_{pr}$).

The enhancement of the optical activity of Pasteur medium is observed when a Polaritonic branch "intersects" the preserving region. In Section 13.6.2, the negative regions of DCT (see Figure 13.18) are the result of the crossing of a Polaritonic branch with the preserving region. Thus, the enhancement is found by choosing the length of the Pasteur medium and an oscillator strength to fall in one of those regions where DCT is negative. It is important to notice that the enhancement can be found in a low coupling regime or in a strong coupling regime.

Figure 13.25 shows the DCT of the Pasteur medium and ΔDCT for illumination at normal incidence. Polaritons are generated at $\hbar\omega_{0,Pasteur} = 1.4\,\mathrm{eV}$ and the Upper branch crosses the preserving region for an intermediate oscillator strength of approximately $(\hbar\omega_p\sqrt{f_0})_{Pasteur} = 0.4\,\mathrm{eV}$. The length is tuned to fall in the negative DCT region, in accordance with the chosen oscillator strength. This choice of parameters produces a visible peak (the yellow shaded region) of enhancement in the proximity of the preserving region ($\hbar\omega \rightarrow \hbar\omega_{pr} = 1.5\,\mathrm{eV}$). The peak is about one order of magnitude higher than the DCT signal of the Pasteur medium. Interestingly, the shape of ΔDCT is well-reproduced by the analytical formula given by eq. (13.14) (see Figure 13.26).

Figure 13.27 shows another case of enhancement. The parameters are different but the mechanism that generates the enhancement is the same. ***It shows that the enhancement can reach two orders of magnitude higher than the DCT signal of the Pasteur medium, alone. $\boldsymbol{\Delta DCT}$ changes the sign by reversing the sign of $\boldsymbol{\kappa_p}$. The change of sign confirms that the chirality of the molecules is strongly enhanced by the chirality of the mirrors, for a low, intermediate and strong oscillator strength.***

In conclusion, $\boldsymbol{\Delta DCT}$ is the "good" observable to record an appreciable change in optical activity due to the interaction between the "engineered chirality" of chiral mirrors and natural chirality of molecules.

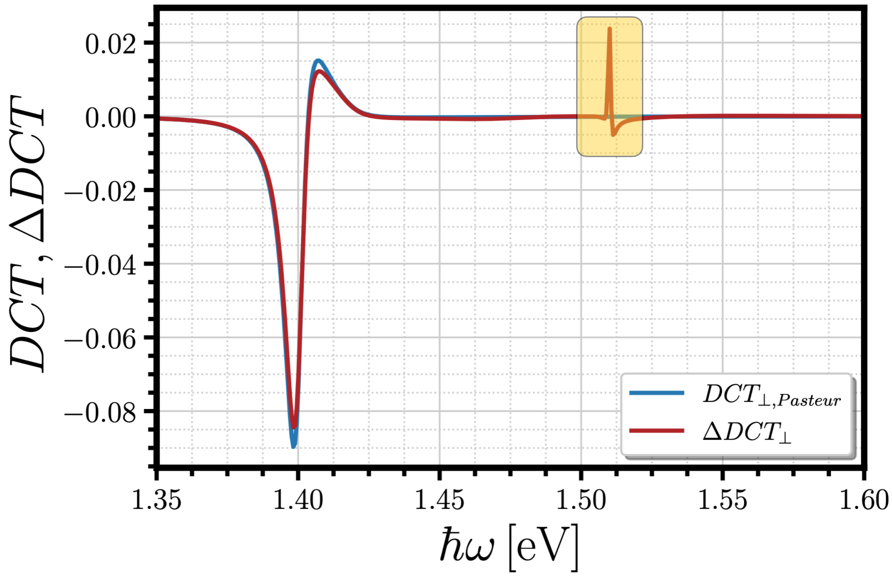

Figure 13.25: $DCT_{\perp}$ for the Pasteur medium (light-blue line) and $\Delta DCT_{\perp}$ for the full system (red line) as a function of $\hbar\omega$ in the unit of eV. The yellow shaded region is the enhancement of the optical activity of the Pasteur medium by proximity of the helicity-preserving region. Parameters are as follows: $\hbar\omega_{pr} = 1.5\,\text{eV}$, $\hbar\gamma_{pr} = 0.02\,\text{eV}$, $\varepsilon_{\infty,Pasteur} = 2.89$, $(\hbar\omega_p\sqrt{f_0})_{Pasteur} = 0.4\,\text{eV}$, $\hbar\gamma_{Pasteur} = 0.01\,\text{eV}$, $\hbar\omega_{0,Pasteur} = 1.4\,\text{eV}$, $\kappa_p = 10^{-3}$, $d_{Pasteur} = 85.6\,\text{nm}$ and $\theta = 0$.

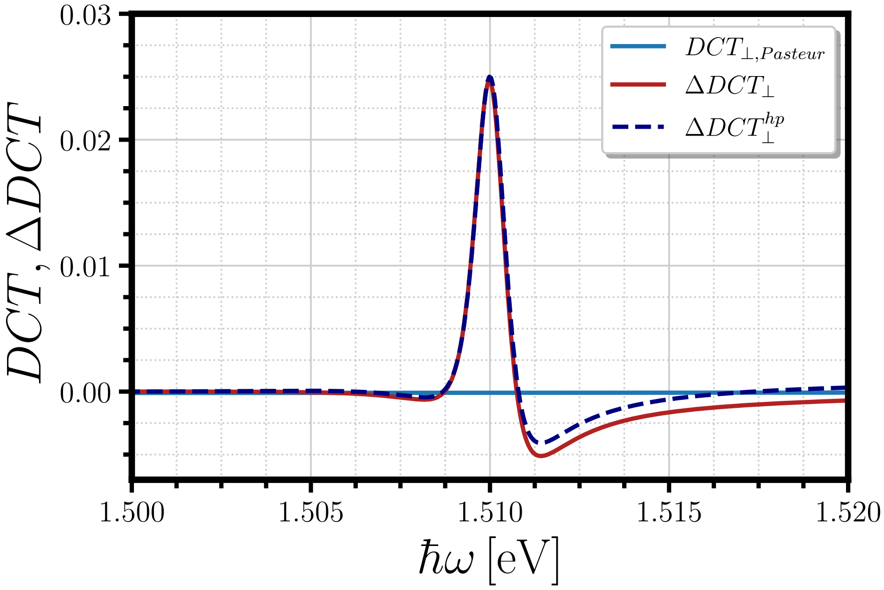

Figure 13.26: $DCT_{\perp}$ for the Pasteur medium (light-blue line), $\Delta DCT_{\perp}$ for the full system (red line) and $\Delta DCT_{\perp}$ for the analytical approach (see eq. (13.14)) (blue dashed line) as a function of $\hbar\omega$ in the unit of eV. Parameters are those of Figure 13.25, except that $d_{Pasteur} = 85.5\,\text{nm}$.

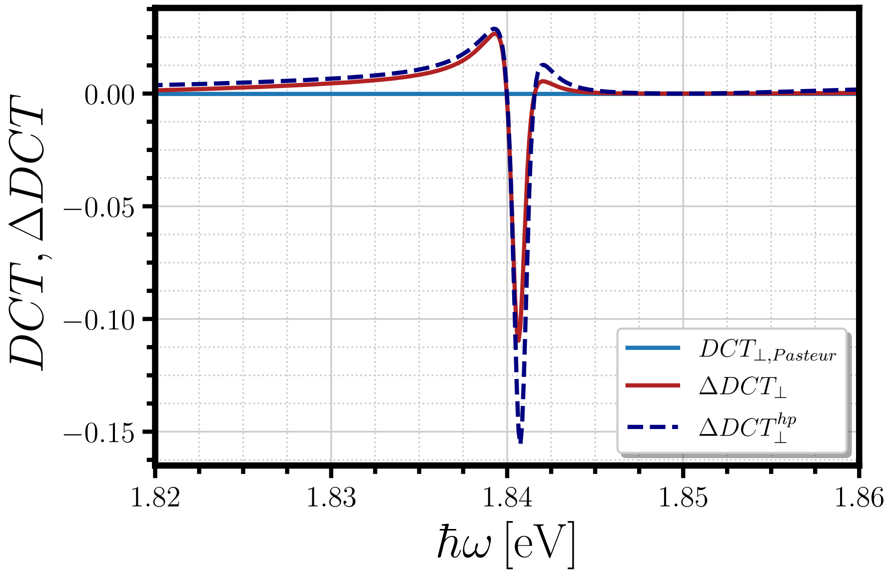

Figure 13.27: $DCT_\perp$ for the Pasteur medium (light-blue line), $\Delta DCT_\perp$ for the full system (red line) and $\Delta DCT_\perp$ for the analytical approach (see eq. (13.14)) (blue dashed line) as a function of $\hbar\omega$ in the unit of eV. Parameters are as follows: $\hbar\omega_{pr} = 1.85\,\text{eV}$, $\hbar\gamma_{pr} = 0.02\,\text{eV}$, $\varepsilon_{\infty,Pasteur} = 2.89$, $(\hbar\omega_p\sqrt{f_0})_{Pasteur} = 1.0\,\text{eV}$, $\hbar\gamma_{Pasteur} = 0.01\,\text{eV}$, $\hbar\omega_{0,Pasteur} = 1.6\,\text{eV}$, $\kappa_p = 10^{-3}$, $d_{Pasteur} = 169\,\text{nm}$ and $\theta = 0$.

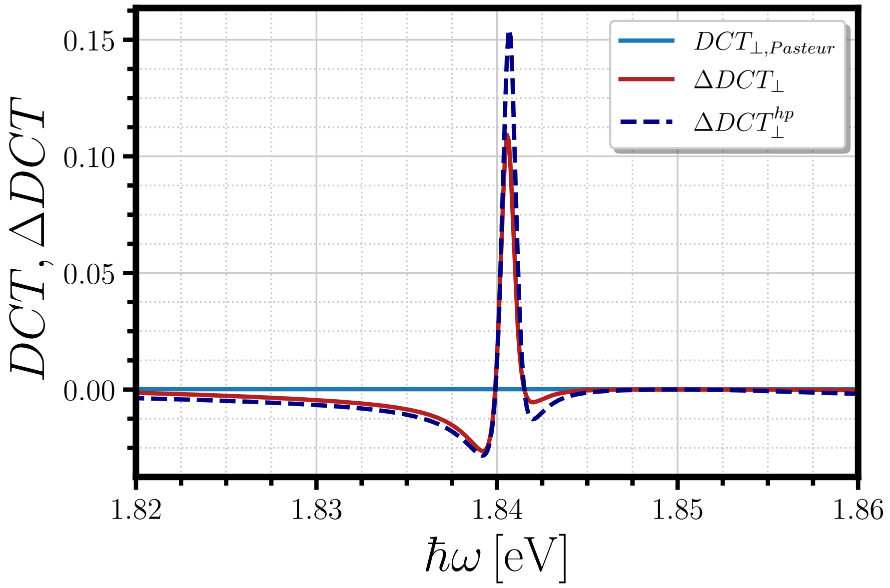

Figure 13.28: $DCT_\perp$ for the Pasteur medium (light-blue line), $\Delta DCT_\perp$ for the full system (red line) and $\Delta DCT_\perp$ for the analytical approach (see eq. (13.14)) (blue dashed line) as a function of $\hbar\omega$ in the unit of eV. Parameters are those of Figure 13.27, except that $\kappa_p = -10^{-3}$.

13.8 Methods

The Figures (plots) in Chapter 11, 12 and 13 are obtained with a transfer matrix method for achiral and chiral layers. The code that generates the Figures has been written by the author of the manuscript in Mathematica [82]. The code has been written by using the references [29, 86, 152] and the dispersive modelling explained in Section 12.1. The code has been also translated and rewritten in Python [162] at Universidad Autónoma de Madrid by Jacopo Fregoni and the author of the manuscript, in the theory group led by Johannes Feist.

14

Conclusion

The second part of the manuscript has as its subject a chiral Fabry-Pérot. Chiral molecules, such as a macroscopic ensemble of molecules of the same handedness, are classically described by the Condon constitutive relations. The resulting molecular isotropic chiral layer (optically active layer), called Pasteur medium, is first probed by circularly polarized light rays (left- or right-handed). The illumination at normal incidence does not reveal a discrimination between left or right-handed transmission. The layer (without including a dispersive modelling) behaves as an achiral layer. The discrimination is quantified with the differential circular transmission (DCT). DCT is not negligible if the oncoming light rays form a finite angle with the chiral layer. In this case, it has been shown that DCT oscillates as a function of energy and the oscillations are the alternation of constructive and destructive interference between the two polarizations.

Eventually, the Pasteur medium is dressed by silver (Ag) mirrors and both the medium and mirrors are modelled taking into account their dispersive and lossy nature. The new system absorbs part of the polarized rays and in particular the chiral medium absorbs more of one polarization than the other (it depends if the Pasteur medium is left or right-handed). In fact, DCT has been shown to be non-zero even at normal incidence. Importantly, DCT at normal incidence, has been calculated analytically and checked numerically. The analytical formula comes from the perfect conversion of polarized light rays in cavity. At each internal reflection the polarization is reversed from right to left (or viceversa) and the final transmitted signal is given by an achiral factor times the absorption factor for the associate polarization. The transmission and the related DCT signal generalize the Beer-Lambert Law in case of isotropic chiral media.

The dispersive and lossy modelling allows for the classical strong coupling regime, *i.e.*, when the oscillator strength is larger than the linewidth of the molecular ensemble and the length of the material is such that the cavity optical mode is at resonance with the molecular transition. These are the conditions to see the Polaritonic splitting. Polaritons, using traditional Ag mirrors and chiral molecules, are achiral in terms of the light part and the associated DCT signal is zero.

Although the chiral layer is probed many times by circularly polarized light, the DCT signal (which is proportional to the magnitude of chirality of the layer) of the Pasteur medium, by itself, is not enhanced by confinement in a Fabry-Pérot cavity, made by Ag mirrors. The illumination at finite angle of incidence produced the same conclusion.

The negligible increase in chirality motivated the investigation of an optically active cavity with chiral mirrors. The modelling of the chiral mirrors is based on existing chiral photonic mirrors [142]. Those mirrors are almost lossless and they fullfill time-reversal symmetry. The symmetry constraints the matrix elements and gives an explanation to the shapes of the simulated transmissions and reflections reported in reference [142]. To complete the modelling of the mirrors, the classical coupled-mode theory is adopted to describe the chiral property of mirrors (they "perfectly" reflect one polarization and they convert the opposite one). Despite only one mode is taken into account, the essential physical mechanism is well reproduced. This approach extracts the necessary ingredients to successfully model the mirrors.

The empty cavity, made by the modelled chiral mirrors, generates a spectral helicity-preserving region (or a fully transmitting region for one polarization) which is not available with a traditional interferometer. It has been shown that region alters the standard achiral light modes. Specifically, when the light mode crosses the preserving region Fano resonances are visible and an additional discrimination occurs. The latter is due to the breaking of perfect conversion of left-to-right (or right-to-left) polarized light rays in the spectral proximity of that atypical region. Surprisingly, the associated DCT signal has been recovered with two different analytical approches (and numerically) to estimate the peaks and deeps as a function of energy. Similar features have been found by inserting the Pasteur medium between the two mirrors. The main difference is an impedance mismatch across the preserving region resulting in a misalignement of the light modes.

A remarkable behaviour has been detected at resonance with the preserving frequency. At strong coupling, Polaritons are generated in the proximity of the preserving region and they are clearly distinguishable by calculating DCT. It means that their light part consists of more one polarization than the other, making them chiral.

The differential circular transmission of the empty cavity is the maximal signal for one polarization, since the mirrors perfectly transmit and convert the polarization that exits the cavity completely. The cavity DCT dominates the DCT signal of the Pasteur medium, when the molecular frequency is close to the preserving frequency. Another observable has been calculated to detect the influence of the engineered chiral mirrors on the optical activity of the Pasteur medium. The observable is ΔDCT and records a significant increase in the chirality of molecules by up to two orders of magnitude. The mechanism that generates the enhancement is the crossing between one Polaritonic branch and the preserving region. The enhancement is revealed if the length of the Pasteur medium and its oscillator strength are tuned so that the crossing takes place in those regions where there is a partial breaking of the internal perfect conversion of polarization. There, polarized light of one handedness probes many times the Pasteur medium of the same handedness resulting in an increase in the natural chirality of the molecular ensemble.

Recent articles [59, 156, 154] draw perspectives on the existence of *chiral Polaritons* and their roles in asymmetric chemistry and new chiral transition pathways. ***This second part shows for the first time (to our knowledge) a cavity, whose chiral mirrors are modelled from an existing mirror, which is able to generate the so-called chiral Polaritons***. The chirality of Polaritons is given by the light part which is polarized by the spectral proximity of the helicity-preserving region. This result clearly opens doors to investigate quantum mechanically the chiral nature of Polaritons in terms of new energy shifts, more available transitions and possible induction of chirality.

As the chiral shape of a mollusk body interacts with the handedness of its shell during evolution, chiral mirrors reshape the chirality of a Pasteur medium during multiple single-handedness reflections, by increasing it. The enhanced sensitivity to the chirality of the molecules is at the heart of chiral sensing. The chiral mirrors could be useful to measure the concentration of the chiral molecules given a mixture of right- and left-handed molecules. The thought experiment is the following: The mixture characterized by a parameter $\mathcal{C} \in [0, 1]$, which describes the presence of left (0), right (1) or an intermediate mixture, is inserted between the two chiral mirrors. The chiral mirrors enhance the signal of the chirality of molecules and ΔDCT is the good observable to measure. It is obtained by measuring the signal of the full system and sutracting the signal of the empty cavity. By doing this, the measured ΔDCT could be used to extract the value $\mathcal{C}$ which is an indicator of how many left- or right-handed molecules are present in the mixture. The mirror increases the signal by an order of magnitude up to two and thus could considerably facilitate the delicate detection.

The modelled chiral Fabry-Pérot cavity is a valuable system and the newly discovered effects might be fundamental for future works. It may be a promising system for biological, chemical and pharmaceutical applications to measure chiral concentration and quantitatively separate enantiomeric forms.

A

Counter-rotating and self-dipole terms

The simplest minimal coupling scheme in Quantum Electrodynamics, within dipole approximation, provides for a single molecule (and single electron of mass m) interacting with a cavity mode

$$\hat{\mathrm{H}} \;=\; \frac{\|\hat{\vec{p}} - e\hat{\vec{A}}(\vec{0})\|^2}{2m} + \mathrm{V}(\vec{x}) + \hbar\omega_c\left(\hat{a}^\dagger\hat{a} + \frac{1}{2}\right) , \tag{A.1}$$

with $\hat{\vec{p}}$ the electronic linear momentum, $\hat{\vec{A}}(\vec{0}) = \vec{\epsilon}(E_0/\omega_c)(\hat{a}+\hat{a}^\dagger)$ the vector potential operator (in Coulomb gauge) evaluated at the molecule position (taken as origin of coordinates) with polarisation $\vec{\epsilon}$, $\mathrm{V}(\vec{x})$ the electrostatic potential, and $a(a^\dagger)$ the annihilation (creation) operator of a cavity-mode photon.

Switching to the dipole representation is equivalent to performing the Göppert-Mayer time-independent unitary transformation [28] $\hat{U} = \exp\left\{-ie/\hbar\hat{\vec{A}}(\vec{0})\cdot\vec{x}\right\}$ on the Hamiltonian of eq. (A.1). The application of the unitary transformation gives

$$\tilde{\hat{\mathrm{H}}} \;=\; \frac{\|\hat{\vec{p}}\|^2}{2m} + \mathrm{V}(\vec{x}) + \hbar\omega_c\left(\hat{a}^\dagger\hat{a} + \frac{1}{2}\right) - \hat{\vec{\mu}}\cdot\hat{\vec{E}}(\vec{0}) + \frac{\|\vec{\epsilon}\cdot\hat{\vec{\mu}}\|^2 E_0^2}{\hbar\omega_c} , \tag{A.2}$$

with $\hat{\vec{\mu}} = e\hat{\vec{x}}$ the electric dipole operator of the molecule, and $\hat{\vec{E}}(\vec{0}) = iE_0(\hat{a}-\hat{a}^\dagger)\vec{\epsilon}$ the electric field operator evaluated at the molecule position. For a molecule acting as a two-level system with ground and excited states $|g\rangle$ and $|e\rangle$ with energies $\varepsilon_g, \varepsilon_e$ respectively, the Hamiltonian of eq. A.2 can be rewritten as

$$\tilde{\hat{\mathrm{H}}} \;=\; \hat{\mathrm{H}}_{\mathrm{m}} + \hat{\mathrm{H}}_{\mathrm{c}} + \hat{\mathrm{V}}_{\mathrm{RWA}} + \hat{\mathrm{V}}_{\mathrm{nR}} + \hat{\mathrm{V}}_{\mathrm{SD}}, \tag{A.3}$$

$$\hat{\mathrm{H}}_{\mathrm{m}} \;=\; \varepsilon_g\,|g\rangle\langle g| + \varepsilon_e\,|e\rangle\langle e| , \tag{A.4}$$

$$\hat{\mathrm{H}}_{\mathrm{c}} \;=\; \hbar\omega_c\left(\hat{a}^\dagger\hat{a} + \frac{1}{2}\right) , \tag{A.5}$$

$$\hat{\mathrm{V}}_{\mathrm{RWA}} \;=\; \frac{\hbar\Omega_R}{2}\left(|e\rangle\langle g|\,\hat{a} + |g\rangle\langle e|\,\hat{a}^\dagger\right) , \tag{A.6}$$

$$\hat{\mathrm{V}}_{\mathrm{nR}} \;=\; \frac{\hbar\Omega_R}{2}\left(|e\rangle\langle g|\,\hat{a}^\dagger + |g\rangle\langle e|\,\hat{a}\right) , \tag{A.7}$$

$$\hat{\mathrm{V}}_{\mathrm{SD}} \;=\; \frac{\hbar\Omega_R^2}{4\omega_c}, \tag{A.8}$$

with $\hat{\mathrm{H}}_{\mathrm{m}}$, $\hat{\mathrm{H}}_{\mathrm{c}}$ the respective Hamiltonian of the free molecule and cavity-mode. $\hat{\mathrm{V}}_{\mathrm{RWA}}$ is the light-matter dipole coupling Hamiltonian written within RWA and involving absorption or emission of a real photon, with $\hbar\Omega_R = 2E_0\vec{\mu}_{eg}\cdot\vec{\epsilon}$ the vacuum Rabi splitting. The last two terms are $\hat{\mathrm{V}}_{\mathrm{nR}}$ the contribution of counter-rotating terms of the dipole interaction involving virtual photon transitions, and $\hat{\mathrm{V}}_{\mathrm{SD}}$ the static dipole term. The sum of those two terms $\delta\hat{\mathrm{V}} = \hat{\mathrm{V}}_{\mathrm{nR}} + \hat{\mathrm{V}}_{\mathrm{SD}}$ is treated as a perturbation to the Hamiltonian written in RWA $\hat{\mathrm{H}}_{\mathrm{RWA}} = \hat{\mathrm{H}}_{\mathrm{m}} + \hat{\mathrm{H}}_{\mathrm{c}} + \hat{\mathrm{V}}_{\mathrm{RWA}}$.

The contribution of counter-rotating terms $\hat{\mathrm{V}}_{\mathrm{nR}}$ to the ground-state Lamb-shift $\Delta\varepsilon_g$, is obtained at resonance ($\varepsilon_e - \varepsilon_g = \hbar\omega_c$), using second-order perturbation theory

$$\begin{aligned}
\Delta\varepsilon_g &\approx -\frac{\hbar\Omega_R^2}{8}\left\{\frac{1}{2\omega_c + \frac{\Omega_R}{\sqrt{2}}} + \frac{1}{2\omega_c - \frac{\Omega_R}{\sqrt{2}}}\right\} && \text{(A.9)}\\
&\approx -\frac{\hbar\Omega_R^2}{8\omega_c}\,. && \text{(A.10)}
\end{aligned}$$

The corrections due to $\hat{\mathrm{V}}_{\mathrm{SD}}$ are of the same order. For $\hbar\omega_c = 2.8$ eV and $\hbar\Omega_R = 0.7$ eV, the correction $\Delta\varepsilon_g \approx 0.78\%\hbar\omega_c$. This small correction justifies the choice to neglect these effects for the analytical derivation in the first part of the manuscript.

B

Adiabatic approximation for the analytical PES

This appendix provides some supplementary informations regarding the derivation of the PES for the Lower Polariton. The starting point is the Holstein-Tavis-Cummings Hamiltonian (see eq. (4.22)), keeping only one vibrational mode of frequency ω_{v} and the states coupled to the cavity mode:

$$\begin{aligned}\hat{\mathrm{H}}_{\mathrm{Nmol}} = \sum_{i=1}^{N} \left\{ \left[\varepsilon_g + \frac{1}{2}\omega_{\mathrm{v}}^2 \left(Q_{\mathrm{v},i} - \overline{Q}_{\mathrm{v},g} \right)^2 \right] \left| g_i \right\rangle \left\langle g_i \right| + \left[\varepsilon_e + \frac{1}{2}\omega_{\mathrm{v}}^2 \left(Q_{\mathrm{v},i} - \overline{Q}_{\mathrm{v},e} \right)^2 \right] \left| e_i \right\rangle \left\langle e_i \right| \right\} + \\ + \hbar\omega_c \hat{a}^\dagger \hat{a} + \frac{\hbar\Omega_R}{2} \sum_{i=1}^{N} \left(\left| e_i \right\rangle \left\langle g_i \right| \hat{a} + \left| g_i \right\rangle \left\langle e_i \right| \hat{a}^\dagger \right),\end{aligned} \tag{B.1}$$

Defining the Huang-Rhys factor $g_{\mathrm{v}} = \overline{Q}_{\mathrm{v},e}/2x_{0\mathrm{v}}$ ($\overline{Q}_{\mathrm{v},g} = 0$) with $x_{0\mathrm{v}} = \sqrt{\hbar/2\omega_{\mathrm{v}}}$, and the dimensionless displacement of molecule i by $q_{\mathrm{v},i} = Q_{\mathrm{v},i}/x_0$, the eq. (B.1) can be rewritten as

$$\tilde{\hat{\mathrm{H}}}_{\mathrm{Nmol}} = \hat{\mathrm{H}}_0 + \hat{\mathrm{V}}_{\mathrm{eph}}, \tag{B.2}$$

$$\hat{\mathrm{H}}_0 = \sum_{i=1}^{N} \left\{ \left(\varepsilon_g + \frac{\hbar\omega_{\mathrm{v}}}{4} q_{\mathrm{v},i}^2 \right) \left| g_i \right\rangle \left\langle g_i \right| + \left(\varepsilon_e + \frac{\hbar\omega_{\mathrm{v}}}{4} q_{\mathrm{v},i}^2 \right) \left| e_i \right\rangle \left\langle e_i \right| \right\} + \tag{B.3}$$

$$+ \hbar\omega_c \hat{a}^\dagger \hat{a} + \frac{\hbar\Omega_R}{2} \sum_{i=1}^{N} \left(\left| e_i \right\rangle \left\langle g_i \right| \hat{a} + \left| g_i \right\rangle \left\langle e_i \right| \hat{a}^\dagger \right) \tag{B.4}$$

$$\hat{\mathrm{V}}_{\mathrm{eph}} = \sum_{i=1}^{N} g_{\mathrm{v}} \hbar\omega_{\mathrm{v}} \left(g_{\mathrm{v}} - q_{\mathrm{v},i} \right) \left| e_i \right\rangle \left\langle e_i \right| , \tag{B.5}$$

where $\hat{\mathrm{H}}_0$ is the Hamiltonian in absence of coupling to the vibrational mode ($g_{\mathrm{v}} = 0$) and $\hat{\mathrm{V}}_{\mathrm{eph}}$ the electron-phonon interaction. The electron-phonon coupling strength of $\hat{\mathrm{V}}_{\mathrm{eph}}$ can be measured either by g_{v} or $\lambda_{\mathrm{v}} = g_{\mathrm{v}}^2 \hbar\omega_{\mathrm{v}}$. These two parameters are “small” compared to $\tilde{\Omega}_R$ in the light-matter strong coupling regime of Fig. 4.9 of the manuscript.

In the following, the analysis focuses on the single-molecule strong coupling regime (but the arguments are similar for N molecules). The Hamiltonian in eq. (B.2) becomes

$$\hat{\mathrm{H}}_{1\mathrm{mol}} = \begin{pmatrix} \hbar\omega_c + \varepsilon_g + \hbar\omega_{\mathrm{v}} q_{\mathrm{v}}^2/4 & \hbar\Omega_R/2 \\ \hbar\Omega_R/2 & \varepsilon_e + \hbar\omega_{\mathrm{v}} \left(q_{\mathrm{v}} - 2g_{\mathrm{v}} \right)^2/4 \end{pmatrix}. \tag{B.6}$$

The diagonalization of $\hat{\mathrm{H}}_{1\mathrm{mol}}$ gives the exact expression for the PES of Lower Polariton:

$$\mathcal{E}_- = \frac{1}{2} \left(\varepsilon_g + \varepsilon_e + \hbar\omega_c - \hbar\sqrt{\left(\delta + g_{\mathrm{v}}\omega_{\mathrm{v}} \left(q_{\mathrm{v}} - g_{\mathrm{v}} \right) \right)^2 + \Omega_R^2} \right) + \frac{\hbar\omega_{\mathrm{v}}}{4} \left(q_{\mathrm{v}}^2 + 2g_{\mathrm{v}} \left(g_{\mathrm{v}} - q_{\mathrm{v}} \right) \right), \tag{B.7}$$

where the detuning is defined as $\delta \equiv \omega_c + \varepsilon_g/\hbar - \varepsilon_e/\hbar$.
The expansion at second-order in $g_\mathrm{v} \ll 1$ gives:

$$\mathcal{E}_{-,\,g_\mathrm{v}^2} = \frac{1}{2}\left(\varepsilon_g+\varepsilon_e+\hbar\omega_c-\hbar\sqrt{\delta^2+\Omega_R^2}\right)+\frac{\hbar\omega_\mathrm{v}}{4}\left(q_\mathrm{v}^2+\frac{2g_\mathrm{v}\left(g_\mathrm{v}-q_\mathrm{v}\right)\left(\delta+\sqrt{\delta^2+\Omega_R^2}\right)}{\sqrt{\delta^2+\Omega_R^2}}-\frac{\omega_\mathrm{v} q_\mathrm{v}^2 g_\mathrm{v}^2\Omega_R^2}{\left(\delta^2+\Omega_R^2\right)^{3/2}}\right). \tag{B.8}$$

Instead, the expansion of the exact PES at first order in $\lambda_\mathrm{v}/\hbar\sqrt{\delta^2+\Omega_R^2} \ll 1$ produces

$$\mathcal{E}_{-,\,adiab} = \frac{1}{2}\left(\varepsilon_g+\varepsilon_e+\hbar\omega_c-\hbar\sqrt{\delta^2+\Omega_R^2}\right)+\frac{\hbar\omega_\mathrm{v}}{4}\left(q_\mathrm{v}^2+\frac{2g_\mathrm{v}\left(g_\mathrm{v}-q_\mathrm{v}\right)\left(\delta+\sqrt{\delta^2+\Omega_R^2}\right)}{\sqrt{\delta^2+\Omega_R^2}}\right) \tag{B.9}$$

The eq. (B.9) corresponds to the strong-coupling "adiabatic" approximation performed in the first part of the manuscript (see Section 4.3.2). The expansion in g_v (see eq. (B.8)) contains an additional term with respect to the adiabatic expansion (see eq. (B.9)). This term of order $\lambda_\mathrm{v}/\hbar\Omega_R$ can be seen as a renormalization of the vibrational frequency ω_v mediated by electron-phonon coupling. In the regime of weak electron-phonon coupling adopted in Section 4.3.2 $\left(\lambda_\mathrm{v} \ll \hbar\sqrt{\delta^2+\Omega_R^2}\right)$, the eq. (B.8) converges to the result of eq. (B.9). Although similar, the adiabatic approximation is simpler and allows a tractable extension to the case of N molecules coupled to the cavity mode.

The corresponding equilibrium positions for the nuclei (minimum of the PPES) within the two approximations are:

$$\Delta\overline{Q}_{\mathrm{v},-,\,adiab} = g_\mathrm{v}\frac{\delta+\sqrt{\delta^2+\Omega_R^2}}{\sqrt{\delta^2+\Omega_R^2}}, \tag{B.10}$$

$$\Delta\overline{Q}_{\mathrm{v},-,\,g_\mathrm{v}^2} = -g_\mathrm{v}\frac{\left(\delta^2+\Omega_R^2\right)\left(\delta+\sqrt{\delta^2+\Omega_R^2}\right)}{\omega_\mathrm{v} g_\mathrm{v}^2\Omega_R^2-\left(\delta^2+\Omega_R^2\right)^{3/2}}. \tag{B.11}$$

Figure B.1 and Figure B.2 show the comparison of these approximate equilibrium positions and PES with the exact one, as a function of both g_v and detuning δ. The "adiabatic" approximation ($\Delta\overline{Q}_{\mathrm{v},-,\,adiab}$ and $\mathcal{E}_{-,\,adiab}$) provides a very accurate agreement with the exact result even at finite g_v and δ, in the strong coupling regime, while $\Delta\overline{Q}_{\mathrm{v},-,\,g_\mathrm{v}^2}$ and $\mathcal{E}_{-,\,g_\mathrm{v}^2}$ converge to the expected result only at low electron-phonon coupling, and at resonance.

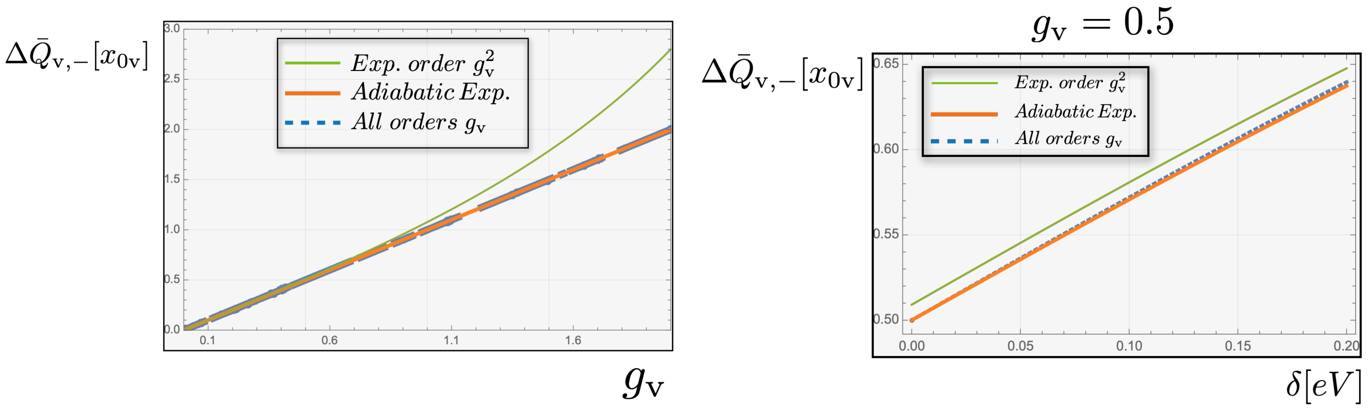

Figure B.1: (a) Nuclei position $\Delta\overline{Q}_{\mathrm{v},-}$ corresponding to the minimum of the LP PES, varying g_v at resonance ($\delta = 0$), for the exact expression (dashed blue line), the adiabatic expansion (orange line) and the expansion at order g_v^2 (green line). The parameters are as follows: $\varepsilon_g = 0$ eV, $\varepsilon_e = 2.8$ eV, $\hbar\omega_c = 2.8$ eV, $\hbar\omega_\mathrm{v} = 0.05$ eV and $\hbar\Omega_R = 0.7$ eV. (b) Same plot as a function of detuning δ with $g_\mathrm{v} = 0.5$.

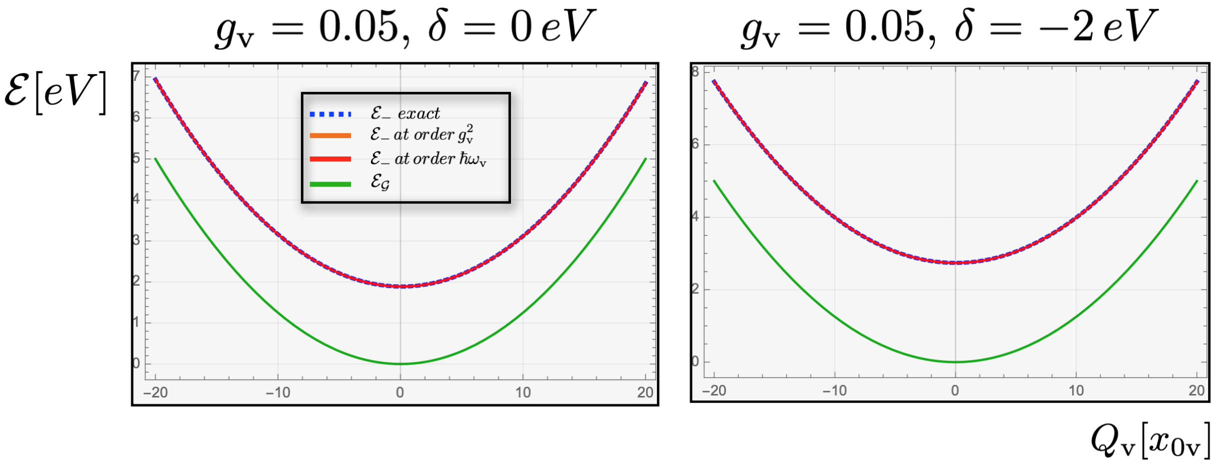

Figure B.2: PPES for the LP (ε_-) varying the reaction coordinate ($\Delta\overline{Q}_{\mathrm{v}}$), for the exact numerical expression (dashed blue line), the expansion at order g_{v}^2 (orange line) and the adiabatic expansion (red line). The ground state is shown as a green line. On the left the resonant condition and on the right the PES is out of resonance with respect to the cavity mode. Except for the resonance condition, $\varepsilon_e = \hbar\omega_c = 2.8$ eV, and the out of resonance for which $\varepsilon_e = 4.8$ eV $\neq \hbar\omega_c = 2.8$ eV all the others parameters are the same as Figure B.1.

This analysis justifies the choice of the adiabatic approximation in Section 4.3.2, which is also easily extended to the case of N molecules, providing the PPES in eq. (4.32).

C

Achiral mirrors which preserve the handedness

An ideal case is to suppose that the mirrors are not chiral but they can still preserve the polarization inside the cavity. This means that they fulfill the usual relations at the boundary between different materials, and at normal incidence the transmittances and the reflectances are simply $T_{1,+,hp} = T_{1,-,hp} \equiv T_1$, $T_{2,+,hp} = T_{2,-,hp} \equiv T_2$ and $R_{1,\pm,hp} = R_{2,\pm,hp} \equiv R$, respectively. Inserting these simplifications in eq. (13.14), the DCT gets

$$DCT_{\perp}^{ahp} = 2\frac{\left(e^{-\alpha_+ L} - e^{-\alpha_- L}\right)\left(1 - R^2 e^{-2\alpha L}\right) + 2Re^{-2\alpha L}\left(\cos 2\beta_+ - \cos 2\beta_-\right)}{\left(e^{-\alpha_+ L} + e^{-\alpha_- L}\right)\left(1 + R^2 e^{-2\alpha L}\right) - 2Re^{-2\alpha L}\left(\cos 2\beta_+ + \cos 2\beta_-\right)}, \tag{C.1}$$

where the superscript *ahp* means an achiral mirror (“normal mirror”) with the property to preserve the handedness of the reflected rays of light in cavity.

Figure C.1 shows the differential circular transmission at normal incidence for an interferometer with “normal” mirrors and for the same interferometer with achiral mirrors which preserve the handedness. It is assumed that the interferometer with helicity preserving mirrors has a constant reflectance equals to 0.95. The cavity with preserving helicity mirrors enhances the DCT of about one order of magnitude, with respect to the chiral parameter $\kappa_p = 10^{-3}$. The enhancement takes place around 3.7 eV, far away from the resonance of the material under investigation. This discrepancy between the two DCTs is mainly due to the presence of the real part of the refractive index in $DCT_{\perp}^{ahp}$, term contained in $\beta_{\pm} = kn'_{\pm,re}$. The real part of the refractive index, directly connected to the optical rotation, dominates over the absorption coefficients $\alpha_{\pm}$ producing a behaviour similar to the real part of κ_p (see eq. (12.7)) at resonance and an enhanced change of sign around 3.7 eV. Going to higher frequencies similar patterns appear for the periodic nature of the terms $\cos 2\beta_{\pm}$ in the numerator and the denominator of eq. (C.1).

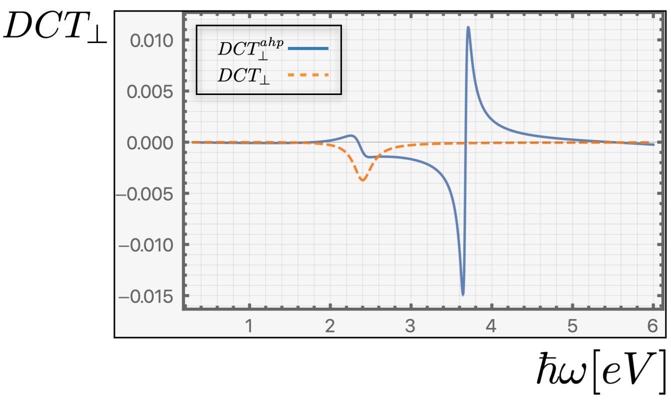

Figure C.1: DCT for the analytical formula of the helicity preserving mirror (see eq. (C.1)) (light-blue line) and for the analytical one (see eq. (12.34)) (orange dashed line) from a Fabry-Pérot interferometer, composed by air-chiral P3HT-air, as a function of $\hbar\omega$ in unit of eV. Parameters are as follows: $n = 1$, $R = 0.95$, $L_{P3HT} = 100\,\mathrm{nm}$, $\varepsilon_{\infty,P3HT} = 2.89$, $(\hbar^2\omega_p^2 f_0)_{P3HT} = 0.3\,\mathrm{eV}^2$, $\hbar\omega_{0,P3HT} = 2.4\,\mathrm{eV}$, $\hbar\gamma_{P3HT} = 0.28\,\mathrm{eV}$, and $\kappa_p = 10^{-3}$.

Bibliography

[1] V. Agranovich, H. Benisty, and C. Weisbuch. Organic and inorganic quantum wells in a microcavity: Frenkel-wannier-mott excitons hybridization and energy transformation. *Solid State Communications*, 102(8):631–636, 1997.

[2] P. W. Anderson. Absence of diffusion in certain random lattices. *Phys. Rev.*, 109:1492–1505, Mar 1958.

[3] D. F. Arago. Sur une modification remarquable qu'éprouvent les rayons lumineux dans leur passage à travers certaines corps diaphanes, et sur quelques autres nouveaux phénomènes d'optique. *Mem.Inst.*, 1:93–134, 1811.

[4] P. Atkins and R. Friedman. *Molecular Quantum Mechanics*. Oxford University Press, 2011.

[5] Alexandre Bachelet, Marion Chabot, Abduleziz Ablat, Kazuo Takimiya, Lionel Hirsch, and Mamatimin Abbas. Low voltage operating organic light emitting transistors with efficient charge blocking layer. *Organic Electronics*, 88:106024, 2021.

[6] Hadi Bahsoun, Thibault Chervy, Anoop Thomas, Karl Börjesson, Manuel Hertzog, Jino George, Eloïse Devaux, Cyriaque Genet, James A. Hutchison, and Thomas W. Ebbesen. Electronic Light–Matter Strong Coupling in Nanofluidic Fabry–Pérot Cavities. *ACS Photonics*, 5(1):225–232, January 2018.

[7] Denis G. Baranov, Battulga Munkhbat, Nils Odebo Länk, Ruggero Verre, Mikael Käll, and Timur Shegai. Circular dichroism mode splitting and bounds to its enhancement with cavity-plasmon-polaritons. *Nanophotonics*, 9(2):283–293, 2020.

[8] S. Bassiri, C. H. Papas, and N. Engheta. Electromagnetic wave propagation through a dielectric–chiral interface and through a chiral slab: errata. *J. Opt. Soc. Am. A*, 7(11):2154–2155, Nov 1990.

[9] D. Beutel, P. Scott, M. Wegener, C. Rockstuhl, and I. Fernandez-Corbaton. Enhancing the optical rotation of chiral molecules using helicity preserving all-dielectric metasurfaces. *Applied Physics Letters*, 118(22):221108, 2021.

[10] Iwo Bialynicki-Birula and Zofia Bialynicka-Birula. *Journal of Physics A: Mathematical and Theoretical*, 46(15):159501, apr 2013.

[11] J. B. Biot. Mémoire sur un nouveau genre d'oscillations que les molécules de la lumière éprouvent, en traversant certaines cristaux. *Mem.Inst.*, 1:1–372, 1812.

[12] B. V. Bokut and F. I. Federov. Reflection and refraction of light in optically isotropic active media. *Opt. Spektrosk.*, 9:334–336, 1960.

[13] M. Born and E. Wolf. *Principles of Optics*. Pergamon, New York, 1980.

[14] T. Botzung, D. Hagenmüller, S. Schütz, J. Dubail, G. Pupillo, and J. Schachenmayer. Dark state semilocalization of quantum emitters in a cavity. *Phys. Rev. B*, 102:144202, Oct 2020.

[15] Petr Bouchal, Josef Kapitán, Martin Konečný, Marek Zbončák, and Zdeněk Bouchal. Non-diffracting light in nature: Anomalously reflected self-healing bessel beams from jewel scarabs. *APL Photonics*, 4(12):126102, 2019.

[16] Dorje C Brody. Biorthogonal quantum mechanics. *J. Phys. A: Math. Theor.*, 47(3):035305, 2014.

[17] J.A. Campos-Gonzalez-Angulo, R.F. Ribeiro, and J. Yuen-Zhou. Resonant catalysis of thermally activated chemical reactions with vibrational polaritons. *Nature Communications*, 10(1):1–8, 2019.

[18] Antoine Canaguier-Durand, Eloïse Devaux, Jino George, Yantao Pang, James A Hutchison, Tal Schwartz, Cyriaque Genet, Nadine Wilhelms, Jean-Marie Lehn, and Thomas W Ebbesen. Thermodynamics of Molecules Strongly Coupled to the Vacuum Field. *Angew. Chem. Int. Ed.*, 52(40):10533–10536, 2013.

[19] Antoine Canaguier-Durand, Cyriaque Genet, Astrid Lambrecht, Thomas W. Ebbesen, and Serge Reynaud. Non-Markovian polariton dynamics in organic strong coupling. *Eur. Phys. J. D*, 69(1):24, January 2015.

[20] Rémi Carminati, Manuel Nieto-Vesperinas, and Jean-Jacques Greffet. Reciprocity of evanescent electromagnetic waves. *J. Opt. Soc. Am. A*, 15(3):706–712, Mar 1998.

[21] H. B. G. Casimir. On onsager's principle of microscopic reversibility. *Rev. Mod. Phys.*, 17:343–350, Apr 1945.

[22] Hsing-Ta Chen, Zeyu Zhou, Maxim Sukharev, Joseph E. Subotnik, and Abraham Nitzan. The interplay between disorder and collective coherent response: Superradiance and spectral motional narrowing in the time domain, 2022.

[23] Yang Chen, Weijin Chen, Xianghong Kong, Dong Wu, Jiaru Chu, and Cheng-Wei Qiu. Can weak chirality induce strong coupling between resonant states? *Phys. Rev. Lett.*, 128:146102, Apr 2022.

[24] Rohit Chikkaraddy, Bart De Nijs, Felix Benz, Steven J Barrow, Oren A Scherman, Edina Rosta, Angela Demetriadou, Peter Fox, Ortwin Hess, and Jeremy J Baumberg. Single-molecule strong coupling at room temperature in plasmonic nanocavities. *Nature*, 535(7610):127–130, 2016.

[25] Régis Chirat, Alain Goriely, and Derek E. Moulton. The physical basis of mollusk shell chiral coiling. *Proceedings of the National Academy of Sciences*, 118(48):e2109210118, 2021.

[26] Cristiano Ciuti and Iacopo Carusotto. Input-output theory of cavities in the ultrastrong coupling regime: The case of time-independent cavity parameters. *Phys. Rev. A*, 74(3):033811, 2006.

[27] Claude Cohen-Tannoudji, Bernard Diu, and Franck Laloë. *Mécanique quantique.* Hermann, EDP Sciences, 1998.

[28] Claude Cohen-Tannoudji, Jacques Dupont-Roc, and Gilbert Grynberg. *Atom-Photon Interactions: Basic Processes and Applications.* WILEY-VCH, Weinheim, 2004.

[29] E. U. Condon. Theories of optical rotatory power. *Rev. Mod. Phys.*, 9:432–457, Oct 1937.

[30] David Parker Craig and Thiru Thirunamachandran. *Molecular Quantum Electrodynamics: An Introduction to Radiation-Molecule Interactions.* Academic Press, INC., London, 1984.

[31] Justyna A. Ćwik, Peter Kirton, Simone De Liberato, and Jonathan Keeling. Excitonic spectral features in strongly coupled organic polaritons. *Phys. Rev. A*, 93(3):033840, March 2016.

[32] M. Decker, M. Ruther, C. E. Kriegler, J. Zhou, C. M. Soukoulis, S. Linden, and M. Wegener. Strong optical activity from twisted-cross photonic metamaterials. *Opt. Lett.*, 34(16):2501–2503, Aug 2009.

[33] Courtney A. DelPo, Saeed-Uz-Zaman Khan, Kyu Hyung Park, Bryan Kudisch, Barry P. Rand, and Gregory D. Scholes. Polariton decay in donor–acceptor cavity systems. *The Journal of Physical Chemistry Letters*, 12(40):9774–9782, 2021.

[34] Courtney A. DelPo, Bryan Kudisch, Kyu Hyung Park, Saeed-Uz-Zaman Khan, Francesca Fassioli, Daniele Fausti, Barry P. Rand, and Gregory D. Scholes. Polariton transitions in femtosecond transient absorption studies of ultrastrong light–molecule coupling. *The Journal of Physical Chemistry Letters*, 11(7):2667–2674, 2020. PMID: 32186878.

[35] Maria C. di Gregorio, Assaf Ben Moshe, Einat Tirosh, Luciano Galantini, and Gil Markovich. Chiroptical study of plasmon–molecule interaction: The case of interaction of glutathione with silver nanocubes. *The Journal of Physical Chemistry C*, 119(30):17111–17116, 2015.

[36] R. H. Dicke. Coherence in Spontaneous Radiation Processes. *Phys. Rev.*, 93(1):99–110, January 1954.

[37] R. R. Dogonadze, A. M. Kuznetsov, and M. A. Vorotyntsev. On the theory of nonradiative transitions in polar media i. processes without “mixing” of quantum and classical degrees of freedom. *physica status solidi (b)*, 54(1):125–134, 1972.

[38] Marcin Dukalski and Yaroslav M Blanter. High Jaynes-Cummings pseudospins eigenstates in the homogeneous Tavis-Cummings model. *arXiv:1301.4857*, 2013.

[39] Thomas W. Ebbesen. Hybrid Light–Matter States in a Molecular and Material Science Perspective. *Acc. Chem. Res.*, 49(11):2403–2412, November 2016.

[40] M. G. Evans and M. Polanyi. Some applications of the transition state method to the calculation of reaction velocities, especially in solution. *Trans. Faraday Soc.*, 31(0):875–894, January 1935.

[41] H. Eyring, J. Walter, and G. Kimball. *Quantum Chemistry.* Wiley, New York, 1944.

[42] Henry. Eyring. The Activated Complex and the Absolute Rate of Chemical Reactions. *Chem. Rev.*, 17(1):65–77, August 1935.

[43] Shanhui Fan and J. D. Joannopoulos. Analysis of guided resonances in photonic crystal slabs. *Phys. Rev. B*, 65:235112, Jun 2002.

[44] Shanhui Fan, Wonjoo Suh, and J. D. Joannopoulos. Temporal coupled-mode theory for the fano resonance in optical resonators. *J. Opt. Soc. Am. A*, 20(3):569–572, Mar 2003.

[45] Zhiyuan Fan and Alexander O. Govorov. Plasmonic circular dichroism of chiral metal nanoparticle assemblies. *Nano Letters*, 10(7):2580–2587, 2010. PMID: 20536209.

[46] Francesca Fassioli, Kyu Hyung Park, Sarah E. Bard, and Gregory D. Scholes. Femtosecond photophysics of molecular polaritons. *The Journal of Physical Chemistry Letters*, 12(46):11444–11459, 2021. PMID: 34792371.

[47] Joshua Feis, Dominik Beutel, Julian Köpfler, Xavier Garcia-Santiago, Carsten Rockstuhl, Martin Wegener, and Ivan Fernandez-Corbaton. Helicity-preserving optical cavity modes for enhanced sensing of chiral molecules. *Phys. Rev. Lett.*, 124:033201, Jan 2020.

[48] Johannes Feist, Javier Galego, and Francisco J. Garcia-Vidal. Polaritonic chemistry with organic molecules. *ACS Photonics*, 5(1):205–216, 2018.

[49] Simone Felicetti, Jacopo Fregoni, Thomas Schnappinger, Sebastian Reiter, Regina de Vivie-Riedle, and Johannes Feist. Photoprotecting uracil by coupling with lossy nanocavities. *The Journal of Physical Chemistry Letters*, 11(20):8810–8818, 2020. PMID: 32914984.

[50] Johannes Flick, Michael Ruggenthaler, Heiko Appel, and Angel Rubio. Atoms and molecules in cavities, from weak to strong coupling in quantum-electrodynamics (qed) chemistry. *Proceedings of the National Academy of Sciences*, 114(12):3026–3034, 2017.

[51] Karl F. Freed and Joshua Jortner. Multiphonon Processes in the Nonradiative Decay of Large Molecules. *J. Chem. Phys.*, 52(12):6272–6291, June 1970.

[52] Jacopo Fregoni, Giovanni Granucci, Maurizio Persico, and Stefano Corni. Strong coupling with light enhances the photoisomerization quantum yield of azobenzene. *Chem*, 6(1):250–265, 2020.

[53] A. Fresnel. Mémoire sur la double réfraction que les rayons lumineux éprouvent en traversant les aiguilles de cristal de roche suivant des directions parallèles à l'axe. *Oeuvres*, 1:731–751, 1822.

[54] Javier Galego, Clàudia Climent, Francisco J. Garcia-Vidal, and Johannes Feist. Cavity casimir-polder forces and their effects in ground-state chemical reactivity. *Phys. Rev. X*, 9:021057, Jun 2019.

[55] Javier Galego, Francisco J. Garcia-Vidal, and Johannes Feist. Cavity-Induced Modifications of Molecular Structure in the Strong-Coupling Regime. *Phys. Rev. X*, 5(4):041022, November 2015.

[56] Javier Galego, Francisco J. Garcia-Vidal, and Johannes Feist. Suppressing photochemical reactions with quantized light fields. *Nat. Commun.*, 7:13841, December 2016.

[57] Javier Galego, Francisco J. Garcia-Vidal, and Johannes Feist. Many-Molecule Reaction Triggered by a Single Photon in Polaritonic Chemistry. *Phys. Rev. Lett.*, 119(13):136001, September 2017.

[58] Crispin W Gardiner and Matthew J Collett. Input and output in damped quantum systems: Quantum stochastic differential equations and the master equation. *Phys. Rev. A*, 31(6):3761, 1985.

[59] Jérôme Gautier, Minghao Li, Thomas W. Ebbesen, and Cyriaque Genet. Planar chirality and optical spin–orbit coupling for chiral fabry–perot cavities. *ACS Photonics*, 9(3):778–783, 2022.

[60] Jino George, Atef Shalabney, James A. Hutchison, Cyriaque Genet, and Thomas W. Ebbesen. Liquid-Phase Vibrational Strong Coupling. *The Journal of Physical Chemistry Letters*, 6(6):1027–1031, March 2015.

[61] Maxim V. Gorkunov, Alexander A. Antonov, and Yuri S. Kivshar. Metasurfaces with maximum chirality empowered by bound states in the continuum. *Phys. Rev. Lett.*, 125:093903, Aug 2020.

[62] Alexander O. Govorov. Plasmon-induced circular dichroism of a chiral molecule in the vicinity of metal nanocrystals. application to various geometries. *The Journal of Physical Chemistry C*, 115(16):7914–7923, 2011.

[63] Gilbert Grynberg, Alain Aspect, Claude Fabre, and Claude Cohen-Tannoudji. *Introduction to Quantum Optics: From the Semi-classical Approach to Quantized Light.* Cambridge, September 2010.

[64] Etienne Guyon, Jean-Pierre Hulin, and Luc Petit. *Hydrodynamique physique.* EDP Sciences, 2001.

[65] Serge Haroche and Daniel Kleppner. Cavity Quantum Electrodynamics. *Physics Today*, 42:24, 1989.

[66] Tor S. Haugland, Enrico Ronca, Eirik F. Kjønstad, Angel Rubio, and Henrik Koch. Coupled cluster theory for molecular polaritons: Changing ground and excited states. *Phys. Rev. X*, 10:041043, Dec 2020.

[67] Tor S. Haugland, Christian Schäfer, Enrico Ronca, Angel Rubio, and Henrik Koch. Intermolecular interactions in optical cavities: An ab initio qed study. *The Journal of Chemical Physics*, 154(9):094113, 2021.

[68] Federico J. Hernández and Felipe Herrera. Multi-level quantum rabi model for anharmonic vibrational polaritons. *The Journal of Chemical Physics*, 151(14):144116, 2019.

[69] Felipe Herrera and Jeffrey Owrutsky. Molecular polaritons for controlling chemistry with quantum optics. *The Journal of Chemical Physics*, 152(10):100902, 2020.

[70] Felipe Herrera and Frank C. Spano. Cavity-Controlled Chemistry in Molecular Ensembles. *Phys. Rev. Lett.*, 116(23):238301, June 2016.

[71] Manuel Hertzog, Mao Wang, Jürgen Mony, and Karl Börjesson. Strong light–matter interactions: a new direction within chemistry. *Chem. Soc. Rev.*, 48:937–961, 2019.

[72] Kenji Hirai, James A. Hutchison, and Hiroshi Uji-i. Recent progress in vibropolaritonic chemistry. *ChemPlusChem*, 85(9):1981–1988, 2020.

[73] Kenji Hirai, Rie Takeda, James A. Hutchison, and Hiroshi Uji-i. Modulation of prins cyclization by vibrational strong coupling. *Angewandte Chemie International Edition*, 59(13):5332–5335, 2020.

[74] Norah M. Hoffmann, Lionel Lacombe, Angel Rubio, and Neepa T. Maitra. Effect of many modes on self-polarization and photochemical suppression in cavities. *The Journal of Chemical Physics*, 153(10):104103, 2020.

[75] Th Holstein. Studies of polaron motion: Part I. The molecular-crystal model. *Ann. Physics*, 8(3):325–342, 1959.

[76] J. J. Hopfield. Electron Transfer Between Biological Molecules by Thermally Activated Tunneling. *PNAS*, 71(9):3640–3644, September 1974.

[77] R. Houdré, R. P. Stanley, and M. Ilegems. Vacuum-field Rabi splitting in the presence of inhomogeneous broadening: Resolution of a homogeneous linewidth in an inhomogeneously broadened system. *Phys. Rev. A*, 53(4):2711–2715, April 1996.

[78] Kun Huang and Avril Rhys. Theory of light absorption and non-radiative transitions in F-centres. In *Selected Papers Of Kun Huang: (With Commentary)*, pages 74–92. World Scientific, 2000.

[79] James A. Hutchison, Andrea Liscio, Tal Schwartz, Antoine Canaguier-Durand, Cyriaque Genet, Vincenzo Palermo, Paolo Samorì, and Thomas W. Ebbesen. Tuning the Work-Function Via Strong Coupling. *Advanced Materials*, 25(17):2481–2485, May 2013.

[80] James A. Hutchison, Tal Schwartz, Cyriaque Genet, Eloïse Devaux, and Thomas W. Ebbesen. Modifying Chemical Landscapes by Coupling to Vacuum Fields. *Angew. Chem. Int. Ed.*, 51(7):1592–1596, February 2012.

[81] Tomoyuki Ikai, Kokoro Takayama, Yuya Wada, Serena Minami, Chanokporn Apiboon, and Ken-ichi Shinohara. Synthesis of a one-handed helical polythiophene: a new approach using an axially chiral bithiophene with a fixed syn-conformation. *Chem. Sci.*, 10:4890–4895, 2019.

[82] Wolfram Research, Inc. Mathematica, Version 13.0.0. Champaign, IL, 2021.

[83] Nur Ismail, Cristine Calil Kores, Dimitri Geskus, and Markus Pollnau. Fabry-pérot resonator: spectral line shapes, generic and related airy distributions, linewidths, finesses, and performance at low or frequency-dependent reflectivity. *Opt. Express*, 24(15):16366–16389, Jul 2016.

[84] J. D. Jackson. *Classical Electrodynamics*. Wiley, California, 1999.

[85] D. L. Jaggard, A. R. Mickelson, and C. J. Papas. On electromagnetic waves in chiral media. *Appl. Phys.*, 18(2):211–216, 1979.

[86] Dwight L. Jaggard and Xiaoguang Sun. Theory of chiral multilayers. *J. Opt. Soc. Am. A*, 9(5):804–813, May 1992.

[87] R. Clark Jones. A new calculus for the treatment of optical systemsi. description and discussion of the calculus. *J. Opt. Soc. Am.*, 31(7):488–493, Jul 1941.

[88] Y. Kaluzny, P. Goy, M. Gross, J. M. Raimond, and S. Haroche. Observation of self-induced rabi oscillations in two-level atoms excited inside a resonant cavity: The ringing regime of superradiance. *Phys. Rev. Lett.*, 51:1175–1178, Sep 1983.

[89] Neil R. Kestner, Jean Logan, and Joshua Jortner. Thermal electron transfer reactions in polar solvents. *J. Phys. Chem.*, 78(21):2148–2166, October 1974.

[90] Jens Koch, Felix von Oppen, and A. V. Andreev. Theory of the franck-condon blockade regime. *Phys. Rev. B*, 74:205438, Nov 2006.

[91] A. V. Kondratov, M. V. Gorkunov, A. N. Darinskii, R. V. Gainutdinov, O. Y. Rogov, A. A. Ezhov, and V. V. Artemov. Extreme optical chirality of plasmonic nanohole arrays due to chiral fano resonance. *Phys. Rev. B*, 93:195418, May 2016.

[92] H. A. Kramers. Brownian motion in a field of force and the diffusion model of chemical reactions. *Physica*, 7(4):284–304, April 1940.

[93] Makoto Kuwata-Gonokami, Nobuyoshi Saito, Yusuke Ino, Martti Kauranen, Konstantins Jefimovs, Tuomas Vallius, Jari Turunen, and Yuri Svirko. Giant optical activity in quasi-two-dimensional planar nanostructures. *Phys. Rev. Lett.*, 95:227401, Nov 2005.

[94] I.J. Lalov and A.I. Miteva. Optically active fabry-perot etalon. *Journal of Modern Optics*, 38(2):395–411, 1991.

[95] L. D. Landau and E. M. Lifshitz. *Course of Theoretical Physics: Fluid Mechanics*. Pergamon Press, 1987.

[96] Jyoti Lather, Pooja Bhatt, Anoop Thomas, Thomas W. Ebbesen, and Jino George. Cavity catalysis by cooperative vibrational strong coupling of reactant and solvent molecules. *Angewandte Chemie International Edition*, 58(31):10635–10638, 2019.

[97] John Lekner. Optical properties of isotropic chiral media. *Pure and Applied Optics: Journal of the European Optical Society Part A*, 5(4):417–443, jul 1996.

[98] IV Leontyev and M Tachiya. The reorganization energy of electron transfer in nonpolar solvents: Molecular level treatment of the solvent. *J. Chem. Phys.*, 123(22):224502, 2005.

[99] V. G. Levich. *Advan. Electrochem. Electrochem. Eng.*, 4(249), 1966.

[100] Tao E. Li, Abraham Nitzan, and Joseph E. Subotnik. On the origin of ground-state vacuum-field catalysis: Equilibrium consideration. *The Journal of Chemical Physics*, 152(23):234107, 2020.

[101] D. G. Lidzey, D. D. C. Bradley, M. S. Skolnick, T. Virgili, S. Walker, and D. M. Whittaker. Strong exciton–photon coupling in an organic semiconductor microcavity. *Nature*, 395:53–55, 1998.

[102] I. V. Lindell, A. Sihvola, A. Viitanen, and S. Tretyakov. *Electromagnetic waves in chiral and bi-isotropic media*. Artech House Publishers, 1994.

[103] T. M. Lowry. *Optical Rotatory Power*. Dover, New York, 1964.

[104] Hoi Ling Luk, Johannes Feist, J. Jussi Toppari, and Gerrit Groenhof. Multiscale molecular dynamics simulations of polaritonic chemistry. *Journal of Chemical Theory and Computation*, 13(9):4324–4335, 2017. PMID: 28749690.

[105] H. A. Macleod. *Thin-Film Optical Filters*. CRC Press, 2010.

[106] Arkajit Mandal, Todd D Krauss, and Pengfei Huo. Polariton-Mediated Electron Transfer via Cavity Quantum Electrodynamics. *J. Phys. Chem. B*, 124:6321–6340, 2020.

[107] R. A. Marcus. On the Theory of Oxidation-Reduction Reactions Involving Electron Transfer. I. *J. Chem. Phys.*, 24(5):966–978, May 1956.

[108] R. A. Marcus. Nonadiabatic processes involving quantum-like and classical-like coordinates with applications to nonadiabatic electron transfers. *J. Chem. Phys.*, 81(10):4494–4500, November 1984.

[109] Rudolph A. Marcus. Electron transfer reactions in chemistry. Theory and experiment. *Rev. Mod. Phys.*, 65(3):599–610, July 1993.

[110] Luis A Martínez-Martínez and Joel Yuen-Zhou. Comment on 'Quantum theory of collective strong coupling of molecular vibrations with a microcavity mode'. *New J. Phys.*, 20(1):018002, feb 2018.

[111] L. Mauro, K. Caicedo, G. Jonusauskas, and R. Avriller. Charge-transfer chemical reactions in nanofluidic fabry-pérot cavities. *Phys. Rev. B*, 103:165412, Apr 2021.

[112] Michael Maus and Wolfgang Rettig. The Excited State Equilibrium between Two Rotational Conformers of a Sterically Restricted Donor-Acceptor Biphenyl As Characterized by Global Fluorescence Decay Analysis. *J. Phys. Chem. A*, 106(10):2104–2111, March 2002.

[113] V. May and O. Kühn. *Charge and Energy Transfer Dynamics in Molecular Systems*. WILEY-VCH, Verlag, 2011.

[114] P. Mazzoldi, M. Nigro, and C. Voci. *Fisica*. Edises, Napoli, 2016.

[115] J. R. Miller, L. T. Calcaterra, and G. L. Closs. Intramolecular long-distance electron transfer in radical anions. the effects of free energy and solvent on the reaction rates. *Journal of the American Chemical Society*, 106(10):3047–3049, 1984.

[116] Kalaivanan Nagarajan, Anoop Thomas, and Thomas W. Ebbesen. Chemistry under vibrational strong coupling. *Journal of the American Chemical Society*, 143(41):16877–16889, 2021. PMID: 34609858.

[117] Abraham Nitzan. *Chemical Dynamics in Condensed Phases*. Oxford University Press, Oxford, 2006.

[118] Sang Soon Oh and Ortwin Hess. Chiral metamaterials: enhancement and control of optical activity and circular dichroism. *Nano Convergence*, 2(24), 2015.

[119] E. Orgiu, J. George, J. A. Hutchison, E. Devaux, J. F. Dayen, B. Doudin, F. Stellacci, C. Genet, J. Schachenmayer, C. Genes, G. Pupillo, P. Samorì, and T. W. Ebbesen. Conductivity in organic semiconductors hybridized with the vacuum field. *Nature Materials*, 14(11):1123, November 2015.

[120] Yuri I Ozhigov. Space of Dark States in Tavis-Cummings Model. *Modern Information Technologies and IT-Education*, 15:13–26, 2019.

[121] Yantao Pang, Anoop Thomas, Kalaivanan Nagarajan, Robrecht M. A. Vergauwe, Kripa Joseph, Bianca Patrahau, Kuidong Wang, Cyriaque Genet, and Thomas W. Ebbesen. On the role of symmetry in vibrational strong coupling: The case of charge-transfer complexation. *Angewandte Chemie International Edition*, 59(26):10436–10440, 2020.

[122] Sindhana Pannir-Sivajothi, Jorge A. Campos-Gonzalez-Angulo, Luis A. Martínez-Martínez, Shubham Sinha, and Joel Yuen-Zhou. Driving chemical reactions with polariton condensates. *Nature Communications*, 13(1645), 2022.

[123] A. Papakostas, A. Potts, D. M. Bagnall, S. L. Prosvirnin, H. J. Coles, and N. I. Zheludev. Optical manifestations of planar chirality. *Phys. Rev. Lett.*, 90:107404, Mar 2003.

[124] R. G. Parr and W. Yang. *Density-Functional Theory of Atoms and Molecules.* Oxford Science Publications, New York, 1989.

[125] L. Pasteur. Sur les relationes qui peuvent exister entre la forme cristalline, la composition chimique et le sens de la polarisation rotatoire. *Ann. Chim. Phys.*, 24:442–459, 1848.

[126] Harry Paul. Induzierte emission bei starker einstrahlung. *Annalen der Physik*, 466(7-8):411–412, 1963.

[127] Linus Pauling. *General chemistry.* Dover Pubblications, INC., New York, 1988.

[128] Frank L. Pedrotti, Leno M. Pedrotti, and Leno S. Pedrotti. *Introduction to Optics.* 2017.

[129] Javier del Pino, Johannes Feist, and Francisco J. Garcia-Vidal. Quantum theory of collective strong coupling of molecular vibrations with a microcavity mode. *New J. Phys.*, 17(5):053040, 2015.

[130] Eric Plum and Nikolay I. Zheludev. Chiral mirrors. *Applied Physics Letters*, 106(22):221901, 2015.

[131] E. J. Post. *Formal Structure of Electromagnetics.* North-Holland Publishing Company, Amsterdam, 1962.

[132] Gerhard Rempe, Herbert Walther, and Norbert Klein. Observation of quantum collapse and revival in a one-atom maser. *Phys. Rev. Lett.*, 58:353–356, Jan 1987.

[133] Raphael F Ribeiro, Luis A Martínez-Martínez, Matthew Du, Jorge Campos-Gonzalez-Angulo, and Joel Yuen-Zhou. Polariton chemistry: controlling molecular dynamics with optical cavities. *Chem. Sci.*, 9(30):6325–6339, 2018.

[134] R. R. Riso, Tor S. Haugland, Enrico Ronca, and Henrik Koch. Molecular orbital theory in cavity qed environments. *Nature Communications*, 13(1368), 2022.

[135] Bart Rosenzweig, Norah M. Hoffmann, Lionel Lacombe, and Neepa T. Maitra. Analysis of the classical trajectory treatment of photon dynamics for polaritonic phenomena. *The Journal of Chemical Physics*, 156(5):054101, 2022.

[136] Michael Ruggenthaler, Johannes Flick, Camilla Pellegrini, Heiko Appel, Ilya V. Tokatly, and Angel Rubio. Quantum-electrodynamical density-functional theory: Bridging quantum optics and electronic-structure theory. *Physical Review A*, 90(1):012508, July 2014.

[137] David S. Saxon. Tensor scattering matrix for the electromagnetic field. *Phys. Rev.*, 100:1771–1775, Dec 1955.

[138] Gregory D. Scholes, Courtney A. DelPo, and Bryan Kudisch. Entropy reorders polariton states. *The Journal of Physical Chemistry Letters*, 11(15):6389–6395, 2020. PMID: 32678609.

[139] T. Schwartz, J. A. Hutchison, C. Genet, and T. W. Ebbesen. Reversible Switching of Ultrastrong Light-Molecule Coupling. *Phys. Rev. Lett.*, 106(19):196405, May 2011.

[140] Tal Schwartz, James A Hutchison, Jérémie Léonard, Cyriaque Genet, Stefan Haacke, and Thomas W Ebbesen. Polariton Dynamics under Strong Light-Molecule Coupling. *ChemPhysChem*, 14(1):125–131, 2013.

[141] Alexander Semenov and Abraham Nitzan. Electron transfer in confined electromagnetic fields. *J. Chem. Phys.*, 150(17):174122, 2019.

[142] B. Semnani, J. Flannery, and R. Al Maruf. Spin-preserving chiral photonic crystal mirror. *Light: Science & Applications*, 9(23), 2020.

[143] A. Shalabney, J. George, J. Hutchison, G. Pupillo, C. Genet, and T. W. Ebbesen. Coherent coupling of molecular resonators with a microcavity mode. *Nature Communications*, 6:5981, January 2015.

[144] Atef Shalabney, Jino George, Hidefumi Hiura, James A. Hutchison, Cyriaque Genet, Petra Hellwig, and Thomas W. Ebbesen. Enhanced Raman Scattering from Vibro-Polariton Hybrid States. *Angewandte Chemie International Edition*, 54(27):7971–7975, June 2015.

[145] P. Siders and R. A. Marcus. Quantum effects in electron-transfer reactions. *J. Am. Chem. Soc.*, 103(4):741–747, February 1981.

[146] Dominik Sidler, Michael Ruggenthaler, Heiko Appel, and Angel Rubio. Chemistry in quantum cavities: Exact results, the impact of thermal velocities, and modified dissociation. *The Journal of Physical Chemistry Letters*, 11(18):7525–7530, 2020. PMID: 32805122.

[147] Dominik Sidler, Michael Ruggenthaler, Christian Schäfer, Enrico Ronca, and Angel Rubio. A perspective on ab initio modeling of polaritonic chemistry: The role of non-equilibrium effects and quantum collectivity. *The Journal of Chemical Physics*, 156(23):230901, 2022.

[148] Dominik Sidler, Christian Schäfer, Michael Ruggenthaler, and Angel Rubio. Polaritonic chemistry: Collective strong coupling implies strong local modification of chemical properties. *The Journal of Physical Chemistry Letters*, 12(1):508–516, 2021. PMID: 33373238.

[149] Ludwig Silberstein. Elektromagnetische grundgleichungen in bivektorieller behandlung. *Annalen der Physik*, 327(3):579–586, 1907.

[150] M. P. Silverman. Reflection and refraction at the surface of a chiral medium: comparison of gyrotropic constitutive relations invariant or noninvariant under a duality transformation. *J. Opt. Soc. Am. A*, 3(6):830–837, Jun 1986.

[151] M. P. Silverman and J. Badoz. Light reflection from a naturally optically active birefringent medium. *J. Opt. Soc. Am. A*, 7(7):1163–1173, Jul 1990.

[152] M. P. Silverman and J. Badoz. Interferometric enhancement of chiral asymmetries: ellipsometry with an optically active fabry–perot interferometer. *J. Opt. Soc. Am. A*, 11(6):1894–1917, Jun 1994.

[153] W. P. Su, J. R. Schrieffer, and A. J. Heeger. Solitons in Polyacetylene. *Phys. Rev. Lett.*, 42(25):1698, 1979.

[154] Shichao Sun, Bing Gu, and Shaul Mukamel. Polariton ring currents and circular dichroism of mg-porphyrin in a chiral cavity. *Chem. Sci.*, 13:1037–1048, 2022.

[155] Shota Takahashi, Kazuya Watanabe, and Yoshiyasu Matsumoto. Singlet fission of amorphous rubrene modulated by polariton formation. *The Journal of Chemical Physics*, 151(7):074703, 2019.

[156] Alexey Taradin and Denis G. Baranov. Chiral light in single-handed fabry-perot resonators. *Journal of Physics: Conference Series*, 2015(1):012012, nov 2021.

[157] Michael Tavis and Frederick W. Cummings. Exact Solution for an N-Molecule−Radiation-Field Hamiltonian. *Phys. Rev.*, 170(2):379–384, June 1968.

[158] A. Thomas, L. Lethuillier-Karl, K. Nagarajan, R. M. A. Vergauwe, J. George, T. Chervy, A. Shalabney, E. Devaux, C. Genet, J. Moran, and T. W. Ebbesen. Tilting a ground-state reactivity landscape by vibrational strong coupling. *Science*, 363(6427):615–619, 2019.

[159] Anoop Thomas, Jino George, Atef Shalabney, Marian Dryzhakov, Sreejith J. Varma, Joseph Moran, Thibault Chervy, Xiaolan Zhong, Eloïse Devaux, Cyriaque Genet, James A. Hutchison, and Thomas W. Ebbesen. Ground-State Chemical Reactivity under Vibrational Coupling to the Vacuum Electromagnetic Field. *Angewandte Chemie*, 128(38):11634–11638, September 2016.

[160] Anoop Thomas, Jino George, Atef Shalabney, Marian Dryzhakov, Sreejith J. Varma, Joseph Moran, Thibault Chervy, Xiaolan Zhong, Eloïse Devaux, Cyriaque Genet, James A. Hutchison, and Thomas W. Ebbesen. Ground-state chemical reactivity under vibrational coupling to the vacuum electromagnetic field. *Angewandte Chemie International Edition*, 55(38):11462–11466, 2016.

[161] John C. Tully. Perspective on “Zur Quantentheorie der Molekeln”. *Theor. Chem. Acc.*, 103(3-4):173–176, February 2000.

[162] Guido Van Rossum and Fred L. Drake. *Python 3 Reference Manual.* CreateSpace, Scotts Valley, CA, 2009.

[163] Daniel Vestler, Assaf Ben-Moshe, and Gil Markovich. Enhancement of circular dichroism of a chiral material by dielectric nanospheres. *The Journal of Physical Chemistry C*, 123(8):5017–5022, 2019.

[164] Evaristo Villaseco Arribas, Federica Agostini, and Neepa T. Maitra. Exact factorization adventures: A promising approach for non-bound states. *Molecules*, 27(13), 2022.

[165] D. F. Walls and G. J. Milburn. *Quantum Optics.* Springer, Berlin, Heidelberg, 2008.

[166] Shaojun Wang, Thibault Chervy, Jino George, James A Hutchison, Cyriaque Genet, and Thomas W Ebbesen. Quantum Yield of Polariton Emission from Hybrid Light-Matter States. *J. Phys. Chem. Lett.*, 5(8):1433–1439, 2014.

[167] Shaojun Wang, Arkadiusz Mika, James A. Hutchison, Cyriaque Genet, Abdelaziz Jouaiti, Mir Wais Hosseini, and Thomas W. Ebbesen. Phase transition of a perovskite strongly coupled to the vacuum field. *Nanoscale*, 6(13):7243–7248, June 2014.

[168] H. Weber. *Die Partielllen Differential-Gleichungen Der Mathematischen Physik: Nach Riemann's Vorlesungen Bearbeitet von Heinrich Weber.* braunschweig:Friedrich Vieweg und Sohn, 1901.

[169] Werner S. Weiglhofer. *Advances in Electromagnetics of Complex Media and Metamaterials.* Springer, Netherlands, 2002.

[170] D. Wellnitz, G. Pupillo, and J. Schachenmayer. A quantum optics approach to photoinduced electron transfer in cavities. *The Journal of Chemical Physics*, 154(5):054104, 2021.

[171] Garret D. Wiesehan and Wei Xiong. Negligible rate enhancement from reported cooperative vibrational strong coupling catalysis. *The Journal of Chemical Physics*, 155(24):241103, 2021.

[172] E. Wigner. The transition state method. *Trans. Faraday Soc.*, 34(0):29–41, January 1938.

[173] Ning Wu, Johannes Feist, and Francisco J Garcia-Vidal. When polarons meet polaritons: Exciton-vibration interactions in organic molecules strongly coupled to confined light fields. *Phys. Rev. B*, 94(19):195409, 2016.

[174] V.A. Yakovlev, V.G. Nazin, and G.N. Zhizhin. The surface polariton splitting due to thin surface film lo vibrations. *Optics Communications*, 15(2):293–295, 1975.

[175] SeokJae Yoo and Q-Han Park. Chiral light-matter interaction in optical resonators. *Phys. Rev. Lett.*, 114:203003, May 2015.

[176] M Ahsan Zeb, Peter G Kirton, and Jonathan Keeling. Exact States and Spectra of Vibrationally Dressed Polaritons. *ACS Photonics*, 5:249–257, 2018.

[177] Shuang Zhang, Yong-Shik Park, Jensen Li, Xinchao Lu, Weili Zhang, and Xiang Zhang. Negative refractive index in chiral metamaterials. *Phys. Rev. Lett.*, 102:023901, Jan 2009.

[178] Vladimir P. Zhdanov. Vacuum field in a cavity, light-mediated vibrational coupling, and chemical reactivity. *Chemical Physics*, 535:110767, 2020.

[179] Xiaolan Zhong, Thibault Chervy, Shaojun Wang, Jino George, Anoop Thomas, James A. Hutchison, Eloise Devaux, Cyriaque Genet, and Thomas W. Ebbesen. Non-Radiative Energy Transfer Mediated by Hybrid Light-Matter States. *Angewandte Chemie International Edition*, 55(21):6202–6206, May 2016.

[180] Xiaolan Zhong, Thibault Chervy, Lei Zhang, Anoop Thomas, Jino George, Cyriaque Genet, James A. Hutchison, and Thomas W. Ebbesen. Energy Transfer between Spatially Separated Entangled Molecules. *Angewandte Chemie International Edition*, 56(31):9034–9038, July 2017.

[181] Yifu Zhu, Daniel J. Gauthier, S. E. Morin, Qilin Wu, H. J. Carmichael, and T. W. Mossberg. Vacuum rabi splitting as a feature of linear-dispersion theory: Analysis and experimental observations. *Phys. Rev. Lett.*, 64:2499–2502, May 1990.